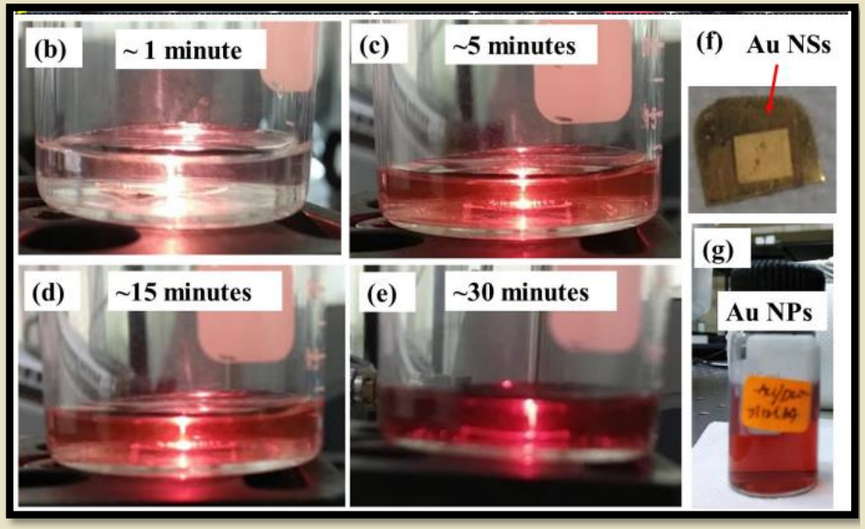

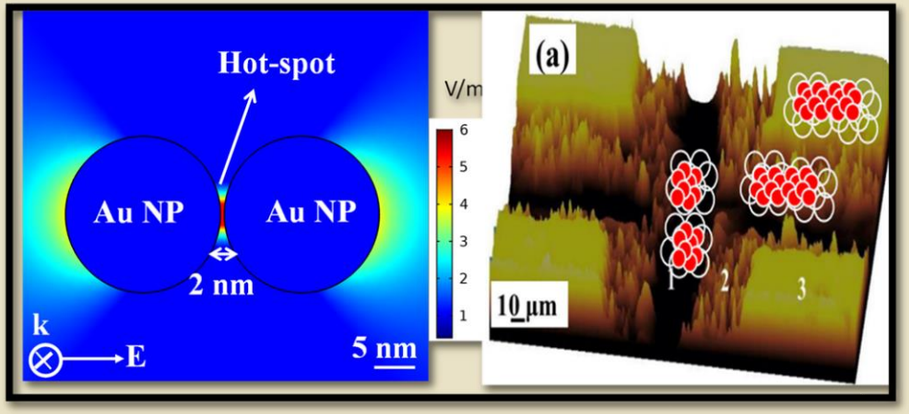

Rigid, Flexible SERS Substrates Fabricated using Femtosecond Laser Pulses for Explosives Detection

Ph.D. Thesis

Rigid, Flexible SERS Substrates Fabricated using Femtosecond Laser Pulses for Explosives Detection

Moram Sree Satya Bharati

Advanced Centre for Research in High Energy Materials **(ACRHEM)**
School of Physics, University of Hyderabad,
Hyderabad 500046, Telangana, India

June 2020

Ph.D. thesis

Rigid, Flexible SERS Substrates Fabricated using Femtosecond Laser Pulses for Explosives Detection

Submitted to the

University of Hyderabad

Towards partial fulfillment for the degree of

Doctor of Philosophy

in

Physics

by

Moram Sree Satya Bharati (15ACPA09)

Under the supervision of

Prof. Soma Venugopal Rao

Advanced Centre for Research in High Energy Materials **(ACRHEM)**
School of Physics, University of Hyderabad
Hyderabad 500046, Telangana, India

June 2020

Declaration

I, **Moram Sree Satya Bharati** hereby declare that this thesis entitled "Rigid, Flexible SERS Substrates Fabricated using Femtosecond Laser Pulses for Explosives Detection" Submitted by me under the guidance and supervision of **Professor Soma Venugopal Rao,** ACRHEM, School of Physics, University of Hyderabad, Telangana, India. is a bonafide research work.

I also declare that it has not been submitted previously in part or in full to this University or any other University or Institution for the award of any degree or diploma.

The report on plagiarism statistics from university libriarian also enclosed.

And also I agree that my thesis can be deposited in Shodhganga/INFLIBNET

Moram Sree Satya Bharati

Regd. No: 15ACPA09

Professor Soma Venugopal Rao,

Thesis supervisor
ACRHEM
School of Physics, University of Hyderabad
Hyderabad 500046, Telangana, India

Dr. Soma Venugopal Rao
Professor
Tel.: +91-40 2313 8811
Fax: +91-40 2301 2800
E-mail: svrsp@uohyd.ernet.in
Soma_venu@yahoo.com

ACRHEM
University of Hyderabad,
Prof. C. R. Rao Road,
Gachibowli,
Hyderabad – 500 046,
Telangana, India.

Certificate

This is to certify that the thesis entitled **"Rigid, Flexible SERS Substrates Fabricated using Femtosecond Laser Pulses for Explosives Detection"** being submitted to the University of Hyderabad by **Moram Sree Satya Bharati** (Reg. No. 15ACPA09), for the award of the degree of Doctor of Philosophy in Physics, is a record of *bonafide* work carried out by him under my supervision and is free of plagiarism. The matter embodied in this report has not been submitted to any other University or Institution for the award of any degree or diploma.

Supervisor
Prof. Soma Venugopal Rao
ACRHEM
University of Hyderabad

Director,
ACRHEM
University of Hyderabad

Dean,
School of Physics
University of Hyderabad

Certificate

This is to certify that the thesis entitled "**Rigid, Flexible SERS Substrates Fabricated using Femtosecond Laser Pulses for Explosives Detection**" submitted by **Moram Sree Satya Bharati** bearing registration number **15ACPA09** in partial fulfillment of the requirements for award of **Doctor of Philosophy in physics at ACRHEM, School of physics, University of Hyderabad** is a bonafide work carried out by him under my supervision and guidance.

This thesis is free from plagiarism and has not been submitted previously in part or in full to this or any other University or Institution for award of any degree or diploma.

Further, the student has the following publications before submission of the thesis for adjudication.

1. **M.S.S. Bharati**, B. Chandu, S. Venugopal Rao, "Femtosecond Laser Fabricated Ag@Au and Cu@Au Alloy Nanoparticles for SERS based Explosives Detection," Frontiers in Physics (Optics and Photonics), 6, Art # 28, 2018. **[Chapter 3]**
2. **M.S.S. Bharati**, B. Chandu, S. Venugopal Rao, "Explosives Detection Using Ag-Cu alloy Nanoparticles Synthesized by Femtosecond Laser Ablation and Irradiation," RSC Advances, 9(3), 1517-1525, 2019. **[Chapter 3]**
3. **M.S.S. Bharati**, S. Abdul Kalam, B. Chandu, S. Hamad, S. Venugopal Rao, "Instantaneous Trace Detection of Nitro-explosives and Mixtures with Nanotextured Silicon Decorated with Ag-Au Alloy Nanoparticles using the SERS Technique," Analytica Chimica Acta 1101, 157-168, 2020. **[Chapter 4]**
4. **M.S.S. Bharati**, B. Chandu, N.S. Sini, Ch. Bindumadhuri, S. Venugopal Rao, "Ag/Au Nanoparticle Loaded Paper-based Versatile SERS Substrates for Explosives Detection," ACS Omega, 3, 8190-8201, 2018. **[Chapter 5a]**
5. **M.S.S. Bharati**, B. Chandu, S. Venugopal Rao, "Gold Nanoparticles and Nanostars Loaded Paper-based SERS Substrates for Sensing Nanogram-level Picric Acid with a Portable Raman Spectrometer," Bulletin of Materials Science, 43, 53, 2020 **[Chapter 5B]**
6. **M. S. S. Bharati**, B. Chandu, K Nehra, P. S. Kumar, and S Venugopal Rao, Filter Paper Loaded with Gold Nanoparticles as Flexible SERS Substrates for Sensing Applications, AIP Conf. Proc., 2020. **[Chapter 5B]**
7. **M.S.S. Bharati**, B. Chandu, P. Lakshmi, S. Venugopal Rao, "Commercial DVDs loaded with Femtosecond Laser Prepared Gold Nanoparticles as SERS Substrates," IEEE WRAP-2019 Proc., 1-3, 2019. **[Appendix B]**
8. S. Venugopal Rao, S. Abdul Kalam, **M.S.S. Bharati**, "Photonics for explosives detection," Wiley Encyclopedia of Applied Physics, 1-31, 2019. (Book Chapter) http://dx.doi.org/10.1002/3527600434.eap826

S No.	Course offered at	Title of the Course	Credits	Pass/Fail
1	SEST	Characterization of Material-Microscopy	4	Pass
2	SEST	Material Processing and Characterization	4	Pass
3	ACREHM	Non-linear Optics	4	Pass
4	ACRHEM	Research Methodology	4	Pass
5	SOP	Advanced Experimental techniques	4	Pass

Supervisor
Dr. Soma Venugopal Rao,
Professor,
ACRHEM, University of Hyderabad,
Hyderabad.

Director,
ACRHEM
University of Hyderabad,
Hyderabad.

Dean
School of Physics,
University of Hyderabad,
Hyderabad.

Acknowledgement

I would like to express my sincere devotion to guru Lord SAIBABA for his blessings to overcome all obstacles and challenges in the life with patience.

I would like to express my heart felt gratitude to my supervisor, Prof. Soma Venugopal Rao for his invaluable guidance and great support throughout my Ph.D. His strong motivation, punctuality, patience, and passion in research inspired me to work hard to complete this work within the time frame. I am immensely thankful to him for giving me a platform to resume my carrier in research field after a gap in my academics. And also, I am very thankful to him by giving an opportunity to become a member in his collaborations and research projects.

I sincerely thank my doctoral committee members Prof. A K Chaudhary and Prof. Suneel Singh for their constructive comments and suggestions. I am privileged to thank Dr. Prem Kiran, Dr. Manoj Kumar, Dr. Sree Harsha, Dr. G S Vaitheeswaran, Dr. Anuj A Vargeese and Dr. Balaka Barkakaty for their support.

It is my pleasure to thank Dr V. Kameswara Rao, Director, ACRHEM; former directors of ACRHEM; Prof. Ashok Chatterjee, Dean School of Physics (SoP); former deans of SoP, University of Hyderabad, for their support towards completion of this work. I would like to thank Defence Research and Development Organization (DRDO), India for providing me the financial support (through ACRHEM) in my PhD.

It is my pleasure to express appreciation to all my seniors and present lab mates for creating productive research environment Dr. G Krishna, Dr.Syed Hamad, Dr. P T Anusha, Dr. Chandu, Dr Abdul Kalam, Dr. Balaji, Mrs Phani Sri, Mr Prathap kumar, Mr. Sarang, Mr K Krishnakanth, Ms Somdatta, Dr. Manikanta, Dr P Venkateswarlu, Dr.Sai shiva, Dr. G Ravi Kiran, Mr N Linga murthy, Mr D Ganesh, Mr J Rajendhar, Mr G Nagaraju, Mr John, Mr Subratho, Ms Archana, Ms Kamalesh Nehra, Mr Samuel, Mr Moses, Mr Yelliah, Mr Dipanjan, Ms Reshma, Mr Mangababu, Mr Jagannath, Mr Arun Prakash, Ms Bhavya, Ms Sini, Mrs Bindu, Mrs. Jyoti, Mrs Kranthi, Ms Priya, Mr Nagaraju Menchu, Mr Naveen, Mr Akash, Mr Sai Krishna, Mr Chandan, Mr Rajesh, and all others. My school teachers Mr. sai sir (primary school), Mr Kadali Saibabu (mathematics), Mrs Hemalatha (science) and my colleagues in teaching Mr Musavir, Mr Sattar for their motivation and there are still many people I have to show my appreciation.

My acknowledgement also goes to all the technical staff for their assistance Mr M Durga Prasad and Mr Pankaj for TEM; Mr M Durga Prasad, Ms Sunitha and Mr Prasant for FESEM, Ms Reshma for Raman, Ms Jyothi for XRD.

Lastly, I dedicate this thesis to my family members for their encouragement to undertake the decision to enter into the research field.

I thank my parents M Suribabu & Padmaja and my parents in-law S. Pattabhiramaih & S V Lakshmi for their blessings and lovable guidance throughout my entire life. I thank my sister Mrs. Siva Ramesh and her son Jesvik for all the lovely distractions to reboot from stress. At the end, of course to my husband Sunkara Venkata Ramana to share my life and for being with me at every single moment of my life with his endless love and support. I would like to give special thanks to him for understanding me to work late in the lab or to work in the weekends.

Table of contents

List of figures

List of tables

Abbreviations

Abbreviations	Description
a.u.	Arbitrary unit
AN	Ammonium nitrate
CCD	Charge-coupled device
CE	Chemical enhancement
CV	Crystal violet
DI water	Deionized water
DNT	2,4 di-nitro-toluene
EDX	Energy dispersive X-Ray spectroscopy
EF	Enhancement factor
EM	Electromagnetic
eV	Electron Volt
FCC	Face centered cubic
FESEM	Field emission electron microscopy
FIBS	filament-induced breakdown spectroscopy
FP	Filter paper
Fs	Femtosecond
FT-IR	Fourier transfer infrared
FWHM	Full width half maxima
HAZ	Heat effected zone
He-Ne laser	Helium neon laser
HMX	1,3,5,7-Tetranitro-1,3,5,7-tetrazocane
HRTEM	High resolution transmission electron microscopy
IR	infrared
KHz	Kilo Hertz
LAL	laser ablation in liquids
LASER	Light Amplification by stimulated emission of radiation
LIBS	laser-induced breakdown spectroscopy
LOD	limit of detection
LSPR	Localized surface plasmon resonance
MB	Methylene blue
MG	Malachite green
MNPs	Metal nanoparticles
MSA	Micro squared array
MS	Methyl salicylate
NA	Numerical Aperture
NB	Nile blue
NIR	Near-infrared
nm	nanometer
NMs	nanomaterials
NPs	Nanoparticles

NS	nanostructure
Ns/ns	nanosecond
PA	Picric acid
PAS	photoacoustic spectroscopy
PCA	principal component analysis
PML	Perfectly matched layer
Ps	Picosecond
R6g	Rhodamine 6g
RDX	1,3,5-Trinitroperhydro-1,3,5-triazine
RSD	Relative standard deviation
SAED	Selected Area Electron Diffraction
SEM	Scanning electron microscopy
SERS	surface-enhanced Raman spectroscopy
Si	Silicon
SORS	spatial offset Raman spectroscopy
SPR	Surface plasmon resonances
TEM	Transmission electron microscopy
THz	Terahertz
TNT	trinitrotoluene, 2-Methyl-1,3,5-trinitrobenzene
ULAL	Ultrafast laser ablation in liquids
UV	ultraviolet
XRD	X-ray diffraction

Chapter 1

Introduction

Abstract

Investigations on the surface-enhanced Raman scattering (SERS) performance of colloidal (simple plasmonic nanoparticles), hybrid (femtosecond laser structured substrates + femtosecond laser prepared nanoparticles), paper-based (nanoparticles loaded in filter paper), nanofiber-based (nanoparticles loaded in nanofibers) substrates towards the detection of common explosives/explosive mixtures and, significantly, using a portable Raman spectrometer are presented in this thesis. Femtosecond laser ablation in liquids technique was utilized for preparing a variety of nanoparticles (Ag, Au, Au-Cu, Ag-Cu, etc.). The chapter begins with a short introduction to high energy materials (explosives are a particular class of these materials) and various detection techniques in practice and reported recently. Subsequently, the fundamentals of Raman spectroscopy, surface-enhanced Raman scattering (SERS), the mechanisms involved in the Raman signal enhancement, ideal requirements of a SERS substrate are discussed. Additionally, various fabrication methods for SERS substrates, among which the potential of laser ablation in liquid (LAL) technique is also highlighted. Furthermore, the mechanisms involved in LAL for synthesizing the nanoparticles (NPs) and nanostructures (NSs) are also discussed. The differences (advantages and disadvantages) between rigid and flexible SERS substrates are also explored. Finally, a brief chapter-wise content description is provided at the end of this chapter.

1.1 Motivation and Introduction

According to the data from the global terrorism database,[1] from the past two decades, the usage of explosive devices in terrorist attacks has increased intensely. The detection of high energy materials/explosive materials is necessary to ensure the safety and security of the civilian population across the world. One of the best spectroscopic methods, i.e., "Surface-enhanced Raman spectroscopy (SERS)," has recently perceived tremendous interest from the scientific community and has become a fascinating analytical tool. On-site sample detection is now possible with the development/availability of portable/hand-held/home-built Raman spectrometers and the versatile SERS substrates. Apart from explosive detection, SERS substrates are widely used in various fields such as the detection of pesticide residues on the vegetables/fruits, hazardous dye molecules, environmental pollutants, and drugs (critical for human health), disease diagnosis (e.g., cancer), etc. Various new methodologies have been used to prepare the SERS substrates for on-site molecular level detection because of its advantages of outstanding sensitivity, non-destructive, and finger-print nature. The motivation for us is from an interest in developing various rigid and flexible SERS substrates for the rapid detection and identification of high energy materials (explosives)/dyes/pesticides in pure and mixture form using portable Raman spectrometer.

1.2 Techniques for explosives detection

High energy materials (HEMs)/explosives contain energetic groups and release enormous energy in the form of light, heat when subjected to external stimuli such as a spark, shock, or friction. Explosives are generally categorized as primary and secondary explosives based on their detonation parameters and sensitivity. Primary explosives are very sensitive and release enormous energy, even with a small shock or collision. Therefore, it is troublesome to handle the primary explosives. They act as boosters or initiators for detonating secondary explosives. Lead azide and mercury fulminate are a few examples of primary explosives while 1,3,5,7-Tetranitro-1,3,5,7-tetrazocane (HMX), 1,3,5-Trinitroperhydro-1,3,5-triazine (RDX), trinitrotoluene (TNT), etc. are a few examples of secondary explosives.[2-3] However, there are few homemade explosives utilized in the preparation of improvised explosive devices (IEDs), which are easily synthesized at the laboratory level from simple molecules such as ammonium nitrate (AN), dinitrotoluene

(DNT), picric acid (PA), etc. These materials identification and detection is a primary concern for various countries and is extremely essential for homeland security. Various analytical methods exist for the detection of high energy materials either in residue form or in hidden places (e.g., surface offset Raman spectroscopy) and the samples from post-detonation areas. Some of the tested techniques include ion-mobility spectroscopy (IMS), terahertz spectroscopy (THz), laser-induced breakdown spectroscopy (LIBS), Raman spectroscopy, gas chromatography, photo-acoustic etc.[4-11] Some of these approaches either cause sample destruction or isolation of sample or do not favor the low quantity samples or require a skilled person for instrument calibration. Furthermore, high water absorption, poor specificity, and difficulty in instrumentation limits the usage of these techniques for on-field explosive detection.[12-13] Raman spectroscopy is a simple, quick, and non-destructive molecular spectroscopic technique. The Raman spectrum provides straightforward information and is used to convey chemical and structural information of explosives in pure form or even in the mixture form, whether in solid, liquid, powder and gas state.[14-18]

1.3 Raman spectroscopy

Figure 1.1 The first Raman spectrometer, built by Sir. C.V. Raman[19]

The Raman effect was initially observed by Sir Chandrasekhar Venkata Raman in 1928. Sir C.V. Raman, Indian physicist, who has first found the "scattering of light experimentally," observed in inelastically scattered photons with the change of

frequency.[20] This phenomenon is named "Raman Scattering," for which in the year 1930 Sir. C. V. Raman was recognized with a prestigious Nobel prize in Physics. The simple, innovative instrument used by Sir. C.V. Raman is shown in figure 1.1.

1.3.1 Scattering

When the light is incident on atoms/molecules, they absorb the light energy and re-emits the radiation in different directions and with different intensity. In scattering, the energy of an incident photon is not required to be equal to the energy difference between two discrete energy levels of the specimen like adsorption mechanism. The amount of scattering depends on the size of a particle, medium refractive index, and wavelength of the incident radiation. There are two classes of scattering: (1) elastic scattering and (2) in-elastic scattering. If the photon energy ($E = h\nu$) of the incident light is conserved, it is termed as elastic scattering, (ex. Mie scattering and Rayleigh scattering). If the photon energy ($E = h\nu$) of the incident light is not conserved, it is called in-elastic scattering (ex. Brillouin scattering and Raman scattering). Scattering that occurs from larger scattering centers (particle size higher than the wavelength of the incident light) like dust particles is called Tyndall or Mie scattering. Brillouin scattering occurs when a photon interacts with material waves in the medium (phonons, polarons, etc.) with a typical energy shift of <1 cm^{-1} produced by the refractive index change.[21]

1.3.2 Raman scattering

The photons of the incident light having wavelength smaller than the size of the particle (atoms/molecule) undergo Rayleigh scattering and Raman scattering. If the frequency (energy) of the scattered photon is identical to the incident photon frequency (ν_0), then the process is labeled as Rayleigh scattering (elastically scattered radiation). However, if the energy of scattered photons ($E_1 = \pm nh\nu_1$) is shifted (lower or higher) in comparison with the incident energy ($E_0 = nh\nu_0$), the process is termed as the Raman scattering (in-elastically scattered radiation). When the incident radiation is shifted to a lower energy/frequency ($\nu_0 - \nu_1$), because some of the energy of incident radiation is transferred to the vibrational mode of the molecule, it gives a Stokes shift. When the incident radiation is shifted to a higher frequency ($\nu_0+\nu_1$), the energy transferred from the vibrational mode of the molecule and is termed the anti-Stokes shift. This shift provides vital information

about the sample. Fluorescence occurs when the incident radiation has sufficient energy to excite electrons of the molecule from the ground state to an excited electronic state. If the energy of incident radiation is close to the electronic transition energy of the material, the scattering process takes place via an excited energy level of the material, described as resonance Raman scattering.[21] The energy level diagram for various scattering mechanisms is illustrated in figure 1.2. Most of the incident photons undergo Rayleigh scattering while a tiny fraction (1 in 10^6 -10^8 photons) experience the Raman scattering. In the Raman spectrum, Stokes and anti-Stokes Raman lines are distributed symmetrically with respect to the Rayleigh line. However, Stokes lines of the Raman spectra typically used because they are more intense than anti-Stokes lines. The intensity of stokes and anti-Stoke lines depends on the number of molecules available in the ground and excited states, respectively. According to Boltzmann distribution, the majority of the molecules are in the ground vibrational state compared to the first vibrational excited state at room temperature. Therefore, there is a more probability for a molecule to be in the ground vibrational state leads to more intense Stoke lines. [21]

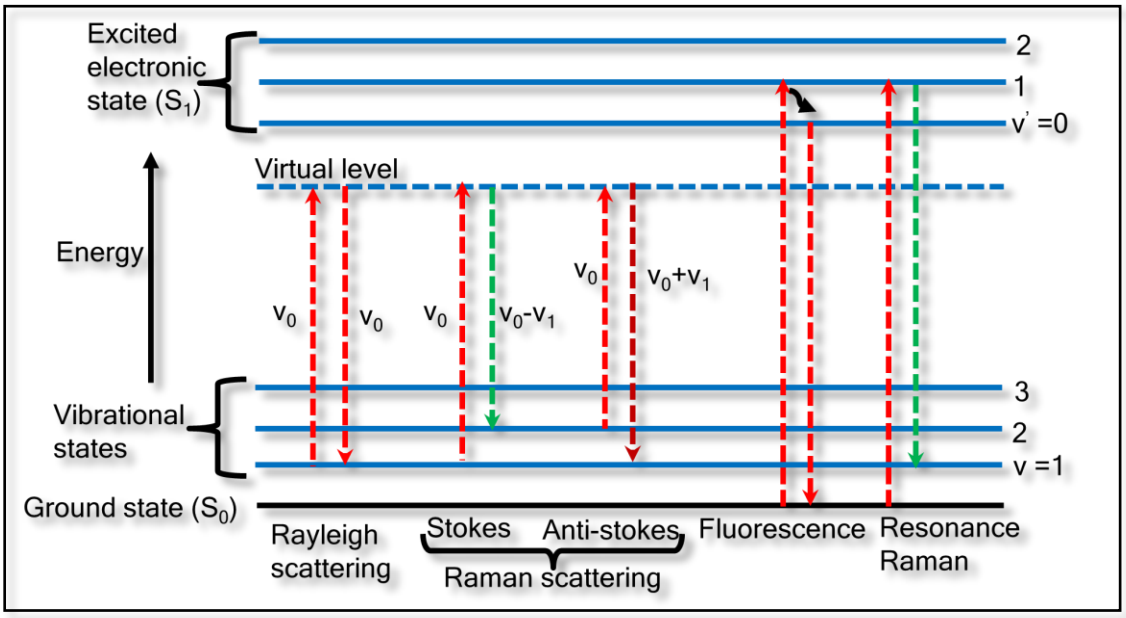

Figure 1.2 Energy level diagram for (a) Rayleigh scattering, (b) Stokes Raman scattering (c) Anti-Stokes Raman scattering, and (d) Fluorescence and (e) Resonance Raman scattering.

1.3.3 The classical theory of Raman scattering

When the electromagnetic radiation is incident on a molecule, the force acting on the electron cloud around the nuclei gets polarized, F = q E, where q is the net charge of the electron (C), and E is the electromagnetic field (V m^{-1}). This force induces an electric

dipole moment p = q d (C m) where d is the displacement vector. The induced oscillating electric dipole vector of a molecule can be expressed as μ = α E, where α is polarizability (C V^{-1} m^{-2}). During a molecular vibration, there may change in the dipole moment or a change in the polarizability. Therefore, the magnitude of this induced dipole moment (μ) $|\mu|==\alpha|E|= \alpha E_0 \sin 2\pi\nu t \rightarrow (1)$.

The net polarizability, $\alpha= \alpha_0+\frac{\partial\alpha}{\partial Q}Q + \cdots \rightarrow (2)$

Where α_0 is the equilibrium polarizability and $\frac{\partial\alpha}{\partial Q}$ is the rate of change of polarizability with respect to the normal coordinates (Q). Q varies periodically as $Q_0 \sin 2\pi\nu' t. \rightarrow (3)$

The electromagnetic radiation coupled with the induced dipole moment and polarizability as $\frac{\partial\alpha}{\partial Q} = 0$ in IR absorption and $\frac{\partial\alpha}{\partial Q} \neq 0$ in Raman scattering.

From equations (1) (2) and (3), polarizability, $\alpha= \alpha_0+\frac{\partial\alpha}{\partial Q}Q_0 \sin 2\pi\nu' t$ (neglecting higher-order terms)

Dipole moment $|\mu| = \alpha|E|$

$$= \left[\alpha_0 + \frac{\partial\alpha}{\partial Q}Q_0 \sin 2\pi\nu' t\right] E_0 \sin 2\pi\nu t$$

$$= \alpha_0 E_0 \sin 2\pi\nu t + \frac{\partial\alpha}{\partial Q} E_0 Q_0 \sin 2\pi\nu' t. \sin 2\pi\nu t$$

$$= \alpha_0 E_0 \sin 2\pi\nu t + \frac{\partial\alpha}{\partial Q}\frac{E_0 Q_0}{2}[\cos 2\pi(\nu_0 - \nu')t - \cos 2\pi(\nu_0 + \nu')t] \rightarrow (4)$$

In the above equation (4), the first term represents Rayleigh scattering (inelastic), the second term [lower frequency$(\nu_0 - \nu')$] represents Stokes Raman scattering and the third term [higher frequency$(\nu_0 + \nu')$] represents anti-stokes Raman scattering. Raman spectrum features several peaks, and each peak is the difference between the initial and final vibrational levels of the molecule, which resembles a specific molecular bond vibration.[21]

The formula of Raman shift expressed can be as,

$$\boldsymbol{Raman\ shift}(\Delta\boldsymbol{\vartheta}) = \frac{\mathbf{1}}{\boldsymbol{\lambda_{excitation}}} - \frac{\mathbf{1}}{\boldsymbol{\lambda_{Raman}}}$$

The Raman shift typically reported in wavenumbers (cm^{-1}), [reciprocal of the wavelength (cm)]. The energy of a vibrational mode depends on the vibrational force constant, which is contingent on molecular structure (atomic mass, bond order, and bond length). It is independent of the excitation laser wavelength.

1.3.4 Advantages

Some of the exquisite advantages of the Raman technique are:

- ✓ Non-destructive technique.
- ✓ This technique is suitable for the study of any type of sample, i.e., solid, liquid, and vapor, and no sample preparation is needed.
- ✓ It can provide the molecular vibrational fingerprint, which reveals the chemical composition of the specimen, chemical structure, and molecular interactions.
- ✓ Fast data collection time, the Raman spectra typically acquired in few seconds to minutes.
- ✓ Raman experiments can also be performed with laboratory table-top arrangements.

1.3.5 Limitations of normal Raman spectroscopy

- ❖ Intrinsically low signal intensity for low concentration molecules either in a solution or a mixture form.
- ❖ Overlap with the fluorescence band, and inefficient light collection and detection methods.

To overcome the probability of Raman scattering, a variety of Raman spectroscopic techniques have emerged like surface-enhanced Raman scattering (SERS), coherent anti-Stokes Raman scattering (CARS), surface-enhanced resonance Raman scattering (SERRS), tip-enhanced Raman scattering (TERS), spatially offset Raman scattering (SORS), etc.

1.4 Surface-enhanced Raman scattering

Martin Fleischmann and co-workers reported a fortunate discovery in 1974 in which they observed enhanced Raman signals of a pyridine molecule adsorbed on an electrochemically rough silver surface.[22] They reported the enhancement in Raman cross-section of pyridine vibrations by about a factor of ~10^6. This enhancement of the Raman signal in the vicinity of the metal nanostructure was named as “surface-enhanced Raman scattering.” In 1977, Van Duyne[23] and Albrecht[24] groups explained the mechanism of enhanced Raman signals from the metal surface. In 1985, Moskovits[25] summarized all the

primary explanations for the enhancement mechanisms such as electromagnetic (EM) and chemical enhancement (CM). The long-range EM enhancement is ascribed to the localized surface plasmon resonance (LSPR) in the near-field metallic surface, and the short-range chemical enhancement is because of the charge transfer mechanism between the analyte molecule and the substrate. Generally, the CM is at least 2-3 orders of magnitude smaller than that of EM enhancement.

1.4.1 Electromagnetic enhancement

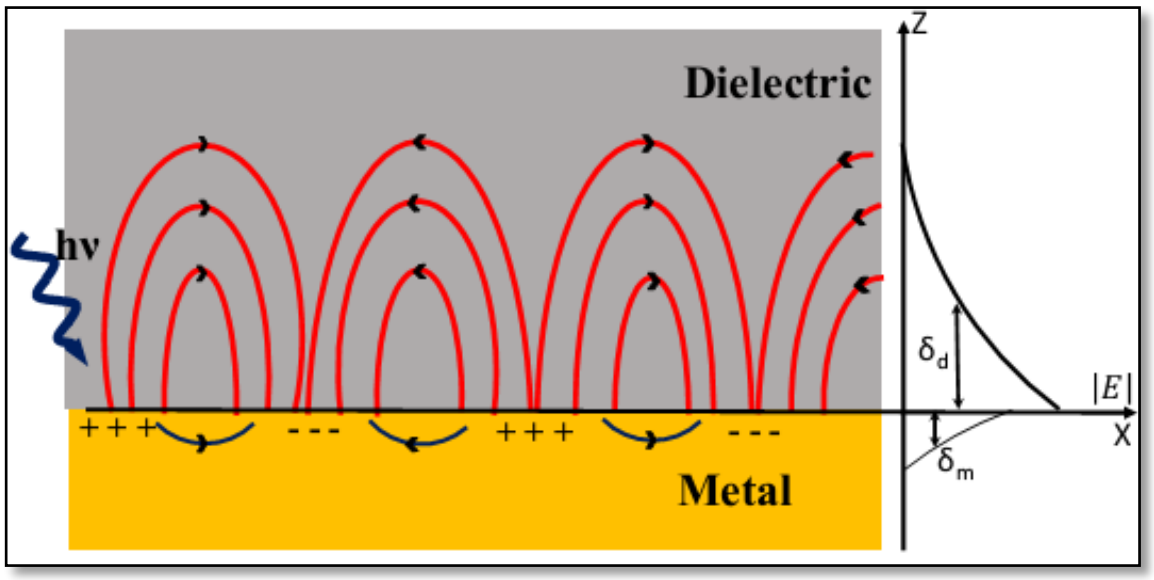

Figure 1.3 Schematic representation of an electron density wave propagating along a metal-dielectric interface.

The electromagnetic enhancement occurs because of the resonant interaction between the photons and plasmons at the nanostructured metal surface. Plasmons are the collective oscillations of conductive electrons in metals. Fermi model describes the Plasmons as a negatively charged electron cloud coherently displaced from its equilibrium position around a positively charged lattice ion.[26-27] The electron charge density oscillates with the plasma frequency $(\omega_p) = \sqrt{\frac{n_e e^2}{m^* \epsilon_0}}$, where n_e is the number density of electron, e is the charge of the electron (1.6×10^{-19} C), m* is the effective mass of an electron, and ϵ_0 (8.85×10^{-12} F/m) is the permittivity of free space. For example, (a) for copper n_e ~8.5×10^{28} /m^3, which gives ω_p of ~1.64×10^{16} rad s^{-1}, and $\lambda_p = 2\pi c/\omega_p$ = 114 nm (b) for gold n_e ~5.9×10^{28} /m^3, which gives ω_p of ~1.36×10^{16} rad s^{-1}, and $\lambda_p = 2\pi c/\omega_p$ = 139 nm and (c) for silver n_e ~5.86×10^{28} /m^3, which gives ω_p of ~1.36×10^{16} rad s^{-1}, and $\lambda_p = 2\pi c/\omega_p$ = ~138 nm.

From the Drude-Sommerfeld model for the free-electron gas, the dielectric constant of metal is $\varepsilon\ (\omega) = 1 - \frac{\omega_p^2}{\omega^2 + i\Gamma\omega}$, where ω_p is the volume plasma frequency and Γ is damping coefficient. Therefore, the light with the frequency below the plasmon frequency is reflected, [$\omega < \omega_p$: ε (ω) is negative] because of the electric field of the light is screened by the electrons in the metal. Light with a frequency above the plasma frequency is transmitted [$\omega > \omega_p$: ε (ω) is positive] since the electrons cannot respond fast enough to screen it. Most metals are reflective in the visible spectral range because their plasmon frequency is in the ultraviolet region.[28]

Surface plasmons are the plasmons that occur at the metal-dielectric interface, which play a crucial role in the Raman signal enhancement. The electron oscillations (plasmons) associated with the electromagnetic field (photons), called surface plasmon polariton, is shown in figure 1.3. Surface plasmons can either be propagating or localized.[29] Propagating surface plasmons (PSP) are excited by the evanescent field of light at the planar metal-dielectric interface and lose its energy while propagating along with the interface. The generated field penetrates a certain depth into the metal (δ_m), which can be controlled by the skin depth of the material. The skin depth of metals is in the order of 10-20 nm. William et al.[30] reviewed the length scales of SPP like penetration depth and propagation length and are dependent on wavelength and dielectric constant of the medium. For example, the surface plasmon propagation length values for Ag, Cu, and Au are 84 μm, 24 μm, and 20 μm at wavelengths λ=650 nm; and 340 nm, 190 nm, and 190 nm at λ=1000 nm, respectively.[31] Localized surface plasmons[32] are the confined surface plasmons on the surface of metallic nanoparticles (MNPs) whose size is comparable with the wavelength of the light. When light interacts with the nanoparticle, the conduction electrons displace from their nuclei. Hence, the opposite charges will form upon the particle's surface and act as a restoring force for the oscillating electrons, as illustrated in figure 1.4. These oscillations are maximized when the frequency of light matches with the inherent oscillating frequency of the nanoparticles.[33] Consider a sphere of radius 'a' and dielectric function ε(ω) surrounded by the medium with dielectric constant ε_m, resulting in the polarization of the sphere with polarizability (α) by the applied electric field E_0, is given by[34]

$$\alpha = 4\pi\varepsilon_0 \left(\frac{\varepsilon(\omega) - \varepsilon_m}{\varepsilon(\omega) + 2\varepsilon_m}\right) a^3$$

The polarizability will be maximum at $\varepsilon(\omega) + 2\varepsilon_m$is minimum, i.e., when $\varepsilon(\omega) = -2\varepsilon_m$. This resonance condition is called the Fröhlich condition. The electric field is gained as the gradient of the potential ($E = -\nabla\varphi$), where the potential inside (φ_1) and outside (φ_2) the spherical NPs are given as follows:

$$\varphi_1 = -E_0 \frac{3\epsilon_2}{\epsilon_1 + 2\epsilon_2} r\, cos\theta$$

$$\varphi_2 = -E_0\, r\, cos\theta + E_0 \frac{\epsilon_1 - \epsilon_2}{\epsilon_1 + 2\epsilon_2} a^3 \frac{cos\theta}{r^2}$$

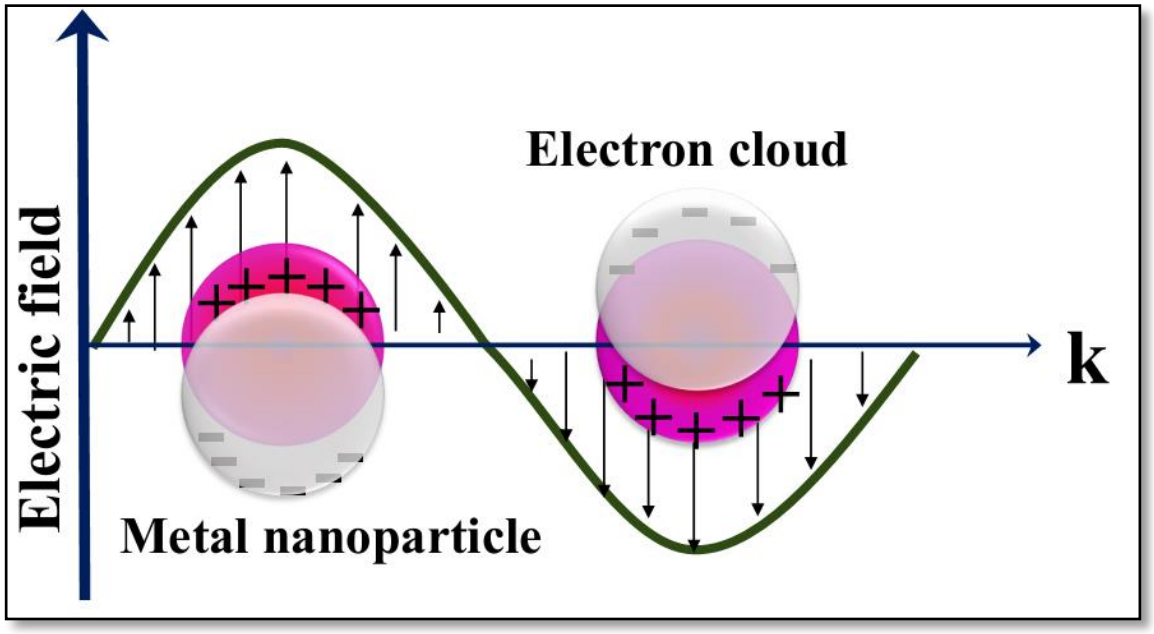

Figure 1.4 Schematic of the localized surface plasmons on the surface of metal nanoparticles, the plasmonic resonance showing the oscillatory motion of free electrons interacting with light.

In the case of MNPs, the confined electron oscillations induce an electric field around the NP surface that can be much superior to the incident light. If the probe molecule is in the vicinity of this magnified electric filed, the intensity of incident light will be enhanced and leads to excitation of the vibrational modes of the probe molecule, thereby increasing the Raman signal. At each stage, i.e., both the incident and the scattered electric field are enhanced and, therefore, the intensity of the Raman signal is enhanced as[35] $I_{SERS} = I_{incident} \times I_{scattered} = |E_{incident}|^2 |E_{scattered}|^2$. Therefore, the total enhancement will be ~E^4. A typical enhancement in the Raman intensity of a probe molecule (methylene blue, MB) observed in the presence of Au NPs. Without Au NPs on the silicon wafer, there is no evidence of the Raman modes of probe molecule, which is represented in figure 1.5.

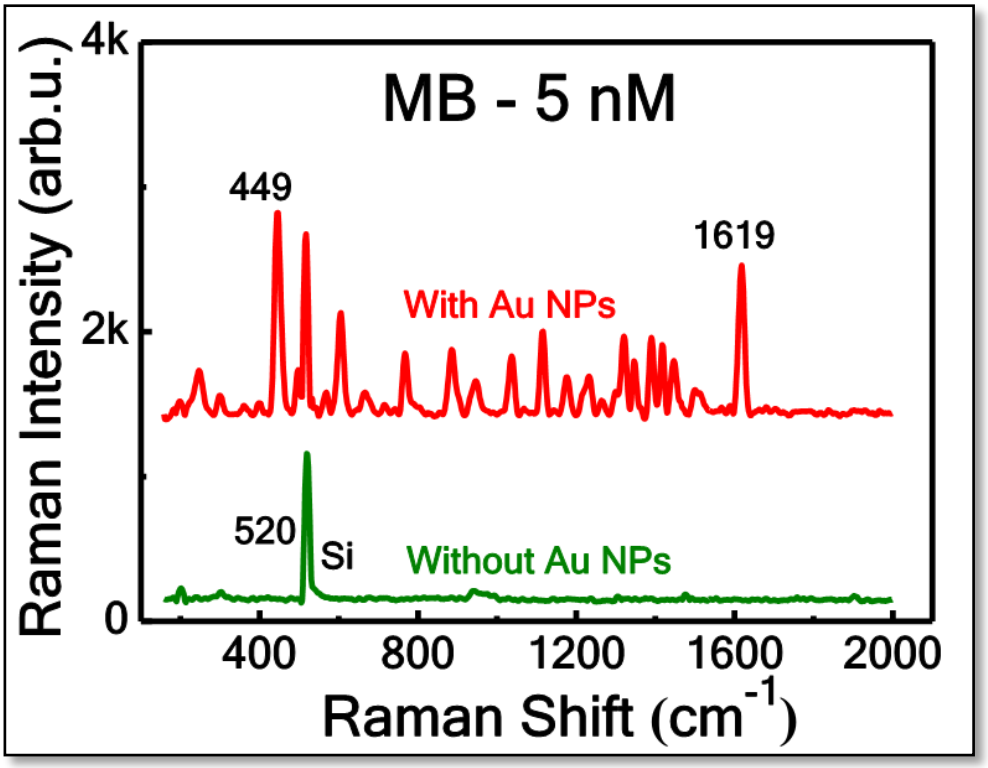

Figure 1.5 Raman spectra of MB-5 nM with and without Au NPs

1.4.2 Chemical enhancement

Chemical enhancement (CM) originates from the charge transfer between the probe molecules and the SERS substrate. The probe molecule is expected to chemisorb on the metal that allows the formation of a charge-transfer complex. The general model of the charge-transfer process comprises the electron transfer from the Fermi level of the metal to the lowest unoccupied molecular orbital (LUMO) of the molecule. The incident photon energy is in resonance with a charge-transfer transition of the newly formed surface-adsorbate complex.[36] Subsequently, the electron relaxes back to the metal and resides in the molecule long enough; the scattered photon will carry vibrational information of the molecule. Furthermore, this CM makes the molecule raise polarizability to increase the Raman scattering cross-section. Though usually it is expected that comparing to EM the CM is not as much responsible for the total enhancement and the EF is typical of the order of 10^2-10^4, depending on the chemical structure, the orientation/interaction with the metal surface, and specific vibration along with the excitation wavelength.

Noble-metal-free SERS materials, for example nanostructured semiconductors[37], two-dimensional (2D) layered materials (e.g., graphene[38] and MoS_2[39-40]) have been recently investigated intensively and demonstrated to be useful in the Raman filed enhancement

and majority of it has been attributed to the chemical enhancement. Some researchers have developed hybrid materials like TiO_2-Au[41], TiO_2-MBA-Ag[42] for further improvement in the sensitivity of SERS substrates, mechanism illustrated in figure 1.6. Lee et al.[43] reviewed the various strategies and challenges for the fabrication of hybrid materials as SERS active sensors. However, the SERS signals from the molecule are different from the Raman signal from the same molecule in the bulk form. The changes may occur in (1) peak positions (2) half-width (3) ratio of the intensity of different lines and (4) new peaks may also appear.[44]

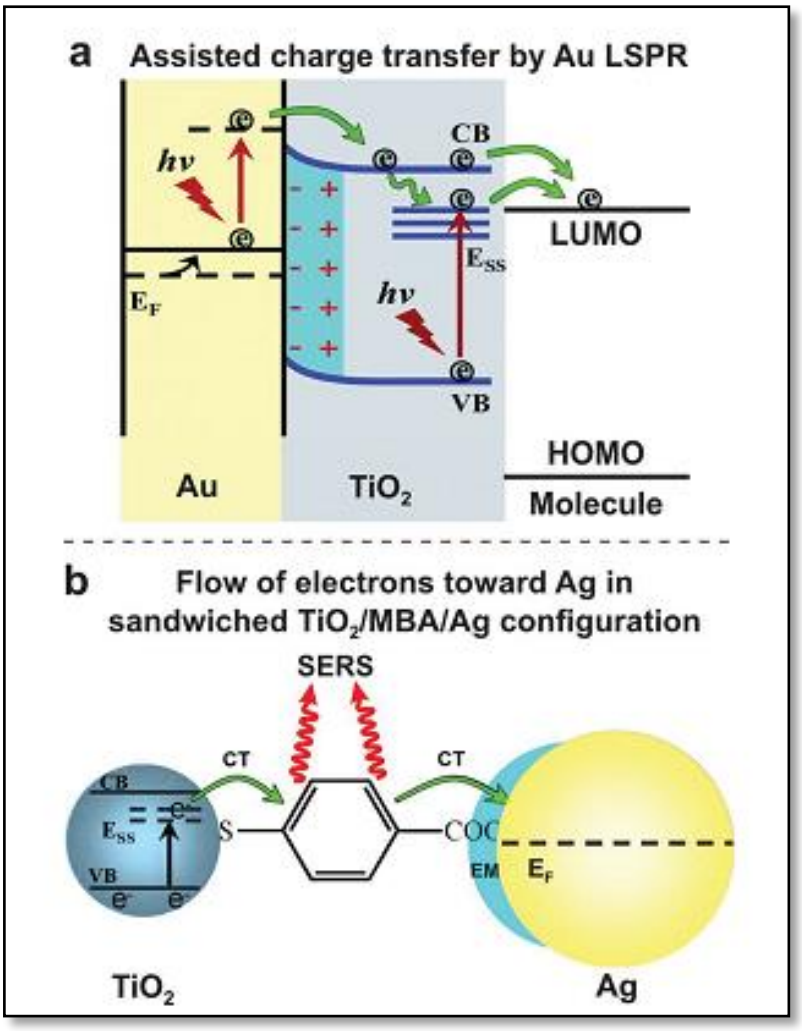

Figure 1.6 Synergistic chemical enhancement of semiconductor/metal hybrid SERS structures. (a) SERS enhancement mechanism of 4-MBA adsorbed on Au–TiO_2.[41] (b) Charge transfer mechanism associated with a sandwiched TiO_2/MBA/Ag configuration.[42] [adopted from Jiang et al.[41-42]]

1.5 Factors affecting the enhancement

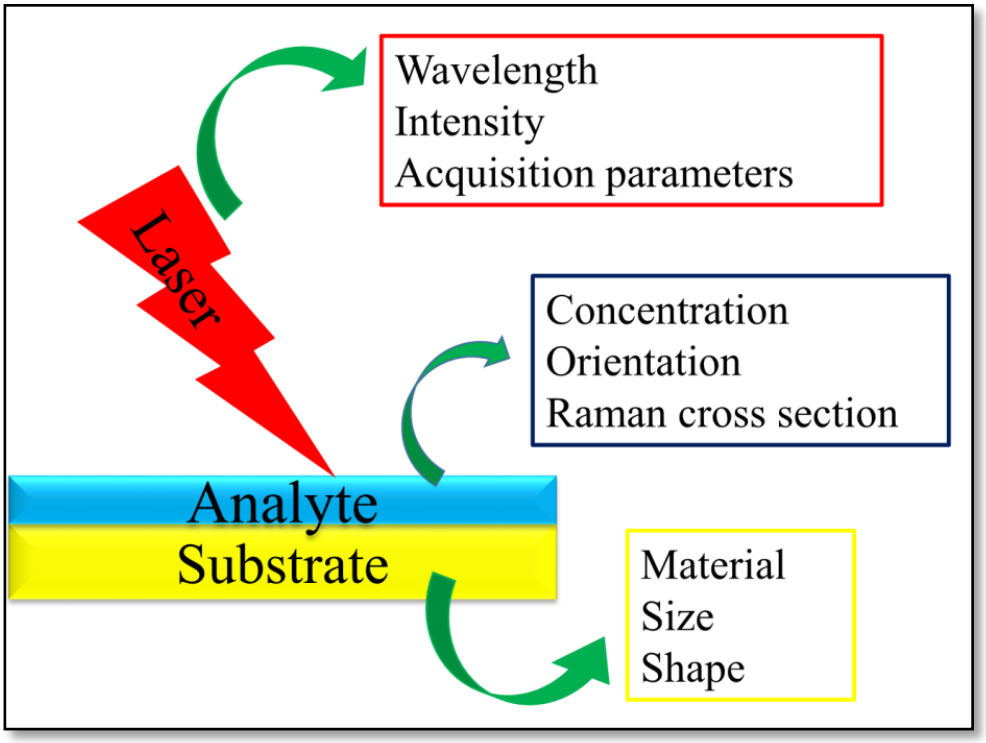

Figure 1.7 Schematic of the parameter effecting the enhanced Raman signal

During the last two decades, several scientists have extensively studied the effective parameters influencing the enhancement of the SERS signal. The enhancement of the Raman signal is the result of several contributions, and it is virtually difficult to separate them into distinct components. The factors (base-substrate, molecule-analyte, and excitation-laser) that affect the enhancement of the Raman signals are illustrated as a schematic in figure 1.7 and concisely discussed as follows.

- ✓ Material
- ✓ Size of the NPs
- ✓ The shape of the NPs
- ✓ Distance between the NPs
- ✓ Distance between the NPs and molecule
- ✓ The orientation of the NPs
- ✓ Excitation laser parameters (wavelength, intensity)
- ✓ Molecule parameters (Concentration, Raman cross-section, absorption wavelength of the molecules being investigated)

1.5.1 Materials

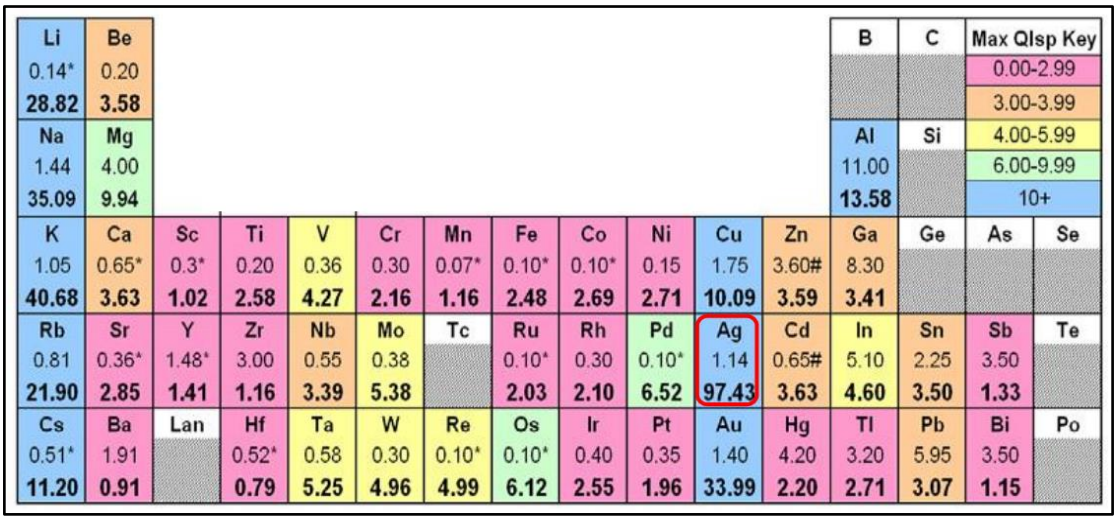

Li	Be											B	C	Max QIsp Key	
0.14*	0.20													0.00-2.99	
28.82	3.58													3.00-3.99	
Na	Mg											Al	Si	4.00-5.99	
1.44	4.00											11.00		6.00-9.99	
35.09	9.94											13.58		10+	
K	Ca	Sc	Ti	V	Cr	Mn	Fe	Co	Ni	Cu	Zn	Ga	Ge	As	Se
1.05	0.65*	0.3*	0.20	0.36	0.30	0.07*	0.10*	0.10*	0.15	1.75	3.60#	8.30			
40.68	3.63	1.02	2.58	4.27	2.16	1.16	2.48	2.69	2.71	10.09	3.59	3.41			
Rb	Sr	Y	Zr	Nb	Mo	Tc	Ru	Rh	Pd	Ag	Cd	In	Sn	Sb	Te
0.81	0.36*	1.48*	3.00	0.55	0.38		0.10*	0.30	0.10*	1.14	0.65#	5.10	2.25	3.50	
21.90	2.85	1.41	1.16	3.39	5.38		2.03	2.10	6.52	97.43	3.63	4.60	3.50	1.33	
Cs	Ba	Lan	Hf	Ta	W	Re	Os	Ir	Pt	Au	Hg	Tl	Pb	Bi	Po
0.51*	1.91		0.52*	0.58	0.30	0.10*	0.10*	0.40	0.35	1.40	4.20	3.20	5.95	3.50	
11.20	0.91		0.79	5.25	4.96	4.99	6.12	2.55	1.96	33.99	2.20	2.71	3.07	1.15	

Figure 1.8 Periodic table of the elements colored by maximum Q_{LSP} (in bold) [adopted from Blaber et al.[45]]

The complex dielectric function describes the electronic response of the material at a frequency $\varepsilon(\omega) = \varepsilon' + i\varepsilon''$. The plasmonic performance of materials is defined by the quality factor, and it is a ratio of real to imaginary values of the dielectric constant. The quality factor of all elements and the frequencies at which they occur is illustrated in figure 1.8 [which has been adopted from Blaber et al.[45]]. Coinage metals such as gold (Au), silver (Ag) and copper (Cu), support strongly localized surface plasmon resonances in the visible and NIR region while aluminum (Al), gallium (Ga), platinum (Pt) palladium (Pd), titanium (Ti), bismuth (Bi), indium (In), rhodium(Rh), ruthenium (Ru), etc. exhibit the plasmonic resonance in the deep ultraviolet (UV) region. Therefore, depending on the excitation wavelength, various [Ag, Au, Cu, Pt, and Al] NPs have been preferred for SERS substrates preparation. However, only limited studies have been reported on UV excitation because of the costly laser equipment. Note that Ag is a much better plasmonic metal than Au; its quality factor is several-fold higher than that of Au. This is because the imaginary part of Au is much higher than Ag, i.e., Au suffers many losses than Ag in the visible range, as illustrated in figure 1.9 (which has been adopted from Balčytis et al.[46]). Because of the high-quality factor and minimum loss, Ag gives the maximum enhancement factor (EF) among the three metals. However, it faces the stability issue because of oxidation. In contrast, Au has higher chemical stability and biocompatibility compared to Ag and Cu; but it has lower plasmonic efficiency than Ag.

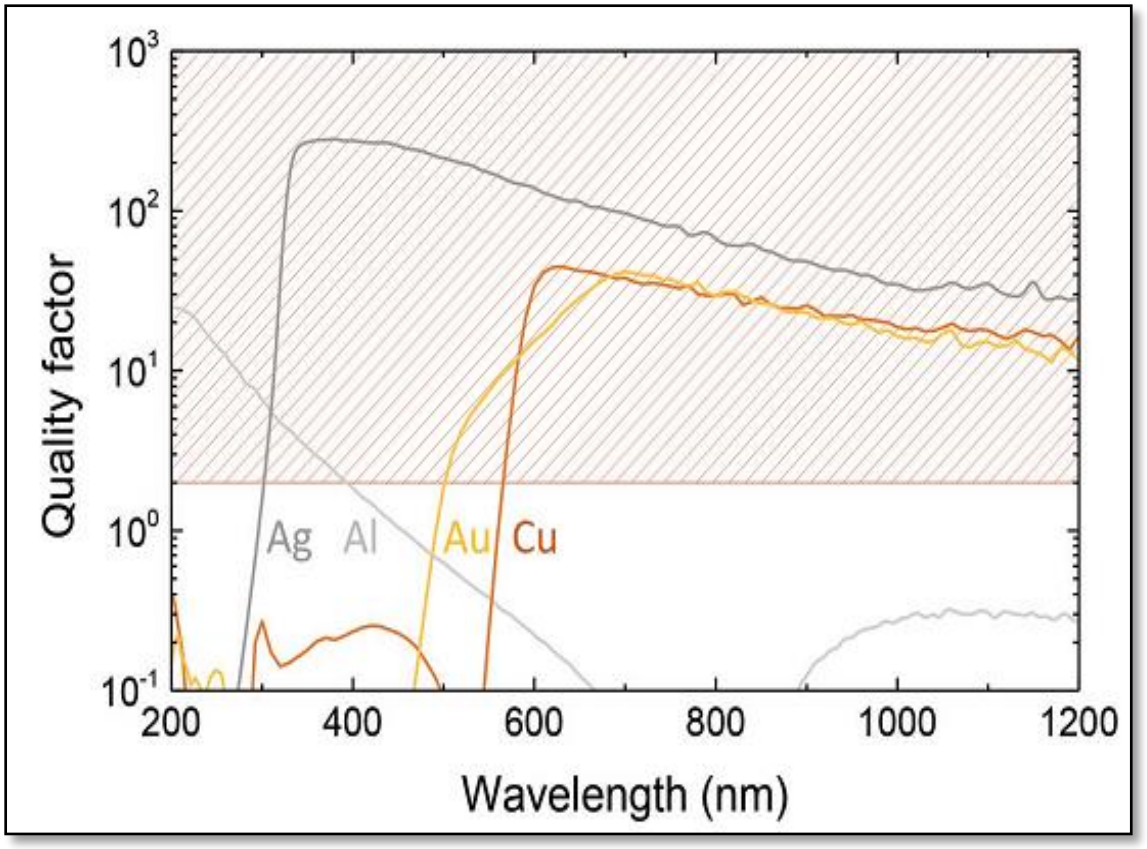

Figure 1.9 Approximate quality factor spectra of Ag, Au, Cu, and Al.[quality factor> 2 shown in the shaded region. [adopted from Balčytis et al.][46]

Furthermore, several researchers working on different compositions of bi-metallic/tri-metallic NPs in alloy/bimetallic/core-shell/Janus form to achieve both stability and plasmonic efficiency.[47-48] The position, intensity, and full width half maxima (FWHM) of the LSPR band depends on the type of nanomaterials, size, shape, and also the local dielectric environment. The material composition of alloy NPs allows the tuning of plasmon resonance, Raman activity, and their chemical stability. Byram et al.[49] recently demonstrated a higher enhancement of Ag-Au alloy NPs/NSs compared to monometallic NPs/NSs. Albrecht et al.[50] demonstrated high thermal stability (~100^{o} C) of Au–Ag, Au–Pt, and Au–Pd core-shell nanorods (NRs) compared to monometallic NRs. Vassalini et al.[51] investigated the enhancement of oxygen evolution reaction activity using Au–Fe nanoalloys. Messina et al.[52] tuned the SPR peak Au_xNi_{1-x} alloy NPs using different Au and Ni@NiO ratio. Apart from the metals and their alloy, there are inorganic semiconductor-based platforms, and hybrid materials such as TiO_2, SiO_2, and Si, with Ag, Au, also served as superior SERS substrates.

1.5.2 Size of the NPs

The NPs with diameters (d) much smaller than the excitation light wavelength (d << λ) will act as electric dipoles upon the laser excitation and lead to the localized surface plasmons. Moreover, MNPs with sizes smaller than the corresponding metal's skin depth (for a given wavelength) sustain the plasmonic excitation. The NPs of size less than 5 nm starts electronic screening, leads to feeble polarizability, and hence degrades the SERS effect.[53] For small sizes, absorption (absorption cross-section, d^3) will be the dominant phenomenon than the scattering (scattering cross-section, d^6). Conversely, on increasing the size of the particle, the total surface area per unit volume decreases. Therefore, the size of the NPs is sensibly considered to optimize the SERS activity. Most importantly, the size effect on SERS efficiency strongly depends on material, shape and excitation wavelength. Experimentally, the size of the NPs on the SERS effect can be possible by synthesizing NPs with a high degree of low polydispersity.

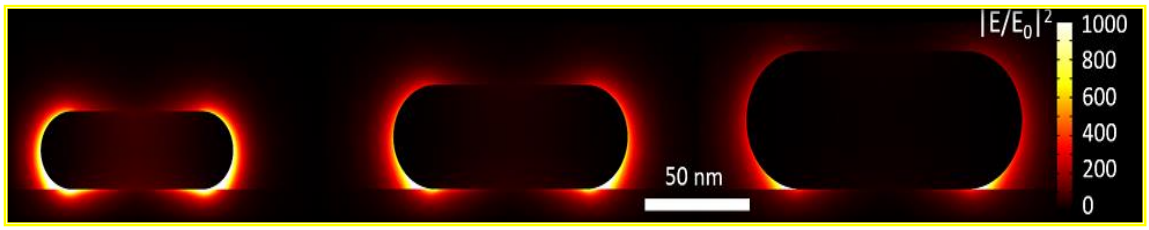

Figure 1.10 Theoretical simulated local electric fields of three different sizes Au nanorods [adopted from Lin et al.] [54]

For instance, Stamplecoskie et al.[55] studied the Ag NPs size effect (20.6 to 69.5 nm) on the detection of R6G with 785 nm laser excitation and observed the efficient SERS performance for the NPs with a size of 50 nm. Lin et al.[54] utilized the three different size of gold nano-rods (small → L/D ~ 85 ± 5 nm/22 ± 2 nm; medium →116 ± 6 nm/34 ± 1 nm and large → 129 ± 5 nm/45 ± 2 nm) and noticed more reliable SERS signals for smaller nanorods with an excitation close to the LSPR wavelength and the electric field distribution around the nanorod as described from the simulation results and is depicted in figure 1.10. Weng et al.[56] studied Ag triangular nano-plates SERS performance with edge lengths of 30, 34, 44, 50, 75, and 85 nm. They observed the superior SERS performance for smaller Ag nano triangles deposited on a glass substrate. In contrast, large Ag triangular nano-plates exhibited a better SERS effect when they are deposited on the paper substrates. Ying Lin et al.[57] synthesized Ag nanocubes with edge lengths between the 50 nm -1400 nm and observed a prominent SERS performance for sizes of 80 nm, 110 nm, and 130 nm

using 532 nm, 638 nm, and 785 nm laser excitations, respectively. Samal et al.[58] reported Au@Ag core−shell NPs of 32 nm, 77 nm, and 110 nm sizes and found an increase in the SERS efficiency with size. Bell et al.[59] synthesized Au colloids having various sizes 20–150 nm and observed that the colloids with size <30 nm and >100 nm are significantly less enhancing, while the sizes in between 30–70 nm have shown the significant enhancement at 785 nm laser excitation.

1.5.3 Shape of the NPs

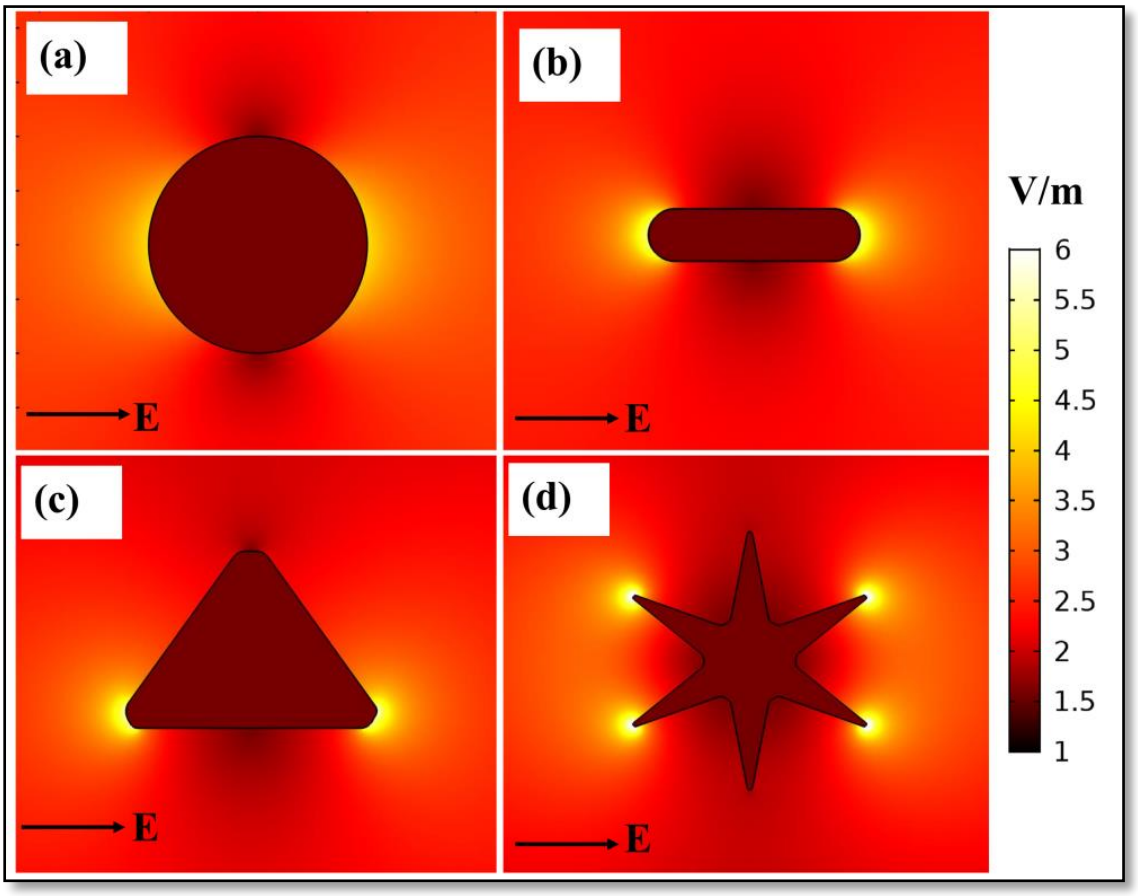

Figure 1.11 Electric field contours of Au NPs having different shapes (a) spherical (b) rod (c) triangular and (d) star obtained using COMSOL simulations (785 nm excitation wavelength).

The shape of NPs demonstrates a crucial role in SERS enhancements that determines the nature of the surface plasmon resonance and exhibits the maximum field at the sharp edges. Diverse geometries such as spheres, rods, triangles, hexagons, prisms, urchins, cubes, wires, and stars were used alternatives for enhancing the Raman signals in different proportions. A higher/energetic electric field is generally produced with sharp features such as corners/edges/tips of various geometries compared to other areas on the NPs

surface and is called as the lightning rod effect/optical antenna effect.[60] Figure 1.11 illustrates the electric field (V/m) amplitude distribution for the different shape of Au NPs: (a) spherical (b) rod (c) triangle and (d) star. The maximum field is observed at the sharp features of the NPs, i.e., at edge/tips. This could be because of increased surface area to volume ratio at the sharp features of NPs, leading to increased distribution of free electrons across the NPs surface and thus resulting in a stronger electric field.[61] This follows that the polarizability becomes anisotropic for different shaped NPs, exhibiting different optical responses along with the different directions, which is highly responsible for the tuning of LSPR resulting in multimode (dipole, quadrupole) resonance.[62]

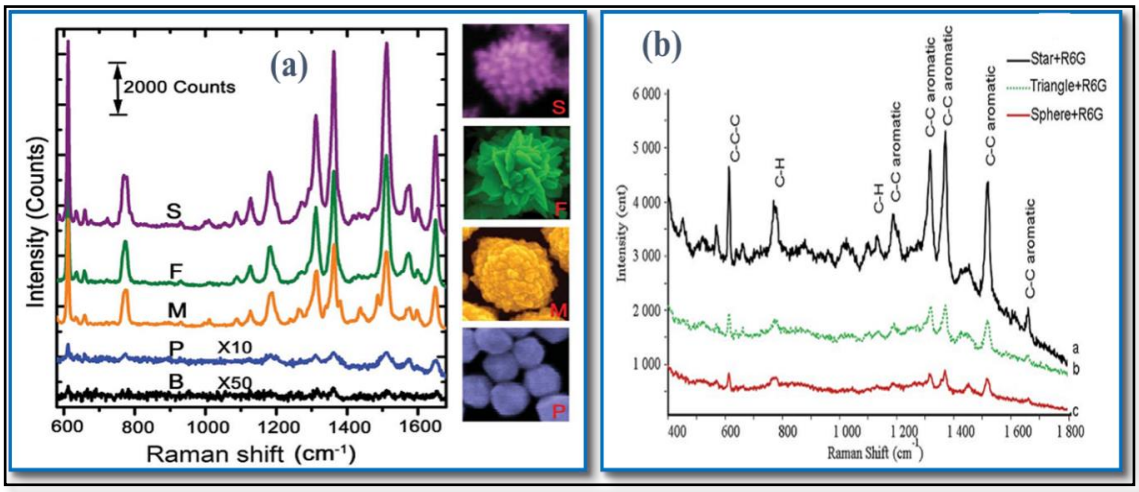

Figure 1.12 (a) SERS spectrum of R6G adsorbed on the surface of the substrates contributed by different gold meso particle films: S: sea urchin-like, F: flower-like, M: meatball-like, and P: polyhedral. B indicates 'background'.[63] (b) Comparison of 5 µM R6G SERS spectrum in solutions of gold nanostars (a dark) nano-triangles (b, green dash) and aggregated nano-spheres (c, red)[64] [adopted from You et al.[63] and Tian et al.[64]]

Tian et al.[64] demonstrated the SERS performance of various shapes of NPs and the variation in SERS enhancements as nano-stars > nano-triangles > nano-sphere aggregates > nano-spheres Au NPs. The SERS spectra for different shapes of NPs are shown in figure 1.12 (b). Tiwari et al.[65] synthesized nano-spheres, triangular nanoprisms, and nanorods - shaped Ag colloids using the solution-based method. Non-resonant SERS studies performed with R6G molecule and noticed the superior signal enhancements for the nanoprisms. Lorenzo et al.[66] demonstrated the superior SERS signals of phenol using gold nanostars with 785 nm laser excitation. Hu et al.[67] studied the SERS performance on different shaped Au NPs, such as nanorods, tetrapods, cubes, dogbones, and spheres with metal-molecule-metal nanosystems (Ag NPs/4-ATP/Au NPs).

1.5.4 Distance between the NPs

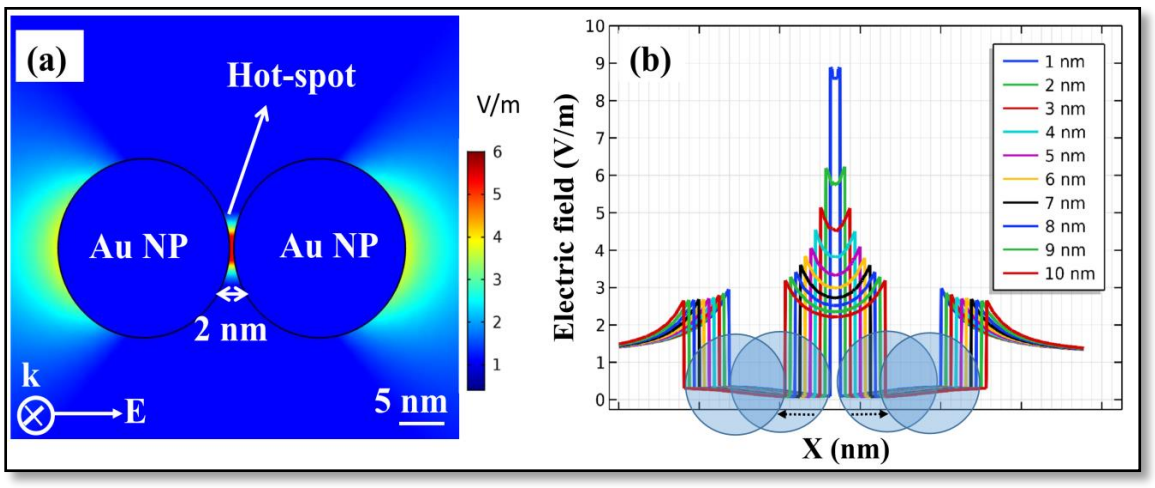

Figure 1.13 COMSOL simulated (a) electric field contour maps of an Au dimer with inter-particle distance 2 nm (b) relative electric field enhancement as a function of inter-particle distance from 1 to 10 nm for Au nano-spheres.

Practically in SERS, there is a limited role of the single non-interacting isolated NP. Therefore, the cluster of NPs either ordered or disordered arrays (aggregates) shows a prominent role in the enhancement of the Raman signals. When metal NPs come close together, their induced dipoles begin to interact, and the local electromagnetic field gets enhanced in the small gap region. The field amplitude in the gap is much higher than the amplitude produced by single particles, called "hotspots," which are critically responsible for the increase of the Raman signals. Consider two adjacent Au NPs aligned along the direction of the incident field that induces two in-phase dipoles to strengthen each other. The produced electric field is concentrated within the narrow gap between the NPs termed as a "hot spot." Figure 1.13 (a) illustrates the COMSOL simulation result of two Au NPs having size 20 nm are separated with a 2-nm gap, while figure 1.13 (b) displayed the variation of the electric field when two Au NPs separated from 1 to 10 nm. The generated electric field magnitude becomes higher and higher as the gap becomes narrower and narrower. The hotspots can generate strong local electric fields at the position of adsorbed species, which provides a giant SERS effect. If the NPs are far from each other, the plasmon interaction is quite weak because of the field attenuation deviating from either side of the gap. Hence, it is more evident that the use of sharp metallic tip NPs/aggregation of NPs/self-assembly of gold nano chains/combination of NSs and NPs will enhance the filed. Moreover, time-dependent density functional theory proved that a significant SERS enhancement at the junction between two Ag_{20} clusters for pyrazine molecule.[68] He et

al.[69] studied the inter-particle gap as 2 nm < gap < 8 nm of gas-phase deposited Ag NPs and found the superior SERS enhancements at a gap of 3 nm. Kleinman et al.[70] reviewed the creation of SERS hot spots such as self-assembly of NPs controlled aggregation of NPs for the amplification of SERS signal. Haidar et al.[71] revealed that isolated Au NRs exhibit two-orders of magnitude drop in the SERS enhancement compared to gold nanorods (AuNRs) dimers in the detection of BPE.

1.5.5 Orientation of the NPs

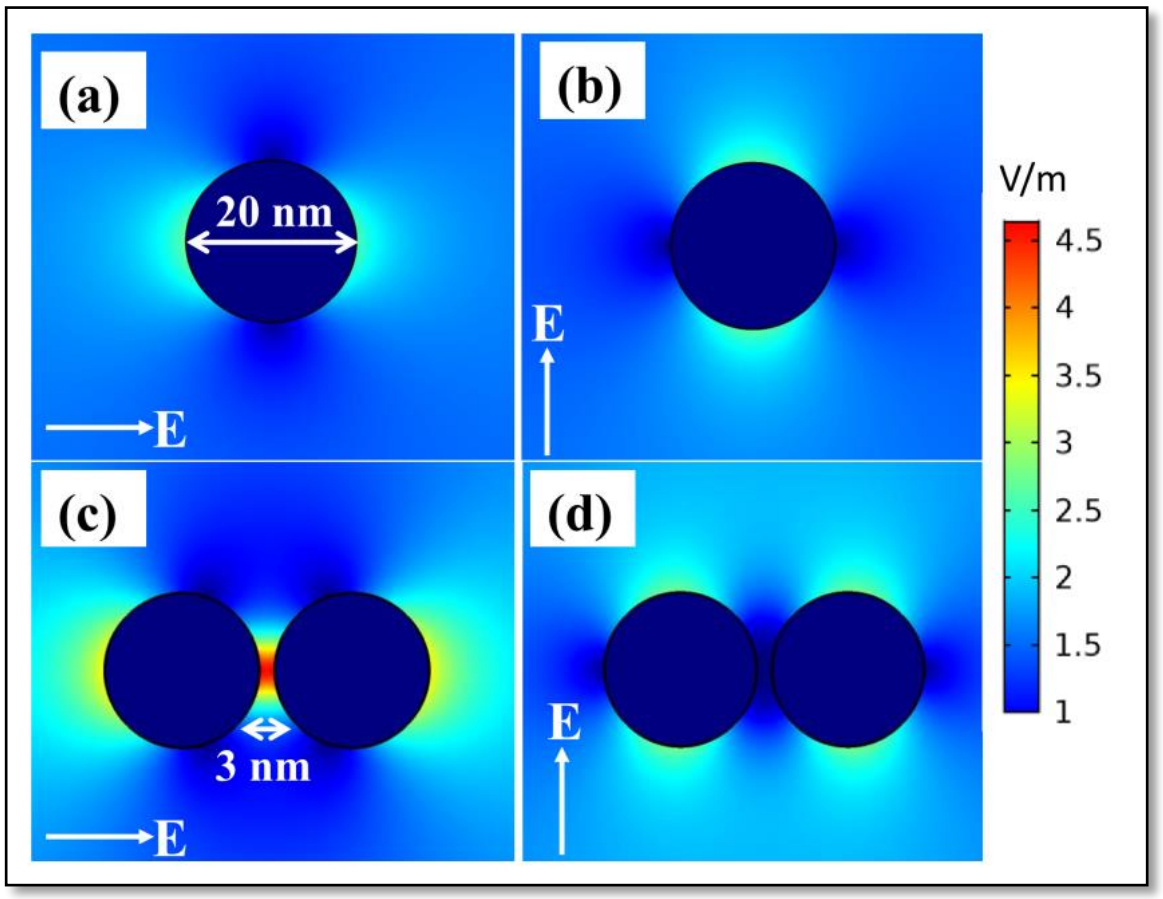

Figure 1.14 COMSOL simulations of local electric field distribution (a) and (b) for single Au NPs (c) and (d) Au NPs dimer for excitation electric field polarizations along and across the dimer axis with 785 nm incident light. The arrows represent the polarization directions.

The orientation of NPs with the polarization of the excitation field also affects the collective response of the generated plasmonic field. The polarization of excitation laser affects the favorable locations of localized enhancement of the EM field. A simple illustration of the electric field polarized along X and Y directions, where the proximity of the charges on the surface of NPs leads the field distribution along filed directions, illustrated in figure 1.14 (a) and 1.14 (b), respectively. The most straightforward system

of Au NPs dimers is used to discuss the plasmonic field localizations. Two Au NPs are having a size of 20 nm separated by 3 nm surrounded by air (n=1). Here, two different ways of the orientation of dimers are considered, parallel- and orthogonal- polarized light (785 nm) for illumination, as shown in figures 1.14 (c) and (d), respectively. If the incident electric field is in the direction of the inter-particle axis of NP dimer, opposite charge distribution on the sides of the NPs will weaken the repulsive forces and undergoes to the localized surface plasmon coupling. In the other case, when the incident electric field is in the perpendicular direction to the dimer axis, the charge distribution on the surface of NPs will increase the repulsive force; therefore, the interstitial region is not favorable for the SERS activity.

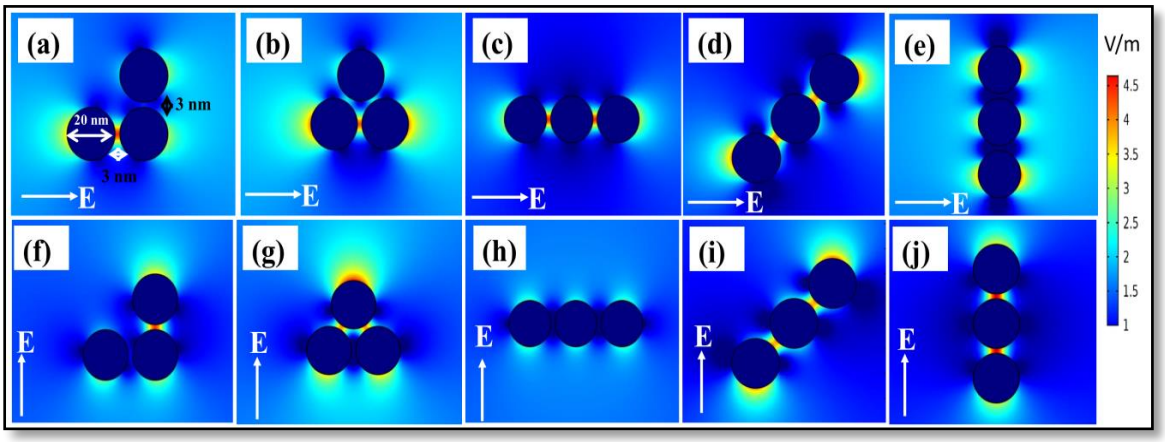

Figure 1.15 COMSOL simulations of Au trimer molecule in different orientations (a-e) parallel to the x-axis and (f-j) parallel to the y-axis

Similarly, the possible alignments of Au NPs trimer with respect to the incident field polarization and favorable for the interstitial region is illustrated in figures 1.15 (a)–1.15 (e) with E_x and figures 1.15 (f)- 1.15 (j) with E_y. Therefore, higher SERS intensity can occur at hotspots of a dimer/trimer with the axis oriented parallel to the incident electromagnetic field. Yi et al.[72] reported a similar trend of plasmons interactions of NPs trimer (60 nm) oriented in different directions with respect to 514 nm excitation laser using 3D-FETD simulations. McLellan et al.[73] observed variations in SERS intensity on the different orientation of silver nanocubes relative to the excitation laser polarization. Hrelescu et al.[74] systematically studied Plasmonic hotspots in single gold nanostars through the polarization of the excitation light.

1.5.6 Distance between NPs and the molecule

The electromagnetic enhancement of the SERS signal does not necessitate direct contact between the molecule and MNPs/NSs. The enhancement monotonically decreases with the molecule - NP separation d, which for a sphere of radius 'r' is proportional to $\left[\frac{r}{r+d}\right]^3$. Hence the maximum enhancement is at d = 0, the field of a dipole decrease as $(1/d)^3$ with increasing distance. The electric dipole field decays as $1/d^3$, and the plasmonic field decays even more quickly as $1/d^{12}$, revealing that at large distances there will be no SERS enhancement. Recently, Kumari et al.[75] investigated the SERS effect by varying the distance between the Ag NP and analyte molecule using silicon coating on the NPs surface. Furthermore, they studied the minimum distance at which SERS capability varies as a function of NPs size, i.e., 2.8 nm from the analyte to 30 nm NP surface, 3.2 nm for 45 nm NPs, 4.4 nm for 75 nm and 5 nm for 90 nm.

1.5.7 Excitation Laser parameters

A strong monochromatic light source is generally required to illuminate the specimen for acquiring the Raman signal. Laser parameters such as wavelength, intensity, and other acquisition parameters affect the obtained signals. Nowadays, lasers with different wavelengths are available; usually, 244 nm is employed in resonance Raman scattering for the characterization of the biological molecules, whereas 325 nm gives benefit in the semiconductors and electronic field. Visible lines (488, 514, 532, and 633 nm) are commonly used (inorganic and organic material), and NIR lines (785 and 830 nm) are generally used in medical and biological fields. Especially the specimens with native fluorescence in the visible region will photodegrade without difficulty. And also, the excitation wavelength of the laser gets shorter, the Raman scattering efficiency increases, but the effect of fluorescence, the specimen damage, and the price of the spectrometer increases. When the laser excitation wavelength coincides with the electronic transition of the molecule, it leads to the resonance Raman (RR) effect.[76] This, in combination with the SERS effect, gives rise to surface-enhanced resonance Raman scattering (SERRS). It leads to a higher magnitude of enhancements than regular SERS mediated by the overlap of the excitation wavelength with the electronic transition of the probe molecule. Furthermore,

SERS enhancement depends on the LSPR position of NPs used as an enhancer of the Raman signal. It is not required to be in an exact match with the laser excitation with the LSPR maximum.[76] A´´lvarez-Puebla et al.[77] reported the SERS studies at three excitation wavelengths, i.e., 514.5 nm, 633 nm, and 785 nm for a 2-NAT molecule with absorption maxima at 242 nm using bimetallic Ag-Au nanoshells with LSPR peak from 533 to 949 nm. The simultaneous depiction of the LSPR extinction spectra the corresponding EFs calculations for each excitation line was presented and they noticed the best excitation source was slightly blue-shifted with reference to the LSPR maximum. Furthermore, the intensity of the laser affects the Raman spectra as the peak intensity rises with an increase in the excitation laser intensity. Additionally, the high-intensity laser excitation of the sample may result in different effects such as photo-degradation, photo-catalysis, photo-bleaching, or photo-desorption. Therefore, the optimization of intensity is also needed to acquire the information from the sample without damage. Moreover, the irradiation time may affect the signal because it may rise up to levels where sublimation of the specimen is possible. Hence, the excitation laser parameters have to be considered carefully while collecting an efficacious SERS signal.

1.5.8 Molecule parameters

The molecule parameters such as concentration, scattering cross-section, absorption wavelength, orientation etc. can also affect the SERS signals.[78] Generally, fluorescent dyes and other chromophores like Rhodamine 6G (R6G), Malachite green (MG), Crystal violet (CV), Carboxyfluorescein (FAM), Methylene blue (MB), malachite green isothiocyanate (MGITC), etc. are often considered as Raman reporters because they have large Raman scattering cross-sections, polarizability, photo-stability (at low power), and binding affinity. Explosive molecules usually have very low Raman cross-sections. For example, for PETN it is ~10^{-30} cm^2 per molecule, for TNT it is ~10^{-30} cm^2 $molecule^{-1}$, TATP has ~10^{-31} cm^2 $molecule^{-1}$, and RDX has a cross-section of ~ 10^{-32} cm^2 $molecule^{-1}$.[79] This is one of the factors initiating the variation in SERS intensities between the dye and explosive molecules.[80] Compared to other spectroscopic techniques such as UV (~10^{-18} cm^2 per molecule), IR (~10^{-21} cm^2 per molecule), and fluorescence (~10^{-24}–10^{-14} cm^2 per molecule), Raman spectroscopy is rather limited because it has a very low scattering cross-section (~10^{-29}–10^{-30} cm^2 per molecule). Kneipp et al.[81] reported scattered signals are

directly proportional to the concentration, laser intensity, and scattering cross-section of the molecule. To obtain better SERS performance, one can select the appropriate experimental parameters for the preparation of the SERS substrate.

1.6 The requirements of SERS substrate

Since its discovery, the SERS technique has been developed into a powerful analytical/detection tool. In our daily life, sensors are playing an extending role in various aspects, including environmental monitoring, drug detection, explosive analysis, food quality analysis, and healthcare diagnostics.[82-83] The choice of appropriate substrate is essential; the ideal requirements of SERS substrates are sensitivity, uniformity, reproducibility, and recyclability as well as low fabrication cost.

1.6.1 Sensitivity

The main advantage of SERS is the detection of molecules at very low concentrations/traces. The sensitivity is expressed in terms of the lowest amount of probe molecules detection possible with the SERS substrate. The signal disappears when the molecule concentrations reach a limiting value. The sensitivity of the SERS substrate varies from molecule to molecule. The sensitivity of the SERS substrate was estimated by the enhancement factor or limit of detection for a particular vibration mode of the probe molecules. Therefore, one should choose the substrate with a higher enhancement factor or a lower limit of detection (LOD) over the range of analytes.

1.6.2 Uniformity/Reproducibility

The SERS intensity variation of the probe molecule over the NS surface describes the uniformity, which mainly depends on the distribution of hotspots on the substrate. The low reproducibility of the substrate affects the potential usage of practical detection. It is challenging to produce a highly reproducible SERS platform with a highly homogeneous distribution of hotspots. The fluctuations of the SERS signals were calculated statistically with relative standard deviation (RSD) of the particular mode intensity. The magnitude of % RSD, indicative of the coefficient of variation, gives the uncertainty in the measurement. It can be calculated by collecting spectra from different locations within the same SERS

substrate. The variation in the signal intensity depends on the deposition of NPs colloidal or the evaporation of droplets. The signal variation within a certain error range, i.e., <20% is acceptable.[84]

1.6.3 Repeatability/Recyclability

Repeatability is also another essential factor to test whether the as-prepared SERS substrate can generate the same sensitive SERS signals under similar preparation processes. Recyclability is the process of reusing the same substrate after detecting one/two molecules, followed by proper cleaning procedure. Nowadays, various research groups have been investigating recyclable SERS substrates. For example, Wang et al.[85] developed a recyclable Au@Ag/TiO_2 NTs microfluidic SERS chip. Huang et al. [86] developed a recyclable TiO_2-Ag substrate for the identification of R6G and CV molecules, while Sajanlal et al.[87] fabricated reusable Ni-Au hybrid carpet for the detection of DNT, DPA, TNT, and RDX.

1.6.4 Fabrication cost

Despite the long history of SERS, the cost of fabrication facilities and complexity in preparation steps to produce uniform, stable, and highly sensitive SERS substrates are the major obstacle for the real field applications. The fabrication cost of the substrate affects the bulk production and commercialization of the technique for regular daily usage. Most of the researchers have focused on developing the paper, fabric-based substrates with high sensitivity, reproducibility, and recyclability.

1.7 Various methods of fabrication of SERS substrate

There are various methods to develop SERS substrates, such as nanolithography, vapor deposition, etching, chemical methods, etc..[43] In general, these techniques can be categorized into two main classes: top-down and bottom-up approaches. In top-down approaches, bulk materials are reduced into smaller parts to produce the NPs, whereas bottom-up approaches start from the molecules or atoms to synthesize the NPs with appropriate size. The standard top-down methods are milling, nanolithography, sputtering, etc. and a few common bottom-up methods include chemical reduction method, microemulsion method, chemical vapor deposition.[88] Although all of these methods have

certain benefits in terms of SERS measurements, they commonly involve multiple fabrication processes. Additionally, there is a possibility of the existence of impurities and requires purification methods. The laser ablation method overcomes all of these limitations and produces NPs with surfaces free from extraneous ions or other chemicals. Laser ablation in liquids (LAL) is considered as combined top-down [solid target → NPs] and bottom-up [nucleation and growth of atom → NPs] processes. Moreover, it is an competent procedure to produce both NPs and NSs with one attempt.

1.7.1 Ultrafast Laser ablation

Laser ablation defined as the removal of materials from the surface of a sample due to high intense laser interaction. It is a versatile technique to synthesis various NPs without any stabilizing agents. Laser ablation in the liquid is an efficient procedure to produce both NPs and NSs in one experiment. Several studies have demonstrated the various mechanisms involved in the NPs formation,[89-90] and the involved processes in the LAL technique are shown as a flow chart below (figure 1.16).

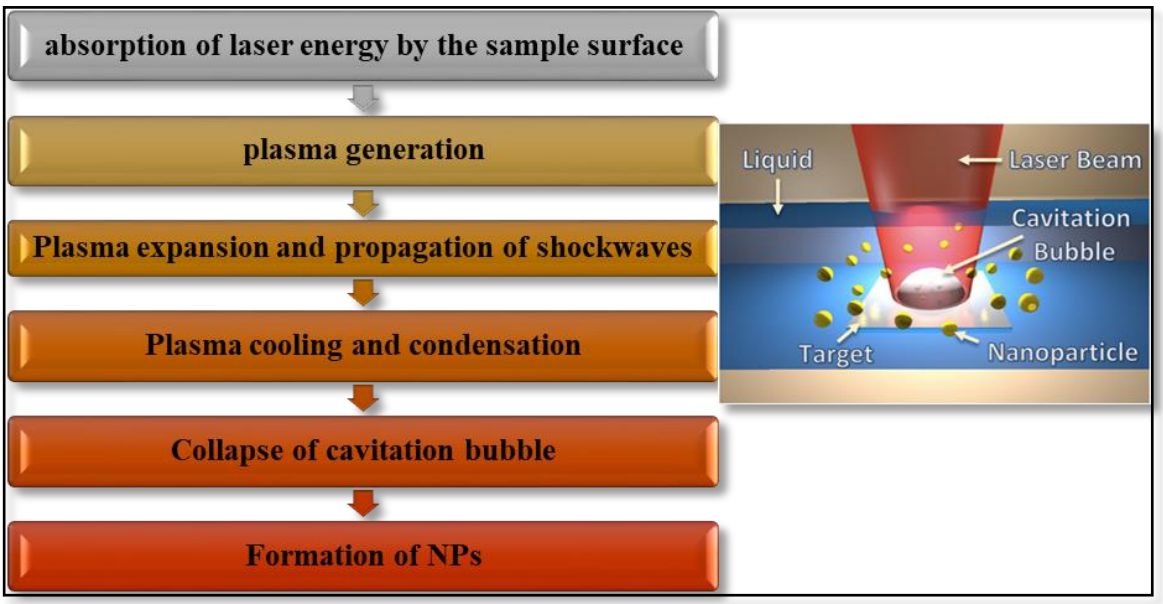

Figure 1.16 Schematic of laser ablation in liquid with mechanism flow chart [adopted from Zhang et al.[91]]

The first stage of laser ablation is the absorption of the laser energy by the sample, and then a plasma plume is formed. To attain this, the pulse energy of the laser must be greater than the binding energy of the target atoms. (> threshold fluence). Because of photoionization (multi-photon absorption/tunneling ionization), a massive number of

electrons are pulled out from the material, forming a considerable number of ions, which leads to the formation of an excess number of positive ions. Therefore, the plasma generated on the target surface contains electrons, atomic species, and ions. The plasma pressure and the temperature are as high as hundreds of megapascals and thousands of kelvins. The plasma plume expands in the liquid environment, and this liquid creates a stronger compression of the expanding plasma plume. It vaporizes the liquid at the plasma-liquid interface, leading to the generation of liquid plasma. At the same time, a pressure wave/shock is generated at the sample surface. At the initial stages, a cavitation bubble is formed because of the interaction of the expanding material plasma with the liquid plasma. Inside the cavitation bubble, the ablated species from the sample (ions, atoms, and atom clusters of the ablated species) interact with the surrounding liquid. In this stage, chemical reactions such as oxidation, galvanic replacements, etc. are possible, which depends on the target and liquid environments. The cavitation bubble expands with a maximum radius; the consumption of energy ends up and collapse, followed by nucleation and growth of the NPs.[92-93] The NPs dispersed in the solution, and NS remains on the target surface after the collapse of the cavitation bubble. The mechanism flow chart and the schematic are shown in figure 1.16. Ando et al.[94] recently studied bubble dynamics of LAL (Ag film on glass substrate) by the laser scattering images superposed on the shadowgraph images and observe no scattering signals are found outside the cavitation bubble. And the signature of the NPs formation around the two areas inside the bubble, i.e., apex inside the bubble and around the central area. Therefore, noticed almost all NPs are formed inside the cavitation bubble.

The productivity, size, morphology, and mechanism involved depends on laser parameters such as pulse duration, pulse energy, wavelength, and pulse number and also on the surrounding medium. The penetration depth and the ablation threshold of the material are dependent on the laser wavelength.[95] The penetration depth is higher for higher wavelength; therefore, the yield of NPs per pulse increases with the laser wavelength. Matsutani et al.[96] performed wavelength-dependent studies on laser ablation of graphite and observed high yield for 1064 nm compared to 355 nm. The size distribution of the NPs may depend on the laser wavelength because of the occurrence of laser ablation and laser fragmentation simultaneously; these are favorable at smaller wavelengths. Giorgetti et al.[97] fabricated laser-ablated Au NPs in acetone at different wavelengths 1064 and 532 nm and

noticed small-sized particles 2-3 nm at lower wavelength than that with a higher wavelength. Laser pulse duration affects the heat propagation and dissipation time scales in any material. During the laser ablation, the time required to transmit the generated heat through collisions of electrons with lattice is referred to as electron relaxation time. In ultrafast (fs) laser ablation, the fast electron cooling time than the pulse duration and reduced electron-lattice coupling lead solid-vapor transition. For longer pulses, the thermal process induces the melting of the material, which leads to the heat-affected zone (HAZ). Amoruso et al.[98] described the comparison dynamics of ultrafast ablation between picosecond (ps) and femtosecond (fs) regimes. For the production of the NPs, ps laser ablation showing a superior yield of NPs than the fs laser ablation. Barcikowski et al.[99] verified the yield of Ag NPs in distilled water as 7.7 µg/s for ps laser ablation and 2.2 µg/s for fs laser ablation. Instead of NSs, craters are formed during ps ablation due to the HAZ; fs ablation produces NSs with smooth boundaries because of minimal HAZ.[100] Streubel et al.[101] demonstrated more than 4 g/h productivity of NPs (Pt, Au, Ag, Al, Cu, and Ti) by utilizing 500 W, 3 ps, 10 MHz laser pulses synchronized with a polygon scanner.

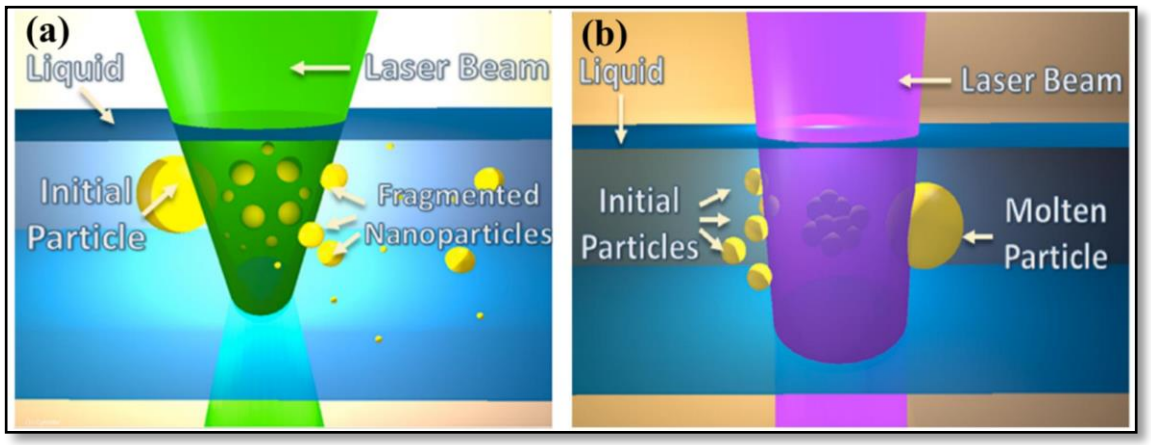

Figure 1.17 Scheme of (a) Laser fragmentation and (b) laser melting in liquid [adopted from Zhang et al.[91]]

The size of the NPs obtained from laser ablation can be modified with laser fragmentation and laser melting in liquid; schematics are shown in figures 1.17(a) and 1.17(b), respectively. Zhang et al.[91] reviewed all the processes of laser colloidal synthesis of various NPs. Laser fragmentation in liquids (LFL), the colloidal NPs are fragment into smaller NPs in liquids resulting in a reduction in the size of the NPs because of the Coulomb explosion and photothermal evaporation. The LFL of NPs can be attained by high pulse energy (> particle absorption energy) without focusing or by low pulse energy

with short focal distance or with a white light continuum (filament). Kamat et al[102] first reported laser fragmentation of Ag NPs having 40-60 nm size into 5-20 nm with 6 ns, 355 nm laser for 3 minutes. Takami et al.[103] reported laser irradiation of Au NPs leads to size reduction from >50 nm to >10 nm using 532 nm, 7 ns for 5 minutes. Furthermore, a larger size of the colloids is excited at higher fluences, resulting in fragmentation of NPs produced by the earlier pulses. Laser melting in liquids (LML) of NPs, the smaller NPs melted and fused into bigger NPs by the laser beam. LML occurs at lower fluence wherein the laser absorbed by the NPs (>melting temperature) enables the local heating on the surface of the NPs. Subsequently, they come close together and reduce their surface energy resulting in bigger sized NPs creation. Wang et al.[104] described the transformation of CuO particles in acetone from 34 nm to 300 nm using 355 nm, 10 ns, 30 Hz, 30 min. Kawasoe et al.[105] synthesized TiN submicron spherical particles 50-600 nm from TiN raw particles using 532 nm, 13 ns, 10 Hz, 28–350 mJ/cm^2 for 30 mins. LML also used to change the shape of NPs, such as the fusing of NPs/nanorods into chains/wires.[106]

In laser irradiation, apart from the physical effects (size/shape changes), there are photo-induced chemical reactions (oxidation/reduction), which alters the particle composition. Bimetallic/alloy NPs were fabricated by re-irradiation of corresponding elemental colloidal NPs or successive ablation of those two elements. Messina et al.[52] synthesized Au-Ni alloy NPs by laser irradiation of Au and Ni NPs mixture in different volumes with unfocussed 532 nm, 10 ns, 10 Hz, 0.2 J/cm^2 for 3 hours. Sebastian et al.[107] synthesized Au core-Ag shell NPs by laser ablation of Ag in Au colloidal NPs using 1064 nm, 9 ns, 10 Hz, 10^3 J/cm^2 for 35 minutes.

1.8 Rigid and flexible SERS substrate

The straightforward method to acquire the SERS-active substrates is to dry the colloidal NPs solution on the glass/silicon/paper/metal surface. Depending on the platform where the NPs/NSs are deposited, SERS substrates can be rigid or flexible. The rigid substrates are made via deposition of the colloidal solution on the surface of the glass/silicon/metal sheet, patterned glass/silicon/metal sheet. On the other hand, the flexible SERS platforms are made of cellulose paper, polymer, textile films, etc. Both rigid and flexible SERS substrates have their unique advantages and disadvantages. Solid substrates exhibit better recyclability, signal homogeneity, higher enhancement factors, but the cost and sample

collection have a considerable impact on daily practical usage. Recently, flexible SERS substrates have gained tremendous research interest due to their inexpensive, easy-to-use nature for on-site detection of a wide range of probe molecules. Further, the flexible substrates are capable of collecting the sample from any uneven surface by simple swabbing (ex. from the surface of any fruit). Apart from the detection of molecules, flexible substrates have potential in several applications such as fabrication of electronic devices[108] (diodes, transistors, energy storage devices, etc.), food safety [109], cancer screening[110], and catalysis, and are illustrated in figure 1.18.

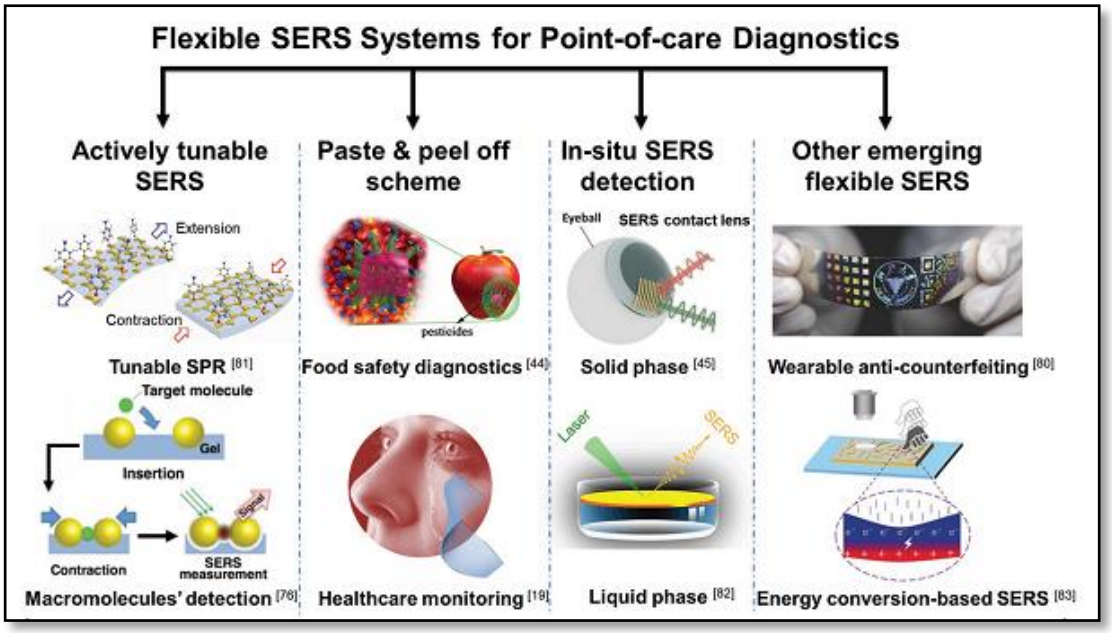

Figure 1.18 Applications of flexible SERS substrates [adopted from Xu et al.[111]]

1.8.1 Paper-based SERS substrates

Various papers used as a base material to prepare the SERS substrates such as filter paper,[112] chromatography paper,[113] A4 paper,[114] tissue paper,[115], and GCM different grade papers.[116] The porosity of the paper (few µm) may affect the NPs retention on its surface. There are numerous approaches for the fabrication of paper-based SERS substrates such as physical vapor deposition,[117-118] dipping,[110, 112] in-situ growth of metal NPs, hydrophilic wells by wax printing followed by drop-casting of NPs,[119] pen-on-paper,[114] inkjet printing,[113, 120], etc. The schematic of the fabrication of paper substrates, from a few reports, are illustrated in figure 1.19.

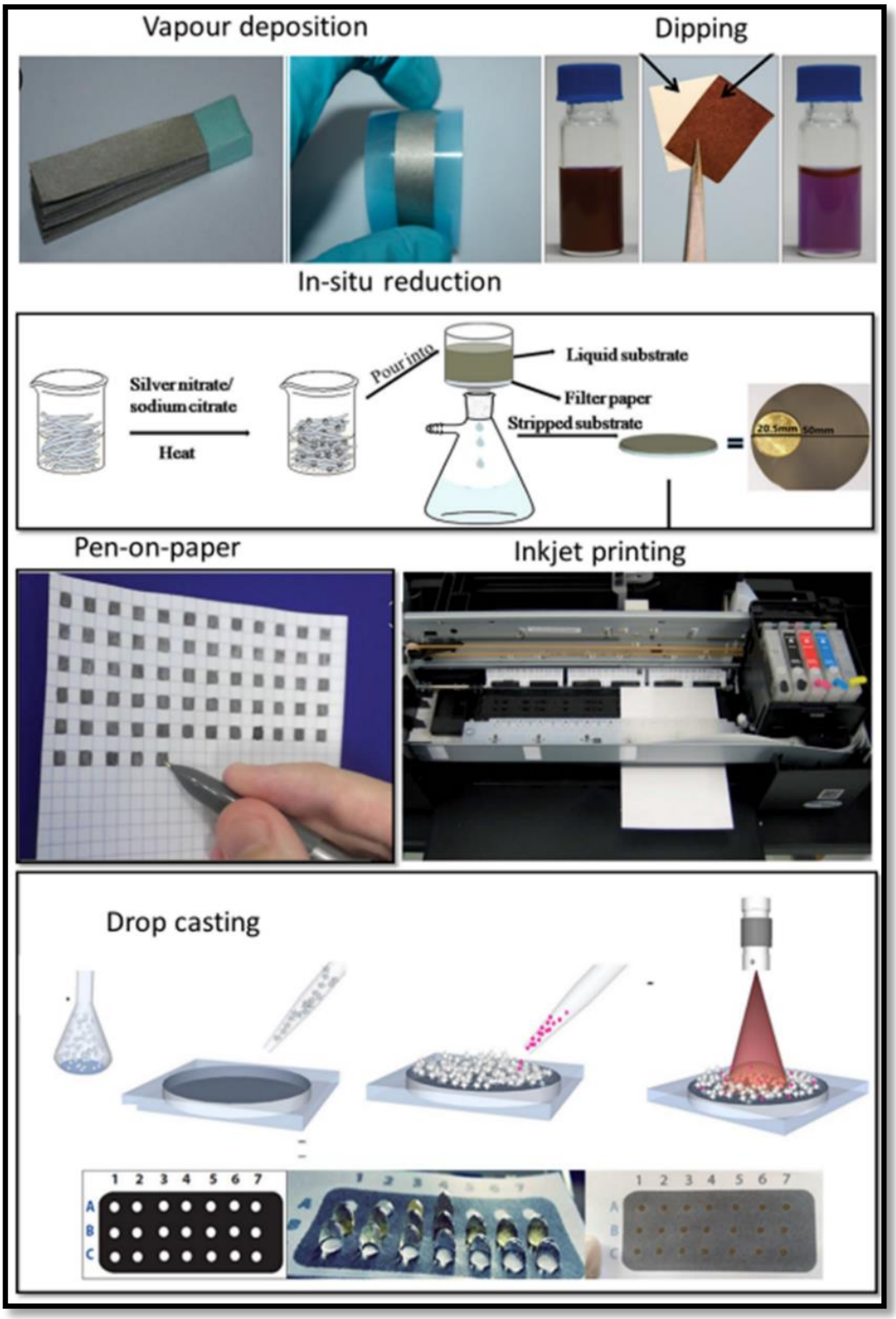

Figure 1.19 Various fabrication techniques for achieving paper-based SERS substrates (1) vapor deposition [adopted from Zhang et al.[118]] (2) dipping method [adopted from Lee et al.[112]] (3) in-situ reduction [adopted from Xian et al.[121]] (4) pen-on-paper [adopted from Polavarapu et al.[114]] (5) inkjet printing [adopted from Wei et al.[113]] (6) drop-casting on hydrophilic wells [adopted from Oliveira et al.[119]]

The in-situ synthesis means soaking of cellulose paper in metal salts such as $AgNO_3$/$HAuCl_4$ along with reducing agents $NaBH_4$/citric acid/Tollens agent, which later

requires the heating/plasma treatment/rinsing/cleaning procedure; therefore, it needs multiple cycle processes.[122-124] Dip coating is a simple method in which the NPs have to be first synthesized, then deposit those NPs on to the paper. However, the NPs loading depends on the absorbance and soaking time of the paper. Several studies have demonstrated the utility of different approaches for improving the loading, like prior soaking of paper in NaCl, Glycidyl-trimethyl-ammonium chloride (GTAC).[125-126] The advantage of dip coating/immersion method is its ability to deposit any different shape/size/composition NPs on the paper, to enhance the Raman signal.[127-129] Another fabrication method is inkjet/screen printing, which is a simple method of deposition of NPs on paper using a commercial desktop printer. The efficacy of the substrate depends on the designing of substrate patterns, preserving the viscosity and surface tension of the NPs ink and printing cycles to increase the density of NPs. Inkjet printing offers easy-to-design complex geometries using a computer, and it is possible to print already prepared NPs and also in-situ synthesis while loading precursor agents in different color ink cartridges.[130] Moreover, to improve the substrate efficiency and to avoid unwanted spreading of NPs, the hydrophobic modification of paper has been utilized before the printing of NPs.[131] The SERS performance of the various paper-based substrates is compared and are presented in Appendix A.

1.8.2 Electrospinning nanofibers

Electrospinning is a method of translation of polymeric solution/melt (with or without additives) into solid nanofibers by applying the electric field. The electrospun nanofiber films are almost identical to a paper substrate like its flexibility, porosity, and as well as a high surface area. Moreover, morphology, the thickness of the fibers, porosity, etc. of the nanofiber films can be varied by choosing the experimental parameters, i.e., the solution parameters, process parameters, and ambient parameters.[132-135]

Solution parameters

The polymer solution can be any synthetic/natural polymers, two or more polymer mixers, and polymer solution with functional nanomaterials. Concentration, molecular weight, viscosity are the valid parameters that alter the morphology of fibers. The concentrations of polymer solution show an essential role in the electrospun fiber fabrication. At a very

low concentration of the polymer solution, electrospray occurs instead of electrospinning. Therefore, micro/nanodroplets are deposited on the collector. With a slight increase in polymer solution concentration, the mixture of microbeads and fibers is observed. Smooth nanofibers are observed at a suitable concentration. If the concentration is very high, nanofibers will not be formed, only micro-ribbons will be observed. Therefore, with an increase in the concentration of the polymer solution, the obtained fiber diameter will increase. Usually, viscosity and surface tension of the solution can be changed by altering the concentration of the polymer. At a very low viscosity or surface tension, continuous and smooth fibers cannot be attained. If the viscosity of the solution is very high, it results in the hard ejection of polymer jet from the syringe needle. The polymer molecular weight also affects the fiber morphology as a decrease in the molecular weight tends to form more beads rather than smooth fibers. Husain et al.[136] analyzed the fiber morphology of PLGA [poly (lactic-co-glycolic acid)] in acetone with a varying concentration between 2 and 25 wt%. At low concentration (2 - 4 wt %), a mixture of particles and beads-on strings are observed, and at high concentration (20-25 wt %), only fibers are obtained.

Process parameters

The fiber morphology can be tuned with the processing parameters such as applied voltage for the electrostatic force, flow rate, nozzle-collector distance, fiber collector, etc. Therefore, the following factors are to be considered: (i) the applied voltage should be large enough to eject the polymer jet and transfer it to the collector. The typical potential difference applied is in the range of 10-30 kV (ii) the flow rate of the sample within the syringe is another significant parameter. Generally, a lower flow rate of 0.3 -0.6 ml/hr is more favorable (iii) the nozzle to collector distance, i.e., the distance between the collector and the syringe tip; if it is short, the polymer fiber will not have sufficient time to solidify before reaching the collector. Therefore, optimum distance is recommended for the electrospun fiber dryness from the solvent. Usually, the typical inter-electrode distance is in the range of 10-30 cm (iv) The rotating conductive collectors and flat conductive collectors in horizontal and vertical modes also affect fiber production. The rotating disk collector is appropriate for fiber direction control and also the collection area is really small. Therefore, all the electrospinning parameters have to be optimized to achieve smooth polymer nanofibers.

Ambient parameters

The fiber diameter is affected by ambient parameters like humidity and temperature. Increasing the temperature benefits the formation of thinner fiber diameter, but it may affect the solution viscosity. Low humidity will cause an increase in the solvent evaporation and will lead to dry the solvent completely.

Electrospinning polymer fibers can be used as SERS substrates by loading plasmonic NPs, similar to paper substrates, several methods are reported for embedding metal NPs onto the electrospun polymer films like dispersion of metal precursor/ pre-mixing of metal NPs into the polymer solution and surface medications after electrospinning. Chamuah et al.[137] demonstrated the Au deposition after electrospinning PVA nanofiber. Recently, Motamedi et al.[138] added laser-ablated Au NPs in Polyvinylidene fluoride (PVDF) solution before electrospinning. Zhang et al.[139] trialed the addition of Au nanorods in the PVA solution before electrospinning. Zhang et al.[140] again synthesized polyacrylonitrile (PAN) nanofibers decorated with Ag NPs via electrospinning followed by seed-mediated electro-less plating.

1.8.3 Textile based SERS substrate

The textile fabric is also an attractive SERS substrate like paper and electrospun fiber substrate because the fabric is a naturally strong, flexible, soft, and lightweight material. In textile, various materials are available such as cotton, wool, and silk, etc. Similar to other flexible substrates the loading of NPs can be done in two ways, i.e., in-situ synthesis [soaking in metals salts] and direct deposition of NPs [anisotropic silver nano-prisms and nano-disks to wool fabric[141]]. Liu et al.[142] synthesized silk fabrics SERS substrate by soaking in $HAuCl_4$ (0.1–0.6 mM, 50 mL) for 30 minutes, followed by heating and cleaning. These Au NPs loaded silk fabrics used to detect CV, 4-MPy, and PATP. Chen et al.[143] fabricated Ag-based cotton fabric by soaking in $AgNO_3$ (50 – 250 mM) followed by reducing-drying (30^{o}C for 30 min) process. The fabric soaked in 200 mM demonstrated better sensitivity (10^{-12} M) with 20% reproducibility and 57 days stability in the detection of p-Aminothiophenol. Furthermore, these fabric substrates are having other applications UV protection, antibacterial, and self-cleaning.[144-145]

1.9 Overview of thesis

The principal objective of this thesis work is to detect various explosives at very low concentrations (μM-nM-pM) using surface-enhanced Raman scattering (SERS) technique and a portable Raman spectrometer. There are many challenges in developing novel SERS substrates over the last two decades, such as sensitivity, stability, reproducibility, low-cost, and accessible sample collection. To achieve this, several systematic studies were implemented to fabricate colloidal, hybrid, and flexible SERS substrates. To fulfill this broad objective, three categories of SERS substrates have been envisaged and are demonstrated:

- Synthesizing plasmonic metal alloy NPs using fs LAL and irradiation techniques.
- Hybrid Si micro-squared arrays prepared using femtosecond pulses in conjunction with alloy NPs (obtained using fs LAL).
- Flexible substrates (paper-based/nanofiber-based) achieved using fs LAL prepared NPs impregnated into filter paper and electrospun nanofibers.

These NPs/NSs were synthesized using the LAL technique (either using fs or ps pules). Other strategies followed for the production of high-density hotspots were by using (a) the filter paper with the aggregated NPs (b) fabricating anisotropic gold (Au) NPs by chemical methods and loading them in polymer nanofibers using the electrospinning technique. Furthermore, detailed COMSOL Multiphysics simulations were performed to investigate and visualize the near field distributions of metal NPs.

1.9.1 Chapter-wise summary

This thesis contains six chapters and is organized as follows. The below schematic represents the contents of various working chapters:

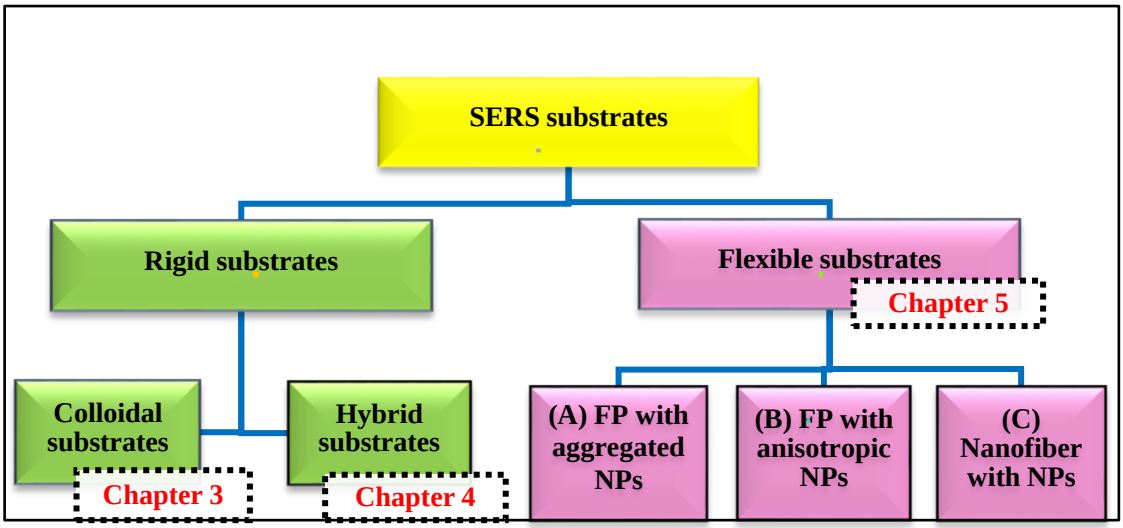

Chapter 1

This thesis starts with a short introduction to the high energy materials and details of various detection techniques, basics of Raman spectroscopy, development of surface-enhanced Raman scattering: enhancement mechanisms, the parameters influencing the enhanced Raman signal of the target molecule such as material, size, shape of the NPs and excitation laser; the requirement of ideal SERS substrates, various fabrication techniques to synthesis SERS substrates: laser ablation technique and the mechanism involved in NPs formation, summary of rigid and flexible SERS substrates; advantages and filter paper SERS substrate, preparation techniques of plasmonic papers, electrospinning to synthesis polymer nanofibers and the effective parameters on the fiber morphology, and fabric-based SERS substrates are presented.

Chapter 2

This chapter comprises an overview of the experimental details and characterization techniques. Femtosecond (fs) laser details used to perform the ablation experiments; the characteristics of fs amplifier pulses such as pulse width and beam diameter measurements are presented. Experimental procedures for the fabrication of alloy nanoparticle (NPs), silicon micro squared arrays, paper-based substrates, anisotropic gold NPs via chemical methods, nanofibers using electrospinning technique are summarized. Furthermore, characterization techniques of fabricated colloidal NPs/solid substrates, including UV-Visible absorption spectroscopy, transmission electron microscope (TEM), field emission electron microscope (FESEM) with energy dispersive spectroscopy (EDS), and X-ray

diffraction (XRD) are explained. Finally, details of the micro- and portable Raman spectrometers used for various SERS measurements are discussed. The brief description of SERS substrate preparation and the enhancement factor calculations were included.

Chapter 3

This chapter describes the synthesis of various metal alloy NPs, i.e., Ag-Cu, Ag-Au, and Cu-Au, which were fabricated using fs (with ~50 fs pulses at 800 nm) LAL technique. Ag-Cu alloy NPs were prepared via mixing and irradiation of already prepared Ag and Cu NPs. Ag-Au and Cu-Au alloy NPs were prepared by the laser ablation of Ag and Cu targets in the $HAuCl_4$ solution. The formation of alloy NPs was confirmed by different characterization techniques such as UV-Visible absorption spectra, TEM, XRD, and FESEM-mapping. The SERS performance of Ag, Cu, and Ag-Cu alloy NPs was investigated with a dye molecule (methylene blue - MB). The alloy NPs exhibited superior SERS signals (1.3 times higher EF) compared to pure metal NPs (Ag or Cu). Further, Ag-Cu alloy NPs were utilized for the detection of dye MB (5 nM), explosive molecules PA (5 µM) and AN (5 µM) with EF's of 3×10^7, 2.8×10^4 and 3.3×10^4, respectively. Moreover, Ag-Au and Cu-Au alloy NPs were also utilized for the detection of MB -5 nM and PA-5 µM, and dinitrotoluene (DNT)-1 µM and the obtained EFs were ~10^4, 10^5 and 10^7 for PA, DNT, and MB, respectively. The reproducibility of three alloys NPs was verified, and the obtained RSD was >10% for Ag-Cu and Ag-Au alloy NPs and >12% for Au-Cu alloy NPs. Among these alloys NPs, Ag-Au alloy NPs were observed to be superior SERS substrates.

Chapter 4

This chapter demonstrates the further improvement in the SERS performance of Ag-Au alloy NPs [from chapter 3] by changing the base/support from plain silicon to femtosecond laser textured silicon. The base morphology effect on SERS was examined with MB using a micro-Raman spectrometer, and the maximum SERS signal was observed from the edges of MSA because of the micro-protrusions and/or nanocavities originating from the redistribution of ablated mass. Therefore, micro square arrays (MSA) were fabricated on Si using fs laser ablation of silicon in ambient air at different input pulse energies (10, 20, 30, 50, and 100 µJ). The SERS performance on base morphology/roughness was examined with MB - 5 nM and noticed the Si MSA substrate fabricated at 30 µJ (and coated with

Ag-Au alloy NPs) had demonstrated the best SERS enhancement. The optimized substrate Si MSA (30 µJ) with Ag-Au alloy NPs were able to detect MB- 10 pM with RSD >13%. Consequently, this superior substrate was then used to identify the explosive molecules (PA, RDX) in pure form, and the achieved EF is ~10^{10} for MB, ~10^{6} for PA, and ~for RDX: 10^{4}. The estimated LOD values for the MB, PA, and RDX were ~5 pM, ~36 nM, and ~400 nM, respectively. The SERS studies continued with mixture form, i.e., dye-explosive mixture (PA-MB, DNT-MB), and explosive-explosive mixture (PA-DNT) with various concentrations. The repeatability and reproducibility also confirm the efficiency of the SERS substrate. The strength of the rigid substrate was verified with the commercially available substrate [Ag deposited ITO] provided by the SERSitive (Poland) company with MB-5 nM and PA-50 µM.

Chapter 5

This chapter deals with low cost, flexible SERS substrates, which are discussed in three different sections. The first section of this **chapter, represented as 5A,** discusses the fabrication of flexible filter paper (FP) with aggregated Ag/Au NPs. The aggregated Ag/Au NPs were achieved by mixing different concentrations (1 mM to 1 M) of NaCl to the prior fs laser-ablated Ag and Au NPs. Colloidal Ag/Au NPs were characterized by UV−visible absorption and TEM. The morphologies of the FP loaded with aggregated NPs were investigated using FESEM. The optimization of NaCl concentration was obtained by performing SERS measurement of dye molecule (MB) on the aggregated Ag/Au NPs loaded FP substrates. The Ag/Au NPs with an optimized concentration of NaCl (50 mM) loaded FP was used to detect MB-5 nM and obtained EF's 3.4×10^{7} and 7.9×10^{6} for aggregated Ag and Au NPs- FP substrate, respectively. Further Ag-based FP substrate was used in explosive detection [PA-5 µM, DNT-1 µM, and NTO-10 µM] with EF in the order of ~10^{4}, and the RSD >16%. The stability studies (Intensity degradation with respect to time) were conducted on FP with Ag and Au NPs in the detection of dye (MB – 5 µM) and pesticide (Thiram-10 µM) molecules. The SERS signal intensity dropped by ~89 % and ~40 % for Ag and Au substrates in 15 days. Because of the high plasmonic nature, Ag demonstrated better SERS signal in the early days compared to Au based substrate. From the stability studies, we observed a ~ 90% drop of SERS intensity in ~30 days for FP with Ag NPs and a ~55 % drop in 45 days for FP with Au NPs. Therefore, we believe that Au NPs loaded FP substrates have exhibited consistent SERS performance.

The second section of this chapter viz. **chapter 5B** describes the intriguing SERS performance of filter paper (FP) with anisotropic Au NPs. Three different shapes, i.e., spherical, triangular, and star shapes, were used to study the shape effect in SERS efficiency. Spherical Au NPs were synthesized using fs LAL; triangular and star-shaped Au NPs were prepared by colloidal chemical methods. The shape of the NPs and the distribution of NPs on the FP were characterized by TEM and FESEM. The superior signals SERS were observed from the star-shaped Au NPs than the triangle and spherical Au NPs using a dye molecule Nile blue (NB). FP with star-shaped Au NPs proved to be capable of detecting NB of 10 pM concentration, and the estimated enhancement factor was ~3.7×10^{10}. Further, a computational [COMSOL Multiphysics] method is presented that investigated the near field distributions of these Au NPs, and as expected, the strongly enhanced near-field intensity at the sharp features was observed. Moreover, this section continues with the comparison of the aggregation of spherical Au NPs with optimized NaCl concentration (50 mM) [chapter 5A], with the star shape NPs [chapter 5B]. In this case, the possible hot-spots locations were the aggregated spherical NPs junctions and sharp tips of the star-shaped NPs. Two probe molecules NB-5 nM and PA -5 µM are considered to evaluate the SERS performance of both FP with aggregated spherical and star Au NPs. Both the substrates found to exhibit the same order of enhancement ~10^8 for NB and ~10^4 for PA.

The third section of this chapter, namely, **Chapter 5C,** introduces other flexible substrates, i.e., polymer nanofiber mat, which are fabricated by electrospinning technique. The fabrication of PVA nanofiber was initiated to synthesize by varying the concentration of the PVA (5, 10, and 30 wt %) at a fixed nozzle-collector distance and the applied electric potential. The nanofiber's morphology and size were characterized by FESEM. Picosecond laser (~30 ps, 1064 nm, 10 Hz) fabricated Au NPs in distilled water were added to PVA before the electrospinning process. The characterization of the polymer nanofiber with and without NPs was performed using FESEM, TEM, and XRD techniques. Au NPs loaded to the PVA nanofiber were utilized for detecting MB and methyl salicylate. The efficacy of flexible substrates compared with the commercially available flexible substrates [Ag/Au loaded FP] provided by the Metrohm company with MB-5 µM and CV-5µM. The obtained EF's were 2.54×10^4 and 1.46×10^4 for MB; 8.6×10^3 and 2.2×10^3 for CV using Ag and Au based FP substrates, respectively.

Chapter 6

This chapter summarizes the obtained results in this thesis work. It discusses the future scope of this thesis including (i) detection of explosive vapors (ii) further improvement of the flexible substrates by loading various alloy anisotropic NPs (iii) several other flexible substrates like different types of clothes, papers can be explored as SERS substrates (iv) stabilize and optimize the electrospinning fiber mats by modifying the polymer morphology (hollow metal tubes, core-shell fibers) and the loaded NPs (size and shaped NPs) to improve the limit of detection (v) COMSOL simulations have to be extended to the exact representation of the SERS substrates.

Appendix A

Molecular structure and other parameters such as chemical formula, molecular weight, molecular structure and solubility of the probe molecules [5-dye molecules, 5-explosive molecules, 1-pesticide, and 1-easter agent (MS)] is provided. The Raman spectra of all the analyte molecules in pure form (powder) and stock solutions deposited on a silicon wafer (high concentration Raman spectra without NPs). Bare filter paper Raman spectra with and without NPs, analyte molecules drop-casted on FP without NPs are provided. The reported and obtained Raman peaks, and their assignments of all the molecules are presented. The performance of recently reported paper-based SERS substrates is summarized in a table. Details of commercially available rigid and flexible SERS substrate are listed.

Appendix B

Commercially available DVD's were also used as SERS substrates. The polycarbonate film on DVD was peeled off and cleaned in ethanol, performed ultrasonic bath. The periodic pattern with a metal film on DVD (suing blank and written) SERS substrate performance was verified with other base materials such as silicon and glass using NB 500 nM as a probe molecule. Fs LAL fabricated Au NPs deposited DVD -written substrate utilized to detect R6g-5µM, MB-50 nM, NB-50 nM, and CV-50 nM. The intensity of the Raman signal was increased by ~3 times in the presence of Au NPs on the DVD substrate compared to DVD without NPs. The written DVD with Au NPs was able to detect NB having a concentration of 1 nM along with an intensity variation of ~10.46% (RSD) was observed.

1.10 References

1. https://en.wikipedia.org/wiki/global_terrorism_database.
2. Zapata, F.; López-López, M.; García-Ruiz, C., Detection and Identification of Explosives by Surface Enhanced Raman Scattering. *Appl. Spectrosc. Rev.* **2016**, *51*, 227-262.
3. Hoffsommer, J. C., Analysis of Explosives Au - Yinon, Jehuda. *Crit. Rev. Anal. Chem.* **1977**, *7*, 1-35.
4. Wallin, S.; Pettersson, A.; Östmark, H.; Hobro, A., Laser-Based Standoff Detection of Explosives: A Critical Review. *Anal. Bioanal. Chem.* **2009**, *395*, 259-274.
5. Mokalled, L.; Al-Husseini, M.; Kabalan, K. Y.; El-Hajj, A., Sensor Review for Trace Detection of Explosives. *Int. J. Sci. Eng. Res.* **2014**, *5*, 337-350.
6. Singh, S., Sensors—an Effective Approach for the Detection of Explosives. *J. Hazard. Mater.* **2007**, *144*, 15-28.
7. Ruan, S.; Chen, Y.; Zhang, P.; Pan, X.; Fang, C.; Qin, A.; Ebendorff-Heidepriem, H.; Tang, B. Z.; Tang, Y.; Ruan, Y., Online Remote Monitoring of Explosives by Optical Fibres. *RSC Adv.* **2016**, *6*, 103324-103327.
8. Konstantynovski, K.; Njio, G.; Börner, F.; Lepcha, A.; Fischer, T.; Holl, G.; Mathur, S., Bulk Detection of Explosives and Development of Customized Metal Oxide Semiconductor Gas Sensors for the Identification of Energetic Materials. *Sens. Actuators, B* **2018**, *258*, 1252-1266.
9. Wen, P.; Amin, M.; Herzog, W. D.; Kunz, R. R., Key Challenges and Prospects for Optical Standoff Trace Detection of Explosives. *TrAC, Trends Anal. Chem.* **2018**, *100*, 136-144.
10. Davies, A. G.; Burnett, A. D.; Fan, W.; Linfield, E. H.; Cunningham, J. E., Terahertz Spectroscopy of Explosives and Drugs. *Mater. Today* **2008**, *11*, 18-26.
11. Yinon, J., *Counterterrorist Detection Techniques of Explosives*; Elsevier, **2011**.
12. Moore, D. S.; Scharff, R. J., Portable Raman Explosives Detection. *Anal. Bioanal. Chem.* **2009**, *393*, 1571-1578.
13. Christesen, S. D.; Guicheteau, J. A.; Curtiss, J. M.; Fountain, A. W., Handheld Dual-Wavelength Raman Instrument for the Detection of Chemical Agents and Explosives. *Opt. Eng.* **2016**, *55*, 074103.
14. Bowley, H. J.; Gerrard, D. L.; Louden, J. D.; Turrell, G., *Practical Raman Spectroscopy*; Springer Science & Business Media, **2012**.
15. Mosier-Boss, P., Review of SERS Substrates for Chemical Sensing. *Nanomaterials*, **2017**, *7*, 142.
16. Sun, J.; Gong, L.; Wang, W.; Gong, Z.; Wang, D.; Fan, M., Surface-Enhanced Raman Spectroscopy for on-Site Analysis: A Review of Recent Developments. *Luminescence* **2020**, 1-13.
17. Muehlethaler, C.; Leona, M.; Lombardi, J. R., Review of Surface-Enhanced Raman Scattering Applications in Forensic Science. *Anal. Chem.* **2016**, *88*, 152-169.
18. Gares, K. L.; Hufziger, K. T.; Bykov, S. V.; Asher, S. A., Review of Explosive Detection Methodologies and the Emergence of Standoff Deep Uv Resonance Raman. *J. Raman Spectros.* **2016**, *47*, 124-141.
19. http://iacs.res.in/old/nobel-prize.html.
20. Raman, C. V., A New Radiation. **1928**.
21. Long, D. A.; Long, D., The Raman Effect: A Unified Treatment of the Theory of Raman Scattering by Molecules. **2002**.
22. Fleischmann, M.; Hendra, P. J.; McQuillan, A. J., Raman Spectra of Pyridine Adsorbed at a Silver Electrode. *Chem. Phys. Lett.* **1974**, *26*, 163-166.

23. Jeanmaire, D. L.; Van Duyne, R. P., Surface Raman Spectroelectrochemistry: Part I. Heterocyclic, Aromatic, and Aliphatic Amines Adsorbed on the Anodized Silver Electrode. *J. Electroanal. Chem. Interfacial Electrochem.* **1977**, *84*, 1-20.
24. Albrecht, M. G.; Creighton, J. A., Anomalously Intense Raman Spectra of Pyridine at a Silver Electrode. *J. Am. Chem. Soc.*, **1977**, *99*, 5215-5217.
25. Moskovits, M., Surface-Enhanced Spectroscopy. Rev. Mod. Phys. **1985**, 57, 783-826.
26. Maier, S. A., *Plasmonics: Fundamentals and Applications*; Springer Science & Business Media, **2007**.
27. Brongersma, M. L.; Kik, P. G., *Surface Plasmon Nanophotonics*; Springer, **2007**; Vol. 131.
28. Herrera, L. J. M.; Arboleda, D. M.; Schinca, D. C.; Scaffardi, L. B., Determination of Plasma Frequency, Damping Constant, and Size Distribution from the Complex Dielectric Function of Noble Metal Nanoparticles. *J. Appl. Phys.* **2014**, *116*, 233105.
29. Jatschka, J.; Dathe, A.; Csáki, A.; Fritzsche, W.; Stranik, O., Propagating and Localized Surface Plasmon Resonance Sensing — a Critical Comparison Based on Measurements and Theory. *Sens. Bio-Sens. Res.* **2016**, *7*, 62-70.
30. Barnes, W. L., Surface Plasmon–Polariton Length Scales: A Route to Sub-Wavelength Optics. *Journal of Optics A: pure and applied optics* **2006**, *8*, S87.
31. McPeak, K. M.; Jayanti, S. V.; Kress, S. J. P.; Meyer, S.; Iotti, S.; Rossinelli, A.; Norris, D. J., Plasmonic Films Can Easily Be Better: Rules and Recipes. *ACS Photonics* **2015**, *2*, 326-333.
32. Willets, K. A.; Van Duyne, R. P., Localized Surface Plasmon Resonance Spectroscopy and Sensing. *Annu. Rev. Phys. Chem.* **2007**, *58*, 267-297.
33. García, M. A., Surface Plasmons in Metallic Nanoparticles: Fundamentals and Applications. *J. Phys. D: Appl. Phys.* **2011**, *44*, 283001.
34. Amendola, V.; Pilot, R.; Frasconi, M.; Maragò, O. M.; Iatì, M. A., Surface Plasmon Resonance in Gold Nanoparticles: A Review. *J. Phys.: Condens. Matter* **2017**, *29*, 203002.
35. Le Ru, E.; Etchegoin, P., Rigorous Justification of the$|E|^4$ Enhancement Factor in Surface Enhanced Raman Spectroscopy. *Chem. Phys. Lett.* **2006**, *423*, 63-66.
36. Lombardi, J. R.; Birke, R. L.; Lu, T.; Xu, J., Charge-Transfer Theory of Surface Enhanced Raman Spectroscopy: Herzberg–Teller Contributions. *J. Chem. Phys.* **1986**, *84*, 4174-4180.
37. Pellacani, P.; Torres-Costa, V.; Agulló-Rueda, F.; Vanna, R.; Morasso, C.; Manso Silván, M., Laser Writing of Nanostructured Silicon Arrays for the SERS Detection of Biomolecules with Inhibited Oxidation. *Colloids Surf. B* **2019**, *174*, 174-180.
38. Fonsaca, J. E.; Hostert, L.; Orth, E. S.; Zarbin, A. J., Tailoring Multifunctional Graphene-Based Thin Films: From Nanocatalysts to SERS Substrates. *J. Mater. Chem. A* **2017**, *20*, 9591-9603.
39. Jiang, S.; Guo, J.; Zhang, C.; Li, C.; Wang, M.; Li, Z.; Gao, S.; Chen, P.; Si, H.; Xu, S., A Sensitive, Uniform, Reproducible and Stable SERS Substrate Has Been Presented Based on MoS_2@Ag Nanoparticles@Pyramidal Silicon. *RSC Adv.* **2017**, *7*, 5764-5773.
40. Singha, S. S.; Mondal, S.; Bhattacharya, T. S.; Das, L.; Sen, K.; Satpati, B.; Das, K.; Singha, A., Au Nanoparticles Functionalized 3D-MoS_2 Nanoflower: An Efficient SERS Matrix for Biomolecule Sensing. *Biosens. Bioelectron.* **2018**, *119*, 10-17.
41. Jiang, X.; Sun, X.; Yin, D.; Li, X.; Yang, M.; Han, X.; Yang, L.; Zhao, B., Recyclable Au–TiO_2 Nanocomposite SERS-Active Substrates Contributed by

Synergistic Charge-Transfer Effect. *Phys. Chem. Chem. Phys.* **2017**, *19*, 11212-11219.

42. Jiang, X.; Li, X.; Jia, X.; Li, G.; Wang, X.; Wang, G.; Li, Z.; Yang, L.; Zhao, B., Surface-Enhanced Raman Scattering from Synergistic Contribution of Metal and Semiconductor in TiO_2/MBA/Ag (Au) and Ag(Au)/MBA/TiO_2 Assemblies. *J. Phys. Chem. C* **2012**, *116*, 14650-14655.
43. Lee, H. K.; Lee, Y. H.; Koh, C. S. L.; Phan-Quang, G. C.; Han, X.; Lay, C. L.; Sim, H. Y. F.; Kao, Y.-C.; An, Q.; Ling, X. Y., Designing Surface-Enhanced Raman Scattering (SERS) Platforms Beyond Hotspot Engineering: Emerging Opportunities in Analyte Manipulations and Hybrid Materials. *Chem. Soc. Rev.* **2019**, *48*, 731-756.
44. Otto, A., Surface-Enhanced Raman Scattering (SERS), What Do We Know? *Appl. Surf. Sci.* **1980**, *6*, 309-355.
45. Blaber, M. G.; Arnold, M. D.; Ford, M. J., A Review of the Optical Properties of Alloys and Intermetallics for Plasmonics. *J. Phys.: Condens. Matter*. **2010**, *22*, 143201.
46. Balčytis, A.; Nishijima, Y.; Krishnamoorthy, S.; Kuchmizhak, A.; Stoddart, P. R.; Petruškevičius, R.; Juodkazis, S., From Fundamental toward Applied SERS: Shared Principles and Divergent Approaches. *Adv. Opt. Mater.* **2018**, *6*, 1800292.
47. Guisbiers, G.; Khanal, S.; Ruiz-Zepeda, F.; de la Puente, J. R.; José-Yacaman, M., Cu–Ni Nano-Alloy: Mixed, Core–Shell or Janus Nano-Particle? *Nanoscale* **2014**, *6*, 14630-14635.
48. Muñoz-Flores, B. M.; Kharisov, B. I.; Jiménez-Pérez, V. M.; Elizondo Martínez, P.; López, S. T., Recent Advances in the Synthesis and Main Applications of Metallic Nanoalloys. *Ind. Eng. Chem. Res.* **2011**, *50*, 7705-7721.
49. Byram, C.; Soma, V. R., 2, 4-Dinitrotoluene Detected Using Portable Raman Spectrometer and Femtosecond Laser Fabricated Au–Ag Nanoparticles and Nanostructures. *Nano-Structures & Nano-Objects* **2017**, *12*, 121-129.
50. Albrecht, W.; van der Hoeven, J. E. S.; Deng, T.-S.; de Jongh, P. E.; van Blaaderen, A., Fully Alloyed Metal Nanorods with Highly Tunable Properties. *Nanoscale* **2017**, *9*, 2845-2851.
51. Vassalini, I.; Borgese, L.; Mariz, M.; Polizzi, S.; Aquilanti, G.; Ghigna, P.; Sartorel, A.; Amendola, V.; Alessandri, I., Enhanced Electrocatalytic Oxygen Evolution in Au–Fe Nanoalloys. *Angew. Chem. Int. Ed.* **2017**, *56*, 6589-6593.
52. Messina, G. C.; Sinatra, M. G.; Bonanni, V.; Brescia, R.; Alabastri, A.; Pineider, F.; Campo, G.; Sangregorio, C.; Li-Destri, G.; Sfuncia, G., Tuning the Composition of Alloy Nanoparticles through Laser Mixing: The Role of Surface Plasmon Resonance. *J. Phys. Chem. C* **2016**, *120*, 12810-12818.
53. Ko, H.; Singamaneni, S.; Tsukruk, V. V., Nanostructured Surfaces and Assemblies as SERS Media. *Small* **2008**, *4*, 1576-1599.
54. Lin, K.-Q.; Yi, J.; Hu, S.; Liu, B.-J.; Liu, J.-Y.; Wang, X.; Ren, B., Size Effect on SERS of Gold Nanorods Demonstrated Via Single Nanoparticle Spectroscopy. *J. Phys. Chem. C* **2016**, *120*, 20806-20813.
55. Stamplecoskie, K. G.; Scaiano, J. C.; Tiwari, V. S.; Anis, H., Optimal Size of Silver Nanoparticles for Surface-Enhanced Raman Spectroscopy. *J. Phys. Chem. C.* **2011**, *115*, 1403-1409.
56. Weng, G.; Feng, Y.; Zhao, J.; Li, J.; Zhu, J.; Zhao, J., Size Dependent SERS Activity of Ag Triangular Nanoplates on Different Substrates: Glass Vs. Paper. *Appl. Surf. Sci.* **2019**, *478*, 275-283.

57. Lin, Y., et al., Size and Dimension Dependent Surface-Enhanced Raman Scattering Properties of Well-Defined Ag Nanocubes. *Appl. Mater. Today* **2019**, *14*, 224-232.
58. Samal, A. K.; Polavarapu, L.; Rodal-Cedeira, S.; Liz-Marzán, L. M.; Pérez-Juste, J.; Pastoriza-Santos, I., Size Tunable Au@Ag Core-Shell Nanoparticles: Synthesis and Surface-Enhanced Raman Scattering Properties. *Langmuir* **2013**, *29*, 15076-15082.
59. Bell, S. E. J.; McCourt, M. R., SERS Enhancement by Aggregated Au Colloids: Effect of Particle Size. *Phys. Chem. Chem. Phys.* **2009**, *11*, 7455-7462.
60. Agrawal, A.; Kriegel, I.; Milliron, D. J., Shape-Dependent Field Enhancement and Plasmon Resonance of Oxide Nanocrystals. *J. Phys. Chem. C.* **2015**, *119*, 6227-6238.
61. Ma, W.; Yang, H.; Hilton, J.; Lin, Q.; Liu, J.; Huang, L.; Yao, J., A Numerical Investigation of the Effect of Vertex Geometry on Localized Surface Plasmon Resonance of Nanostructures. *Opt. Express* **2010**, *18*, 843-853.
62. Zhou, F.; Li, Z.-Y.; Liu, Y.; Xia, Y., Quantitative Analysis of Dipole and Quadrupole Excitation in the Surface Plasmon Resonance of Metal Nanoparticles. *J. Phys. Chem. C.* **2008**, *112*, 20233-20240.
63. You, H.; Ji, Y.; Wang, L.; Yang, S.; Yang, Z.; Fang, J.; Song, X.; Ding, B., Interface Synthesis of Gold Mesocrystals with Highly Roughened Surfaces for Surface-Enhanced Raman Spectroscopy. *J. Mater. Chem.* **2012**, *22*, 1998-2006.
64. Tian, F.; Bonnier, F.; Casey, A.; Shanahan, A. E.; Byrne, H. J., Surface Enhanced Raman Scattering with Gold Nanoparticles: Effect of Particle Shape. *Anal. Methods* **2014**, *6*, 9116-9123.
65. Tiwari, V. S.; Oleg, T.; Darbha, G. K.; Hardy, W.; Singh, J. P.; Ray, P. C., Non-Resonance SERS Effects of Silver Colloids with Different Shapes. *Chem. Phys. Lett.* **2007**, *446*, 77-82.
66. Rodríguez-Lorenzo, L.; Álvarez-Puebla, R. A.; de Abajo, F. J. G.; Liz-Marzán, L. M., Surface Enhanced Raman Scattering Using Star-Shaped Gold Colloidal Nanoparticles. *J. Phys. Chem. C.* **2010**, *114*, 7336-7340.
67. Hu, X.; Wang, T.; Wang, L.; Dong, S., Surface-Enhanced Raman Scattering of 4-Aminothiophenol Self-Assembled Monolayers in Sandwich Structure with Nanoparticle Shape Dependence: Off-Surface Plasmon Resonance Condition. *J. Phys. Chem. C.* **2007**, *111*, 6962-6969.
68. Zhao, L. L.; Jensen, L.; Schatz, G. C., Surface-Enhanced Raman Scattering of Pyrazine at the Junction between Two Ag20 Nanoclusters. *Nano Letters* **2006**, *6*, 1229-1234.
69. He, L. B.; Wang, Y. L.; Xie, X.; Han, M.; Song, F. Q.; Wang, B. J.; Chen, W. L.; Xu, H. X.; Sun, L. T., Systematic Investigation of the SERS Efficiency and SERS Hotspots in Gas-Phase Deposited Ag Nanoparticle Assemblies. *Phys. Chem. Chem. Phys.* **2017**, *19*, 5091-5101.
70. Kleinman, S. L.; Frontiera, R. R.; Henry, A.-I.; Dieringer, J. A.; Van Duyne, R. P., Creating, Characterizing, and Controlling Chemistry with SERS Hot Spots. *Phys. Chem. Chem. Phys.* **2013**, *15*, 21-36.
71. Haidar, I.; Levi, G.; Mouton, L.; Aubard, J.; Grand, J.; Lau-Truong, S.; Neuville, D. R.; Felidj, N.; Boubekeur-Lecaque, L., Highly Stable Silica-Coated Gold Nanorods Dimers for Solution-Based SERS. *Phys. Chem. Chem. Phys.* **2016**, *18*, 32272-32280.
72. Yi, Z.; Yi, Y.; Luo, J.; Ye, X.; Wu, P.; Ji, X.; Jiang, X.; Yi, Y.; Tang, Y., Experimental and Simulative Study on Surface-Enhanced Raman Scattering of Rhodamine 6g Adsorbed on Big Bulk-Nanocrystalline Metal Substrates. *RSC Adv.* **2015**, *5*, 1718-1729.

73. McLellan, J. M.; Li, Z.-Y.; Siekkinen, A. R.; Xia, Y., The SERS Activity of a Supported Ag Nanocube Strongly Depends on Its Orientation Relative to Laser Polarization. *Nano letters* **2007**, *7*, 1013-1017.
74. Hrelescu, C.; Sau, T. K.; Rogach, A. L.; Jäckel, F.; Laurent, G.; Douillard, L.; Charra, F., Selective Excitation of Individual Plasmonic Hotspots at the Tips of Single Gold Nanostars. *Nano letters* **2011**, *11*, 402-407.
75. Kumari, G.; Kandula, J.; Narayana, C., How Far Can We Probe by SERS? *J. Phys. Chem. C.* **2015**, *119*, 20057-20064.
76. Álvarez-Puebla, R. A., Effects of the Excitation Wavelength on the SERS Spectrum. *J. Phys. Chem. Lett.* **2012**, *3*, 857-866.
77. Alvarez-Puebla, R. A.; Ross, D. J.; Nazri, G. A.; Aroca, R. F., Surface-Enhanced Raman Scattering on Nanoshells with Tunable Surface Plasmon Resonance. *Langmuir*, **2005**, *21*, 10504-10508.
78. Lu, G.; Shrestha, B.; Haes, A. J., Importance of Tilt Angles of Adsorbed Aromatic Molecules on Nanoparticle Rattle SERS Substrates. *J. Phys. Chem. C.* **2016**, *120*, 20759-20767.
79. McCain, S.; Guenther, B.; Brady, D.; Krishnamurthy, K.; Willett, R., *Coded-Aperture Raman Imaging for Standoff Explosive Detection*; SPIE, **2012**; Vol. 8358.
80. Creighton, J., Surface Raman Electromagnetic Enhancement Factors for Molecules at the Surface of Small Isolated Metal Spheres: The Determination of Adsorbate Orientation from SERS Relative Intensities. *Surf. Sci.* **1983**, *124*, 209-219.
81. Kneipp, K.; Moskovits, M.; Kneipp, H., Surface-Enhanced Raman Scattering. *Phys. Today* **2007**, *60*, 40.
82. Wang, S.; Chinnasamy, T.; Lifson, M. A.; Inci, F.; Demirci, U., Flexible Substrate-Based Devices for Point-of-Care Diagnostics. *Trends Biotechnol.* **2016**, *34*, 909-921.
83. Nery, E. W.; Kubota, L. T., Sensing Approaches on Paper-Based Devices: A Review. *Anal. Bioanal. Chem.* **2013**, *405*, 7573-7595.
84. Natan, M. J., Concluding Remarks Surface Enhanced Raman Scattering. *Faraday Discussions* **2006**, *132*, 321-328.
85. Wang, C.; Xu, Y.; Deng, C.; Liu, Z.; Wang, R.; Zhao, H., Design and Preparation of a Recyclable Microfluidic SERS Chip with Integrated Au@Ag/TiO_2 Nts. *RSC Adv.* **2016**, *6*, 113115-113122.
86. Huang, Q.; Li, J.; Wei, W.; Wu, Y.; Li, T., Synthesis, Characterization and Application of TiO_2/Ag Recyclable SERS Substrates. *RSC Adv.* **2017**, *7*, 26704-26709.
87. Sajanlal, P.; Pradeep, T., Functional Hybrid Nickel Nanostructures as Recyclable SERS Substrates: Detection of Explosives and Biowarfare Agents. *Nanoscale* **2012**, *4*, 3427-3437.
88. Aliofkhazraei, M., *Handbook of Nanoparticles*; Springer, **2016**.
89. Amendola, V.; Meneghetti, M., What Controls the Composition and the Structure of Nanomaterials Generated by Laser Ablation in Liquid Solution? *Phys. Chem. Chem. Phys.* **2013**, *15*, 3027-3046.
90. Dell'Aglio, M.; Gaudiuso, R.; De Pascale, O.; De Giacomo, A., Mechanisms and Processes of Pulsed Laser Ablation in Liquids During Nanoparticle Production. *Appl. Surf. Sci.* **2015**, *348*, 4-9.
91. Zhang, D.; Gökce, B.; Barcikowski, S., Laser Synthesis and Processing of Colloids: Fundamentals and Applications. *Chem. Rev.* **2017**, *117*, 3990-4103.

92. Royon, A.; Petit, Y.; Papon, G.; Richardson, M.; Canioni, L., Femtosecond Laser-Induced Photochemistry in Materials Tailored with Photosensitive Agents. *Opt. Mater. Express* **2011**, *1*, 866-882.
93. Hamad, A. H., Effects of Different Laser Pulse Regimes (Nanosecond, Picosecond and Femtosecond) on the Ablation of Materials for Production of Nanoparticles in Liquid Solution. *High Energy and Short Pulse Lasers*, **2016**, 305-325.
94. Ando, K.; Nakajima, T., Clear Observation of the Formation of Nanoparticles inside the Ablation Bubble through a Laser-Induced Flat Transparent Window by Laser Scattering. *Nanoscale* **2020**.
95. Torrisi, L.; Borrielli, A.; Margarone, D., Study on the Ablation Threshold Induced by Pulsed Lasers at Different Wavelengths. *Nucl. Instrum. Methods Phys. Res., Sect. B.* **2007**, *255*, 373-379.
96. Matsutani, R.; Inoue, K.; Wada, N.; Kojima, K., Wavelength Dependence of Polyyne Preparation by Liquid-Phase Laser Ablation Using Pellet Targets. *Chem. Commun.* **2011**, *47*, 5840-5842.
97. Giorgetti, E.; Muniz-Miranda, M.; Marsili, P.; Scarpellini, D.; Giammanco, F., Stable Gold Nanoparticles Obtained in Pure Acetone by Laser Ablation with Different Wavelengths. *J. Nanopart. Res.* **2012**, *14*, 648.
98. Amoruso, S.; Ausanio, G.; Barone, A.; Bruzzese, R.; Gragnaniello, L.; Vitiello, M.; Wang, X., Ultrashort Laser Ablation of Solid Matter in Vacuum: A Comparison between the Picosecond and Femtosecond Regimes. *J. Phys. B: At. Mol. Opt. Phys.* **2005**, *38*, L329.
99. Barcikowski, S.; Menéndez-Manjón, A.; Chichkov, B.; Brikas, M.; Račiukaitis, G., Generation of Nanoparticle Colloids by Picosecond and Femtosecond Laser Ablations in Liquid Flow. *Appl. Phys. Lett.* **2007**, *91*, 083113.
100. Kaakkunen, J., Functional Surfaces Using Ultrashort Laser Pulse Ablation, **2011.**
101. Streubel, R.; Barcikowski, S.; Gökce, B., Continuous Multigram Nanoparticle Synthesis by High-Power, High-Repetition-Rate Ultrafast Laser Ablation in Liquids. *Opt. Lett.* **2016**, *41*, 1486-1489.
102. Kamat, P. V.; Flumiani, M.; Hartland, G. V., Picosecond Dynamics of Silver Nanoclusters. Photoejection of Electrons and Fragmentation. *J. Phys. Chem. B.* **1998**, *102*, 3123-3128.
103. Takami, A.; Kurita, H.; Koda, S., Laser-Induced Size Reduction of Noble Metal Particles. *J. Phys. Chem. B.* **1999**, *103*, 1226-1232.
104. Wang, H.; Pyatenko, A.; Kawaguchi, K.; Li, X.; Swiatkowska-Warkocka, Z.; Koshizaki, N., Selective Pulsed Heating for the Synthesis of Semiconductor and Metal Submicrometer Spheres. *Angew. Chem. Int. Ed.* **2010**, *49*, 6361-6364.
105. Kawasoe, K.; Ishikawa, Y.; Koshizaki, N.; Yano, T.; Odawara, O.; Wada, H., Preparation of Spherical Particles by Laser Melting in Liquid Using Tin as a Raw Material. *Appl. Phys. B.* **2015**, *119*, 475-483.
106. González-Rubio, G.; Guerrero-Martínez, A. s.; Liz-Marzán, L. M., Reshaping, Fragmentation, and Assembly of Gold Nanoparticles Assisted by Pulse Lasers. *Acc. Chem. Res.* **2016**, *49*, 678-686.
107. Sebastian, S.; Linslal, C.; Vallbhan, C.; Nampoori, V.; Radhakrishnan, P.; Kailasnath, M., Formation of Au–Ag Nanoalloy through Au Core/Ag Shell Intermediate Phase by Laser Ablation. *Chem. Phys. Lett.* **2015**, *628*, 25-29.
108. Lin, Y.; Gritsenko, D.; Liu, Q.; Lu, X.; Xu, J., Recent Advancements in Functionalized Paper-Based Electronics. *ACS Appl. Mater. & Interf.* **2016**, *8*, 20501-20515.

109. Kumar, A.; Santhanam, V., Paper Swab Based SERS Detection of Non-Permitted Colourants from Dals and Vegetables Using a Portable Spectrometer. *Anal. Chim. Acta* **2019**, *1090*, 106-113.
110. Liu, Q.; Wang, J.; Wang, B.; Li, Z.; Huang, H.; Li, C.; Yu, X.; Chu, P. K., Paper-Based Plasmonic Platform for Sensitive, Noninvasive, and Rapid Cancer Screening. *Biosens. Bioelectron.* **2014**, *54*, 128-134.
111. Xu, K.; Zhou, R.; Takei, K.; Hong, M., Toward Flexible Surface-Enhanced Raman Scattering (SERS) Sensors for Point-of-Care Diagnostics. *Adv. Sci.* **2019**, *6*, 1900925.
112. Lee, C. H.; Tian, L.; Singamaneni, S., Paper-Based SERS Swab for Rapid Trace Detection on Real-World Surfaces. *ACS Appl. Mater. & Interf.* **2010**, *2*, 3429-3435.
113. Wei, W. Y.; White, I. M., Chromatographic Separation and Detection of Target Analytes from Complex Samples Using Inkjet Printed SERS Substrates. *Analyst* **2013**, *138*, 3679-3686.
114. Polavarapu, L.; Porta, A. L.; Novikov, S. M.; Coronado-Puchau, M.; Liz-Marzán, L. M., Pen-on-Paper Approach toward the Design of Universal Surface Enhanced Raman Scattering Substrates. *Small* **2014**, *10*, 3065-3071.
115. Lan, L.; Hou, X.; Gao, Y.; Fan, X.; Qiu, T., Inkjet-Printed Paper-Based Semiconducting Substrates for Surface-Enhanced Raman Spectroscopy. *Nanotechnology* **2020**, *31*, 055502.
116. Chamuah, N.; Hazarika, A.; Hatiboruah, D.; Nath, P., SERS on Paper: An Extremely Low Cost Technique to Measure Raman Signal. *J. Phys. D: Appl. Phys.* **2017**, *50*, 485601.
117. Yu, C.-C.; Chou, S.-Y.; Tseng, Y.-C.; Tseng, S.-C.; Yen, Y.-T.; Chen, H.-L., Single-Shot Laser Treatment Provides Quasi-Three-Dimensional Paper-Based Substrates for SERS with Attomolar Sensitivity. *Nanoscale* **2015**, *7*, 1667-1677.
118. Zhang, R.; Xu, B.-B.; Liu, X.-Q.; Zhang, Y.-L.; Xu, Y.; Chen, Q.-D.; Sun, H.-B., Highly Efficient SERS Test Strips. *Chem. Commun.* **2012**, *48*, 5913-5915.
119. Oliveira, M. J.; Quaresma, P.; Peixoto de Almeida, M.; Araújo, A.; Pereira, E.; Fortunato, E.; Martins, R.; Franco, R.; Águas, H., Office Paper Decorated with Silver Nanostars - an Alternative Cost Effective Platform for Trace Analyte Detection by SERS. *Sci. Rep.* **2017**, *7*, 2480.
120. Yu, W. W.; White, I. M., Inkjet Printed Surface Enhanced Raman Spectroscopy Array on Cellulose Paper. *Anal. Chem.* **2010**, *82*, 9626-9630.
121. Xian, L.; You, R.; Lu, D.; Wu, C.; Feng, S.; Lu, Y., Surface-Modified Paper-Based SERS Substrates for Direct-Droplet Quantitative Determination of Trace Substances. *Cellulose* **2020**, *27*, 1483-1495.
122. Li, Y.; Zhang, K.; Zhao, J.; Ji, J.; Ji, C.; Liu, B., A Three-Dimensional Silver Nanoparticles Decorated Plasmonic Paper Strip for SERS Detection of Low-Abundance Molecules. *Talanta* **2016**, *147*, 493-500.
123. Marques, P. A.; Nogueira, H. I.; Pinto, R. J.; Neto, C. P.; Trindade, T., Silver-Bacterial Cellulosic Sponges as Active SERS Substrates. *Journal of Raman Spectroscopy* **2008**, *39*, 439-443.
124. Kim, W.; Kim, Y. H.; Park, H.-K.; Choi, S., Facile Fabrication of a Silver Nanoparticle Immersed, Surface-Enhanced Raman Scattering Imposed Paper Platform through Successive Ionic Layer Absorption and Reaction for on-Site Bioassays. *ACS Appl. Mater. & Interf.* **2015**, *7*, 27910-27917.

125. Hasi, W.-L.-J.; Lin, X.; Lou, X.-T.; Lin, S.; Yang, F.; Lin, D.-Y.; Lu, Z.-W., Chloride Ion-Assisted Self-Assembly of Silver Nanoparticles on Filter Paper as SERS Substrate. *Appl. Phys. A* **2015**, *118*, 799-807.
126. Huang, Z.; Cao, G.; Sun, Y.; Du, S.; Li, Y.; Feng, S.; Lin, J.; Lei, J., Evaluation and Optimization of Paper-Based SERS Substrate for Potential Label-Free Raman Analysis of Seminal Plasma. *J. Nanomater.* **2017**, *2017*, 8.
127. Mehn, D.; Morasso, C.; Vanna, R.; Bedoni, M.; Prosperi, D.; Gramatica, F., Immobilised Gold Nanostars in a Paper-Based Test System for Surface-Enhanced Raman Spectroscopy. *Vib. Spectrosc.* **2013**, *68*, 45-50.
128. Wang, C.; Liu, B.; Dou, X., Silver Nanotriangles-Loaded Filter Paper for Ultrasensitive SERS Detection Application Benefited by Interspacing of Sharp Edges. *Sens. Actuators. B* **2016**, *231*, 357-364.
129. Lee, C. H.; Hankus, M. E.; Tian, L.; Pellegrino, P. M.; Singamaneni, S., Highly Sensitive Surface Enhanced Raman Scattering Substrates Based on Filter Paper Loaded with Plasmonic Nanostructures. *Anal. Chem.* **2011**, *83*, 8953-8958.
130. Hoppmann, E. P.; Wei, W. Y.; White, I. M., Highly Sensitive and Flexible Inkjet Printed SERS Sensors on Paper. *Methods* **2013**, *63*, 219-224.
131. Hoppmann, E. P.; Wei, W. Y.; White, I. M., Inkjet-Printed Fluidic Paper Devices for Chemical and Biological Analytics Using Surface Enhanced Raman Spectroscopy. *IEEE J. Sel. Top. Quantum Electron.* **2014**, *20*, 195-204.
132. Huang, Z.-M.; Zhang, Y. Z.; Kotaki, M.; Ramakrishna, S., A Review on Polymer Nanofibers by Electrospinning and Their Applications in Nanocomposites. *Compos. Sci. Technol.* **2003**, *63*, 2223-2253.
133. Teo, W. E.; Ramakrishna, S., A Review on Electrospinning Design and Nanofibre Assemblies. *Nanotechnology* **2006**, *17*, 89-106.
134. Xue, J.; Wu, T.; Dai, Y.; Xia, Y., Electrospinning and Electrospun Nanofibers: Methods, Materials, and Applications. *Chem. Rev.* **2019**, *119*, 5298-5415.
135. Aleisa, R., Electrospinning. In *Handbook of Synthetic Methodologies and Protocols of Nanomaterials*, **2020**.
136. Husain, O.; Lau, W.; Edirisinghe, M.; Parhizkar, M., Investigating the Particle to Fibre Transition Threshold During Electrohydrodynamic Atomization of a Polymer Solution. *Mater. Sci. Eng.* **2016**, *65*, 240-250.
137. Chamuah, N.; Bhuyan, N.; Das, P. P.; Ojah, N.; Choudhary, A. J.; Medhi, T.; Nath, P., Gold-Coated Electrospun Pva Nanofibers as SERS Substrate for Detection of Pesticides. *Sens. Actuators, B* **2018**, *273*, 710-717.
138. Motamedi, A. S.; Mirzadeh, H.; Hajiesmaeilbaigi, F.; Bagheri-Khoulenjani, S.; Shokrgozar, M. A., Piezoelectric Electrospun Nanocomposite Comprising Au NPs/PVDF for Nerve Tissue Engineering. *J. Biomed. Mater. Res. Part A* **2017**, *105*, 1984-1993.
139. Zhang, C. L.; Lv, K. P.; Cong, H. P.; Yu, S. H., Controlled Assemblies of Gold Nanorods in Pva Nanofiber Matrix as Flexible Free-Standing SERS Substrates by Electrospinning. *Small* **2012**, *8*, 648-653.
140. Zhang, L.; Gong, X.; Bao, Y.; Zhao, Y.; Xi, M.; Jiang, C.; Fong, H., Electrospun Nanofibrous Membranes Surface-Decorated with Silver Nanoparticles as Flexible and Active/Sensitive Substrates for Surface-Enhanced Raman Scattering. *Langmuir* **2012**, *28*, 14433-14440.
141. Tang, B.; Wang, J.; Xu, S.; Afrin, T.; Xu, W.; Sun, L.; Wang, X., Application of Anisotropic Silver Nanoparticles: Multifunctionalization of Wool Fabric. *J. Colloid Interface Sci.* **2011**, *356*, 513-518.

142. Liu, J.; Zhou, J.; Tang, B.; Zeng, T.; Li, Y.; Li, J.; Ye, Y.; Wang, X., Surface Enhanced Raman Scattering (SERS) Fabrics for Trace Analysis. *Appl. Surf. Sci.* **2016**, *386*, 296-302.
143. Chen, Y.; Ge, F.; Guang, S.; Cai, Z., Low-Cost and Large-Scale Flexible SERS-Cotton Fabric as a Wipe Substrate for Surface Trace Analysis. *Appl. Surf. Sci.* **2018**, *436*, 111-116.
144. Zheng, Y.; Xiao, M.; Jiang, S.; Ding, F.; Wang, J., Coating Fabrics with Gold Nanorods for Colouring, Uv-Protection, and Antibacterial Functions. *Nanoscale* **2013**, *5*, 788-795.
145. Wang, R.; Wang, X.; Xin, J. H., Advanced Visible-Light-Driven Self-Cleaning Cotton by Au/TiO_2/SiO_2 Photocatalysts. *ACS Appl. Mater. & Interf.* **2010**, *2*, 82-85.

Chapter 2

Experimental details

Abstract

This chapter discusses the methodologies used for the preparation of colloidal nanoparticles (NPs) and nanostructures (NSs) used for all the experiments in this thesis. Details of the femtosecond (fs) laser system that has been used for the laser ablation experiments are included. The characteristics of fs amplifier pulses, such as pulse width and beam diameter measurements, are presented. The procedures for obtaining monometallic, alloy NPs, and silicon micro squared array fabrication via the fs laser ablation, different shaped Au NPs synthesis through chemical approaches, polymer nanofibers preparation using electrospinning technique are discussed in detail. Further, necessary details of the characterization tools which were used for the analysis of the obtained NPs and NSs such as (a) UV-Visible absorption spectroscopy (b) X-ray diffractometer (XRD) (c) Transmission electron microscopy (TEM) and selected area diffraction (SAED) technique (d) Field emission scanning electron microscope equipped with energy-dispersive X-ray spectroscopy (FESEM-EDS) are described meticulously. Finally, details of the micro- and portable Raman spectrometers used for various Raman/SERS measurements presented in this thesis, SERS substrate preparation and enhancement factor calculations are discussed.

2.1 Femtosecond laser system (LIBRA, M/s Coherent)

LIBRA is a femtosecond (fs) amplifier laser system and the main components are (1) Vitesse (seed laser) (2) Evolution [pump laser] (3) stretcher (4) regenerative amplifier and (5) compressor. The layout/picture of the laser system is shown in figure 2.1.[1]

1. Vitesse is a fs laser oscillator. It comprises Verdi laser and Verdi Pumped Ultra-Fast [VPUF] laser head. Neodymium:Yttrium orthovanadate (Nd: YVO_4) is the gain medium in the Verdi laser, which generates 1064 nm radiation. The second harmonic laser at 532 nm is produced from 1064 nm using a LBO (Lithium Triborate, LiB_3O_5) crystal. VPUF laser head includes Ti: sapphire crystal and negative dispersion mirrors (NDMs). Ti: sapphire active medium is pumped by a Verdi laser (532 nm), which generates seed pulses with a central wavelength of 800 nm. The Ti: sapphire crystal has broad absorption and emission peaks in 400-650 nm and 660-1180 nm range, respectively. NDMs are utilized to achieve mode-locking in the seed laser (Vitesse). Therefore, Vitesse generates mode-locked pulses (~100 fs) at 800 nm with a repetition rate of 80 MHz.
2. The evolution (pump laser) supplies pump pulses to the amplifier module. It comprises Nd:$YLiF_4$ (Neodymium Yttrium Lithium Fluoride), which has efficient energy storage for high energy pulse operation at a low repetition rate because of a long upper-state lifetime (~470 μs). It is a diode-pumped Q-switched laser (~100 ns pulse duration) operating at 527 nm and a repetition rate of 1 kHz.
3. Stretcher is used for temporal stretching of the seed laser from ~ fs to ~ ps duration before passing through the amplifier and it is achieved with the help of gratings. The stretcher and compressor are integrated into a single box.
4. The regenerative amplifier consists of Ti: Sapphire laser rod and it is excited by the evolution laser. Synchronization and Delay Generator (SDG) controls the functioning of Pockels cells. Pockels cells are used to trap the pulses in the cavity and allow the multiple passes until it reaches the maximum energy. The energy of the seed pulse is amplified from nJ to mJ and, further, the repetition rate of the amplifier changes to 1 kHz.
5. After the amplification, the pulse enters the compressor part. It is a reverse procedure to that of stretching. Output pulses coming out from the legend amplifier have a pulse duration of ~50 fs, 800 nm wavelength, and 1 kHz repetition rate.

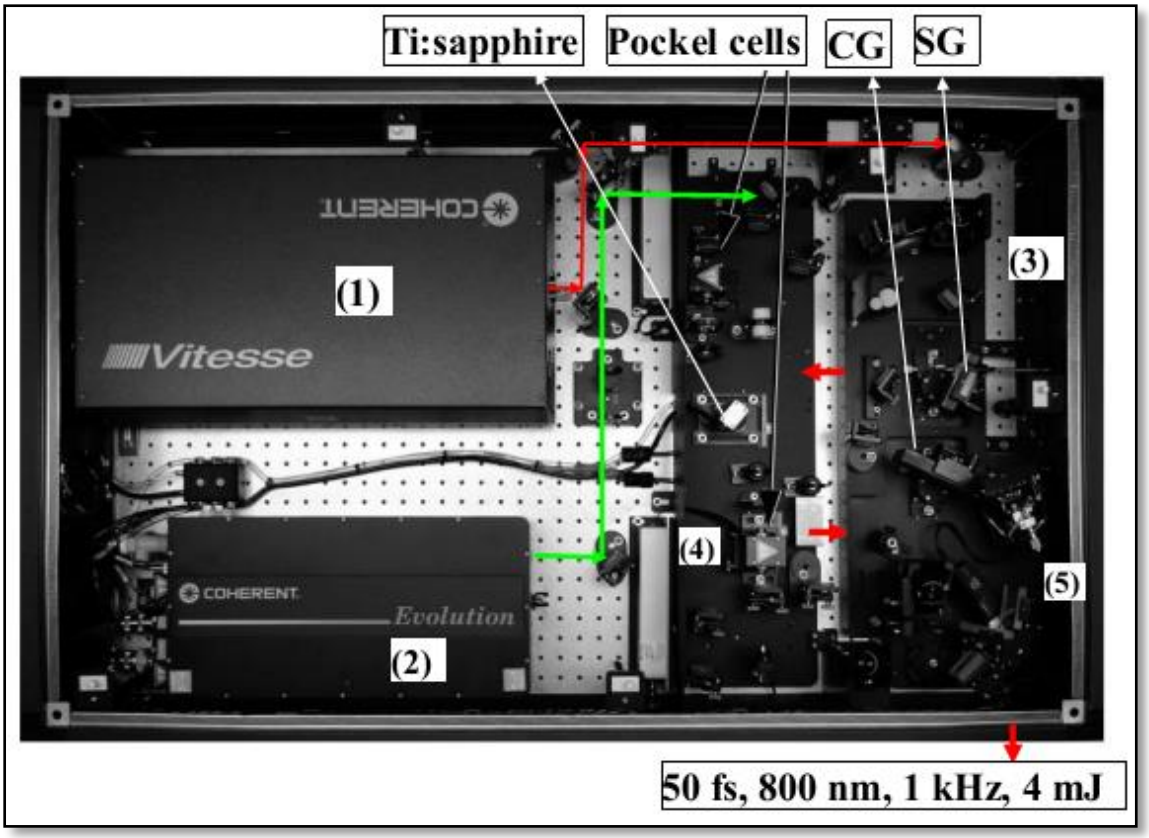

Figure 2.1 LIBRA Femtosecond amplifier system-top view showing (1) Vitesse (seed laser) (2) Evolution (pump laser) (3) Stretcher (4) Regenerative amplifier region and (5) Compressor region (available at ACRHEM, UoH)

2.1.1 Pulse duration measurements

The pulse width/duration of the amplified fs laser pulses (LIBRA, Coherent) was estimated using a single shot auto-correlator (SSA), the layout of which is shown in figure 2.2. The fs pulses from the Libra were fed to the SSA through the mirrors and beam splitters provided. The laser pulses were split into two beams (dotted and solid lines in figure 2.2) and enter into KDP (Potassium Dihydrogen Phosphate) second-order nonlinear optical crystal with a delay. The fundamental wavelength (800 nm) was filtered out using appropriate optics. The auto-correlator signal was detected with a CCD, connected to an oscilloscope. The delay between the beams was varied with the micrometer screw to get the maximum autocorrelation signal on the oscilloscope. The obtained signal is shown in figure 2.2. The pulse duration calculations are described as,

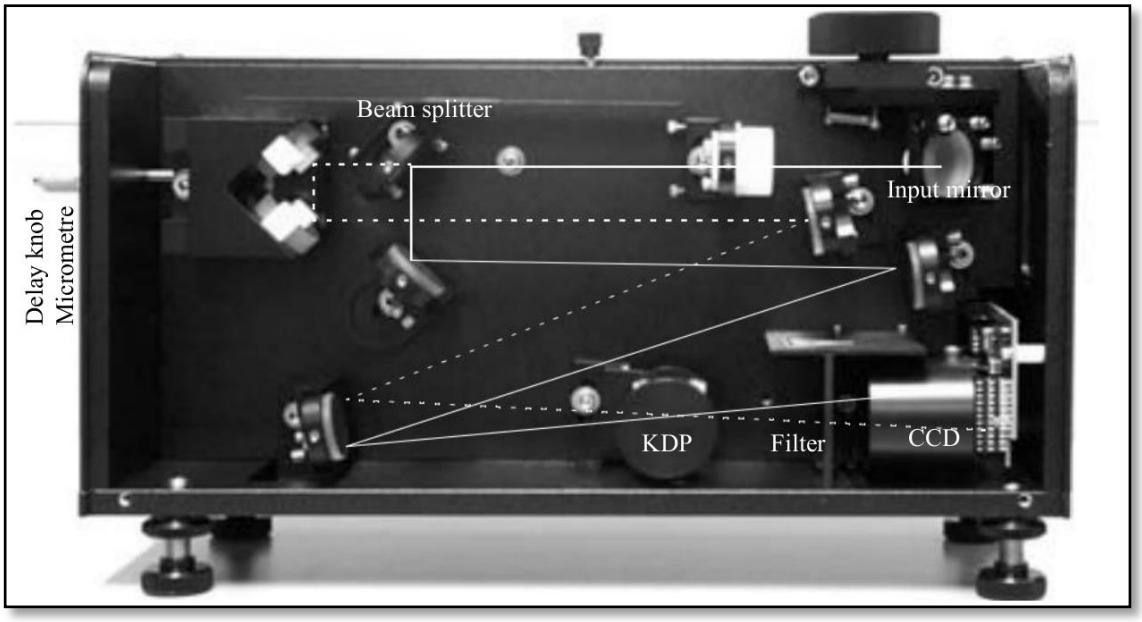

Figure 2.2 Single-shot autocorrelator layout to measure the Libra fs pulse duration (available at ACRHEM, UoH)

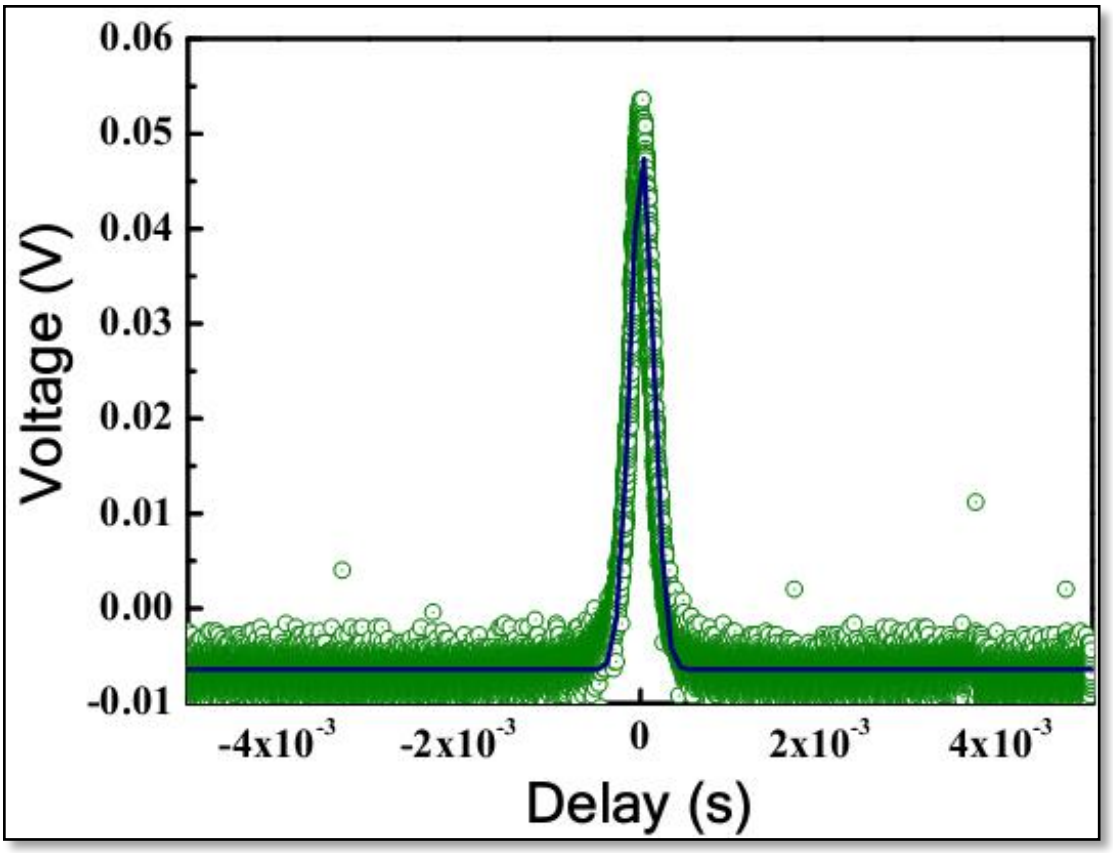

Figure 2.3 Libra fs laser pulses autocorrelation data using SSA (green circles represent data and the solid blue line represents the fit)

From the Gaussian fit, FWHM = 3.05×10^{-4} = 0.305 ms

The distance the delay stage has moved = 0.02 mm

Optical path length change = 0.04 mm

Optical delay change = $4 \times 10^{-5}/3 \times 10^{8} = 1.33 \times 10^{-13} s$

Amount peak moved on oscilloscope = $1.33 \times 10^{-13}/400 \times 10^{-6} = 0.33\ fs/\mu s$

Calibration = $0.33 fs/\mu s \times 0.305\ ms$ =101 fs

The pulse duration for the Gaussian pulse = $101\ fs/\sqrt{2} = 71.4\ fs$

The measured output pulse duration (~71 fs) from SSA is slightly different as compared to the input pulse duration (~50 fs, from company specifications), which can be attributed to the temporal broadening by the dispersive media such as filters, mirrors, and the KDP crystal.

2.1.2 Beam diameter-Knife edge experiment

The schematic of the experiment set up for beam diameter measurements is shown in figure 2.4. The beam diameter was estimated using a knife-edge experiment. A knife-edge mounted normal to the laser beam and photo-detector. Moreover, the knife was fixed on a micropositioner to scan insertion manually and to withdraw from the laser beam. The corresponding output at different positions was noted. The output of the detector was plotted as a function of the knife-edge position, as illustrated in figure 2.5.

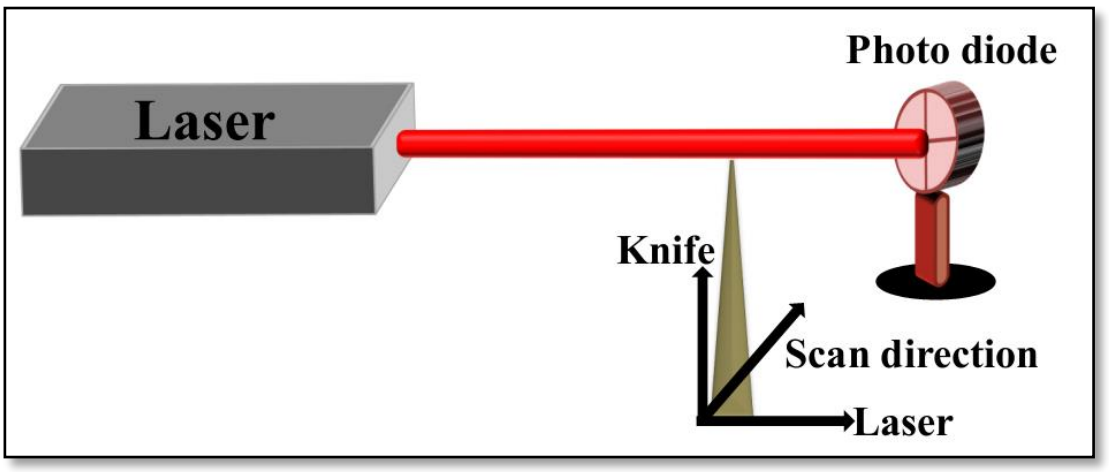

Figure 2.4 Schematic of the knife-edge experiment to measure the beam waist

The irradiance distribution of the Gaussian laser beam as a function of cartesian coordinates is $I = I_0 e^{(-2(x^2+y^2)/\omega_0^2)}$, where $I_0 = 2P/\pi\omega_0^2$, P is the power of the beam; ω_0 is the beam waist radius. Comparing the above equation with probable error (w), at 25 % and 75 % of the relative power, the distance of the knife-edge position identified ($2e_p$), and is equal to the probable error as e_p=0.6745 w. The estimated $2e_p$ from the graph 3.5

mm, the probable error w is 2.6 mm, and the beam spot size $\omega_0 = 4w = 10.4$ mm. These experiments were performed near to experimental ablation setup.

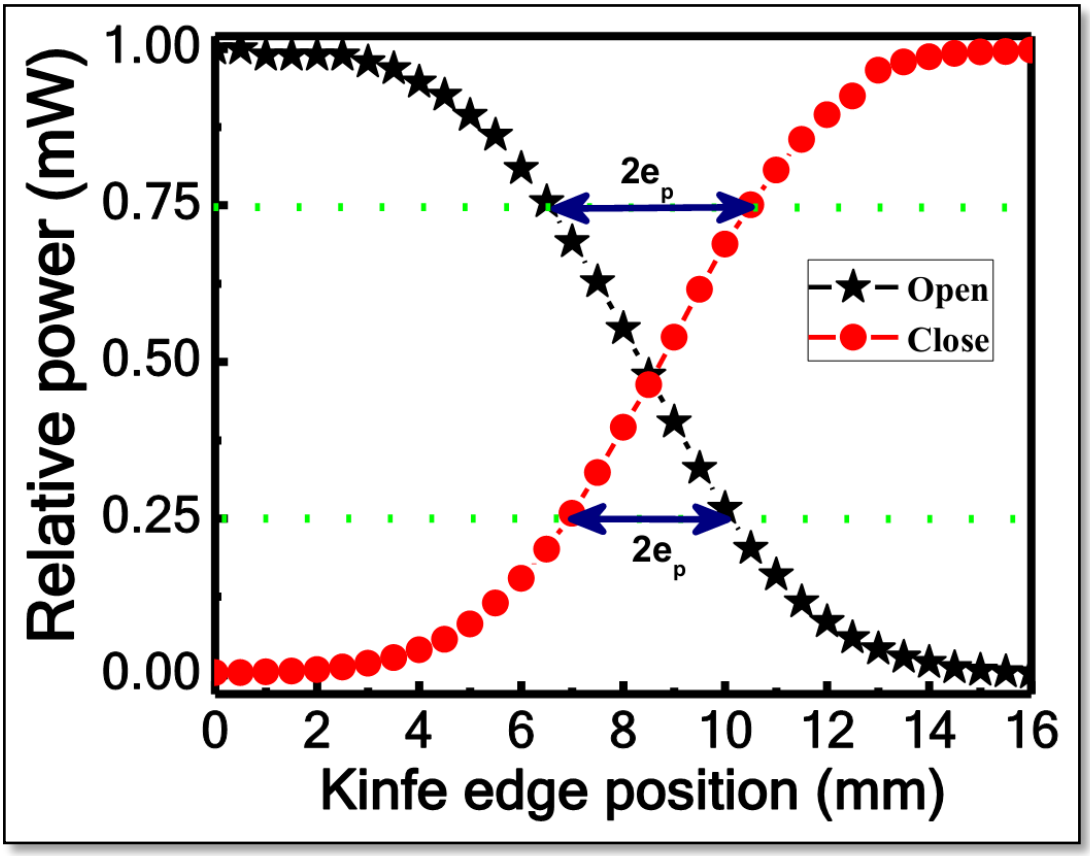

Figure 2.5 Plot of relative power versus knife-edge position in both closing and opening mode.

2.2 Fs laser ablation experimental details

The schematic for synthesizing the nanoparticles (NPs) and nanostructures (NSs) using fs LAL setup is depicted in figure 2.6. NPs were prepared with Ti: Sapphire femtosecond laser system (M/s Coherent, 4 mJ, 1 kHz) operating at a central wavelength of 800 nm and, ~ 50 fs pulse duration. Thus, the average output power of ~4 W derived from the amplifier. The laser beam passed through a combination of a Brewster polarizer (B) and a half-wave plate (H), which was used to tune the input pulse energy. The half-wave plate is typically a polarization rotator and was mounted in a rotating polarizer holder. According to the Malus law ($I=I_0 \cos^2\theta$) intensity ratio (I/ I_0) can be controlled by rotating at the half-wave plate at an angle of 'θ.' Further, the tuned laser beam passing through Brewster's polarizer (B), which was fixed at Brewster angle (this angle depends on the refractive indices of the media, and can be calculated with Brewster's law $\tan\theta=n_2/n_1$, for air-glass interface θ

~56.3^0), which reflects s-polarized light while transmitting p-polarized light. Mirrors M1, M2, and M3 were used to guide the polarized laser beam with the desired pulse laser energy. A Plano-convex lens (L) was used to focus the laser beam on to the sample. The focus was adjusted on the sample surface by noticing the intense plasma plume and listening to the sound produced (also a low power He-Ne laser was used to obtain the exact focusing distance). The NPs were obtained by fixing the sample in a beaker with the desired liquid. The sample/beaker was scanned using computer-controlled X-Y stages (Newport stages with a resolution of 0.1 µm). The sample movement was generally used to achieve the various morphologies and to avoid the single spot ablation. After the ablation, the prepared NPs/NSs were preserved for further usage.

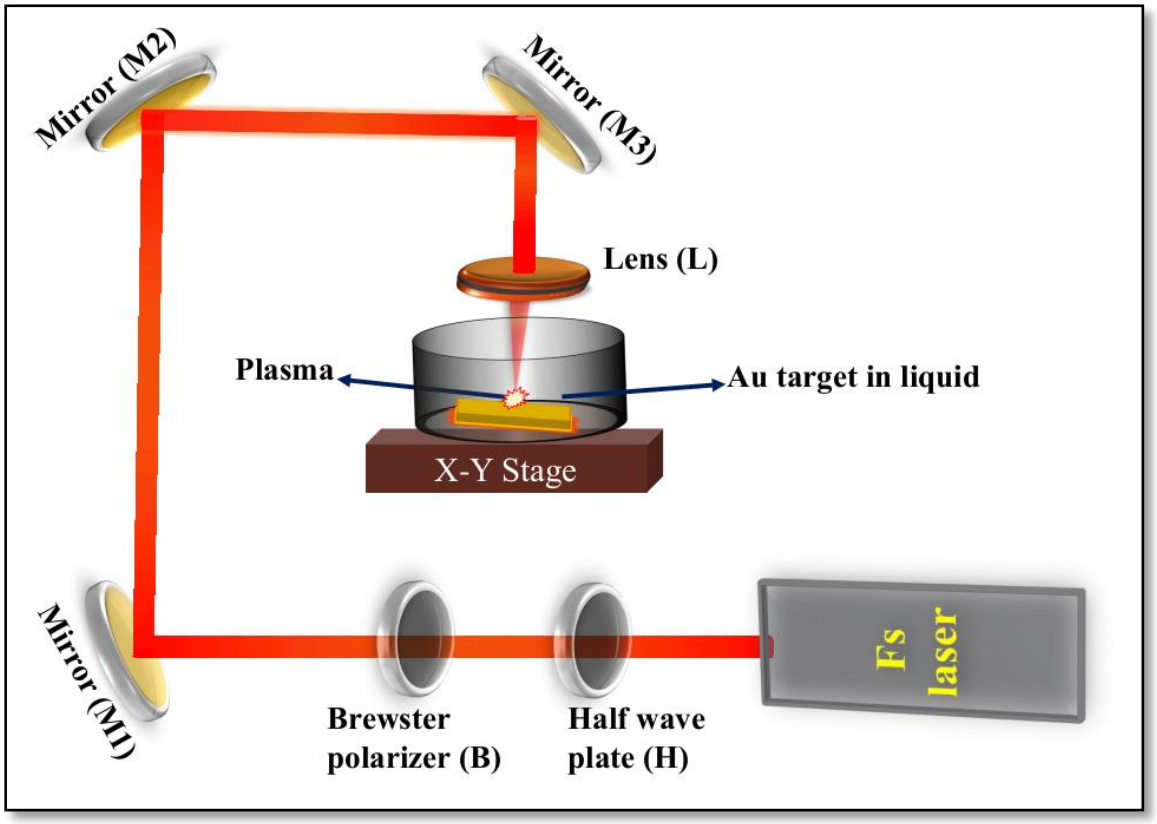

Figure 2.6 Schematic of the LAL setup to prepare nanoparticles (NPs) and nanostructures (NSs)

The photograph of the laser ablation experimental set up is illustrated in figure 2.7(a). The color change of the solution (Au NPs in deionized water) at different time intervals typically 1, 5, 15, and 30 minutes are shown in figures 2.7(b), 2.7(c), 2.7(d), and 2.7(e), respectively. Figure 2.7(f) depicts the laser-ablated area on the Au target while figure 2.7(g) shows the glass vial containing prepared Au NPs (in deionized water).

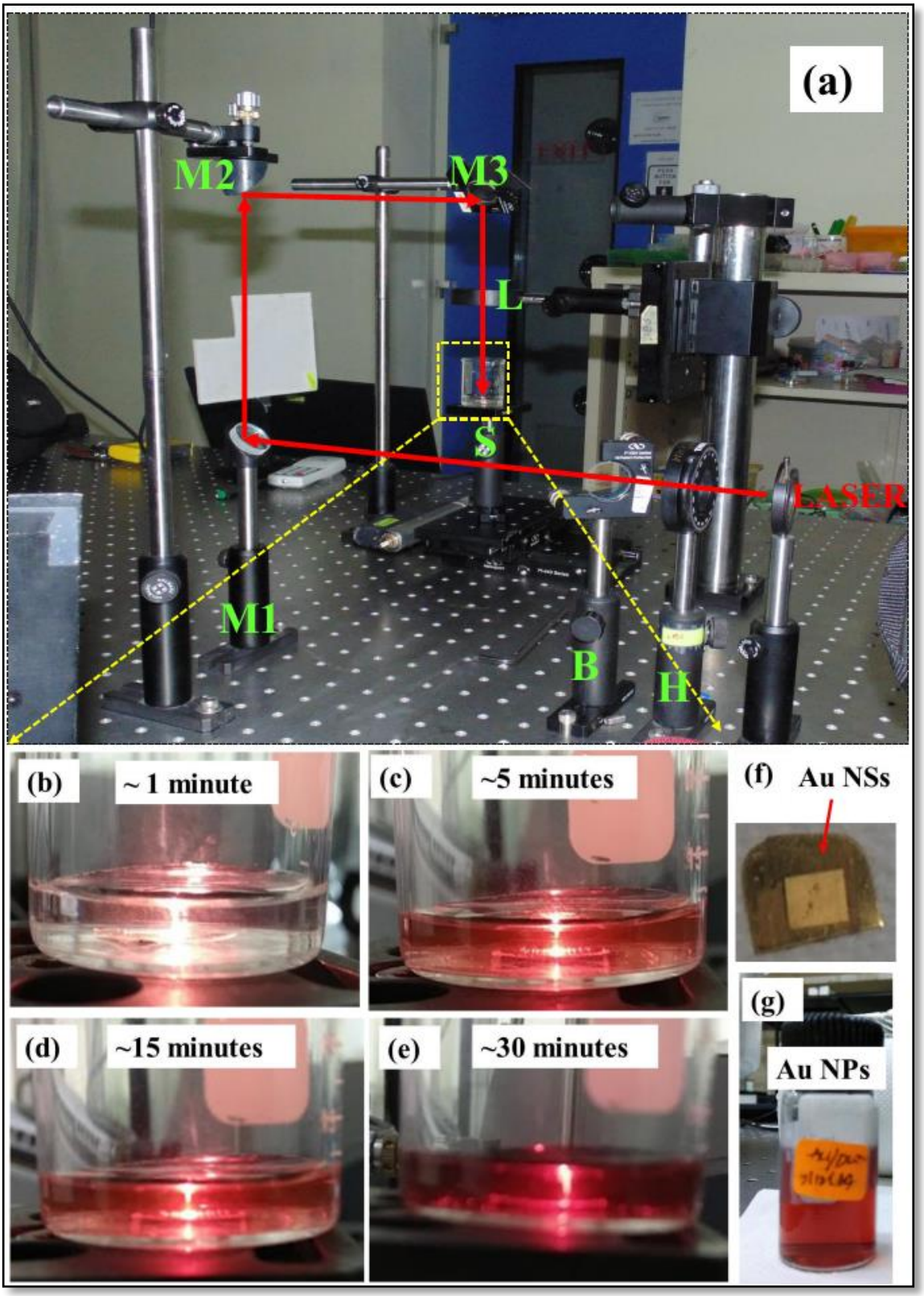

Figure 2.7 Photographs of (a) of laboratory setup of laser ablation technique (b, c d, and e) gold nanoparticles formation during laser ablation at different times (f) laser ablated area (NSs) on gold target (g) glass vials with Au NPs in deionized water (photograph collected while doing experiments at ACRHEM, UoH)

2.2.1 Monometallic NPs preparation

Monometallic Ag, Au, and Cu NPs were synthesized using the fs LAL technique. Prior to LAL experiments, pure metal substrates were cleaned with alcohol and deionized water sequentially for 15 minutes in an ultrasonicator. The cleaned samples were subsequently ablated with laser pulses from a regenerative fs (Ti: sapphire) amplifier (~50 fs, 800 nm, 1 kHz). The laser beam was focused through a plano-convex lens (focal length of 100 mm). The metal target with a thickness of ~1 mm was submerged in 10 mL of deionized water, which was placed in a glass beaker. The sample was scanned with a computer-controlled translational stage and scanned with 0.1 mm/s speed along the X, Y directions with the step size 0.1 mm. Post ablation, the obtained NPs were preserved and subsequently employed for the SERS studies. Photographs of the obtained Ag, Au, and Cu NPs are shown in figure 2.8, and the experimental details of ablation for individual colloids preparation are described in their respective chapters.

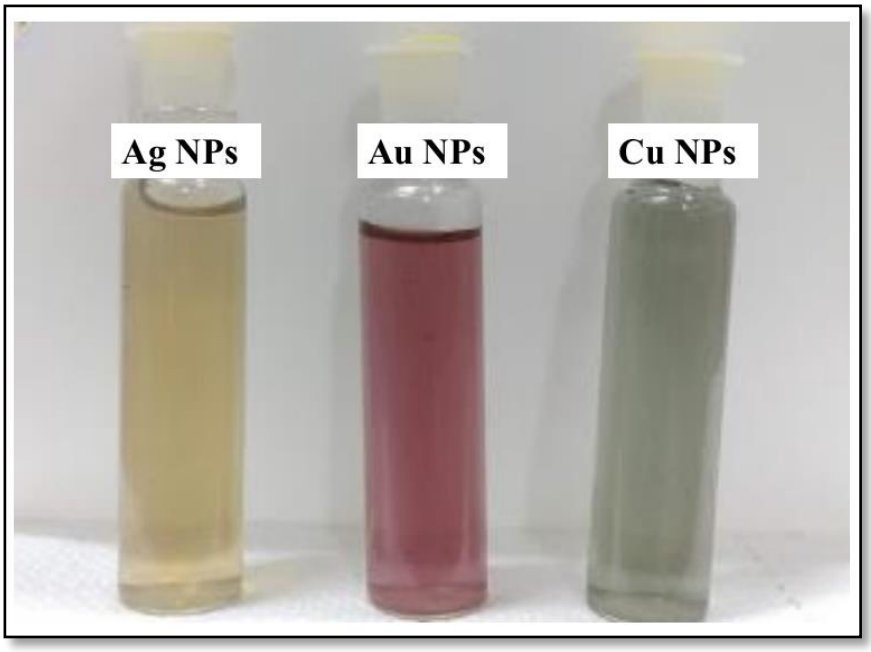

Figure 2.8 Photograph of Ag, Au and Cu NPs obtained by fs laser ablation in liquid technique

2.2.2 Alloy NPs preparation

Alloy metal NPs were synthesized in two different approaches: (a) Mixing and laser irradiation of monometallic NPs and (b) laser ablation of metal (Ag/Cu) in the presence of gold precursor. Ag–Cu alloy NPs are synthesized by mixing Ag and Cu colloidal solutions in equal volumes (2.5 ml each) followed by irradiation (without focusing the laser beam). An unfocused laser beam with an input beam diameter of 10.4 mm and pulse energy of

150 mJ was used for laser irradiation. The colloidal solution was continuously stirred with the help of magnetic stirrer at 50 rpm to avoid the settling of the NPs at the bottom and further to maintain a homogenous irradiation process. Alloy NPs formation was primarily verified by looking at the absorption spectra at different laser irradiation times. Ag-Au and Cu-Au alloy NPs were prepared by the laser ablation of pure Ag and Cu in 5 mM $HAuCl_4$ solution with fs amplifier pulses (~50 fs at 800 nm, 1 kHz) with an energy of ~300 μJ focused onto the Ag/Cu targets using a 100 mm convex lens. The beaker with Ag or Cu targets immersed in a gold precursor solution was rotated so as to avoid the deposition of NPs onto the substrate. The solution color turned into dark pink and dark brown colors (depending on the ablation time) with Ag/Cu targets, respectively. After completing the ablation, the colloidal solutions were centrifuged at 3500 rpm for 15 minutes and thoroughly cleaned with deionized water then dispersed in 5ml ethanol. Experiments details of ablation for individual alloy NPs preparation are described in chapter 3.

2.2.3 Silicon micro squared array preparation

The fs laser ablation of silicon (Si) in the air was performed to prepare Si MSA (micro squared array). Before the ablation process, crystalline Si targets of 1-mm thickness and p-type (100), silver targets (>99% pure, from Sigma Aldrich) were cleaned in an ultrasonic cleaner with acetone to remove the impurities. The pulse energy was tuned with the combination of a half-wave plate and a Brewster polarizer. Five different pulse energies, viz., 10 μJ, 20 μJ, 30 μJ, 50 μJ, and 100 μJ, were employed to fabricate the silicon micro/nanostructures (NSs). A 100-mm focal length convex lens was used to focus the laser onto the target. The Si sample was mounted on a high precision computer-controlled two-axis translation stage. It was utilized to draw periodic lines with scanning speeds of ~0.1 mm/s in both the X- and Y-directions through raster scanning starting at two different positions resulting in a cross-structure over five mm^2 areas. The horizontal scanning length was programmed to be 5 mm, while the vertical spacing between each horizontal line being 50 μm. The laser line scanning on sample turned into a single groove and, hence, an array of grooves was prepared by line-by-line scanning. Thus, the square arrays of 5 mm^2 size were fabricated on a Si surface by applying laser scanning in the horizontal plane along with two orthogonal directions. After the laser interaction, the patterned surfaces or micro-

nano structures were rinsed in deionized water and in acetone. This treatment removed the dust particles and organic contaminants from the laser textured surfaces. All samples were appropriately cleaned, dried, and preserved at room temperature. Details of ablation experiments of Si MSA are described in chapter 4.

2.3 Anisotropic Au NPs-Chemical method

Anisotropic Au NPs were prepared using a single-step wet chemical method. There are several methods that have been developed for synthesizing different shaped Au NPs which were reported in the literature. Kamalesh et al.[2] considered PVP as a reducing agent and proposed various shapes by choosing different solvents viz. for spherical → methanol, for decahedra → ethanol, for the hexagon → 2-propanol, for water → triangular and for star → dimethylformamide (DMF). In this work, triangular and star-shaped gold NPs were prepared by the method proposed by Kamalesh et al.[2] Concisely, triangular shape Au NPs were synthesized by using 0.27 mM aqueous solution of gold precursor [$HAuCl_4.3H_2O$] mixed with 15 ml of 5 mM PVP (2.4 g in 15 ml) solution in deionized water at ambient conditions. Furthermore, the star-shaped Au NPs were also prepared. Briefly, 3 mM PVP was dissolved in 15 ml DMF with 1.5 mM sodium hydroxide (NaOH), 0.27 mM gold salt ($HAuCl_4.3H_2O$). Both the samples were centrifuged five times in ethanol at 5500 rpm to remove any excess PVP in the solution. Subsequently, the prepared NPs were dispersed in 2 ml of ethanol and utilized for further studies. The characterization details are discussed in chapter 5b.

2.4 Polymer nanofiber preparation-Electrospinning technique

Several types of polymers have been utilized to fabricate nanofibers such as synthetic, semisynthetic, and biological polymers.[3] However, it is to be noted that all polymers are not accomplished in making nanofibers. PVA is a hydrophilic, non-toxic, and biocompatible and shows tremendous physical properties such as water-solubility, strength, and thermal stability.[4] For the deposition of PVA nanofibers, an electrospinning system (ESPIN-NANO, India) was utilized at a voltage of 16 kV. The electrospinning experimental setup is demonstrated in figure 2.9(a), and the photograph of the electrospinning instrument is shown in figures 2.9(b) and 2.9(c). The rotating disk with 1500 collector rotations per minute (rpm) was used to collect the sample, which was

covered by an aluminum foil. PVA solution was filled in a 5 ml syringe without air bubbles, and a flow rate of 0.5 ml/h was maintained. The distance between the collector and the tip of the syringe needle was adjusted at ~15 cm. The electrospinning conditions were optimized by investigating the polymer solution concentrations, which is a crucial factor affecting the output. Three different concentrations of PVA solutions (5 wt%, 10 wt%, and 30 wt % of PVA) were prepared in deionized water at 80 °C in the ultrasonic bath. All three concentrations of PVA nanofibers were fabricated on the electrospinning apparatus operated at the same conditions. The photograph of the synthesized flexible polymer nanofiber mat is shown in figure 2.9(d). The best electrospinning condition was filtrated from the FESEM studies of nanofibers. Au NPs loaded polymer nanofibers are used as SERS substrates, and the full details are discussed in chapter 5C.

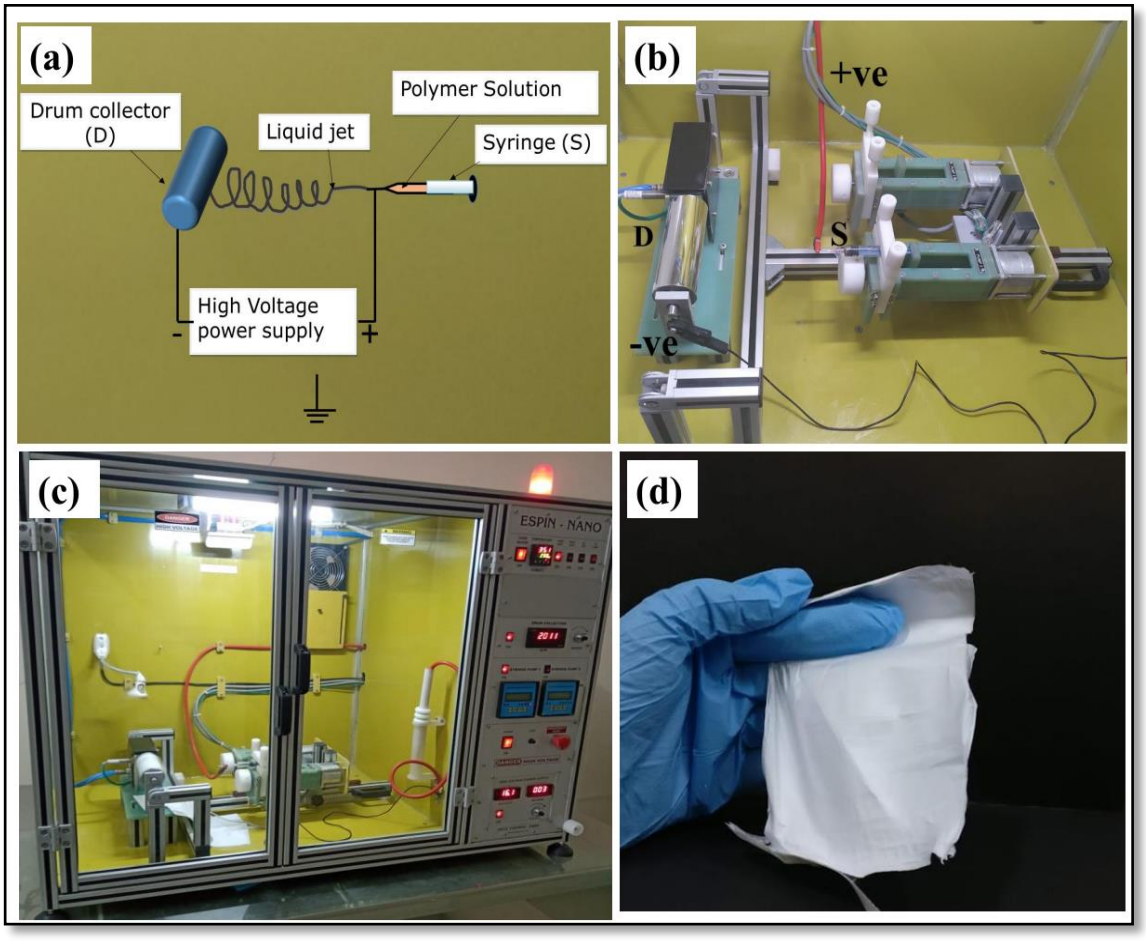

Figure 2.9 (a) Schematic of the electrospinning process (b) and (c) photographs of the ESPIN-NANO electrospinning technique (d) prepared flexible nanofiber mat.

2.5 Characterization techniques

There are various techniques that are available to characterize the NPs, i.e., direct evidence on the existence of NPs in the synthesized sample.[5] The fast and straightforward way to confirm the presence of NPs in a liquid medium is UV-Visible absorption spectroscopy. The size/shape analysis of NP is possible with the help of electron microscopes, i.e., FESEM and TEM. The basic principles of the techniques used for the characterization of the fabricated NPs in this thesis are briefly summarized in this section.

2.5.1 UV-Visible absorption

Optical absorption spectroscopy is the simplest and quickest method to verify the existence of NPs in the liquid medium and the concentration of an analyte in solution. It is not a single particle technique. It provides an average absorption of all the NPs dispersed in the liquid. UV-visible absorption spectroscopy is the measurement of absorbance of light at specific wavelengths being absorbed by the NPs in a sample. The UV-Visible absorption spectra recorded in this work were recorded with Perkin Elmer Lambda 750 UV-Visible absorption spectrometer using two quartz cuvettes of ~1 cm path length, and the solution quantity of 3 ml was used for the measurements.

Instrumentation:

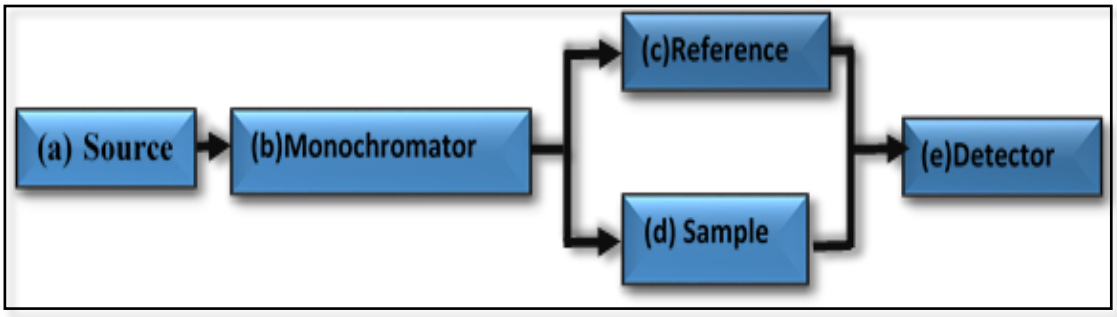

Figure 2.10 Basic construction of Spectrophotometer

(a) Tungsten-halogen and Deuterium lamps were used as the sources for the UV-Visible spectrometer. Tungsten-halogen lamp covers the visible to NIR region (375 to 3300 nm) and the deuterium lamp covers the UV region (165 -375 nm) (b) the monochromator produces a single wavelength from a wide range (of the light source), which is then dispersed with the assistance of rotating prisms and then selected by the slits. It provides a continuous increment in wavelength for easy data recording. Moreover, the beam, in turn, is split into two equal intensity beams. One of the two divided beams pass through

(d) the sample cell containing NPs colloidal solution and the other passes through (c) reference cell just containing only the solvent. Glass cuvettes are not useful due to absorption of UV light. Quartz or silica cuvettes are generally used for the data collection of the sample. Photomultipliers and an array of photodiodes are used as detectors (e). These convert the received light into current; higher the current greater the intensity was perceived. The intensity of light from the sample and reference was measured with respect to the wavelength.[6]

A beam with a varying wavelength from ultraviolet to near-infrared passes through a solution in a cuvette. The sample in the cuvette transmits the radiation depending on its absorption. The fraction of photons that pass through the sample over the incident number of photons called the transmittance of a sample (T). The amount of the light absorbed as the light passing through the sample is based on the Beer-Lambert's law which is given by $A = \log(T) = -\log\left(\frac{I_0}{I_T}\right)$, here I_T is the intensity of the transmitted light through the sample, and I_0 is the incident light intensity [7], as illustrated in figure 2.11.

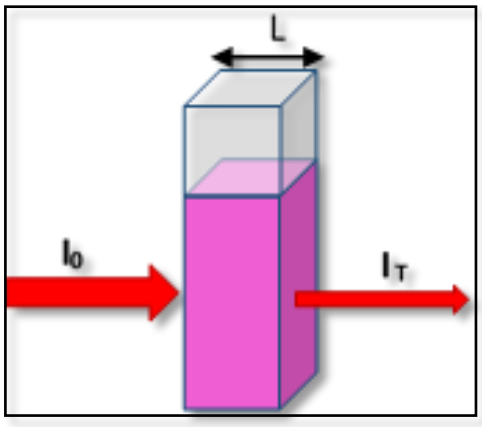

Figure 2.11 Schematic of Beer-Lambert Law

The Beer-Lambert law states that the Absorbance $(A) = \epsilon CL$, where ϵ the coefficient of molar extinction (unit: M^{-1} cm^{-1}), C is the concentration of the sample and L is the sample path length (cuvette thickness). The molar extinction coefficient is a material property, and it cannot be modified. The absorbance of the sample increases with increasing the concentration and length of the sample.[8] The incident light on the metal NPs, which is in resonance with coherent dipole oscillations of conduction electrons in metal nanostructures, produces a sharp resonance absorbance peak called localized surface

Plasmon resonance (LSPR) peak. For metals, this is in the visible range of light and is dependent on size, shape, and surrounding medium of the NPs.[9]

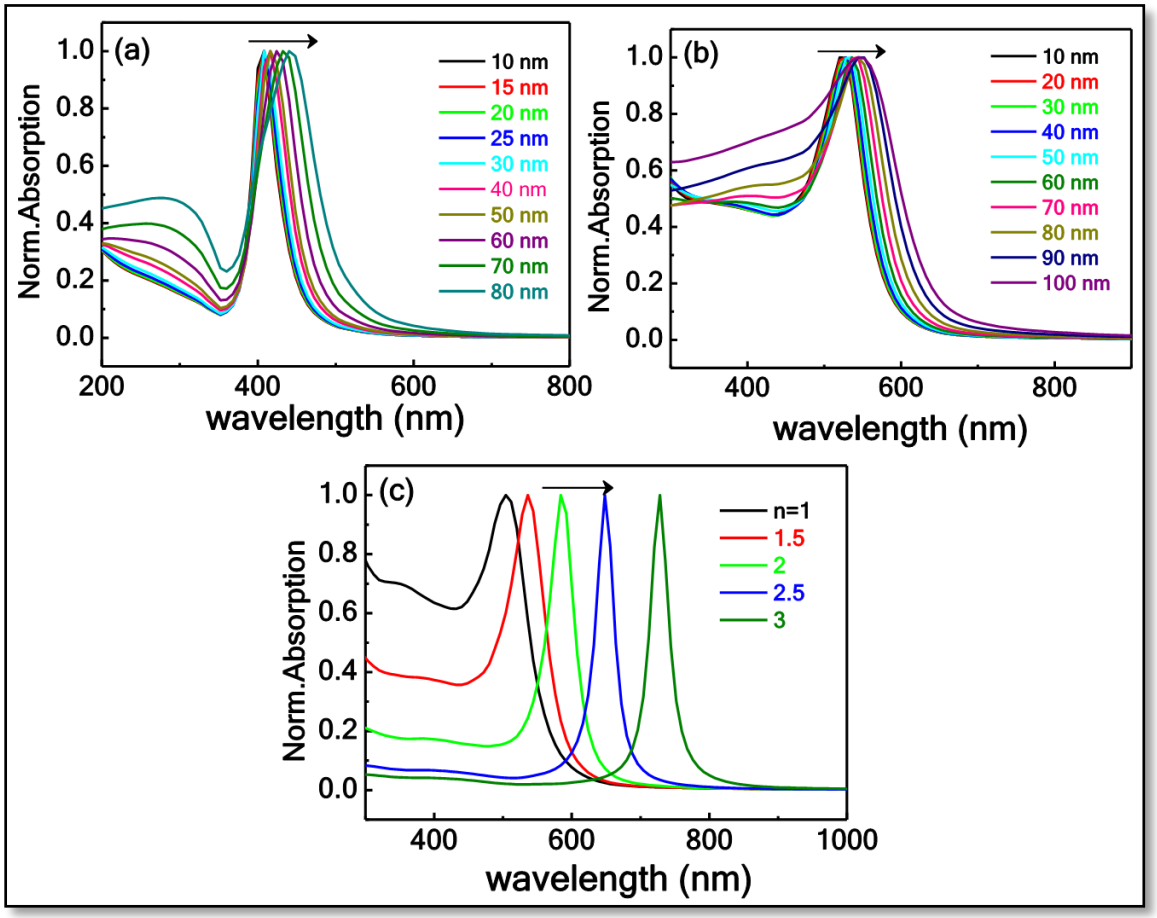

Figure 2.12 Absorption spectra of spherical (a) Ag NPs (b) Au NPs in water (n=1.33) as a function of size from 10 to 100 nm. (c) 10 nm Au NPs in different surrounding medium with refractive index from n=1 to 3.[10]

Figure 2.12 illustrates the variation of the LSPR peak wavelength with increasing size from 10 to 100 nm for spherical (a) Ag and (b) Au NPs in water having a refractive index of 1.33. With the increasing size of NPs, the spectra shift towards the longer wavelength depicting a trend of redshift. Link et al.[11] demonstrated the tuning of absorption peak (SPR) from 517-575 nm by varying the size of Au NPs from 9 to 99 nm. Figure 2.12 (c) illustrates the absorption spectra of 10 nm-sized Au NPs as a function of varying the refractive index of the surrounding medium as 1, 1.5, 2, 2.5, and 3. With increasing refractive index, a similar trend noticed, i.e., a redshift in comparison with size-dependent variation, the maximum shift identified with the in a change in the surrounding medium. The absorption studies of metal NPs gives the preliminary confirmation of the composition.

2.5.2 X-ray diffraction

XRD is a widely used technique for the identification of crystalline structures and atomic spacing. It works on the principle of constructive interference of diffracted X-rays from the crystalline planes, which follows Bragg's Law, $2d \times \sin\theta = n\lambda$, where 'n' diffraction order, 'λ' is the wavelength of incident monochromatic X-ray, 'd' is spacing between diffracting planes and 'θ' is the incident angle. When the X-rays are incident on a regular array of atoms, the secondary spherical waves are produced because of the interaction between X-rays and atoms, leading to the formation of diffraction patterns. By tuning the incident angle θ in a wide range, all possible diffraction direction of the lattice can be obtained. The conversion of diffraction values to d-spacing allows the identification of different crystal structures through the comparison with the standard reference patterns. The X-ray diffraction pattern is obtained by measuring the scattered X-rays intensity versus the angle. It is an abundant characterization technique for identification of the crystal structure, chemical analysis, particle size, lattice strains from doping, defects, or alloying, etc. of the specimen. Individual metal nanostructures give particular peaks depending upon their lattice constant or type of atoms. However, in alloy type nanostructures, the XRD peak shifts according to the content of each metal atom. In this thesis work, XRD measurements were performed on the samples with a BRUKER D8 X-ray diffractometer using Cu K_α 1.54 Å radiation with a resolution of 8×10^{-3} degrees. All the synthesized NPs solutions were prepared as thick-layer through deposition on a glass slide/Si by a simple drop-casting method. The XRD patterns were recorded after drying the sample. The obtained peaks from the sample analyzed by using Joint Committee on Powder Diffraction Standards (JCPDS) files.

2.5.3 Transmission Electron Microscope (TEM)

The TEM works on a similar principle as the optical microscope but uses electrons instead of photons (light). The attainable resolution for TEM images is many orders of magnitude better than that obtained from an optical microscope because the wavelength of electrons is much smaller than that of the photons. The stream of high energy electrons generated by electron source (usually a tungsten filament - thermionic emission) is focused on the sample using an electromagnetic lens (condenser aperture, objective aperture) within a high vacuum. The electron beam transmits into the sample, which carries information and

hits the fluorescent screen. The density variations in the sample areas give rise to a shadow image of the sample with its different parts displayed in color contrast. The resolution of the TEM image is at a few nm. Thus, it can reveal NPs to analyze their shape, size, distribution, etc. Moreover, it provides selected area electron diffraction (SAED) pattern, from X-ray and electron-energy analysis. The electron beam is diffracted by the atomic planes in the sample when the Bragg condition is satisfied. The concentric ring patterns were observed; each ring diameter describes the lattice planes spacing of the material.[12] In this thesis, TEM measurements were performed for the fabricated NPs with a Tecnai G2 S-Twin TEM instrument operated at 200 kV with a 2 nm resolution; a photograph is shown in figure 2.13. The TEM samples are prepared by the deposition of 5 µl NPs suspension on a copper grid coated with copper, allowing it to dry at ambient temperature. A freely accessible Image-J software was used for the analysis of the TEM micrographs. Typically, more than 250 particles were considered to calculate the mean diameter of obtained NPs. The mean size and the size distribution were estimated by the Gaussian curve fitting of the obtained data. HRTEM and SAED patterns were used to investigate the crystallographic planes and structure.

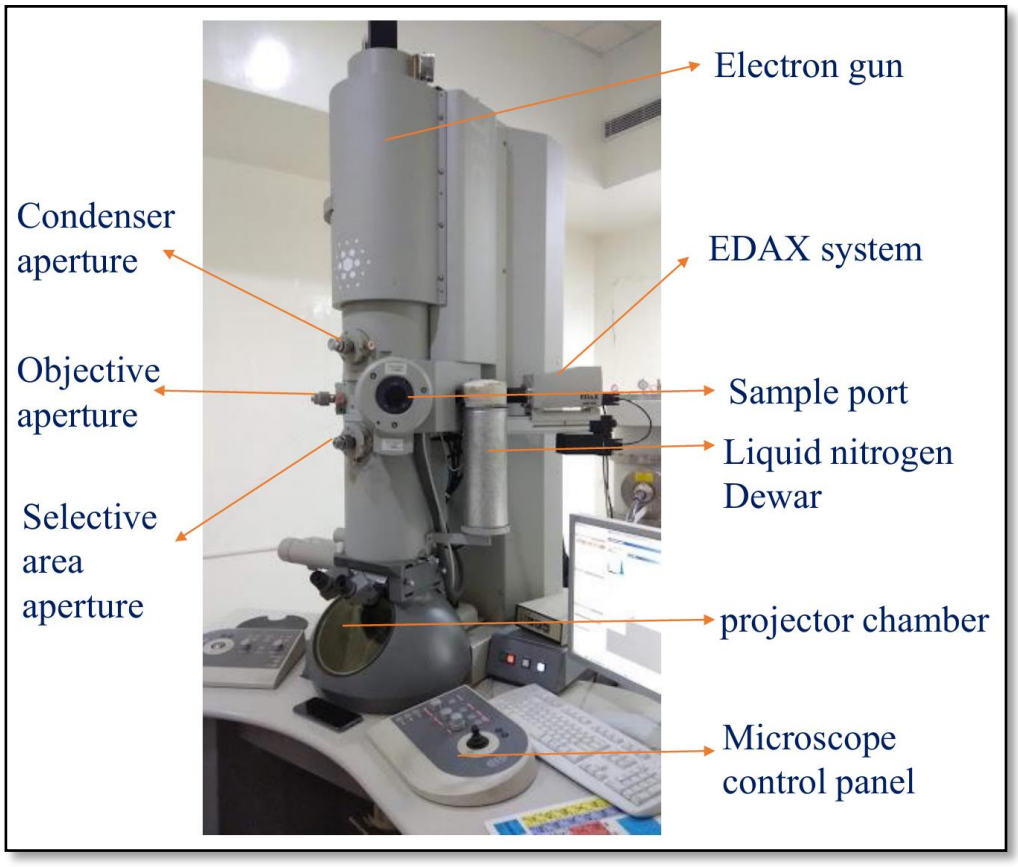

Figure 2.13 Photograph of the TEM available at Nanocenter, UoH.

2.5.4 Field Emission Scanning Electron Microscope (FESEM)

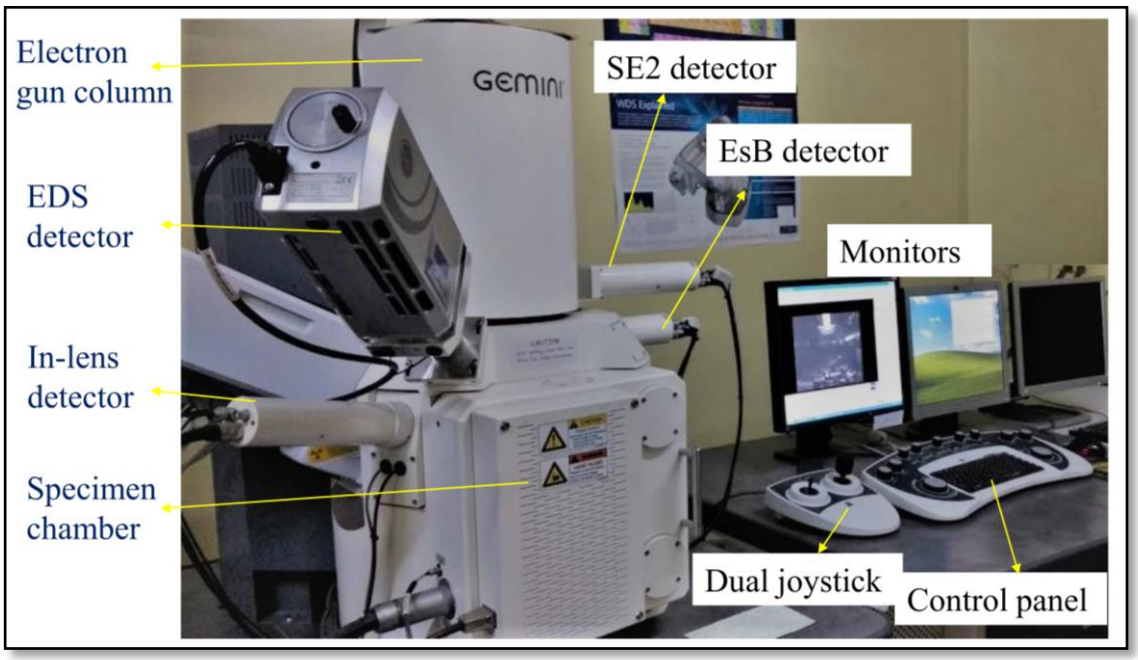

Figure 2.14 Photograph of the FESEM available at School of Physics, UoH

In FESEM, high energy electron ray was focused and scans the surface of the specimen and generates the image of the specimen. The field emission electron gun generates the electron beam, and the samples are placed in a sample chamber and are enclosed in a vacuum system to prevent the collision between the electrons and the gas molecules. The objective lens was used to focus the electron beam (electrostatic and electromagnetic lens) and interacts with the specimen. The secondary electrons are ejected from the valance/conduction band of the atoms in the specimen. The detectors catch all these and produce an electronic signal as a digital image. The in-lens detector, which is located inside the electron column, gives a high-resolution image at very low acceleration potential. A secondary electron detector (SE2) provides the low resolutions images at high acceleration potentials, and the backscattered electrons are the deviated primary electrons due to the interaction with the nuclei. A backscattered electron detector gives a higher atomic number contrast. Typically, heavier elements (bigger nuclei → deflect electrons strongly) appear brighter than the lighter elements. When a high-energy beam is incident on the sample surface, the innermost shell electron can be ejected and an electron-hole is created. Subsequently, an electron with a higher-energy from an outer shell fills the hole in the inner shell. The variance in energy between the higher-energy and lower-energy

leads to the release of an X-ray. The number and energy of the produced X-rays from the samples can be measured by the EDS detector. As each element has an individual atomic structure, a unique group of peaks can be observed on its electromagnetic emission spectra. In this work, Energy Dispersive Spectrometer (EDS) attached Ultra 55 from Carl ZEISS field emission scanning electron microscope (FESEM) operated with 30 kV is utilized, and the photograph is shown in figure 2.14. The FESEM data collected as,

- In the case of alloy NPs mapping, 20 µl of NPs were deposited on cleaned Si wafer.
- In the case of filter paper and electrospinning polymer nanofiber, because of the nonconductive nature of these materials, a thin conductive layer of gold was sputtered on the filter paper/polymer nanofiber to facilitate the lower magnification images.
- In the case of laser patterned portions on the silicon wafer, direct samples are used to collect the FESEM micrographs.

2.6 SERS measurements

The SERS measurements in this thesis are mainly focused on the detection of five dye molecules (MB, NB, CV, MG, and R6G), five explosive molecules (PA, DNT, NTO, RDX and AN), one pesticide molecule (Thiram) along with an inert physical stimulant for the chemical warfare agents (methyl salicylate). These molecules' chemical structures and their features are provided in the Appendix-A (table A1). The Raman spectra of these substances were acquired using portable Raman spectrometer as illustrated in figure A1 for explosives (powder form), A2 for dyes (powder form), A3 for thiram (powder form), A4 for methyl salicylate (pure liquid form) and A5 for stock solution (a higher concentration of ~0.1 M) spectra for all the molecules. The characteristic vibrational modes and their assigned Raman frequencies are illustrated in Appendix A from table A2 to table A14. The SERS substrates were fabricated by several pioneering techniques, including several deposition techniques for colloidal metal NPs on Si/glass/paper such as drop casting, spin coating, soaking and etc., every process has its own advantages and disadvantages. In this work, a simple drop-casting method is followed for the SERS substrate preparation, and the schematic shown in figure 2.15.

- In the case of a rigid SERS substrate, 20 µL of the synthesized NPs were drop-casted and dried on cleaned plane Silicon (chapter 3) /NS silicon (chapter 4). Later, 20 µL of the analyte molecules were dropped over the dried NPs.

- In the case of a flexible SERS substrate, the 1×1 cm FP was soaked in the already prepared NPs solution for 30 minutes. The soaked FP substrate was cut into four pieces (i.e., 2.5 mm^2) and allowed to dry. Subsequently, 10 µL volume of analyte solution was drop-casted on to the paper.

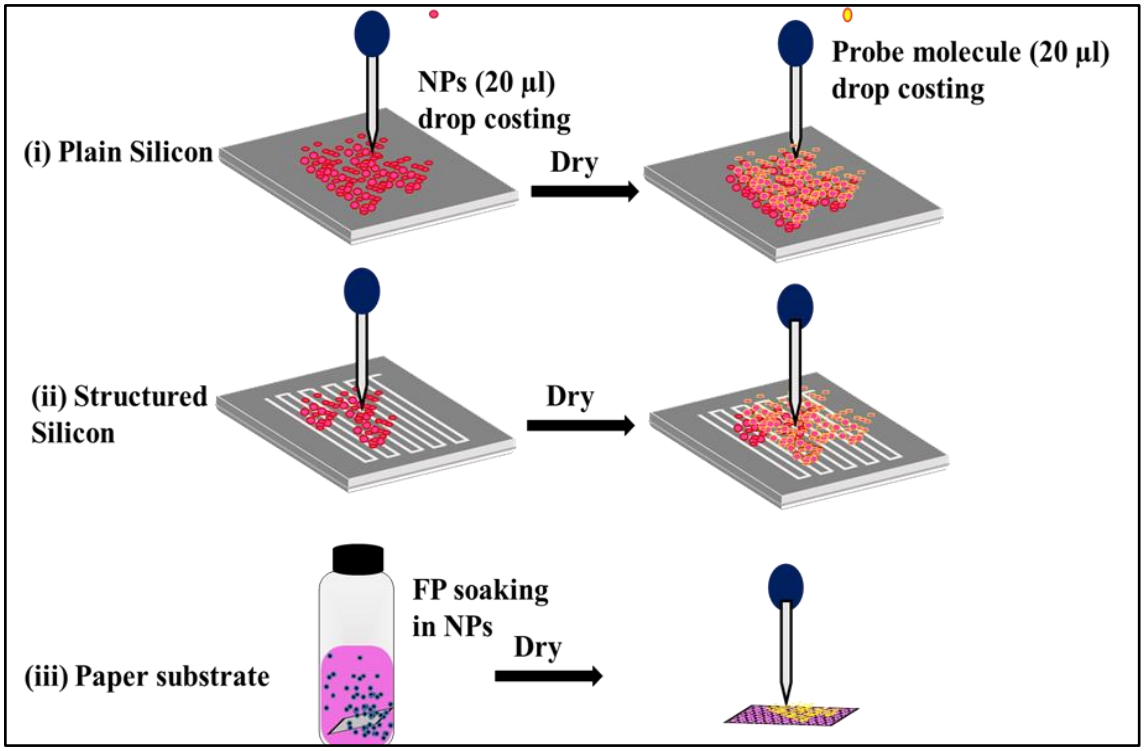

Figure 2.15 Schematic of SERS substrate preparation

2.6.1 Horiba µ-Raman spectrometer

The schematic of the main components of the Raman spectrometer is illustrated in figure 2.16. It includes (1) laser source that used to excite the sample to obtain unique vibrational Raman frequencies. It is necessary to use the laser having a stable frequency with a narrow bandwidth to avoid the errors in the Raman shift. Later, the laser beam is a guide through the spectrometer and the system with low power loss via (2) optics, mirrors, filters. (3) A microscope is used to find the desired location on the sample surface; a white light illumination source (reflection/transmission) is used for that purpose. Objectives are used to focus the light onto the sample and also to collect the scattered light from the sample. The scattered light from the specimen was collected in a backscattering configuration. (4) An X-Y stage is used to scan the sample. (5) Symmetric Czerny Turner spectrometer was equipped with a high sensitivity notch filter, which filters out the Rayleigh lines and

allowing the Raman scattered light, which is incident on the grating and disperses the light. (6) The CCD detector (Syncerity) used to collect the Raman light, and the spectral resolution depends on the CCD pixel size (26 µm × 26 µm).

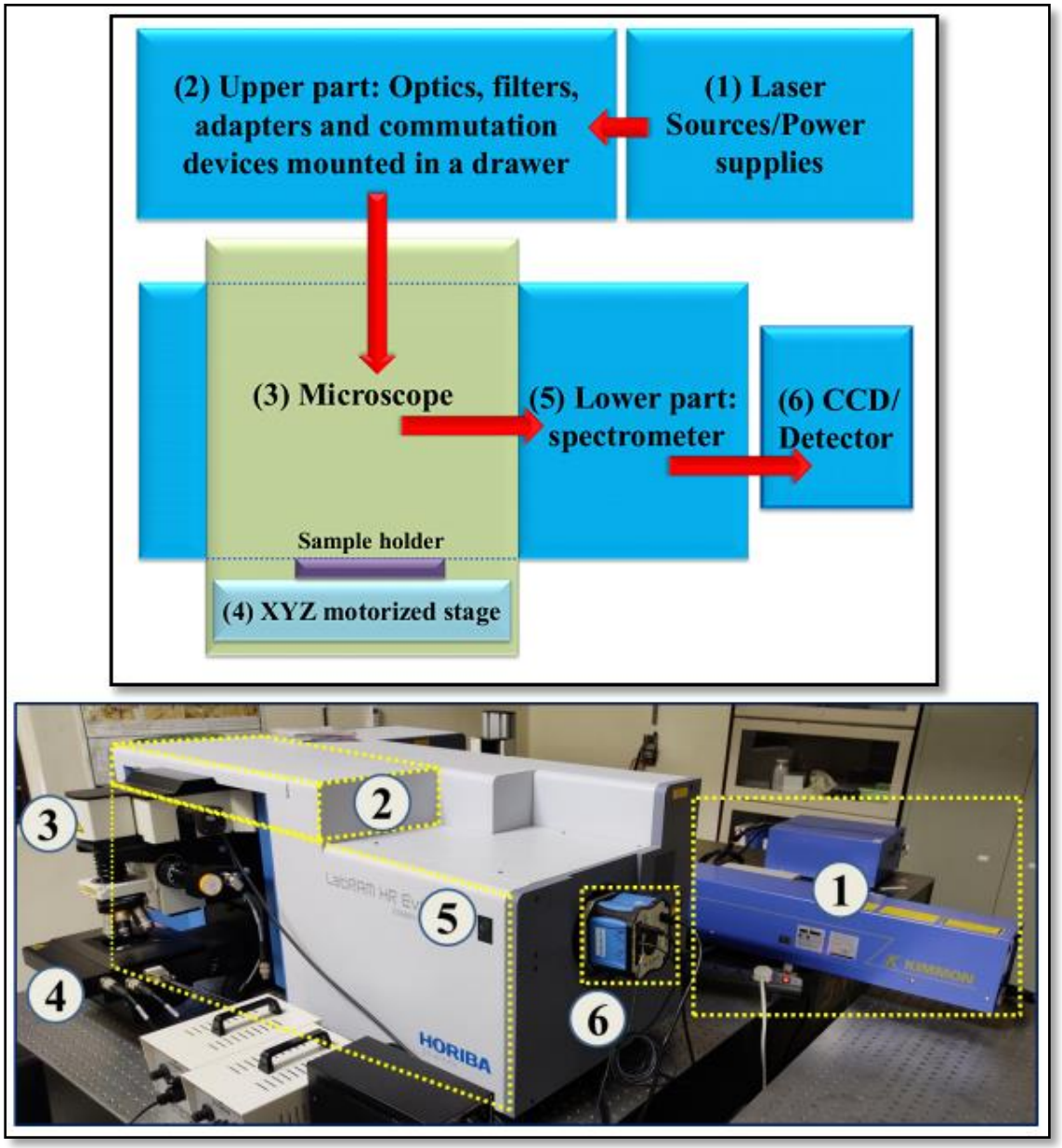

Figure 2.16 Schematic and Photograph of the Raman spectrometer (available at ACRHEM, UoH)

Lab Ram Horiba HR Evolution Jobin, Yvon Raman spectrometer, was used for some of the Raman studies in this work. The system is equipped with four different excitation sources at different wavelengths of 325 nm, 532 nm, 632 nm, and 785 nm. The laser beam was focused using 10X, 20X, 50X, and 100X objectives. The CCD array detector having 1024 × 256 pixels and is used to detect the signals from 1800 grooves per mm grating spectrometer. The resolution of the spectrometer is 0.35 cm^{-1}. Prior to the Raman

measurements, the spectrometer was calibrated with a Si wafer (~520 cm^{-1}). In this thesis, to study the effect of NSs in the SERS effect, a micro-Raman spectrometer was used, and the majority of the SERS measurements were performed with a portable Raman spectrometer.

2.6.2 Portable Raman spectrometer

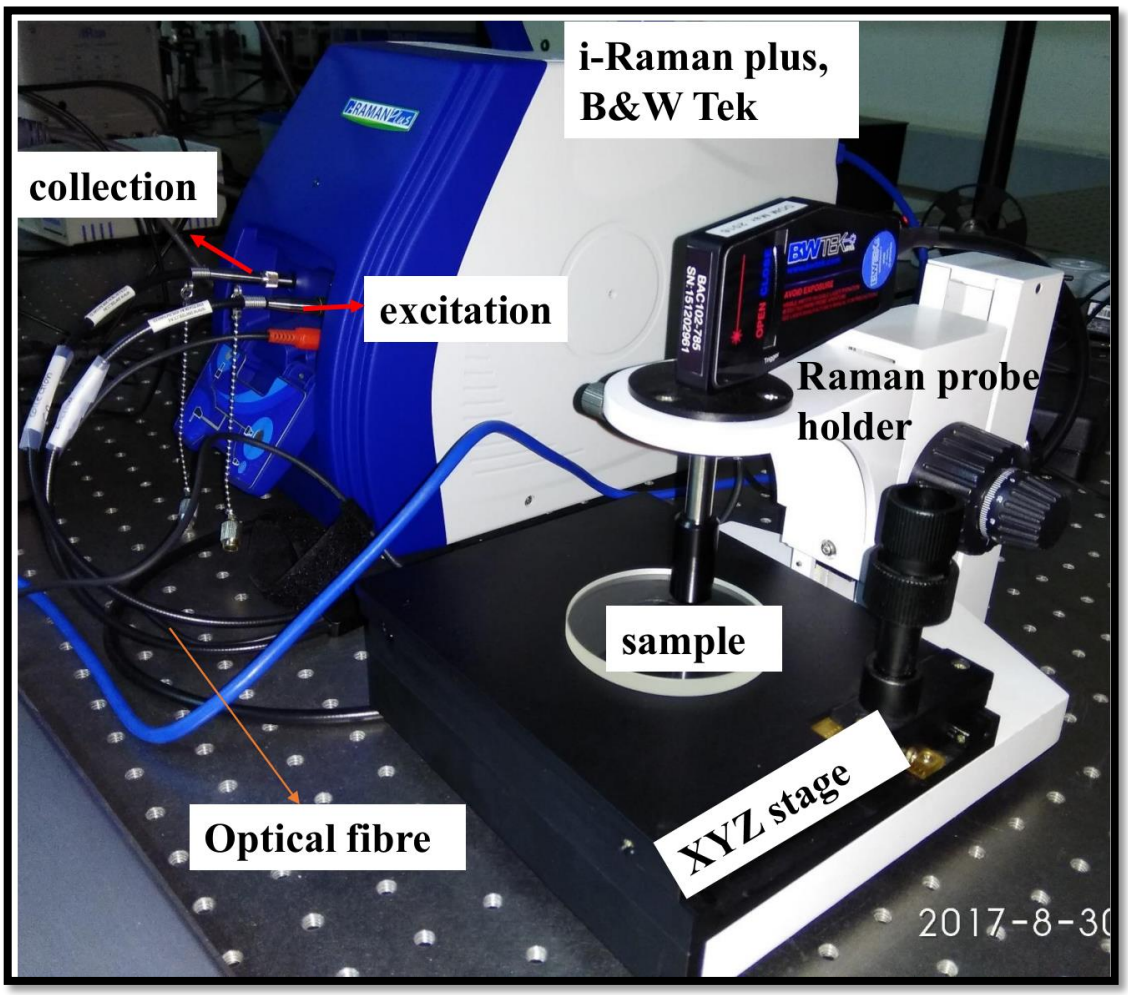

Figure 2.17 Photograph of portable Raman spectrometer (available at ACRHEM, UoH)

A portable Raman spectrometer (B&W Tek, i-Raman plus, USA, BWS465-785S) was used to obtain the Raman spectra of the samples, and the photograph is shown in figure 2.17. This spectrometer is provided with a diode laser that produces a wavelength of 785 nm with a maximum output power of ~300 mW. A Raman probe holder (BAC150) with manual adjustment XYZ stages are used to collect the data from the sample at various positions. To collect the Raman spectra from liquid samples, a 1 cm path length cuvette holder (BCR100A) was used. The resolution of the spectrometer was <4.5 cm^{-1}. A

Whatman Grade 1 filter paper composed of ~98% biodegradable, biocompatible, and recycled α-cellulose was used as a base for SERS substrate preparation. The large fibers were made of micro- and nano cellulose, which provides localization of the plasmonic NPs. The penetration of NPs into the paper depends on various factors such as porosity (pore size), thickness, and hydrophobicity. All the FP Raman and SERS studies were performed with a portable Raman spectrometer with ~25 mW laser power from an average of 3 spectra with 5 s as the integration time. The Raman spectra of FP and the probe molecule Raman spectra on FP without NPs are provided in appendix-A figure A6 and figure A7, respectively.

2.7 Enhancement factor calculations

The scale of the enhancement factor (EF) is defined as how much the Raman signal amplification is achieved from the SERS active platform with respect to the non-plasmonic substrate from the particular Raman mode of the molecule. The sensitivity of the SERS substrates is defined in various ways, such as a limit of detection (LOD), the limit of quantification (LOQ), and EF, amongst EF has received more acceptance.[13] It is one of the important factors to characterize the performance of the SERS active substrate, and it depends on the morphology of the substrate, molecular geometry of the analyte, and the excitation wavelength. EF also depends on the alignment of the probe molecule on the SERS substrate with respect to the local field, the orientation of the substrate with reference to the incident laser direction. This enables a direct comparison of the pros and cons of diverse SERS active substrates. For the measurement of EF, there does not exist a "standard" in the contemporary SERS literature. Le Ru et al.[14] have provided a comprehensive study on the estimation of EFs in SERS studies and classified as (i) Single-Molecule Enhancement Factor (SMEF) (ii) SERS Substrate Enhancement Factor (SSEF)[15] (iii) Analytical Enhancement Factor (AEF). Guicheteau et al.[16] introduced the SERS enhancement value, i.e., $\frac{C_R}{C_{SERS}}$, where C_R and C_{SERS} are the concentrations of the analyte molecules for recording normal Raman and SERS spectra, which producing the same Raman and SERS intensities. Pilot et al.[17] defined the EF as the ratio of cross-section of the molecule under SERS and under Raman (normal conditions); noticed the advantages of the EF measurement using macro Raman with line focus (4 mm × 80 μm) over the micro Raman (~μm). Le Ru et al.[14] defined in terms of number of molecules, i.e., EF = $\frac{I_{SERS}}{I_R}$ ×

$\frac{N_R}{N_{SERS}}$. The estimation of a number of a molecule is different for solid and liquid samples and is described in the review by Ren and co-workers.[13] Guicheteau et al.[18] modified the traditional SERS EF by incorporating the thermodynamical principles; this approach demonstrated the metal-analyte interactions play a role in the SERS phenomenon. Langmuir, Freundlich absorption model is also available to estimate the binding efficiency between the substrate and the analyte in SERS studies.[19]

According to Hamad et al.[27], EF = $\frac{I_{SERS}}{I_R} \times \frac{N_R}{N_{SERS}}$, N_R and N_{SERS} are number of molecules contributing Raman and SERS signal. $N_{SERS} = \eta\, N_A\, C_{SERS}\, V_a \frac{A_{laser}}{A_{NS}}$ and $N_{Raman} = N_A\, C_R\, V_a \frac{A_{laser}}{A_{substrate}}$. Where N_A is Avogadro's number. Laser parameters (effective area of the laser spot size), analyte volume V_a, utilized are kept equal in the collection of the SERS and Raman spectra. Therefore,

$$EF = \frac{I_{SERS}}{I_R} \times \frac{C_R}{C_{SERS}} \times \frac{1}{\eta}$$

The adsorption factor estimation was performed with the Langmuir isotherm model; in this context, lower η ($0 < \eta < 1$) value reflects that more favorable adsorption[28]. And also, from the linearised form of Freundlich adsorption isotherm, i.e., log C versus log I plot of the particular vibrational mode, the slope is a measure of adsorption intensity, here in our studies the obtained slope ranges between 0 and 1.

EF estimated using the simple relation $\mathbf{EF = \frac{I_{SERS}}{I_R} \times \frac{C_R}{C_{SERS}}}$, here we have assumed η=1. Therefore, the achieved EF values are generally under-estimated and it is followed by many researchers in SERS applications. [20-26]

Here I_{SERS} is the Raman signal intensity of the analyte molecules from the NPs on Si/FP, I_R is the Raman intensity of the analyte at a higher concentration from plain Si/FP (without any plasmonic NPs), C_{SERS} is the concentration of the analyte that adsorbed on the substrate of NPs (lowest concentration) which produces I_{SERS} , and C_R is the concentration (higher) of the analyte (0.1 M), which produces the Raman signal (I_R).

When we utilized different analytes to examine the SERS activity of the substrates, the EF may vary due to the analyte molecule's strengths of interaction with the surface of the SERS substrate. Here, the Raman and SERS signals were collected under the same

experimental conditions such as working distance of the objective, laser excitation wavelength, laser power, etc. and the volume of the analyte. In our present study, we adopted the method of "drop and dry protocol" to prepare the SERS active substrates. SERS active substrates were prepared by taking a 20 µL volume of colloidal solution of NPs was deposited with a micro-pipet onto a cleaned Si and was allowed to dry. Next to this, an analyte solution of 20 µL was drop cast with a micro- pipet onto the surface of Si substrate, which already comprises the film of NPs on its top. The schematic of substrate preparation to collect Raman (without NPs) and SERS (with NPs) is shown in figure 2.18.

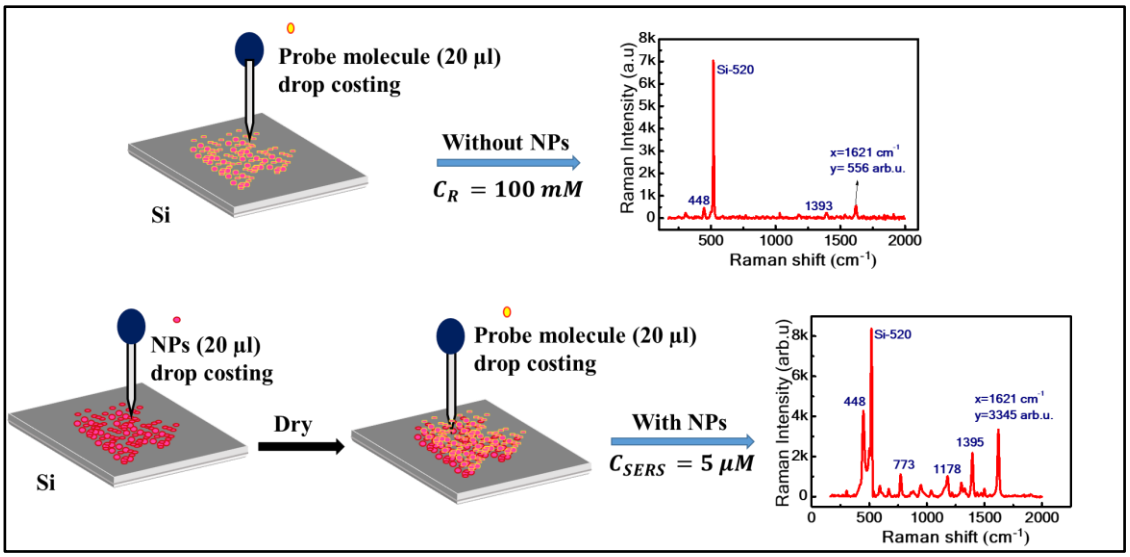

Figure 2.18 Schematic of sample preparation to collect the Raman and SERS spectra for enhancement factor calculations.

2.8 References

1. Chandu, B., Thesis-Femtosecond/Picosecond Laser Fabricated Diverse Nanocolloids/Nanostructures as SERS Substrates for Sensing Hazardous Materials **2020,** Ph.D. thesis, University of Hyderabad, India.
2. Nehra, K.; Pandian, S. K.; Bharati, M. S. S.; Soma, V. R., Enhanced Catalytic and SERS Performance of Shape/Size Controlled Anisotropic Gold Nanostructures. *New J. Chem.* **2019**, *43*, 3835-3847.
3. Teo, W. E.; Ramakrishna, S., A Review on Electrospinning Design and Nanofibre Assemblies. *Nanotechnology* **2006**, *17*, 89-106.
4. Subbiah, T.; Bhat, G.; Tock, R.; Parameswaran, S.; Ramkumar, S., Electrospinning of Nanofibers. *J. Appl. Polym. Sci.* **2005**, *96*, 557-569.
5. Barcikowski, S.; Amendola, V.; Marzun, G.; Rehbock, C.; Reichenberger, S.; Zhang, D.; Gökce, B., Handbook of Laser Synthesis of Colloids. *DuEPublico, Essen* **2016**.
6. Owen, A., Fundamentals of UV-Visible Spectroscopy, Hewlett Packard, **1996**.
7. Mäntele, W.; Deniz, E., UV–Vis Absorption Spectroscopy: Lambert-Beer Reloaded. Elsevier: **2017**.
8. Swinehart, D. F., The Beer-Lambert Law. *Journal of Chemical Education*, **1962**, *39*, 333.
9. Procházka, M.; Mojzeš, P.; Štěpánek, J.; Vlckova, B.; Turpin, P.-Y., Probing Applications of Laser-Ablated Ag Colloids in SERS Spectroscopy: Improvement of Ablation Procedure and SERS Spectral Testing. *Anal. Chem.* **1997**, *69*, 5103-5108.
10. https://nanocomposix.com/pages/mie-theory-calculator.
11. Link, S.; El-Sayed, M. A., Size and Temperature Dependence of the Plasmon Absorption of Colloidal Gold Nanoparticles. *J. Phys. Chem. B* **1999**, *103*, 4212-4217.
12. Carter, B. A.; Williams, D. B.; Williams, D. B.; Carter, C. B., *Transmission Electron Microscopy: A Textbook for Materials Science. Diffraction. Ii*; Springer Science & Business Media, **1996**; Vol. 1.
13. Ren, B.; Pérez-Jiménez, A. I.; Lyu, D.; Lu, Z.; Liu, G., Surface-Enhanced Raman Spectroscopy: Benefits, Trade-Offs and Future Developments. *Chemical Science* **2020**, *18*, 4563-4577.
14. Le Ru, E. C.; Blackie, E.; Meyer, M.; Etchegoin, P. G., Surface Enhanced Raman Scattering Enhancement Factors: A Comprehensive Study. *J. Phys. Chem. C* **2007**, *111*, 13794-13803.
15. Yang, L.; Yang, Y.; Ma, Y.; Li, S.; Wei, Y.; Huang, Z.; Long, N. V., Fabrication of Semiconductor ZnO Nanostructures for Versatile SERS Application. *Nanomaterials* **2017**, *7*, 398.
16. Guicheteau, J. A.; Farrell, M. E.; Christesen, S. D.; Fountain III, A. W.; Pellegrino, P. M.; Emmons, E. D.; Tripathi, A.; Wilcox, P.; Emge, D., Surface-Enhanced Raman Scattering (SERS) Evaluation Protocol for Nanometallic Surfaces. *Appl. Spectros.* **2013**, *67*, 396-403.
17. Pilot, R.; Bozio, R., Validation of SERS Enhancement Factor Measurements. *J. Raman Spectros.* **2018**, *49*, 462-471.
18. Guicheteau, J.; Tripathi, A.; Emmons, E. D.; Christesen, S.; Fountain, A. W., Reassessing SERS Enhancement Factors: Using Thermodynamics to Drive Substrate Design. *Faraday Discussions* **2017**, *205*, 547-560.

19. Xi, W.; Shrestha, B. K.; Haes, A. J., Promoting Intra-and Intermolecular Interactions in Surface-Enhanced Raman Scattering. *Anal. Chem.* **2018**, *90*, 128-143.
20. Rivas, L.; Sanchez-Cortes, S.; Garcia-Ramos, J.; Morcillo, G., Mixed Silver/Gold Colloids: A Study of Their Formation, Morphology, and Surface-Enhanced Raman Activity. *Langmuir* **2000**, *16*, 9722-9728.
21. Langer, J., et al., Present and Future of Surface-Enhanced Raman Scattering. *ACS nano*, **2019**, *1*, 28-117.
22. Korkmaz, A.; Kenton, M.; Aksin, G.; Kahraman, M.; Wachsmann-Hogiu, S., Inexpensive and Flexible SERS Substrates on Adhesive Tape Based on Biosilica Plasmonic Nanocomposites. *ACS Appl. Nano Mater.* **2018**, *1*, 5316-5326.
23. Byram, C.; Moram, S. S. B.; Soma, V. R., SERS Based Detection of Multiple Analytes from Dye/Explosive Mixtures Using Picosecond Laser Fabricated Gold Nanoparticles and Nanostructures. *Analyst* **2019**, *144*, 2327-2336.
24. Radziuk, D.; Moehwald, H., Highly Effective Hot Spots for SERS Signatures of Live Fibroblasts. *Nanoscale* **2014**, *6*, 6115-6126.
25. MacKenzie, M.; Chi, H.; Varma, M.; Pal, P.; Kar, A.; Paterson, L., Femtosecond Laser Fabrication of Silver Nanostructures on Glass for Surface Enhanced Raman Spectroscopy. *Sci. Rep.*, **2019**, *9*, 17058.
26. Parisi, J.; Su, L.; Lei, Y., In Situ Synthesis of Silver Nanoparticle Decorated Vertical Nanowalls in a Microfluidic Device for Ultrasensitive in-Channel SERS Sensing. *Lab on a Chip* **2013**, *13*, 1501-1508.
27. Hamad, S.; Podagatlapalli, G. K.; Mohiddon, M. A.; Soma, V. R., Cost Effective Nanostructured Copper Substrates Prepared with Ultrafast Laser Pulses for Explosives Detection Using Surface Enhanced Raman Scattering. *Appl. Phys. Lett.* **2014**, *104*, 263104.
28. Foo, K. Y.; Hameed, B. H., Insights into the Modeling of Adsorption Isotherm Systems. *Chem. Eng. J.* **2010**, *156*, 2-10.

Chapter 3

Colloidal substrate

Synthesis of alloy NPs (Ag-Cu, Ag-Au, and Cu-Au) by fs laser ablation and their SERS studies

Abstract

In this chapter, we present results from our efforts on the fabrication of various metal alloy nanoparticles (NPs), i.e., Ag-Cu, Ag-Au, and Cu-Au using femtosecond (fs) laser (~50 fs, 800 nm) ablation in liquid (LAL) technique. Ag–Cu alloy NPs were prepared in two steps. In the first step, pure Ag and Cu NPs were prepared separately using the LAL technique, followed by the laser irradiation of the equal volume mixture of Ag and Cu NPs. Ag-Au and Cu-Au alloy NPs were produced in a single-step process through the ablation of pure Ag and Cu targets (bulk) in the $HAuCl_4$ (5 mM) solution. These Ag, Cu, Ag–Cu, Ag-Au, and Cu-Au NPs were characterized by UV-Visible absorption, HRTEM, and XRD techniques. The formation of alloy NPs was confirmed by the existence of a single surface plasmon resonance (SPR) peak in absorption spectra and elemental mapping using FESEM techniques. Furthermore, all synthesized NPs were utilized in surface-enhanced Raman scattering (SERS) studies. The obtained results proved that Ag–Cu alloy NPs possessed a higher enhancement factor (EF) compared to pure Ag/Cu NPs. Further, Ag–Cu alloy NPs were used for the detection of explosive molecules such as 2, 4, 6-trinitrophenol (picric acid: PA –5 μM), ammonium nitrate (AN–5 μM). Similarly, the Ag-Au and Cu-Au alloy NPs SERS performance was verified by testing/detecting three analyte molecules [MB (5 nM), 2, 4-dinitrotoluene (DNT–1 μM) and PA (5 μM)]. All three alloys NPs demonstrated superiority in the detection of various analyte molecules with excellent sensitivity and high reproducibility and EFs in the range of 10^4-10^7. Among these alloys NPs, Ag-Au alloy NPs were observed to be superior SERS substrates.

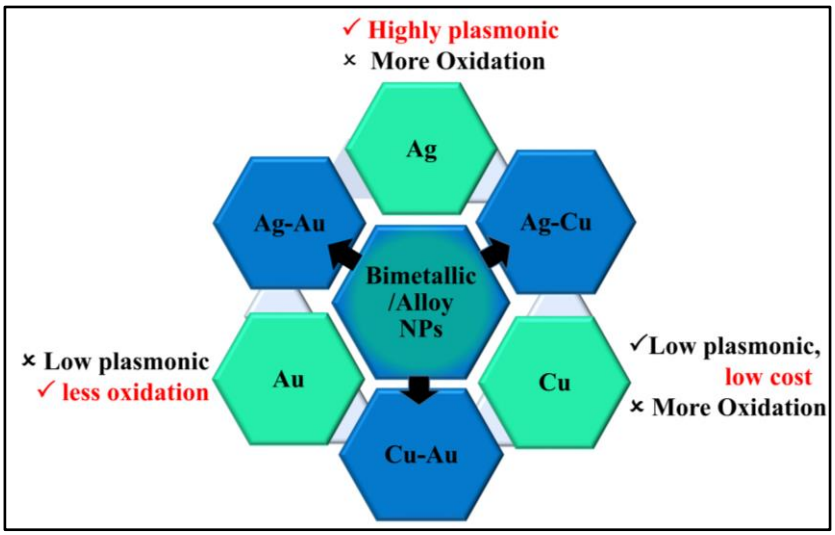

The work presented in this chapter has been published in the following journals

- **M.S.S. Bharati**, B. Chandu, S.V. Rao, Explosives sensing using Ag–Cu alloy nanoparticles synthesized by femtosecond laser ablation and irradiation, *RSC Adv.*, **9** (2019) 1517-1525.
- **M.S.S. Bharati**, B. Chandu, S.V. Rao, Femtosecond Laser Fabricated Ag@ Au and Cu@ Au Alloy Nanoparticles for Surface-Enhanced Raman Spectroscopy Based Trace Explosives Detection, *Front. Phys.*, **6** (2018) 28.

3.1 Introduction

Over the past few decades, techniques used for fabrication of plasmonic metal (Au, Ag, and Cu) and alloy nanoparticles (NPs) have garnered considerable attention in various applications, comprising information storage, optics, electronics, sensors, catalysis, drug delivery, and so on.[1-4] Plasmonic alloys of different metals provide tremendous opportunities for tuning plasmon properties based on the composition of constituents. There are two major types of bimetallic NPs, i.e. (i) core-shell [5-7]: one metal surrounds the other and (ii) alloy[8]: metals are mixed at the atomic scale, so both the atoms are present on the NPs surface. Alloy NPs were fabricated using various techniques such as chemical methods (seed growth method, citrate reduction method), electrodeposition, ion beam mixing, ball milling, laser ablation in liquids (LAL), and electrochemical methods[5, 9-17]. Among the conventional techniques, LAL has been proven as a potential method for producing novel material NPs/NSs at the same time without any reagents/reactants and also proved versatile in synthesizing alloy NPs of any material(s). LAL technique involves several complicated mechanisms in which intense laser pulses are focused on the sample (surrounded by a liquid) which results in plasma formation, shockwave generation, the formation and expansion of cavitation bubble and collapse followed by nucleation and growth of the NPs in the surrounding medium.[18-19] These processes take place in various time scales, starting from a few picoseconds to a few hundreds of microseconds depending on pulse duration and the ablated material properties. The properties of generated NPs through the LAL technique depend on various laser parameters (ex. pulse duration, wavelength, repetition rate, and laser fluence) along with the properties of the surrounding environment (amount and nature of the liquid).[19-21]

However, alloy NPs can be achieved in different ways with laser ablation process, i.e. (i) laser irradiation of colloidal mixtures prepared individually (ii) laser ablation of a metal target in the presence of other prior synthesized colloidal NPs (iii) laser ablation of bulk alloy target immersed in liquid (iv) irradiation of metal target in the presence of other metal precursor solutions ($HAuCl_4$/$AgNO_3$). Among the plasmonic metals, Ag displays the best plasmonic properties due to a low imaginary part of its dielectric function over a broad wavelength region. The alloying of metals Au and Cu with Ag significantly improves stability as well as their plasmonic nature. The plasmonic nature of Au and Cu is significantly enhanced by embedding Ag but the chemical stability of Ag hinders the

application over time. In this work, Ag-Cu, Ag-Au, and Cu-Au alloy NPs were synthesized using a single and two-step laser ablation process.

Several groups have reported the fabrication of bimetallic/alloy NPs. Ganjali et al.[22] demonstrated the synthesis of Au–Cu alloy NPs via laser irradiation of monometallic colloids mixture. Laser (1064 nm, 5 ns, and 10 Hz) ablation of Au and Cu was performed in acetone and irradiation of mixed monometallic Au and Cu colloids was performed with stirring. Podagatlapalli et al.[23] synthesized Ag-Au bimetallic NPs by ultrafast laser (~40 fs, 800 nm, 1 kHz) ablation of the Ag-Au target in acetone prepared from the mixture of Ag and Au bulk targets. Xu et al.[24] recently reported the synthesis of branched bimetallic Ag@Au NPs (~50 nm) by a laser-induced photochemical reaction in three steps (i) laser (532 nm, 6 ns, 10 Hz, 350 mJ) ablation of Au target in the $AgNO_3$ solution (ii) addition of $HAuCl_4$ and ascorbic acid (iii) continuous laser (532 nm) irradiation the solution leads the formation of Ag@Au multi-branched dendrites via a laser-induced photochemical reaction. Hajiesmaeilbaigi et al.[25] have demonstrated the formation of Au-Ag NPs under laser (1064 nm, 20 ns, 10 Hz) irradiation of a mixture of the different ratios of already prepared Ag and Au NPs in distilled water. Byram et al.[26] demonstrated the Ag–Au alloy NPs fabrication from the bulk alloy [prepared via mixing by melting the Au and Ag at different weight proportions] using femtosecond laser (50 fs, 800 nm, 1 kHz, 500 μJ) ablation in acetone. Chen et al.[27] described the Ag–Au alloy NPs fabrication through the unfocussed laser pulse (532 nm, 5 ns, 10 Hz, 7.5 mm) irradiation of Ag and Au NPs. Petrovic et al.[28] generated Cu–Ag NPs by the ablation of Cu target in Ag colloidal solution. Aazadfar et al.[29] have also prepared Au/Copper oxide nano-composites through irradiation of individually prepared copper oxide and Au colloidal mixture. Ag and Au NPs were prepared via chemical methods and were mixed in different volumes 1:2, 1:1 and 2:1 and laser-irradiated at different intervals such as 5, 10, and 25 minutes. The potential advantage of enhanced structural stability with reduced oxidation of Ag–Cu NPs (in comparison to pure Ag/Cu NPs) was studied theoretically by Shin et al.[30] using density functional theory (DFT).

Numerous researchers have utilized the fabricated bimetallic/alloy NPs as SERS substrates because these NPs combines the individual merits of each material. Xu et al.[31] prepared Ag-Cu alloy nanowires by the solid-state ionic method and used as a SERS substrate to detect R6G (10^{-14} mol/l). Xu et al.[24] synthesized Ag@Au bimetallic nanodendrite using

laser-induced photochemical synthesis and achieved an enhancement factor up to 10^{11} and limit of detection of ~10^{-14} M for 4-ATP molecule. Tung et al.[32] synthesized a 3D nickel (Ni) foam caging Ag-Au bimetallic NSs and enabled as SERS substrate for the identification of 0.1 nM -R6G. Jiao et al.[33] constructed the SERS substrates from pure worm-like Au-Ag nano chains for the detection of pesticide at 10^{-7} M concentration (0.03 ppm) on apple surfaces. Lee et al.[34] synthesized raspberry-like bimetallic Ag@Cu NPs and demonstrated for the detection of R6G molecule using three excitation wavelengths 488, 514 and 633 nm.

3.2 Experimental details: synthesis of alloy NPs

3.2.1 Synthesis of Ag, Cu, and Ag-Cu alloy NPs

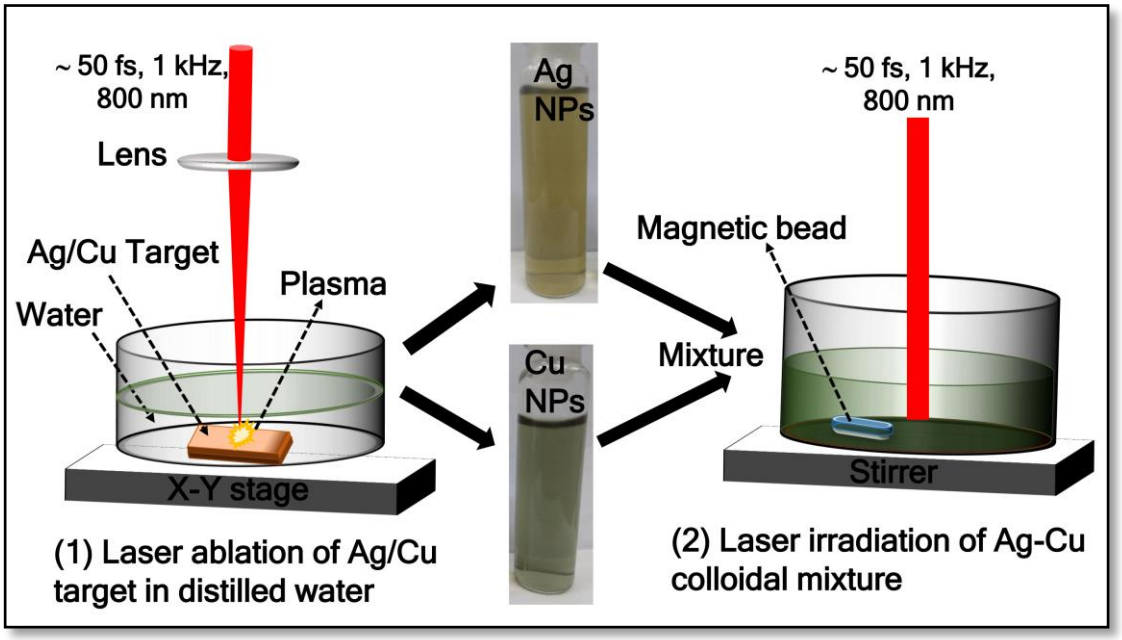

Figure 3.1 Schematic of the fabrication of Ag–Cu alloy NPs (1) laser ablation and (2) laser irradiation. Inset shows photographs of pure Ag and Cu NPs.

Ag–Cu alloy NPs were synthesized through a continuous two-step process, laser ablation followed by laser irradiation and the schematic of the synthesis process is shown in figure 3.1. Ag–Cu alloy NPs were produced by laser irradiation of mixed equal amount of Ag and Cu NPs (1:1 ratio) obtained separately through the LAL process. Ag and Cu NPs were created independently by laser ablation of Ag/Cu target immersed in distilled water (DW) using fs amplifier system (~ 50 fs, 800 nm, and 1 kHz). The laser pulses with an energy of 300 μJ were focused on the sample surface using a plano-convex lens (100 mm). Ag/Cu target (~1 mm thickness) was fixed at the bottom of the glass beaker and filled with 10 ml

of distilled water (DI). The liquid height above the target surface was ~11 mm. Ag/Cu target was translated (0.1 mm/s) using a computer-controlled translational stage to increase the NPs productivity/avoid repeated interaction of laser pulses at the same spot of the sample. The separately prepared Ag and Cu NPs were mixed in equal volumes (2.5 ml each) and then the mixture was irradiated with an unfocused beam (150 μJ pulse energy). The colloidal solution was continuously stirred with the help of magnetic stirrer (50 rpm) for a continuous movement of NPs (and also to avoid gravitational settling). To maintain a homogenous irradiation process and to interact with a large number of NPs, an unfocused laser beam with a laser having spot size (~10 mm) was used. The laser irradiation was carried for different times (i.e., 15, 30, 60, and 90 minutes), and the effect of irradiation time on the colloidal mixture was studied by recording the absorption spectra at each step [data is presented figure 3.4]. The laser irradiation which lasted for 90 minutes demonstrated a single SPR peak in absorption spectra.

3.2.2 Synthesis of Ag-Au and Cu-Au alloy NPs

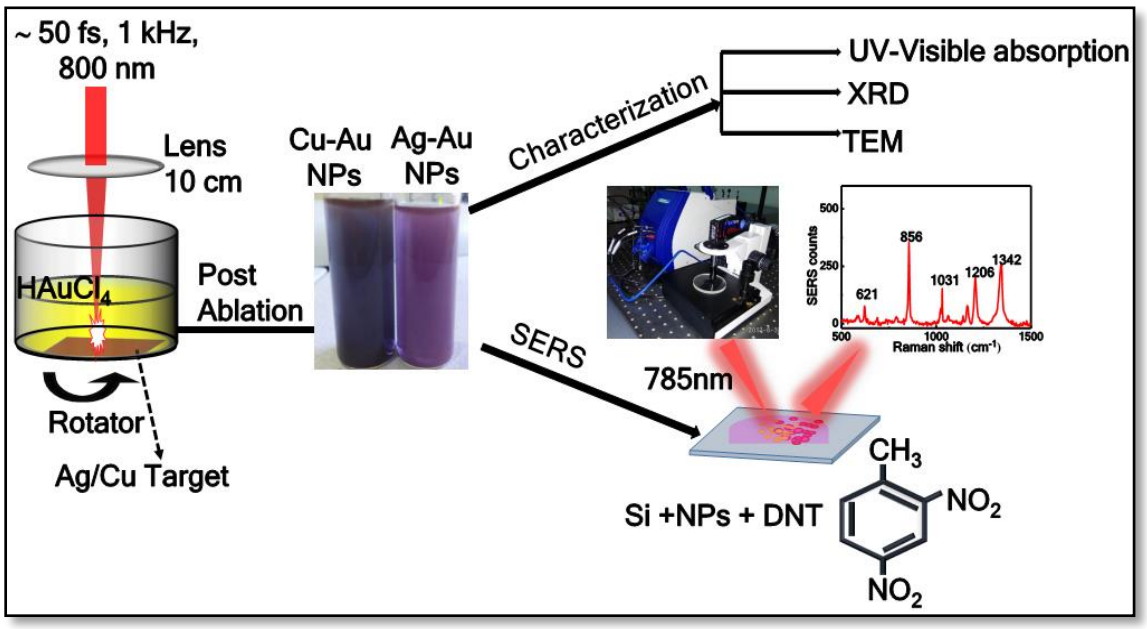

Figure 3.2 Schematic of Ag-Au and Cu-Au NPs synthesis and the SERS measurements using a portable Raman spectrometer.

Figure 3.2 represents the schematic illustration for the synthesis of Ag-Au and Cu-Au alloy NPs. Before the ablation, pure Ag and Cu substrates were thoroughly cleaned in acetone and water to remove the impurities which are present on the sample surfaces and then used for experiments. The Ag and Cu targets were ablated with an input pulse energy of ~300 μJ, which was delivered from the regenerative femtosecond (fs) amplifier [~50 fs, 800

nm, 1 kHz]. A plano-convex lens of 100-mm focal length used to focus the laser beam onto the sample. The sample (Ag/Cu) was placed at the bottom of the glass beaker and filled with a 10 ml $HAuCl_4$ (5 mM). Ag and Cu samples submerged in a beaker and place on a rotator to avoid the deposition of NPs onto the sample during laser irradiation. While performing ablation, the color of the solution changed into dark pink and brown color (shown in the inset of schematic 3.2) because of the replacement reaction between ablated Ag/Cu ions from the target (Ag/Cu) surface and the Au ions from the gold precursor ($HAuCl_4$) solution. Following the LAL, the colloidal solutions were centrifuged at 3500 rpm for 15 minutes. Later, the Ag-Au and Cu-Au NPs were washed with DI several times and dispersed in 5 ml ethanol using an ultrasonic bath for 5 minutes. A possible photo-induced decomposition of $HAuCl_4$ to Au by laser irradiation is briefly described by Zhao et al.[35] and are shown in equations (1) and (2). The gold precursor solution $HAuCl_4$ in H_2O can be reduced or decomposed into free atoms because of the intense filed (nhv) generated by plasma.[36-37]

$$HAuCl_4 + H_2O + nh\nu \rightarrow AuCl_4^- + H^+ + OH^- \rightarrow \quad (1)$$

$$AuCl_4^- + 3e^- \rightarrow Au^0 + 4Cl^- \rightarrow \quad (2)$$

The alloying process of Au ions from the precursor solution and Ag/Cu ions [$Ag + nh\nu \rightarrow Ag^* + e^-$] from the metal target will follow subsequently because of the coalescence and collision between those two atoms in the energetic surroundings in liquid during laser irradiation. [38]

$$Ag^0 \text{ or } Cu^0 + Au^0 \rightarrow AgAu^0 \text{ or } CuAu^0 \rightarrow \quad (3)$$

The possible mechanism for the growth of Ag-Au and Cu-Au NPs can be explained as follows. Briefly, the alloy NPs are controlled by laser-induced replacement reaction, rapid nucleation, and growth processes. The intense fs laser pulses interact with the gold salt solution ($HAuCl_4$), resulting in the formation of Au ions because of photo-reduction. When the laser pulse interacts with the (Ag/Cu) solid target it leads to the formation of plasma plume via different laser-matter interaction mechanisms. As time increases, plasma plume cools down and the energy is transmitted to the surrounding medium triggering the formation of the cavitation bubble. It contains both the ablated matter (Ag/Cu) and liquid-vapor (Au). It expands to a maximum radius (typically ~1 mm) and then collapses. The NPs are ejected into the surrounding liquid following the collapse of the cavitation bubble.

With the presence of high pressure/temperature for a short period, there is possible for a replacement reaction between ablated Ag/Cu and Au ions. The nucleation and growth rapidly occur and lead to the formation of bimetallic/alloy NPs. Because of the high-intensity of the laser pulse, the generation of bimetallic/alloy NPs is favored while suppressing the formation of metal segregation.[39]

3.3 Characterization of Ag-Cu, Ag-Au, and Cu-Au alloy NPs

3.3.1 UV-Visible absorption studies

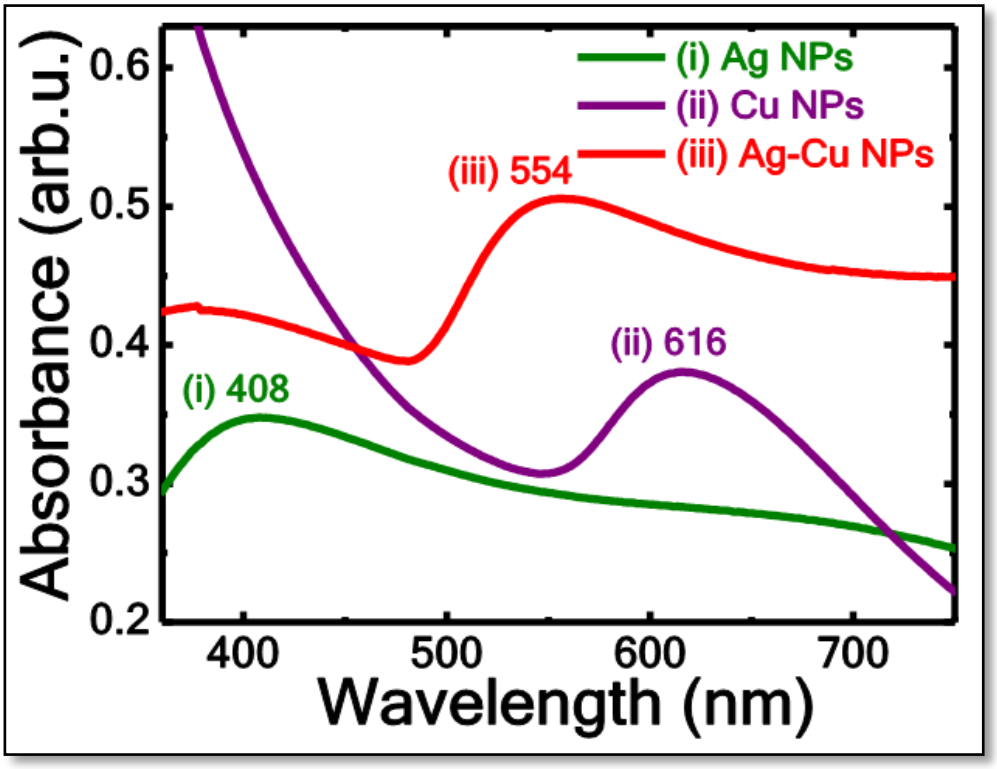

Figure 3.3 UV -visible absorption spectra of Ag, Cu, and Ag-Cu NPs with λ_{max} 408, 616, and 554 nm, respectively.

Figure 3.3 illustrates the UV-visible absorption spectra of fs laser-ablated Ag, Cu NPs and laser-irradiated Ag–Cu alloy NPs (after 90 min irradiation). The presence of the surface plasmon resonance (SPR) peak in the absorption spectra of the synthesized colloidal solutions is evident from the corresponding NPs data. The SPR peak of Ag and Cu NPs were located at 408 nm and 616 nm, respectively, indicating that the obtained NPs were almost spherical in shape. The SPR peak of laser irradiated colloidal solution of Ag and Cu NPs mixture for 90 minutes appeared at ~554 nm, which is in between the separate SPR peaks of pure Ag (408 nm) and pure Cu NPs (616 nm). Figure 3.4 illustrates the

intermediate stages of alloy NPs formation at different ablation times, i.e., 15, 30, and 60 minutes. Two separate SPR peaks were evident in the case of Ag and Cu NPs mixture (before laser irradiation), which indicates the absence of the formation of alloy NPs. The case was similar even after irradiating the colloidal mixture for 15 minutes. As the irradiation time increases, the SPR peak representing pure Ag NPs has undergone a redshift, i.e., from 408 to 413 nm (30 minutes) and 417 nm (60 minutes), and the absorption band intensity has increased gradually. This could be because of the possible fragmentation of bigger size NPs into smaller size NPs through the laser irradiation process, which may lead to an increase in the intensity of absorption peak.

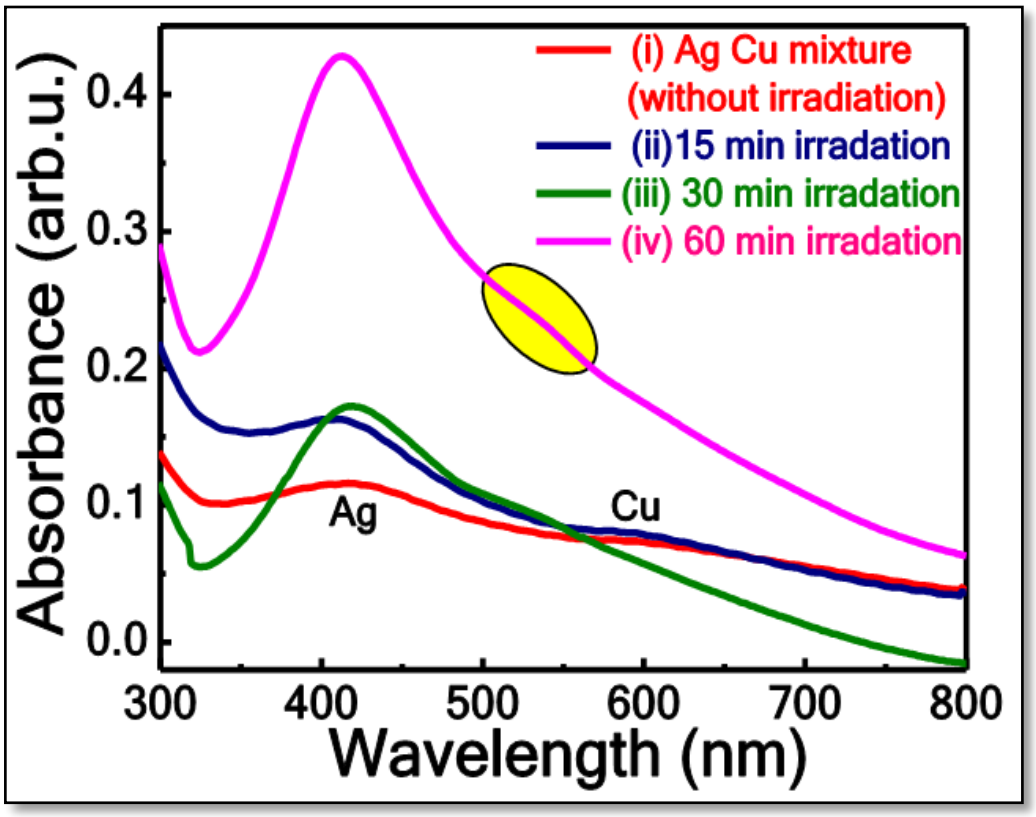

Figure 3.4 UV-visible absorption spectra of non-irradiated Ag and Cu NPs mixture and Ag-Cu NPs at different laser irradiation times 15, 30, and 60 minutes. Yellow highlighted portion illustrates a small hump in the spectrum

The diminution in the size of NPs is also evident from the analysis of TEM images [data presented in a later section, figure 3.7]. From the TEM images, pure Ag and Cu NPs size distribution were in the range of 5-100 nm, whereas in the case of irradiated Ag–Cu alloy NPs size distribution was in the range of 5-50 nm. A sudden drop in the intensity of Cu NPs SPR band was noticed when the irradiation time was changed from 30–90 min, which could be attributed to the broader absorption cross-section of Cu NPs compared with Ag

NPs at 800 nm. Earlier, Ghaforyan et al.[40] proved the melting temperature of metal NPs decreases with the size of the NPs (avg. size of Ag NPs > Cu NPs). However, additional investigations are warranted to understand the behavior of SPR peak intensity for the irradiated NPs. Observed small hump in the 500–600 nm spectral region was highlighted with yellow color (shown in figure 3.4). With an increase in the irradiation time, the two plasmon peaks disappeared and the presence of a single SPR peak confirming the spherical Ag–Cu alloy NPs formation rather than a mixture of two individual metal NPs.

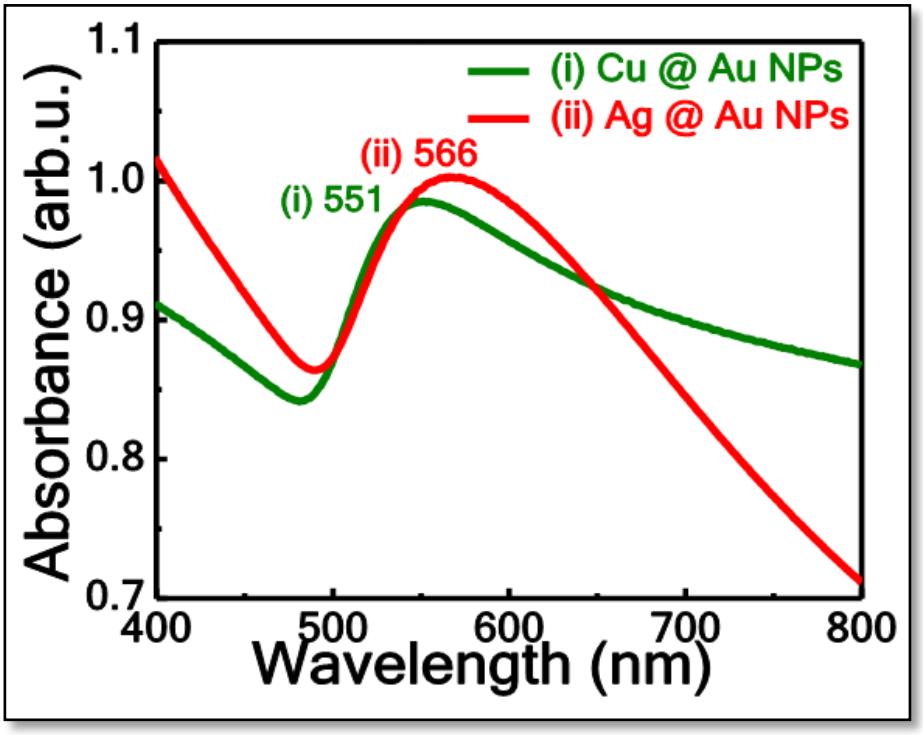

Figure 3.5 UV-Visible absorption spectra of Cu-Au NPs with SPR peak at 551 nm [curve (i) green color] and Ag-Au NPs with SPR peak at 566 nm [curve (ii) red color].

Figure 3.5 illustrates the normalized optical absorption spectra of the prepared NPs and the coloration of NPs shown in figure 3.2. The presence of a single SPR peak in the UV–visible absorption spectrum indicated the formation of bimetallic Ag-Au and Cu-Au NPs. The absence of these two plasmon peaks in the spectrum demonstrated that the prepared NPs were not just a mixture of individual metal NPs and, further, there was no core-shell formation.[41-42] The SPR peak of Ag-Au NPs was noticed at 566 nm, along with a broadening and redshift, which was not in-between SPR positions of pure Au NPs ~520 nm and pure Ag NPs ~400 nm. This could be attributed to a difference in shapes/sizes of NPs and concentration of the precursor solution.[13, 43] The SPR peak shift was mostly

dependent on the size, shape, refractive index of the surrounding liquid and composition of NPs.[44] The SPR peak of Cu-Au NPs was observed at 551 nm, which was in between region of the SPR peaks of Cu and Au NPs at ~620 nm and ~520 nm, respectively. There are many reports from various researchers discussing the multiple factors involved in the tuning of SPR peak in the alloy NP formation concerning the composition of the constituent materials. Based on the previous reports, bimetallic NPs SPR peak shifted to a longer wavelength side because of the (i) concentration of precursor, (ii) irradiation energy, (iii) time of exposure and (iv) material composition.

Xu et al.[24] fabricated the branched bimetallic Ag@Au nano-dendrites and observed a redshift in the SPR peak (~858nm) achieved using laser-induced photo-oxidation. Kuladeep et al.[45] have demonstrated a shift in absorption peak with metal alloy NPs which were prepared under direct laser irradiation of metal precursor solutions. Boyer et al.[46] synthesized Co–Au nanoclusters by laser irradiation of a mixed Co and Au colloids, and their characterization studies confirmed that each NP is composed of both atoms. Jiang et al.[47] synthesized Ag–Cu alloy NPs by the polyol process and observed the single SPR peak at 554 nm for a 1:1 volume ratio of pure Ag and Cu NPs. Messina et al.[48] also demonstrated the tuning of Au_x–Ni_{1-x} alloy NPs composition upon laser irradiation of colloidal mixture with different ratios. Valodkar et al.[49] synthesized Ag–Cu alloy NPs with a green approach and observed the redshift in plasmon band with an increase of Cu content in Ag–Cu alloy NPs from 416 to 584 nm. Compagnian et al.[50] synthesized Au/Ag colloidal nanoalloys by laser ablation and irradiation. They observed the increase of absorption band intensity with increasing irradiation time. Peng et al.[51] reported the synthesize of Au–Ag nanoalloys by laser irradiation of mixed colloids of pure Ag and Au. They found the variation in SPR band intensities while varying the irradiation times 5, 10, 15, 20, and 30 minutes. The observed differences were attributed to the lower melting point of Ag NPs than the Au NPs.

3.3.2 XRD studies

The XRD patterns of Ag, Cu, and Ag–Cu alloy NPs which were drop-casted on Si wafer and Ag-Au, Cu-Au alloy NPs which were drop-casted on glass are shown in figure 3.6. The analysis of XRD results indicates the presence of both Ag and Cu in Ag–Cu alloy NPs with the small shifts compared to pure NPs, the peak noticed at 28.6° corresponds to Si.

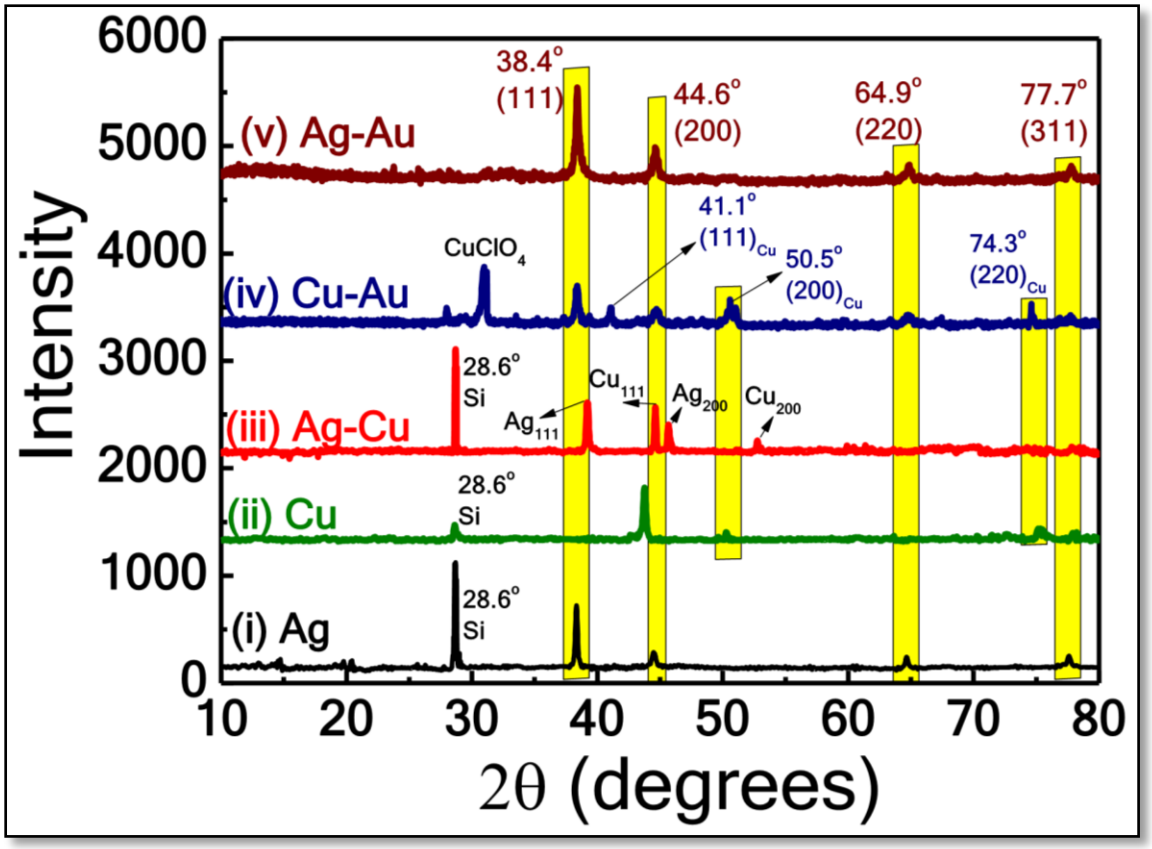

Figure 3.6 X-ray diffraction pattern of synthesized (i) Ag (ii) Cu (iii) Ag-Cu (iv) Au-Cu (v) Ag-Au NPs

The XRD patterns of Ag–Cu alloy NPs with the two peaks located at 39.2° and 45.6° were attributed to the planes of Ag (111), and (200) [JCPDS file number Ag-04-0783] and the other two peaks observed at 44.1° and 52.7° corresponds to the Cu planes (111) and (200) [JCPDS file number Cu-85-1326]. The XRD peaks of Ag-Au NPs are located at 38.4°, 44.6°, 64.8°, and 77.7° which are assigned to (111), (200), (220) and (311) planes (JCPDS file number Ag: 03-0921, Au: 04-0784). Because of the similarities in lattice constants of Au and Ag [Ag (0.40862 nm) and Au (0.40786 nm)], one cannot distinguish the phases of Ag-Au alloy/bimetallic NPs based on only XRD data. The XRD patterns of Cu-Au NPs with the identified peaks at 38.3°, 44.6°, 64.7°, and 77.7° are attributed to (111), (200), (220) and (311) crystal planes of Au [JCPDS file: 04-0784]. The other peaks located at 41.1°, 50.5°, and 74.3° were corresponding to the (111), (200), and (220) crystal planes of Cu (JCPDS file: 03-1005). The additional peaks of 27.90° and 31.10° in the Cu-Au NPs XRD pattern indicate the presence of $CuClO_4$ (JCPDS: 38-0594). The FESEM EDS mapping also revealed that the presence of chlorine in Cu-Au NPs. The obtained XRD

results are similar to those results reported by Malviya et al.[52], who recently analyzed the XRD pattern of Ag–Cu alloy NPs of four different compositions.

3.3.3 TEM studies

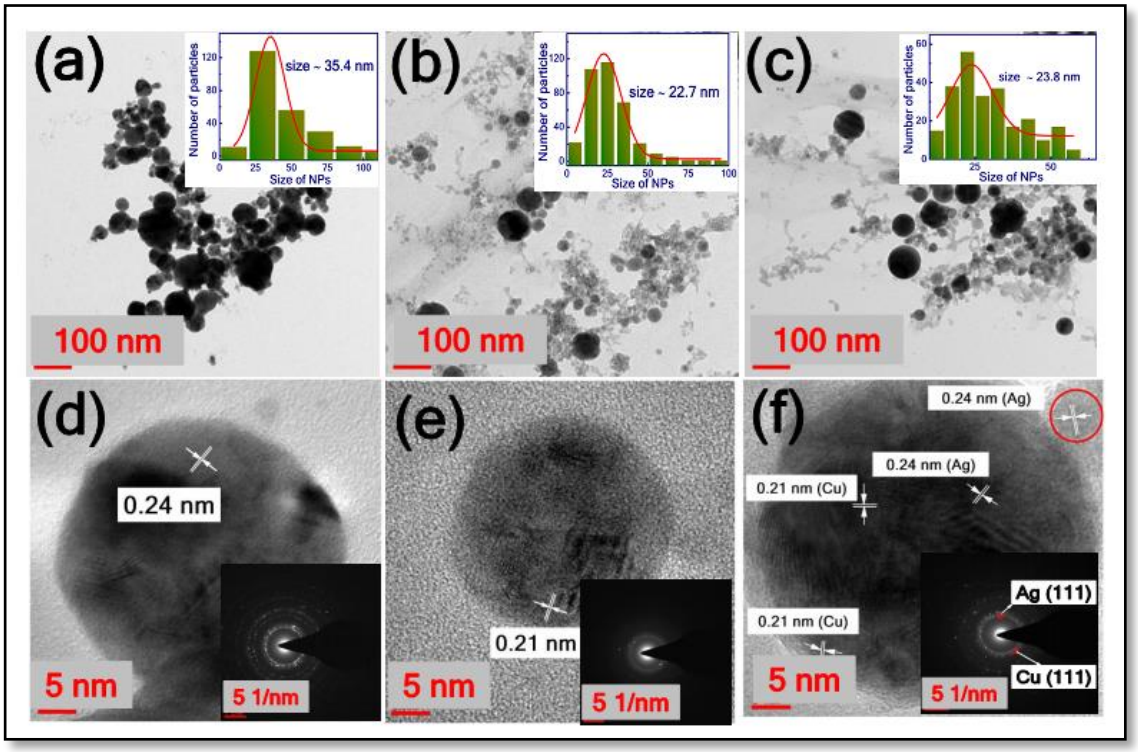

Figure 3.7 TEM and HRTEM images of (a) and (d) Ag NPs (b) and (e) Cu NPs (c) and (f) Ag–Cu NPs. Insets of (a)–(c) and (d)–(f) depict their size distribution and SAED patterns, respectively.

Figure 3.7 illustrates the TEM micrographs of synthesized Ag, Cu, and Ag–Cu alloy NPs. Figures 3.7 (a)–(c) depict the morphology, and their insets depict their corresponding size distribution histograms of pure Ag, Cu, and Ag–Cu NPs, respectively. There was no evidence of morphological changes for Ag–Cu NPs after laser irradiation. Most of the NPs are found to be spherical, with an average diameter of ~35.4 nm for Ag, ~22.7 nm for Cu, and ~23.8 nm for Ag–Cu NPs. Figures 3.7 (d)–(f) represent the HRTEM images while the insets illustrate their selected area electron diffraction (SAED) patterns (Ag, Cu, and Ag–Cu alloy NPs). Both elements have the same face-centered cubic structure[8, 53] differing only in the lattice parameters. The lattice spacing of 0.24 nm confirmed the d-spacing of the Ag $_{(111)}$ plane, and the lattice spacing of 0.21 nm confirmed Cu $_{(111)}$ plane. The presence of both inter-planar spacing in the HRTEM image of Ag–Cu alloy NPs [0.24 nm and 0.21 nm corresponding to both Ag and Cu, respectively] confirms the formation of alloy NPs.

Similarly, the SAED pattern illustrated in the inset of figure 3(f) shows the existence of Ag and Cu constituents in the Ag-Cu alloy NPs.

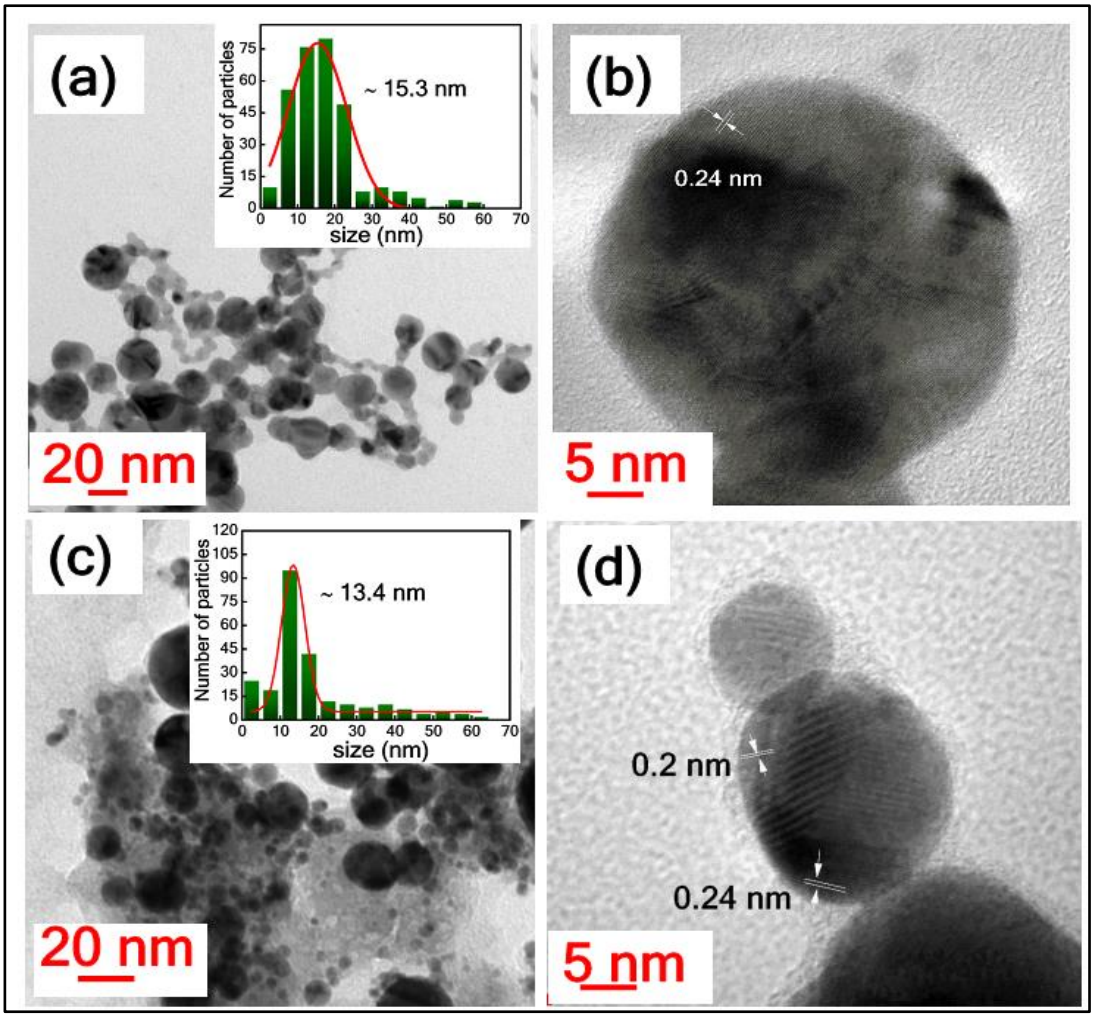

Figure 3.8 TEM and HRTEM images of (a) and (b) Ag-Au NPs (c) and (d) Cu-Au alloy NPs. Insets of (a), (c) depict their size distribution, respectively.

The morphology and crystallographic phases of Ag-Au and Cu-Au NPs was studied with TEM and HRTEM patterns. Figures 3.8 (a)-(d) illustrates the TEM & HRTEM images of Ag-Au and Cu-Au NPs, respectively. The low magnification (20 nm magnification bar) TEM images of NPs presented in figures 3.8(a) and 3.8(c) it is evident that some of the particles are interconnected with a chain-like structure. This could be attributed to the high-pressure and temperature laser-induced plasma near the target-liquid surface. [54] Insets of figure 3.8(a) and 3.8(c) show their corresponding size distribution plots with an average of ~15.3 nm and ~13.4 nm for Ag-Au and Cu-Au NPs, respectively. Figures 3.8(b) and 3.8(d) depict the inter-planar spacing in the HRTEM image of Ag–Au and Cu-Au alloy NPs, respectively [0.24 nm corresponding to Ag/Au and 0.2 nm corresponding to Cu].

3.3.4 FESEM-EDS mapping

Figures 3.9 (a)–(f) depict the FESEM elemental mapping, which further confirmed the alloy formation of Ag–Cu NPs (after 90 min of laser irradiation). The complete elemental distribution in Ag–Cu alloy NPs is depicted in figure 3.9(a). The distribution of Cu (red color) presented in figure 3.9(b) and the distribution of Ag (green color) are shown in figure 3.9(c). The line map of Cu and Ag elements on single-particle, as shown in figures 3.9(d) and 3.9(e), revealed the single NP composed of the Ag rich center. The energy dispersive X-ray spectrum (EDS) displayed the atomic wt % of Ag (55%) and Cu (45%) elements. However, few NPs were observed to be Cu-rich [as seen in Fig. 3.9 (a)] which could be attributed to variation in irradiation effects on different NPs.

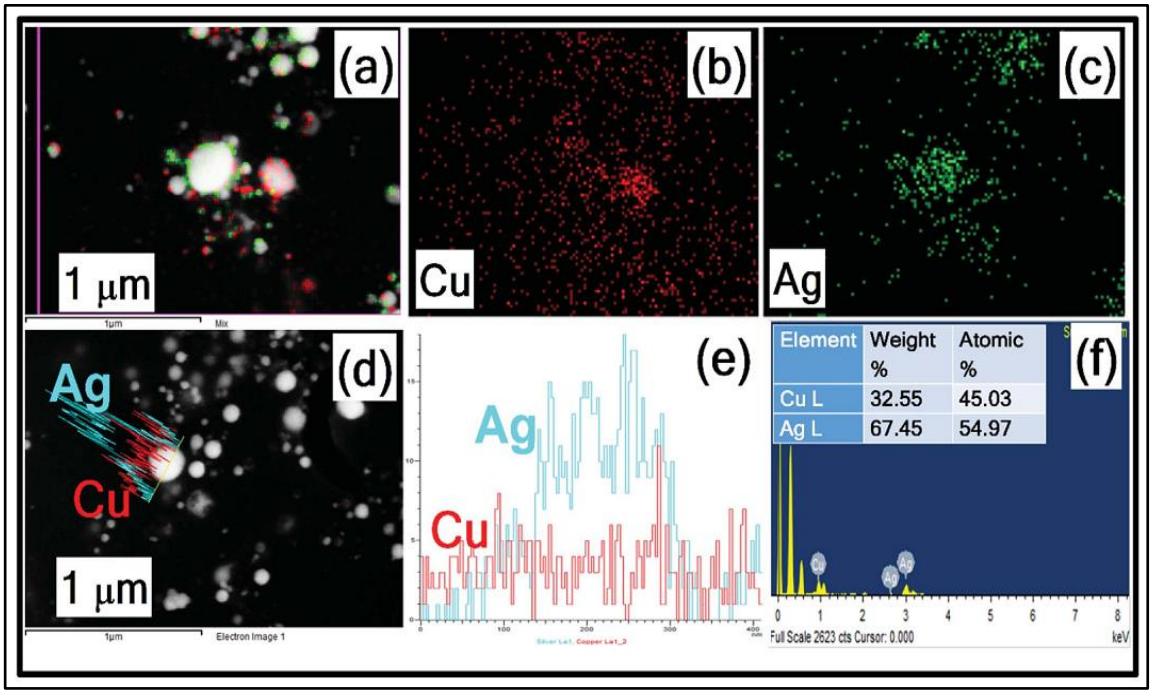

Figure 3.9 FESEM–EDS mapping of Ag–Cu alloy NPs (a) Ag-Cu EDS map (b) Cu EDS map (c) Ag EDS map (d) line profile of single alloy NPs (e) intensity distribution of Ag and Cu (f) EDS spectra with an inset depicting the weight % and atomic % of individual elements.

Generally, an unfocused laser beam is used to irradiate the mixture of the colloidal solution; it avoids the formation of different electron temperatures in the vicinity of different particles. With the unfocused laser irradiation, the temperature conditions at nano colloids are similar and homogeneous. Recently proposed photothermal evaporation model (heating–melting–evaporation) clarified the particle interaction with the laser at different phase transitions of material.[55] In the laser irradiation process, the absorption of laser pulse energy depends on various factors such as shape, size, and absorption cross-section of NPs and also the input laser fluence. The absorption of laser results in the

particle heating and, therefore, the temperature of the Ag/Cu NPs dispersed in the solvent will rise dramatically up to the melting point. Later, the heat loss perhaps leads to particle cooling and also particle solidification. The conceivable solidification could happen in the time scale of 10^{-5} to 10^{-6} s, which is much greater than the input pulse duration (fs). Through repeated multiple pulses interaction, laser energy absorption, and melting–solidification of the NPs might occur.[56] During each small period, diffusion of Ag/Cu NPs in the melt pool and the coalescence between the Ag and Cu atoms could happen, which leading to the formation of Ag–Cu alloy NPs. However, the morphological transitions of Ag–Cu alloy NPs as a function of Ag/Cu concentration need further detailed studies that can be achieved by varying the volume ratios of Ag and Cu NPs.

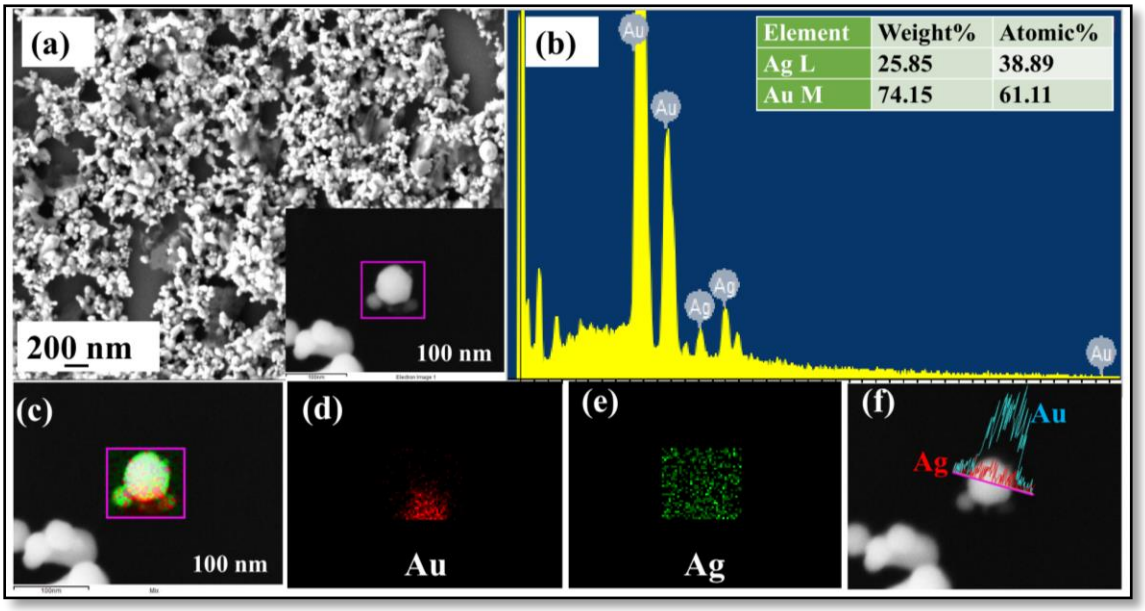

Figure 3.10 (a) FESEM image of Ag-Au NPs with the inset illustrating the single NP image in the 100 nm scale (b) EDS spectra with inset depicting the weight % of individual elements. (c) EDS mapping image of the Ag-Au NPs (d) Au EDS map (e) Ag EDS map (f) Line profile of the Ag-Au particle demonstrating the presence of both.

Figures 3.10 (a)–(f) illustrate the elemental mapping of obtained Ag-Au NPs with FESEM-EDS images. The EDS mapping of a single alloy NPs is depicted in figures 3.10 (c)–(e), which illustrate that the formation of Ag-Au alloy NPs, wherein Ag is shown with green color and is decorated on the surface of Au shown with red color. The line scan on a single NPs discloses that the NP is composed of Au rich center and covered with Ag, which are illustrated in figure 3.10(f). The atomic ratio of single Ag-Au NP determined from FESEM–EDS measurement is 38:61, and the data is shown in figure 3.10(b). The high weight percentage of Au may play a lead role in the stability of Ag-Au NPs.

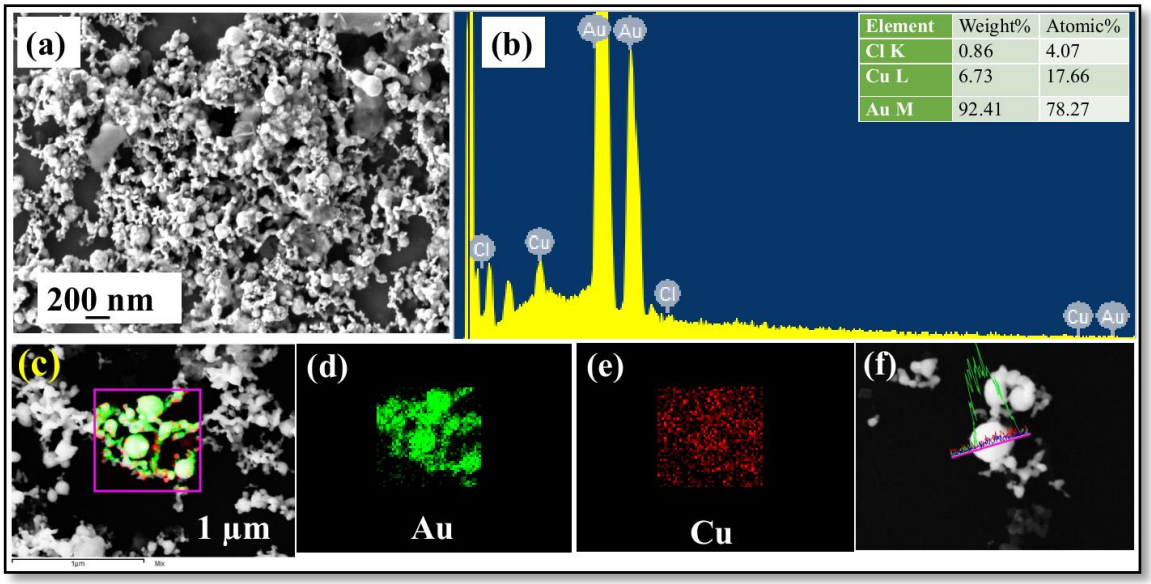

Figure 3.11 (a) FESEM image of Cu-Au NPs (b) EDS spectra with inset depicting the weight % of individual elements. (c) EDS mapping image of the Cu-Au NPs. (d) Au EDS map (e) Cu EDS map. (f) Line profile of the Cu-Au particle demonstrating the presence of both.

FESEM image and EDS mapping of Cu-Au NPs are depicted in figures 3.11(a)–(f), in which Cu and Au elemental mapping are shown in red and green colors [shown in figures 3.11 (c)–(e) and we also observed a small amount of chlorine (data shown in figure 3.11(b)]. This is due to the fs laser pulses interaction with gold salt solution ($HAuCl_4$), resulting in the creation of Au, Cl radicals in the precursor solution. The presence of chlorine in Cu-Au NPs could be ascribed to the fast exchange reaction between the copper and chlorine compared to noble metals (Ag, Au), where the latter is least reactive. This also supports the nonexistence of chlorine in Ag-Au NPs. EDS mapping revealed that the center is rich Au covered with Cu. The atomic weight percentage of Cu: Au is 17:78, and the data are shown in the inset of 3.11(b). Therefore, FESEM- EDS mapping confirmed the formation of Ag-Cu, Ag-Au and Cu-Au alloys nanoparticles.

3.4 SERS studies

3.4.1 Ag, Cu, and Ag-Cu NPs based SERS substrates

The SERS performance of Ag, Cu, and Ag–Cu NPs was studied with a dye molecule methylene blue (MB) as a probe molecule. The SERS spectra of MB having a concentration of 5×10^{-6} M recorded from Cu (blue), Ag (green) and Ag-Cu (red) NP deposited Si substrates, the obtained spectra were depicted in figure 3.12 (a). All the peaks matched well with the previous reports and the complete peak assignments of MB are

provided in Appendix A. The most prominent mode of MB (1621 cm^{-1}) was selected to calculate the efficiency of SERS substrates. The estimated EFs from Cu NPs, Ag NPs, and Ag–Cu alloy NPs substrates were ~7.5×10^2, ~5.5×10^3, and ~7.2×10^3, respectively, and their EFs histogram plot is depicted in figure 3.12(b). The procedure for calculation of enhancement factors was discussed in chapter 2 and the Raman spectrum of MB (0.1 M) is provided in Appendix-A.

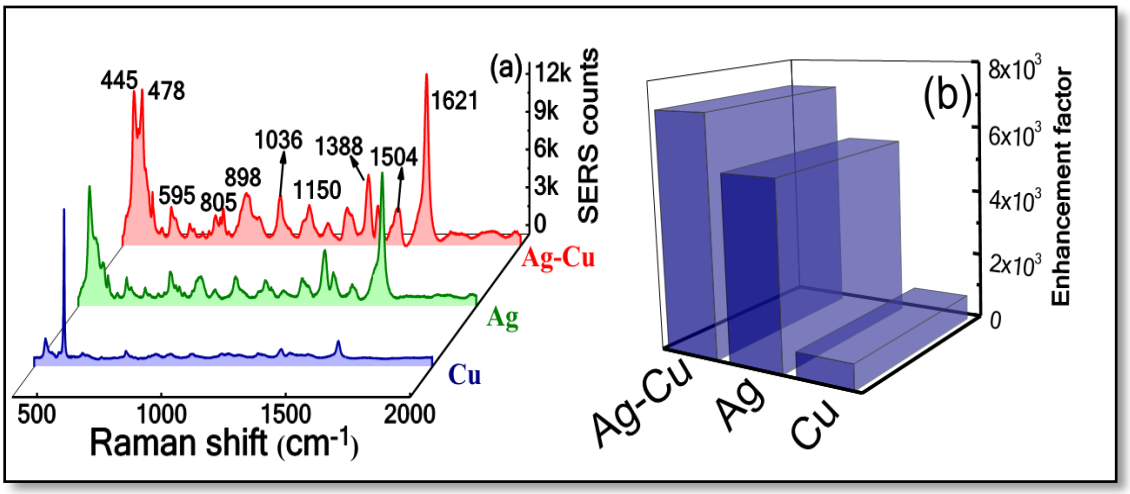

Figure 3.12 (a) SERS spectra of MB achieved using Ag, Cu, and Ag–Cu alloy NPs (b) Enhancement factor comparison histogram for MB (5 µM) by using Ag, Cu, and Ag-Cu alloy NPs substrates.

The lower SERS signals were observed in the case of Cu NPs, because of their inferior plasmonic efficiency compared to Ag. However, Ag–Cu alloy NPs exhibited 1.3 times higher EFs than the Ag NPs which could be because of the superior electromagnetic coupling and synergetic effect at the interface of Cu and Ag.[24, 57] Chang et al.[58] reported an improved SERS efficiency of Ag–Cu nanodendrites (~ 2.6 fold higher peak intensity compared to Ag nanodendrite for rhodamine 6G molecule). Numerous studies have demonstrated the SERS effect of Ag–Cu alloy NPs fabricated from various chemical approaches. Earlier, Li et al.[16] synthesized the Ag-Cu nanodendrite on graphene paper using the electrodeposition method. They observed the significant enhancement in SERS signals of 4-MBA molecule compared to pure Ag and Cu NP substrates because of the synergistic effect of Ag and Cu. Lee et al.[34] fabricated the raspberry-like Ag@Cu bimetal NPs using a stepwise reduction process and also studied the SERS performance of bimetallic NPs in the detection of R6G. The presence of Ag could efficiently prevent Cu NPs from oxidation and increase stability.[49, 59-60] The low cost of such Ag-Cu alloy NPs compared to Au due to the abundant availability of Ag and Cu is also an added advantage.

However, Ag–Cu alloy NPs have rarely utilized in SERS based explosive detection/sensing.

3.4.1.1 Dye molecule (MB) detection

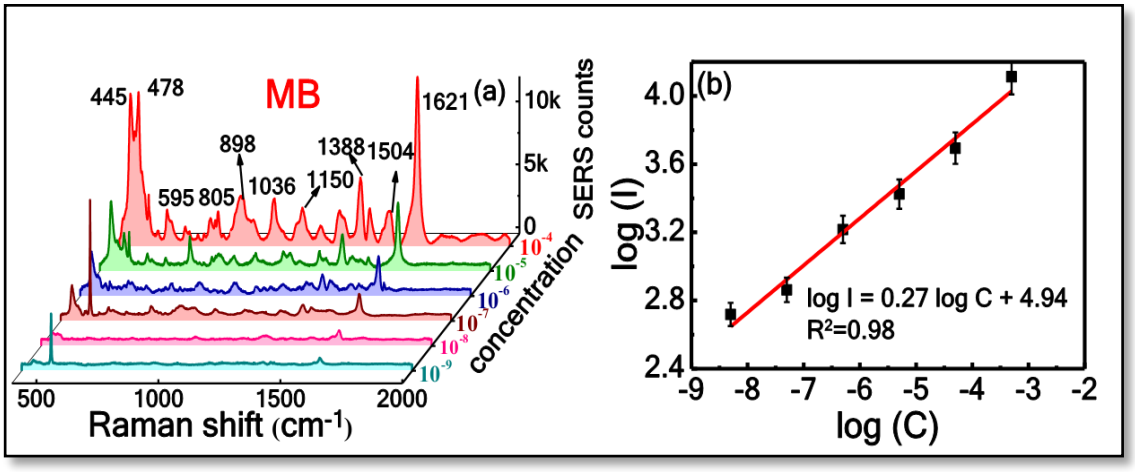

Figure 3.13 Concentration-dependent SERS spectra of (a) MB with concentrations ranging from 5×10^{-4} to 5×10^{-9} M using Ag-Cu alloy NPs and SERS intensity at (b) 1621 cm^{-1} peak intensity versus MB concentration [black squares represent the experimental data while the red lines represent theoretical fit]

The sensitivity of Ag–Cu NPs was studied by collecting the MB SERS spectra with varying concentrations ranging from 0.5 mM to 5 nM, and the data is shown in figure 3.13(a). The prominent peaks of MB clearly noticed at 5 nM, and the obtained EF for MB (5 nM) was ~3×10^{7}. A good correlation observed between the 1621 cm^{-1} peak intensity and the MB concentrations (5×10^{-4} to 5×10^{-9} M). Figure 3.13(b) shows the plot where Y-axis corresponds to the 1621 cm^{-1} peak intensity (in log scale), and X-axis corresponds to the MB concentration (in log scale). The data was fitted with linear (y=mx+c) fit as logI = 0.27 logC+4.94 with R^2 value ~0.98.

3.4.1.2 Explosive molecules (PA, AN) detection

To further investigate the SERS capability of Ag–Cu alloy NPs in the detection of explosive molecules, Picric acid (PA) and Ammonium nitrate (AN) were considered as probe molecules. The SERS spectra of PA were recorded for different concentrations ranging from 5×10^{-3} M to 5×10^{-6} M, and the data is presented in figure 3.14(a). All the observed Raman peaks and their peak assignments were mentioned in Appendix A. The three major characteristic modes were recognized even at a concentration of 5×10^{-6} M. The estimated EF (PA- 827 cm^{-1}) was found to be ~2.8×10^{4}. Figure 3.14(b) represents the

linear logI - logC plot for PA for the prominent peak of 827 cm^{-1} which exhibited a linear relationship [logI = 0.29 logC + 4.1] with an R^2 value of 0.91. Similarly, the SERS spectra of AN were obtained for different concentrations ranging from 5×10^{-3} to 5×10^{-6} M and, the data is shown in figure 3.14(c). All the observed Raman peaks are well-matched with reported data from literature.[61-62] The peaks assignments are summarized in Appendix A. The estimated EF for the main characteristic peak of AN (1047 cm^{-1}) at 5×10^{-6} M was ~3.3 $\times10^4$. Figure 3.14 (d) presents the logI-logC plot, which revealed a clear linear relationship [logI = 0.34 logC + 4.3] with a R^2 value of 0.9.

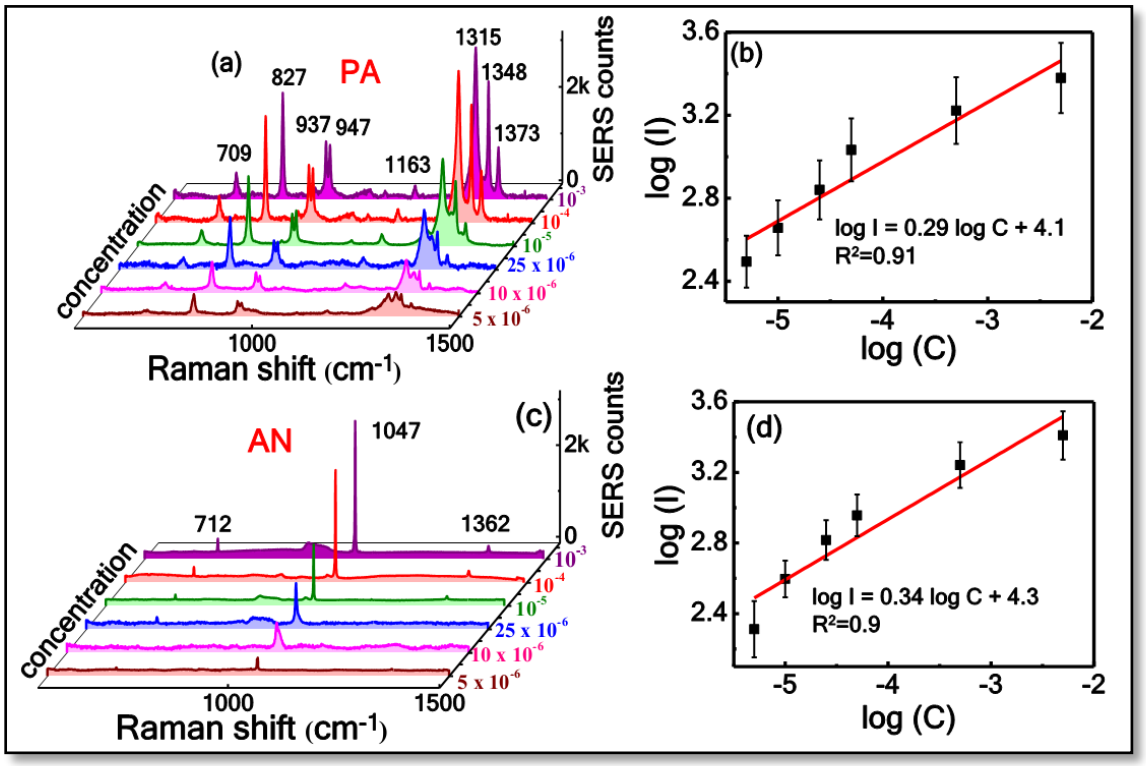

Figure 3.14 Concentration-dependent SERS spectra of (a) PA ranging from 5×10^{-3} to 5×10^{-6} M (c) AN ranging from 5×10^{-3} to 5×10^{-6} M and SERS intensity at (b) 827 cm^{-1} peak intensity versus PA concentration (d) 1047 cm^{-1} peak intensity versus AN concentration using Ag-Cu alloy NPs [black squares represent the experimental data while the red lines represent theoretical fits]

3.4.2 Ag-Au and Cu-Au NPs based SERS substrates

Figure 3.15(a) shows the SERS spectra of MB (5×10^{-9} M) with observed modes at 449, 776, 947, 1175, 1396, and 1621 cm^{-1} are in good agreement with the earlier works [63]. A break in spectra considered to exclude the intense peak of silicon at 520 cm^{-1}, shown in figure 3.15, and also a broad flat-edged peak between 900 and 1000 cm^{-1} representing the 2nd order silicon Raman band.

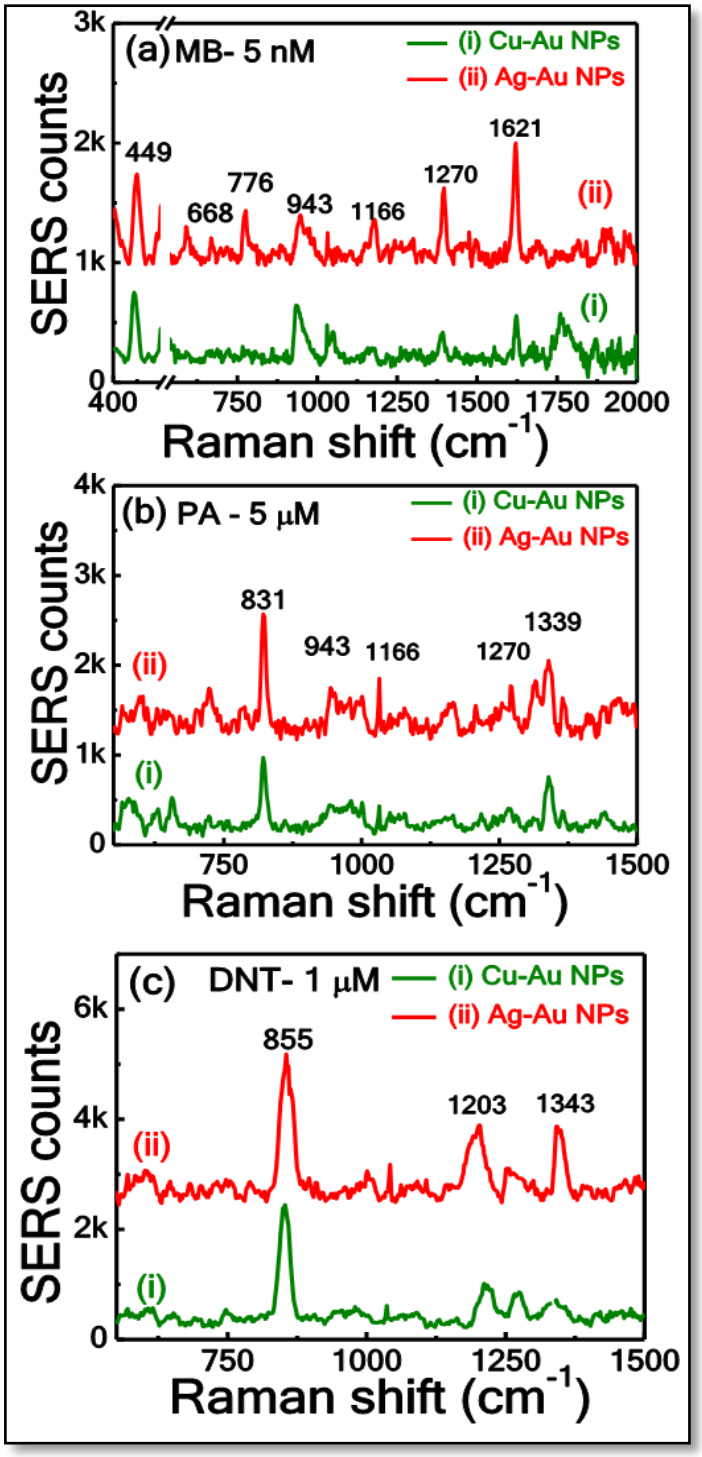

Figure 3.15 SERS spectra of (a) MB (b) PA (c) DNT using Ag-Au [red] and Cu-Au NPs [green] on plain silicon.

The SERS performances of Ag-Au and Cu-Au NPs were verified using explosives like PA and DNT as target molecules. Figure 3.15(b) shows the SERS spectra of PA (5 µM) molecules adsorbed on Ag-Au and Cu-Au NPs films. Similarly, the SERS performance of Ag-Au and Cu-Au NPs substrates was examined with other explosive molecules, DNT,

which is used as a detection marker for landmines and is the main decomposition product of TNT. Figure 3.15(c) shows the SERS spectra of DNT with Raman modes noticed at 855 cm^{-1}, 1203 cm^{-1} peak assignment were mentioned in Appendix A. The calculated EFs for Ag-Au NPs and Cu-Au NPs were 3.45×10^7, 1.44×10^7 for MB (1622 cm^{-1}), 8.22×10^4, 4.47×10^4 for PA (829 cm^{-1}) and 7.5×10^5, 6×10^5 for DNT (855 cm^{-1}), respectively. From the presented data it is evident that Ag-Au NPs substrate depicted superior enhancements in the Raman signals compared to the Cu-Au NPs, which could be due to the strong plasmonic property of silver compared to copper and, further, due to the strong electric field enhancements induced near the NP surfaces because of the nano chain shape of the Ag-Au alloy NPs.

3.4.2.1 Dye molecule (MB) detection

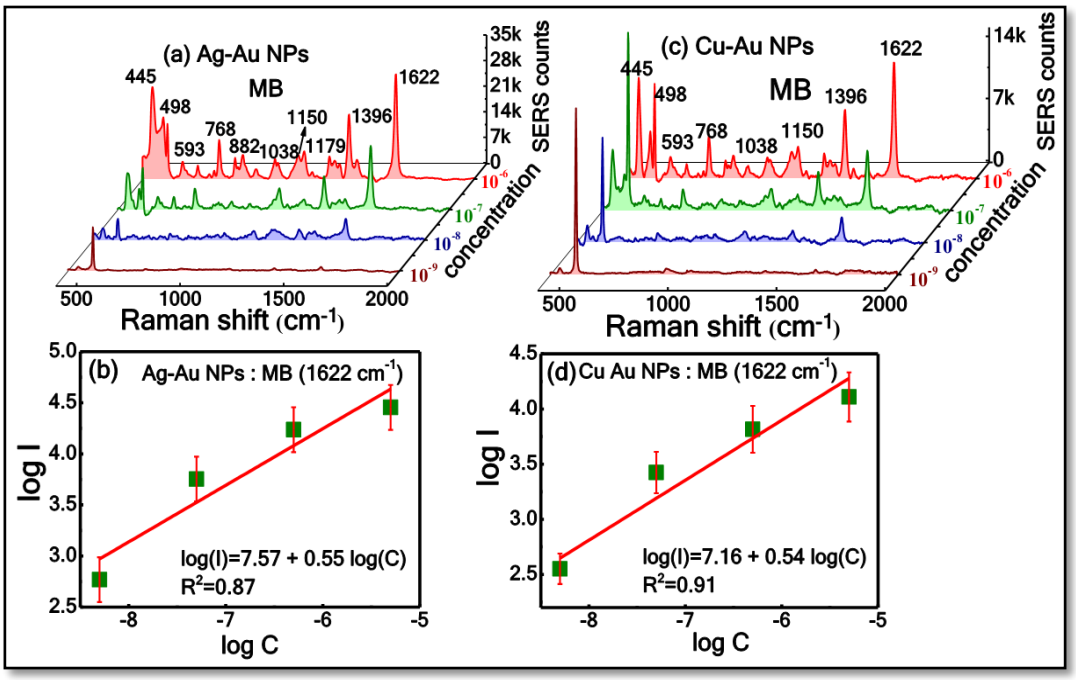

Figure 3.16 Concentration-dependent SERS spectra of MB (5 µM to 5 nM) using (a) Ag-Au NPs (c) Cu-Au NPs and (b) and (d) represents the corresponding linear fit for SERS intensity at 1622 cm^{-1} versus MB concentration (Solid green squares represent the experimental data, and the solid red line represents the theoretical fits)

Figures 3.16(a) illustrates the variation in the SERS intensity with varying MB concentration from 5×10^{-6} M to 5×10^{-9} M recorded Ag-Au NPs substrate. With increasing MB concentration the intensity of SERS signals was increased.[64-66] The Raman modes for MB were identified even at the 10^{-9} M concentration with a good signal-to-noise ratio. Further, linear dependence variation observed between the logI-logC with R^2 of 0.87 for the main characteristic peak of MB (1622 cm^{-1}) and the data is shown in figure 3.16(b).

However, at higher concentrations a slight saturation of the intensity was observed. The calculated EF for the Ag-Au NPs substrate was 3.45×10^{7} for MB (1622 cm^{-1} mode). Figure 3.16 (c) shows the concentration-dependent SERS spectra for MB molecule recorded from the Cu-Au NP substrate. Most of the Raman modes for MB are recognized even at the concentration of 10^{-9} M. Similarly; the linear dependence logI-logC plot is shown in figures 3.16(d) with a reasonable R^2 value of ~0.91.

3.4.2.2 Explosive molecule (PA) detection

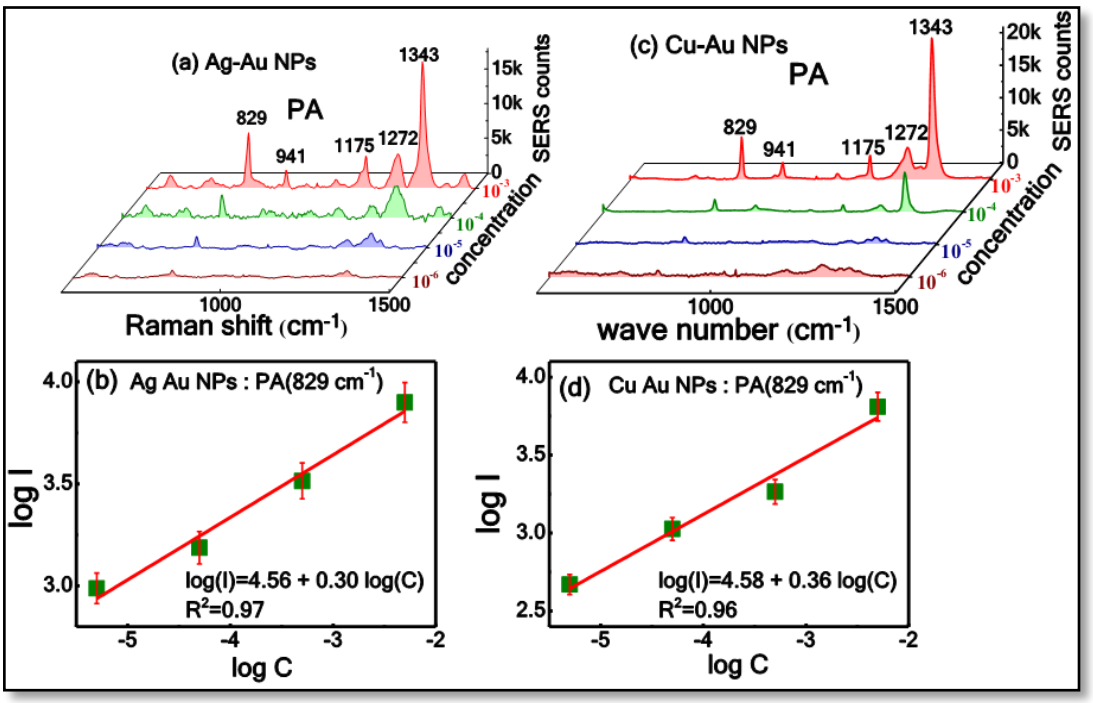

Figure 3.17 Concentration-dependent SERS spectra of PA (5 mM to 5 µM) using (a) Ag-Au NPs (c) Cu-Au NPs and (b) and (d) represents the corresponding linear fit for log SERS intensity versus the log of PA concentration at 829 cm^{-1}

Figures 3.17(a) and 3.17(b) display the PA concentration-dependent SERS spectra obtained from Ag-Au and Cu-Au NPs substrates data illustrate the variation in the SERS intensity with varying PA concentrations from 5×10^{-3} M to 5×10^{-6} M using Ag-Au and Cu-Au NP substrates, respectively. The calibration curves were plotted by monitoring the signal intensity of Raman band at 829 cm^{-1} for PA as a function of log C for both cases of Ag-Au and Cu-Au NPs, which are shown in figure 3.17(b) and 3.17(d), respectively. The linear dependence fitted curves yielded regression equations log I = 4.56 + 0.30 log C in the case of Ag-Au NPs and log I= 4.58 + 0.36 logC in the case of Cu-Au NPs. The correlation coefficients (R^2) for PA was ~0.97 for Ag-Au NPs and ~ 0.96 for Cu-Au NPs. Thus, the concentration-dependent spectra with high linearity indicate the efficiency of the SERS substrates.

3.4.3 Reproducibility Studies

3.4.3.1 Reproducibility of Ag-Cu NPs

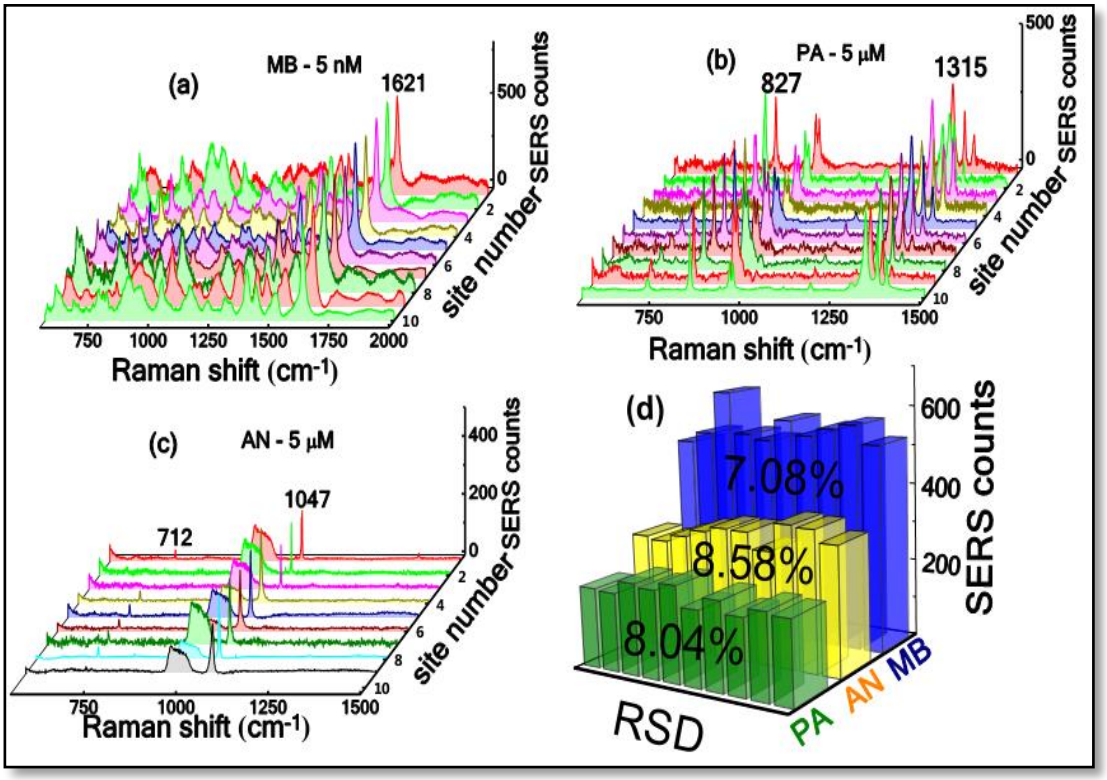

Figure 3.18 Reproducibility of the SERS spectra of (a) MB -5 nM (b) PA-5 µM (c) AN-5µM absorbed on Ag-Cu alloy NPs (d) histogram of the SERS intensities for significant modes.

Apart from the sensitivity, the reproducibility of the SERS substrates is a critical parameter for determining their applications in practical and real-world situations. The homogeneity and reproducibility of the Raman signal for all alloy NPs SERS-active substrates (Ag-Cu, Ag-Au, and Cu-Au NPs) were tested from the low point-to-point variation of Raman intensity over a large area on the SERS substrates. The most moderate relative standard deviation (RSD) values from more than 10 locations demonstrate the sensitivity of highly desirable SERS substrates. Here, the reproducibility of the Ag–Cu NPs substrate was studied using three molecules, i.e., MB, PA, and AN. For each molecule, the spectra were recorded from 10 randomly selected spots on Ag–Cu alloy NPs substrate. The 3D plot of SERS spectra by considering the Raman signals at 10 different sites on the same substrate are illustrated in figure 3.18 (a) MB 5 nM (b) PA 5 µM and (c) AN 5 µM and the measured RSD values for MB (1621 cm^{-1}), PA (827 cm^{-1}) and AN (1047 cm^{-1}) were ~ 7.08%, 8.58%, and 8.08%, respectively. Figure 3.18 (d) shows the histogram plot for the peak intensity of the most prominent peak of each molecule relative to the spot number, which

demonstrates the excellent homogeneity of the SERS substrate even in various analyte molecules identification.

3.4.3.2 Reproducibility of Ag-Au NPs and Cu-Au NPs

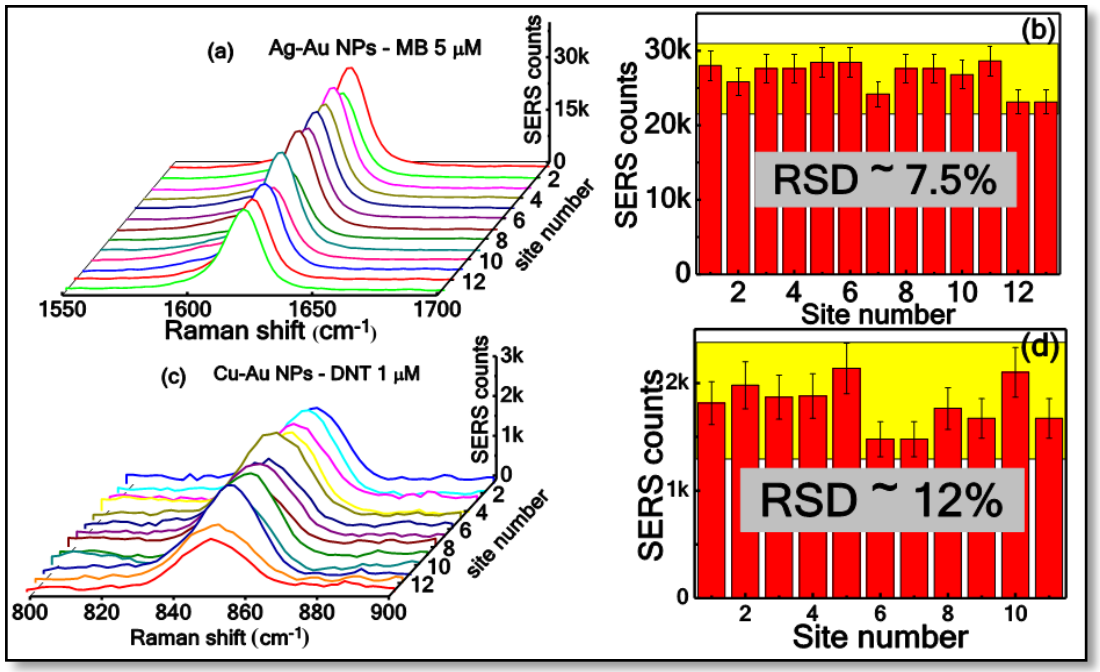

Figure 3.19 (a) SERS spectra of MB (5 µM) recorded at different sites. (b) SERS intensity of 1622 cm^{-1} peak histogram collected using Ag-Au alloy NPs. (c) SERS spectra of DNT (1 µM) recorded at different sites. (d) SERS intensity of 849 cm^{-1} peak histogram using Cu-Au alloy NPs.

Similarly, Ag-Au alloy NPs reproducibility studies were performed with the analyte molecule MB possessing a concentration of 5 $\times 10^{-6}$ M. The obtained SERS spectra are illustrated in figure 3.19(a). The most prominent peak (1620 cm^{-1}) intensity was selected to estimate RSD, and the obtained value was ~7.5% [figure 3.19(b)]. Similarly, the reproducibility of the Cu-Au alloy NPs SERS performance was verified with a probe molecule DNT 1×10^{-6} M. Figures 3.19(c) and 3.19(d) depict the SERS spectra of DNT (1×10^{-6} M) and their corresponding histogram of 849 cm^{-1} peak with RSD value 12%, respectively. These values signify the excellent reproducibility of the SERS signal, which shows the homogeneity of the colloidal SERS substrate.

3.5 Conclusions:

- In two consecutive steps, Ag-Cu NPs were fabricated (1) laser ablation to Ag/Cu targets to prepare to Ag/Cu NPs (2) Laser irradiation of a colloidal mixture of Ag and Cu NPs to prepare Ag-Cu alloy NPs.

- Ag-Au and Cu-Au NPs were fabricated with a simple approach of using laser ablation of the bulk target (Ag/Cu) immersed in the $HAuCl_4$ solution.
- The single SPR peak in the UV-visible absorption spectra and the elemental composition mapping from FESEM-EDS indicates the formation of alloy NPs.
- XRD and HRTEM analyses revealed that alloy NPs were composed of both the atoms.
- The SERS performance of Ag, Cu and Ag-Cu alloy NPs were investigated for a dye molecule viz. MB. The Ag-Cu alloy NPs exhibit better SERS signals compared to pure metal NPs (Ag or Cu).
- These three alloy NPs [Ag-Cu, Ag-Au and Cu-Au] are served as active SERS substrates towards the quantitative detection of explosives and dye molecules at low concentrations. Moreover, these substrates demonstrated higher reproducibility with reasonable RSD values.
- Compared to Ag-Cu and Cu-Au, alloy NPs Ag-Au NPs depicted superior enhancement factors.

Table 3. 1 Alloy NPs SERS performance

S. No	Alloy NPs	Synthesis	Analyte	Concentration	EF
1	**Ag-Cu NPs**	Laser irradiation of Ag and Cu NPs	MB	5 nM	3×10^7
			PA	5 µM	2.8×10^4
			AN	5 µM	3.3×10^4
2	**Cu-Au NPs**	Laser ablation of Cu in $HAuCl_4$	MB	5 nM	1.44×10^7
			PA	5 µM	4.47×10^4
			DNT	5 µM	6.0×10^5
3	**Ag-Au NPs**	Laser ablation of Ag in $HAuCl_4$	MB	5 nM	3.45×10^7
			PA	5 µM	8.22×10^4
			DNT	1 µM	7.5×10^5

3.6 References

1. Tao, Y.; Li, M.; Ren, J.; Qu, X., Metal Nanoclusters: Novel Probes for Diagnostic and Therapeutic Applications. *Chem. Soc. Rev.* **2015**, *44*, 8636-8663.
2. Pearman, W. F.; Fountain, A. W., Classification of Chemical and Biological Warfare Agent Simulants by Surface-Enhanced Raman Spectroscopy and Multivariate Statistical Techniques. *Appl. Spectros.* **2006**, *60*, 356-365.
3. Khan, I.; Saeed, K.; Khan, I., Nanoparticles: Properties, Applications and Toxicities. *Arabian J. Chem.* **2017**, *12*, 908-931.
4. Ye, W.; Long, R.; Huang, H.; Xiong, Y., Plasmonic Nanostructures in Solar Energy Conversion. *J. Mater. Chem. C* **2017**, *5*, 1008-1021.
5. Samal, A. K.; Polavarapu, L.; Rodal-Cedeira, S.; Liz-Marzán, L. M.; Pérez-Juste, J.; Pastoriza-Santos, I., Size Tunable Au@Ag Core–Shell Nanoparticles: Synthesis and Surface-Enhanced Raman Scattering Properties. *Langmuir* **2013**, *29*, 15076-15082.
6. Qi, Y.; Xing, T. Y.; Zhao, J.; Weng, G. J.; Li, J. J.; Zhu, J.; Zhao, J. W., Tuning the Surface Enhanced Raman Scattering Performance of Anisotropic Au Core−Ag Shell Hetero-Nanostructure: The Effect of Core Geometry. *J. Alloys Compd.* **2019**, *776*, 934-947.
7. Khaywah, M. Y.; Jradi, S.; Louarn, G.; Lacroute, Y.; Toufaily, J.; Hamieh, T.; Adam, P.-M., Ultrastable, Uniform, Reproducible, and Highly Sensitive Bimetallic Nanoparticles as Reliable Large Scale SERS Substrates. *J. Phys. Chem. C.* **2015**, *119*, 26091-26100.
8. Hashimoto, Y.; Seniutinas, G.; Balčytis, A.; Juodkazis, S.; Nishijima, Y., Au-Ag-Cu Nano-Alloys: Tailoring of Permittivity. *Sci. Rep.* **2016**, *6*, 25010.
9. Barcikowski, S.; Compagnini, G., Advanced Nanoparticle Generation and Excitation by Lasers in Liquids. *Phys. Chem. Chem. Phys.* **2013**, *15*, 3022-3026.
10. Podagatlapalli, G. K.; Hamad, S.; Mohiddon, M. A.; Rao, S. V., Effect of Oblique Incidence on Silver Nanomaterials Fabricated in Water Via Ultrafast Laser Ablation for Photonics and Explosives Detection. *Appl. Surf. Sci.* **2014**, *303*, 217-232.
11. Fernández-López, C.; Polavarapu, L.; Solís, D. M.; Taboada, J. M.; Obelleiro, F.; Contreras-Cáceres, R.; Pastoriza-Santos, I.; Pérez-Juste, J., Gold Nanorod–Pnipam Hybrids with Reversible Plasmon Coupling: Synthesis, Modeling, and SERS Properties. *ACS Appl. Mater. & Interf.* **2015**, *7*, 12530-12538.
12. Jiang, T.; Song, J.; Zhang, W.; Wang, H.; Li, X.; Xia, R.; Zhu, L.; Xu, X., Au-Ag@Au Hollow Nanostructure with Enhanced Chemical Stability and Improved Photothermal Transduction Efficiency for Cancer Treatment. *ACS Appl. Mater. and Interf.* **2015**, *7*, 21985-21994.
13. Chen, M.; Wang, D.; Liu, X., Direct Synthesis of Size-Tailored Bimetallic Ag/Au Nano-Spheres and Nano-Chains with Controllable Compositions by Laser Ablation of Silver Plate in Haucl4 Solution. *RSC Adv.* **2016**, *6*, 9549-9553.
14. Wang, C.; Li, M.; Li, Q.; Zhang, K.; Wang, C.; Xiao, R.; Wang, S., Polyethyleneimine-Mediated Seed Growth Approach for Synthesis of Silver-Shell Silica-Core Nanocomposites and Their Application as a Versatile SERS Platform. *RSC Adv.* **2017**, *7*, 13138-13148.
15. Mills, D. L.; Maradudin, A. A.; Burstein, E., Theory of the Raman Effect in Metals. *Ann. Phys.* **1970**, *56*, 504-555.
16. Li, D.; Liu, J.; Wang, H.; Barrow, C. J.; Yang, W., Electrochemical Synthesis of Fractal Bimetallic Cu/Ag Nanodendrites for Efficient Surface Enhanced Raman Spectroscopy. *Chem. Commun.* **2016**, *52*, 10968-10971.

17. Wu, F.; Bellon, P.; Melmed, A.; Lusby, T., Forced Mixing and Nanoscale Decomposition in Ball-Milled Cu–Ag Characterized by Apfim. *Acta Mater.* **2001**, *49*, 453-461.
18. Amendola, V.; Barcikowski, S., A Quarter-Century of Nanoparticle Generation by Lasers in Liquids: Where Are We Now, and What's Next? Elsevier: **2017,** *489*, 1
19. Barcikowski, S.; Menéndez-Manjón, A.; Chichkov, B.; Brikas, M.; Račiukaitis, G., Generation of Nanoparticle Colloids by Picosecond and Femtosecond Laser Ablations in Liquid Flow. *Appl. Phys. Lett.* **2007**, *91*, 083113.
20. Zhang, D.; Gökce, B.; Barcikowski, S., Laser Synthesis and Processing of Colloids: Fundamentals and Applications. *Chem. Rev.* **2017**, *117*, 3990-4103.
21. Rao, S. V.; Podagatlapalli, G. K.; Hamad, S., Ultrafast Laser Ablation in Liquids for Nanomaterials and Applications. *J. Nanosci. Nanotechnol* **2014**, *14*, 1364-1388.
22. Ganjali, M.; Ganjali, M.; Khoby, S.; Meshkot, M. A., Synthesis of Au-Cu Nano-Alloy from Monometallic Colloids by Simultaneous Pulsed Laser Targeting and Stirring. *Nano-Micro Letters* **2011**, *3*, 256-263.
23. Podagatlapalli, G. K.; Hamad, S.; Rao, S. V., Trace-Level Detection of Secondary Explosives Using Hybrid Silver–Gold Nanoparticles and Nanostructures Achieved with Femtosecond Laser Ablation. *J. Phys. Chem. C* **2015**, *119*, 16972-16983.
24. Xu, L.; Li, S.; Zhang, H.; Wang, D.; Chen, M., Laser-Induced Photochemical Synthesis of Branched Ag@Au Bimetallic Nanodendrites as a Prominent Substrate for Surface-Enhanced Raman Scattering Spectroscopy. *Opt. Express* **2017**, *25*, 7408-7417.
25. Hajiesmaeilbaigi, F.; Motamedi, A., Synthesis of Au/Ag Alloy Nanoparticles by Nd: Yag Laser Irradiation. *Laser Phys. Lett.* **2006**, *4*, 133.
26. Byram, C.; Soma, V. R., 2, 4-Dinitrotoluene Detected Using Portable Raman Spectrometer and Femtosecond Laser Fabricated Au–Ag Nanoparticles and Nanostructures. *Nano-Structures & Nano-Objects* **2017**, *12*, 121-129.
27. Chen, Y.-H.; Yeh, C.-S., A New Approach for the Formation of Alloy Nanoparticles: Laser Synthesis of Gold–Silver Alloy from Gold–Silver Colloidal Mixtures. *Chem. Commun.* **2001**, *4*, 371-372.
28. Petrović, S.; Salatić, B.; Milovanović, D.; Lazović, V.; Živković, L.; Trtica, M.; Jelenković, B., Agglomeration in Core-Shell Structure of Cuag Nanoparticles Synthesized by the Laser Ablation of Cu Target in Aqueous Solutions. *J. Opt.* **2015**, *17*, 025402.
29. Aazadfar, P.; Solati, E.; Dorranian, D., Properties of Au/Copper Oxide Nanocomposite Prepared by Green Laser Irradiation of the Mixture of Individual Suspensions. *Opt. Mater.* **2018**, *78*, 388-395.
30. Shin, K.; Kim, D. H.; Yeo, S. C.; Lee, H. M., Structural Stability of Agcu Bimetallic Nanoparticles and Their Application as a Catalyst: A Dft Study. *Catalysis today* **2012**, *185*, 94-98.
31. Xu, D.; Kang, W.; Yang, W.; Zhang, S.; Chen, J., Synthesis of Centimeter Level Agcu Alloy Nanowires Via a Solid-State Ionics Method and Their SERS Effect. *J. Alloys Compd.* **2017**, *725*, 248-252.
32. Vu, T. D.; Duy, P. K.; Chung, H., Nickel Foam–Caged Ag-Au Bimetallic Nanostructure as a Highly Rugged and Durable SERS Substrate. *Sens. Actuators, B* **2019**, *282*, 535-540.
33. Jiao, A.; Dong, X.; Zhang, H.; Xu, L.; Tian, Y.; Liu, X.; Chen, M., Construction of Pure Worm-Like Auag Nanochains for Ultrasensitive SERS Detection of Pesticide

Residues on Apple Surfaces. *Spectrochimica Acta Part A: Molecular and Biomolecular Spectroscopy* **2018**, *209*, 241-247
34. Lee, J.-P.; Chen, D.; Li, X.; Yoo, S.; Bottomley, L. A.; El-Sayed, M. A.; Park, S.; Liu, M., Well-Organized Raspberry-Like Ag@ Cu Bimetal Nanoparticles for Highly Reliable and Reproducible Surface-Enhanced Raman Scattering. *Nanoscale* **2013**, *5*, 11620-11624.
35. Zhao, C.; Qu, S.; Qiu, J.; Zhu, C., Photo-induced Formation of Colloidal Au by a near-Infrared Femtosecond Laser. *J. Mater. Res.* **2011**, *18*, 1710-1714.
36. Lu, Y.; Wang, K.; Chen, F. R.; Zhang, W.; Sui, M. L., Extracting Nano-Gold from Haucl4 Solution Manipulated with Electrons. *Phys. Chem. Chem. Phys.* **2016**, *18*, 30079-30085.
37. Tan, D.; Zhou, S.; Qiu, J.; Khusro, N., Preparation of Functional Nanomaterials with Femtosecond Laser Ablation in Solution. *J. Photochem. Photobiol. C; Photochem. Reviews* **2013**, *17*, 50-68.
38. Herbani, Y.; Nakamura, T.; Sato, S., Synthesis of near-Monodispersed Au–Ag Nanoalloys by High Intensity Laser Irradiation of Metal Ions in Hexane. *J. Phys. Chem. C* **2011**, *115*, 21592-21598.
39. Zeng, H.; Du, X. W.; Singh, S. C.; Kulinich, S. A.; Yang, S.; He, J.; Cai, W., Nanomaterials Via Laser Ablation/Irradiation in Liquid: A Review. *Adv. Funct. Mater* **2012**, *22*, 1333-1353.
40. Ghaforyan, H.; Ebrahimzadeh, M.; Mohammadi, B., Study of the Optical Properties of Nanoparticles Using Mie Theory. *World Appl Program* **2015**, *5*, 79-82.
41. Amendola, V.; Meneghetti, M., Size Evaluation of Gold Nanoparticles by Uv− Vis Spectroscopy. *J. Phys. Chem. C* **2009**, *113*, 4277-4285.
42. Amendola, V.; Pilot, R.; Frasconi, M.; Maragò, O. M.; Iatì, M. A., Surface Plasmon Resonance in Gold Nanoparticles: A Review. *J. Phys.: Condens. Matter* **2017**, *29*, 203002.
43. Nigoghossian, K.; Dos Santos, M. V.; Barud, H. S.; Da Silva, R. R.; Rocha, L. A.; Caiut, J. M.; De Assunçao, R. M.; Spanhel, L.; Poulain, M.; Messaddeq, Y., Orange Pectin Mediated Growth and Stability of Aqueous Gold and Silver Nanocolloids. *Appl. Surf. Sci.* **2015**, *341*, 28-36.
44. Sosa, I. O.; Noguez, C.; Barrera, R. G., Optical Properties of Metal Nanoparticles with Arbitrary Shapes. *J. Phys. Chem. B* **2003**, *107*, 6269-6275.
45. Kuladeep, R.; Jyothi, L.; Alee, K. S.; Deepak, K. L. N.; Rao, D. N., Laser-Assisted Synthesis of Au-Ag Alloy Nanoparticles with Tunable Surface Plasmon Resonance Frequency. *Opt. Mater. Express* **2012**, *2*, 161-172.
46. Boyer, P.; Ménard, D.; Meunier, M., Nanoclustered Co− Au Particles Fabricated by Femtosecond Laser Fragmentation in Liquids. *J. Phys. Chem. C* **2010**, *114*, 13497-13500.
47. Jiang, H.; Moon, K.-s.; Wong, C. In *Synthesis of Ag-Cu Alloy Nanoparticles for Lead-Free Interconnect Materials*, Advanced Packaging Materials: Processes, Properties and Interfaces, 2005. Proceedings. International Symposium on, IEEE: **2005**; 173-177.
48. Messina, G. C.; Sinatra, M. G.; Bonanni, V.; Brescia, R. et. al., Tuning the Composition of Alloy Nanoparticles through Laser Mixing: The Role of Surface Plasmon Resonance. *J. Phys. Chem. C* **2016**, *120*, 12810-12818.
49. Valodkar, M.; Modi, S.; Pal, A.; Thakore, S., Synthesis and Anti-Bacterial Activity of Cu, Ag and Cu–Ag Alloy Nanoparticles: A Green Approach. *Mater. Res. Bull.* **2011**, *46*, 384-389.

50. Compagnini, G.; Messina, E.; Puglisi, O.; Cataliotti, R. S.; Nicolosi, V., Spectroscopic Evidence of a Core–Shell Structure in the Earlier Formation Stages of Au–Ag Nanoparticles by Pulsed Laser Ablation in Water. *Chem. Phys. Lett.* **2008**, *457*, 386-390.
51. Peng, Z.; Spliethoff, B.; Tesche, B.; Walther, T.; Kleinermanns, K., Laser-Assisted Synthesis of Au− Ag Alloy Nanoparticles in Solution. *J. Phys. Chem. B* **2006**, *110*, 2549-2554.
52. Malviya, K. D.; Chattopadhyay, K., Synthesis and Mechanism of Composition and Size Dependent Morphology Selection in Nanoparticles of Ag–Cu Alloys Processed by Laser Ablation under Liquid Medium. *J. Phys. Chem. C* **2014**, *118*, 13228-13237.
53. Sebastian, S.; Linslal, C.; Vallbhan, C.; Nampoori, V.; Radhakrishnan, P.; Kailasnath, M., Formation of Au–Ag Nanoalloy through Au Core/Ag Shell Intermediate Phase by Laser Ablation. *Chem. Phys. Lett.* **2015**, *628*, 25-29.
54. Byram, C.; Moram, S. S. B.; Soma, V. R., SERS Based Detection of Multiple Analytes from Dye/Explosive Mixtures Using Picosecond Laser Fabricated Gold Nanoparticles and Nanostructures. *Analyst* **2019**, *144*, 2327-2336.
55. Pyatenko, A.; Wang, H.; Koshizaki, N.; Tsuji, T., Mechanism of Pulse Laser Interaction with Colloidal Nanoparticles. *Laser Photonics Rev.* **2013**, *7*, 596-604.
56. Swiatkowska-Warkocka, Z.; Koga, K.; Kawaguchi, K.; Wang, H.; Pyatenko, A.; Koshizaki, N., Pulsed Laser Irradiation of Colloidal Nanoparticles: A New Synthesis Route for the Production of Non-Equilibrium Bimetallic Alloy Submicrometer Spheres. *RSC Adv.* **2013**, *3*, 79-83.
57. Tan, K. S.; Cheong, K. Y., Advances of Ag, Cu, and Ag–Cu Alloy Nanoparticles Synthesized Via Chemical Reduction Route. *J. Nanopart. Res.* **2013**, *15*, 1537.
58. Chang, K.; Chung, H., Simple Electrochemical Synthesis of an Au–Ag–Cu Trimetallic nanodendrite and its use as a SERS Substrate. *RSC Adv.* **2016**, *6*, 75943-75950.
59. Stelzig, S. H.; Menneking, C.; Hoffmann, M. S. et. al, Compatibilization of Laser Generated Antibacterial Ag-and Cu-Nanoparticles for Perfluorinated Implant Materials. *Eur. Polym. J.* **2011**, *47*, 662-667.
60. Nazeruddin, G.; Prasad, R.; Shaikh, Y.; Shaikh, A., Synergetic Effect of Ag-Cu Bimetallic NPs on Antimicrobial Activity. *Der Pharmacia Lettre.* **2014**, *3*, 129-136.
61. Farrell, M. E.; Holthoff, E. L.; Pellegrino, P. M., Surface-Enhanced Raman Scattering Detection of Ammonium Nitrate Samples Fabricated Using Drop-on-Demand Inkjet Technology. *Appl. Spectros.* **2014**, *68*, 287-296.
62. Acosta-Maeda, T. E.; Misra, A. K.; Muzangwa, L. G.; Berlanga, G.; Muchow, D.; Porter, J.; Sharma, S. K., Remote Raman Measurements of Minerals, Organics, and Inorganics. *Appl. Opt.* **2016**, *55*, 10283-10289.
63. Anastasopoulos, J.; Soto Beobide, A.; Manikas, A.; Voyiatzis, G., Quantitative Surface-Enhanced Resonance Raman Scattering Analysis of Methylene Blue Using Silver Colloid. *J. Raman Spectros.* **2017**,*48*, 1762-1770.
64. Hamad, S.; Podagatlapalli, G. K.; Mohiddon, M. A.; Rao, S. V., Surface Enhanced Fluorescence from Corroles and SERS Studies of Explosives Using Copper Nanostructures. *Chem. Phys. Lett.* **2015**, *621*, 171-176.
65. Brolo, A.; Jiang, Z.; Irish, D., The Orientation of 2, 2′-Bipyridine Adsorbed at a SERS-Active Au (1 1 1) Electrode Surface. *J. Electroanal. Chem.* **2003**, *547*, 163-172.
66. Creighton, J., Surface Raman Electromagnetic Enhancement Factors for Molecules at the Surface of Small Isolated Metal Spheres: The Determination of Adsorbate Orientation from SERS Relative Intensities. *Surf. Sci.* **1983**, *124*, 209-219.

Chapter 4

Hybrid SERS substrates

Abstract

Hybrid SERS substrates are attractive for enhanced performance compared to individual substrates. Herein, we demonstrate a hybrid SERS substrate based on Silicon and Ag-Au alloy nanoparticles (NPs). Instead of plain silicon as a base, a simple hybrid Silicon (Si) nanotextured target-based SERS platform was fabricated through patterning micro square arrays (MSA) on Si. The femtosecond (fs) laser ablation technique was used to fabricate MSA on Si at different input pulse energies. The hybrid SERS substrate, i.e., Si MSA with Ag–Au alloy NPs (shown better SERS performance in Chapter 4) demonstrated trace level (MB-10 pM, PA-50 nM and RDX-10 µM) detection of organic nitro-explosives [picric acid (PA), 2,4-dinitrotoluene (DNT), and 1, 3, 5-trinitroperhydro-1, 3, 5-triazine (RDX)] and their mixtures. The microstructures/nanostructures of MSA fabricated at a pulse energy of 30 µJ, and decorated with Ag–Au alloy NPs exhibited exceptional SERS enhancement factors (EFs) up to ~10^{10} for MB and ~10^{6} for PA and ~10^{4} for RDX. Three binary mixtures, i.e., MB-PA, MB-DNT, PA-DNT at different concentrations, were also investigated using the same SERS substrate to test the efficacy. Furthermore, these SERS substrates possess good reproducibility (RSD values were <15%) and substrate to substrate reproducibility, also verified with a probe molecule malachite green (MG). The SERS performance compared with commercially available rigid SERS substrates.

Graphical abstract

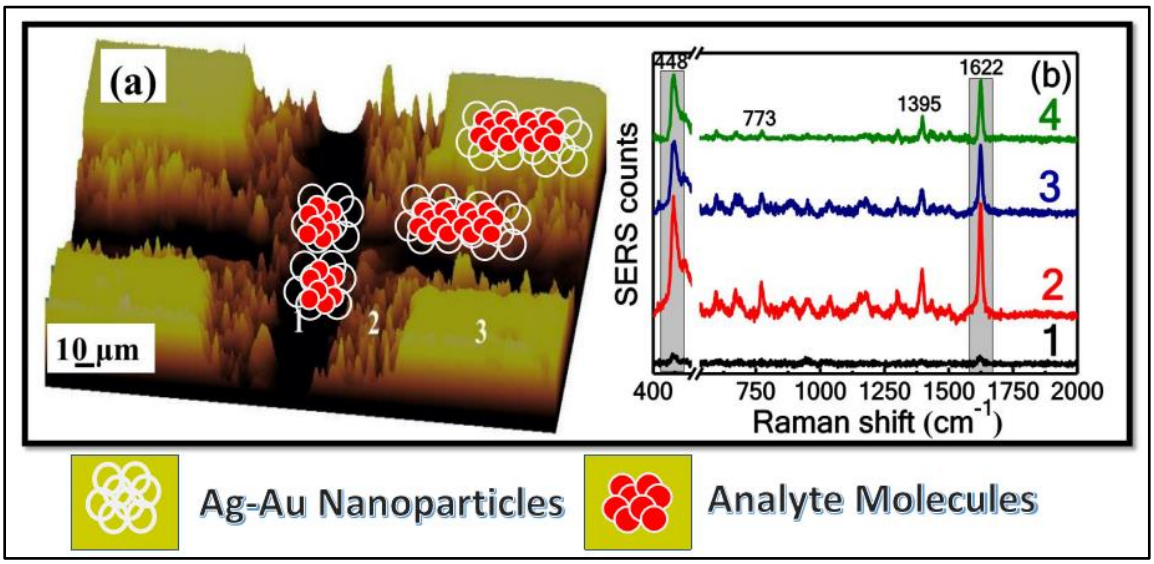

The work presented in this chapter has been published as:

M. S. S. Bharati, S. A. Kalam, B. Chandu, S. Hamad, S. Venugopal Rao," Instantaneous trace detection of nitro-explosives and mixtures with nanotextured silicon decorated with Ag–Au alloy nanoparticles using the SERS technique," *Analytica Chimica Acta*, **1101,** 157-168, 2020.

4.1 Introduction

Many SERS studies have been reported recently using metal nanomaterials (NSs/NPs) deposited on plain silicon (Si) or glass substrates as a base/support through the exploitation of the induced localized surface plasmon resonance (LSPR) resulting in strong electromagnetic enhancements.[1-6] However, few metal-less 2D-materials such as graphene, molybdenum disulfide (MoS_2), tungsten diselenide (WSe_2), Si/SiO_x, etc. have also been shown to contribute to SERS signal through chemical enhancement.[7-9] Therefore, integrating semiconductor silicon (Si/SiO_x), excellent low-cost material with plasmonic NPs could exploit both the electromagnetic and chemical enhancements and such studies are of huge interest towards the development of practical SERS substrates. In line with this, substantial efforts are being directed adapting the morphology changes through fabricating Si nano/micropillars/pyramids using various methods including e-beam lithography, etching, vapor deposition to improve the Raman response.[10-19] However, most of the above-mentioned fabrication methods include a prolonged preparation period, involve considerable cost along with several processing steps. Femtosecond (fs) laser ablation is a powerful yet unpretentious technique to prepare rapid and robust microstructure/nanostructures on several materials. The surface morphology of the NSs is influenced by laser parameters such as wavelength, pulse duration, number of pulses, and pulse energy and also on the properties of surrounding medium (air/liquid/buffer gas). Only a few works have discussed the process of manufacturing Si SERS substrates in a single and two-step process using fs ablation. Lin et al.[20] followed a single-step approach: fs laser ablation of Si in silver nitrate ($AgNO_3$) solution to fabricate Si with Ag adsorbed substrates whereas Yang et al.[21] demonstrated a two-step process: laser scanning microstructures/nanostructured Si followed by deposition of a silver thin film on the fabricated structures. Apart from surface texturing of the base/support, various compositions of NPs made up of two or more compositions of plasmonic materials were synthesized to investigate the Raman response of analyte molecules.[22-26] Ageev et al.[27] fabricated web-like structures with 785 nm, 100 fs laser ablation of silicon in air. Bi et al.[28] observed ~20 times enhancement in the SERS signal using bimetallic gold-silver nanoplate arrays than that of the gold nanoplate arrays. In particular, the fabrication of Ag–Au alloy NPs has received a lot of attention due to their tunable LSPR characteristics through combining the individual properties associated with Ag (superior plasmonic nature

compared to Au) and Au (higher stability compared to Ag) for obtaining superior SERS response. In the previous chapter (# 4), we have discussed the performance of different alloy NPs (Ag–Au, Ag–Cu, and Cu–Au) followed by detailed SERS studies and found that Ag–Au alloy NPs coated plain Si substrate has indeed exhibited superior SERS performance. Herein, micro square arrays (MSA) were fabricated on Si in ambient air using different fs pulse energies (10-100 μJ) and in conjunction with Ag–Au alloy NPs were utilized to demonstrate improved SERS performance. The fabricated SERS substrates morphologies were characterized by field emission scanning electronic microscopy (FESEM) and energy dispersive spectroscopy (EDS) mapping techniques. Significantly, the Si MSA substrate fabricated at 30 μJ, and coated with Ag–Au alloy NPs, has depicted the best SERS enhancement for 10^{-9} M MB molecule compared with other Si-MSA substrates. We believe this is due to the generation of a higher number of hotspots resulting in strongly localized surface plasmons. The best substrate was subsequently used to probe a dye molecule MB (10^{-11} M) and two explosive molecules of PA (50 nM), RDX (1 μM) in their pure form. Further, very few among the earlier studies focused on the detection of analytes in mixtures (binary or ternary). A few studies on SERS have focused on the detection of individual explosive molecules, but in real-time the explosives could possibly be mixed with other molecules to hide their presence. Therefore, this work extended to detect explosive mixtures with various concentrations (PA-MB, DNT-MB, PA-DNT, and MB-PA-DNT) through observing a fingerprint response offered by the SERS technique. Furthermore, these Si NSs loaded with Ag–Au alloy NPs have demonstrated very good reproducibility for all the probe molecules investigated.

4.2 Experimental details

4.2.1 Fabrication of micro squared array on silicon

Figure 4.1(a) depicts the schematic of MSA fabrication on Si using fs ablation. Five different pulse energies, i.e., 10 μJ, 20 μJ, 30 μJ, 50 μJ, and 100 μJ (higher than the ablation threshold of Si, which was 1.5 J/cm^2)[29], were utilized to fabricate the Si microstructure/nanostructures. The Si sample was scanned with speeds of 0.1 and 0.1 mm/s in both X- and Y-directions. The inset in figure 4.1 demonstrates the interaction/scanning path of the laser beam on the surface of Si. In the schematic the length of the scanning lines (5 mm) is represented by ‘a’, and the spacing between two adjacent

scanning lines (50 μm) is represented by 'b'. Every scanning line on Si forms a single groove and, therefore, the line-by-line scanning procedure provided an array of grooves.

4.2.2 Fabrication of Ag-Au alloy NPs

Systematic details of the synthesis of Ag-Au alloy NPs were discussed in chapter 4. Figure 4.1(b) depicts the schematic of the fabrication of Ag-Au alloy NPs.

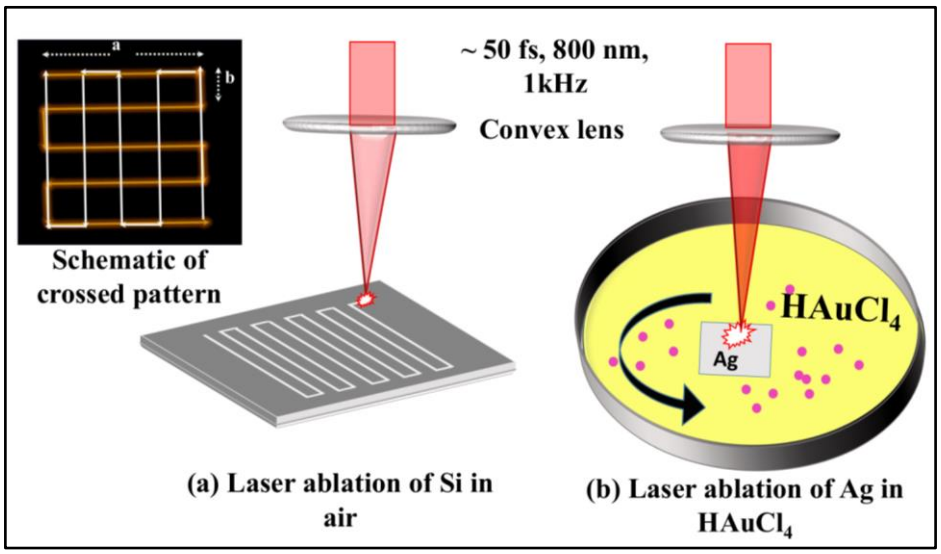

Figure 4.1 Experiment details (a) fs laser ablation of Si (b) synthesis of Ag-Au alloy NPs.

4.3 Characterization of the Si MSA using FESEM

A sequence of magnified images (20 μm, 10 μm and 200 nm) depicting the edge morphology of Si MSA obtained at 10 μJ is shown in figures 4.2(a)-4.2(c). Figures 4.3(a)-4.3(e) and 4.3(f)-4.3(j) illustrate the lower and higher magnification FESEM micrographs, respectively, of Si MSA, fabricated at 10 μJ, 20 μJ, 30 μJ, 50 μJ, and 100 μJ. From figures 4.3(f)–4.3(j) it is evident that semi-spherical shaped Si/SiO_X NPs with fewer voids were noticed at the first two laser energies 10 and 20 μJ while rod-shaped and semi-spherical Si/SiO_X NPs with more nano-cavities, gaps were observed at 30 μJ [Figure 4.3(h)]. At higher pulse energies, large-sized spherical shaped Si/SiO_X NPs with distracted microstructures were observed. The shapes and sizes of the NPs produced in laser ablation with fs pulses depend on the origination of thermo-elastic waves below the surface layer, where the phase explosion (or) coulomb explosion[30] occurs depending on the metallic or dielectric nature of the substance. However, the complete mechanism of phase explosion (or) coulomb explosion associated with the thermo-elastic wave succeeded by NPs generation is not entirely understood.[31-32] From the existing literature believe that low laser

fluences cause negative stress, which ultimately supports and strengthens the repelling force between the atoms, leading to the formation of small-sized Si/SiO_X NPs. However, in the case of higher laser fluences, the repelling force will be stronger than the negative stress and bonds will be broken instantaneously, which may perhaps generate bigger sized Si/SiO_X NPs as well as increased nanostructure deformation/destruction due to the Coulomb explosion.[31-32] The laser ablation of Si in the ambient air leads to a modification in the chemical properties of the Si surface along with its physical properties because of the oxidation effect. During the laser ablation of Si in air, the ablated Si particles in laser-plasma interact with the oxygen present in the surrounding air and re-solidifies in the form SiO/SiO_X on Si MSA. The Si substrates fabricated at different laser energies were studied using EDS spectroscopy to measure the extent of oxidation on Si MSA. Figure 4.3(k)-4.3(o) depicts the EDS spectra, and the inset of each depicts the Si and O weight percentages. The degree of oxidation on Si MSA was observed to increase as the laser pulse energy increased from 10 to 100 μJ, which could probably be attributed to the increased atomization of oxygen from the surrounding air.

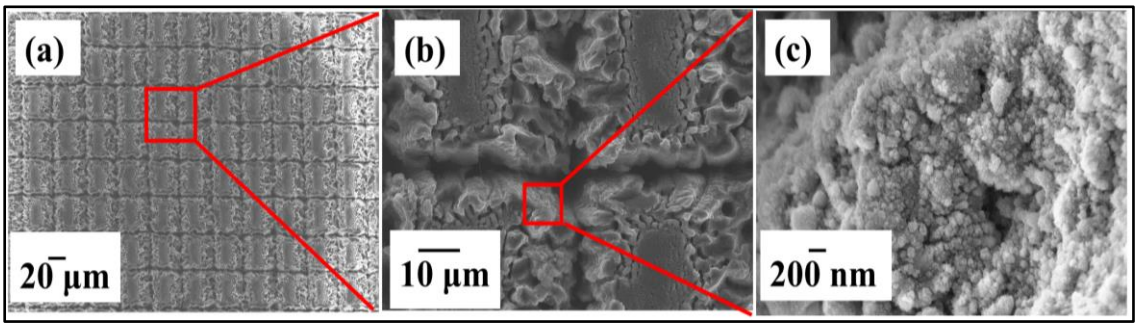

Figure 4.2 SEM images of Si MSA at different magnifications fabricated at 10 μJ.

The Si MSA prepared using 30 μJ was coated with Ag–Au alloy NPs and the distribution of these alloy NPs was examined using FESEM- EDS mapping. Figure 4.4(a) depicts the FESEM images while figure 4.4(b) illustrates the EDS map of Si MSA decorated by Ag–Au alloy NPs and the elemental distribution of each constituent. Figure 4.4(b) illustrates the overall mapping in a selected portion of the target. Figures 4.4(c) – 4.4(e) represent the corresponding elemental mapping images of elemental Si (red color), Ag (yellow color), and Au (green color) on the Si MSA. Figure 4.4(f) shows the EDS spectra while the inset shows the weight percentage of each individual element. The deposited Ag–Au NPs on Si NSs will be able to create more hot spots, leading to the excitation of strongly localized surface plasmons resulting in enormous enhancements of the SERS signal.

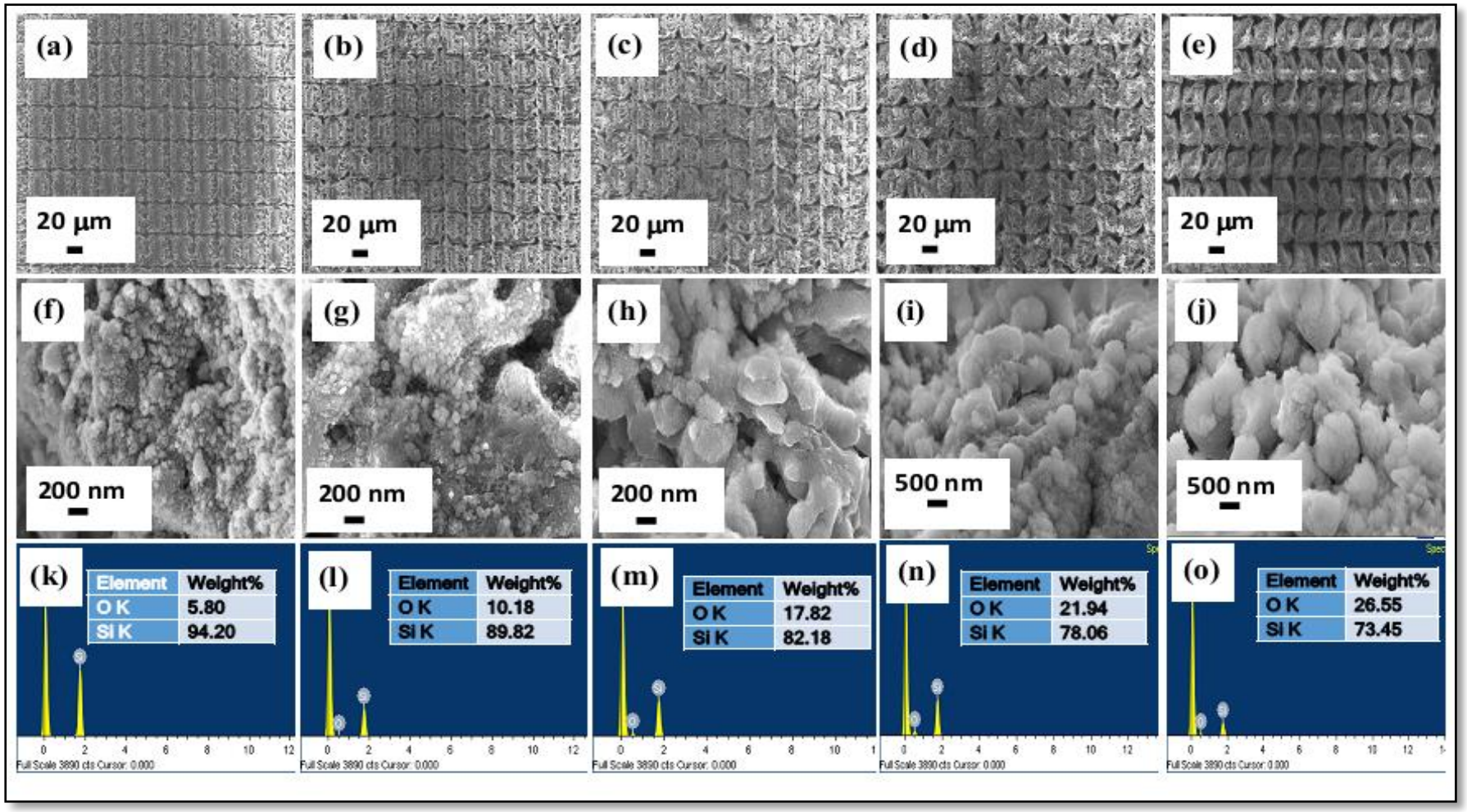

Figure 4.3 FESEM images of fs laser fabricated MSA on Si substrates at different energies (a) 10 µJ (b) 20 µJ (c) 30 µJ (d) 50 µJ and (e) 100 µJ with the scale bar of 20 µm and (f, g, h, i and j) represent their corresponding high-resolution images; (k, l, m, n, and o) represent the corresponding EDS images and insets show atomic weight% of the elements

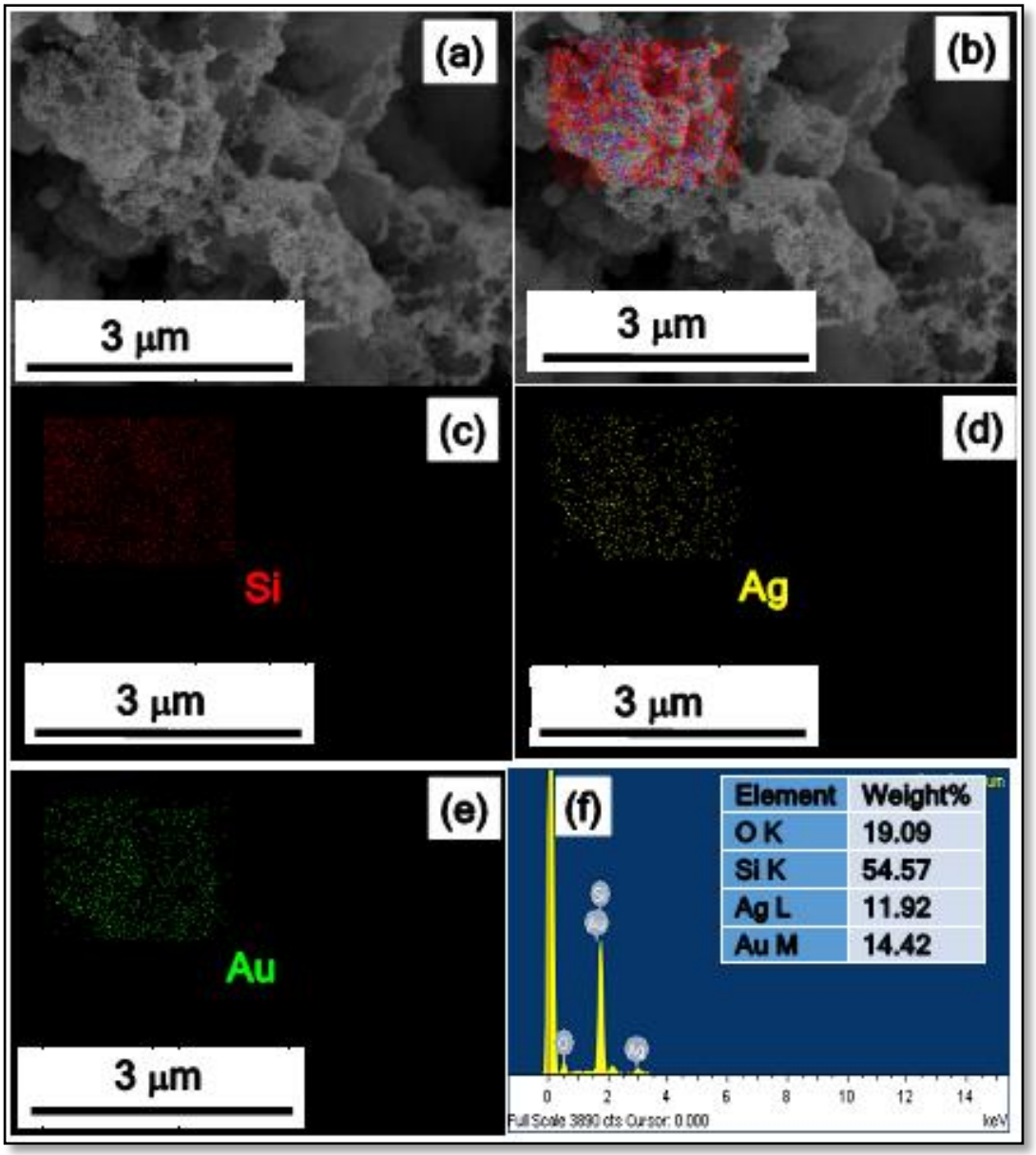

Figure 4.4 (a) FESEM image of edges of Si MSA fabricated at 30 µJ and (b-e) EDS elemental mapping of Ag–Au alloy NPs deposited on Si MSA fabricated at 30 µJ (c) Si (d) Ag (e) Au (f) EDS spectra inset shown the atomic weight % of elements

4.4 SERS studies

4.4.1 Effect of Si MSA morphology

The target Si MSA obtained at 10 µJ was studied region-wise to establish the combined effect of Si MSA as well as Ag–Au alloy NPs towards SERS enhancement using a micro-Raman spectrometer (LabRAM, Horiba Jobin Yvon) and 633 nm as the excitation wavelength. Subsequent SERS studies presented in this work have been performed using a portable Raman spectrometer, which is more practical and easier to transport to the point of interest (field). A

micro-Raman spectrometer was utilized to understand the surface morphology and identify the interesting portions of substrates where the enhancement is higher for the SERS signal. MB dye was chosen as a probe molecule to study the effect of microstructure/nanostructure in the SERS signal. The maximum SERS signal was observed from the edges of MSA because of the micro-protrusions and/or nano-cavities originating from the redistribution of ablated mass in comparison to the regions inside the groove and non-irradiated portions of Si.

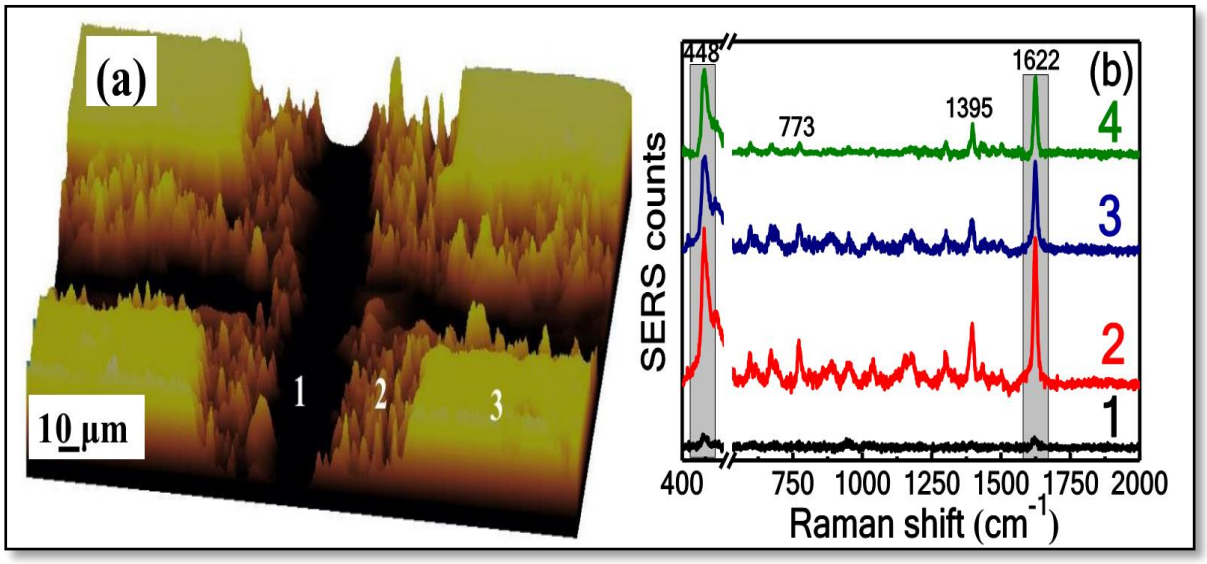

Figure 4. 5 (a) Optical microscope image of laser textured MSA on Si obtained at 10 µJ (b) SERS spectra of MB on different sites (1), (2), and (3) on the Si MSA and (4) on plain Si decorated by Ag-Au alloy NPs.

To illustrate the role of microstructure/nanostructures, the SERS behavior of MSA on Si substrate at 10 µJ (obtained at the lowest pulse energy) decorated with Ag-Au alloy NPs was investigated in detail by choosing three different regions on the Si MSA using a micro-Raman spectrometer (LabRAM, Horiba Jobin Yvon) at 632 nm excitation wavelength. Figure 4.5(a) shows the optical microscope image of Si MSA with the three different locations: (1) within the microgroove (2) the boundaries of micro squares and (3) within the micro square chosen for SERS measurements. The microgroove [region (1)] was formed due to the removal of a large amount of material during the laser interaction. The region (2) indicates the sharp ridges of various sizes resulting in rough surface morphology due to the re-deposition of ablated material on the edges of microgroove. The region (3) indicates the removed Si NPs deposited on the unexposed Si substrate during the ablation. The SERS spectra of MB (5 nM) recorded at these three locations on Si MSA, as well as a SERS spectrum of MB (5 nM) recorded on plain Si with Ag-Au NPs are shown in figure 4.5(b). A break was used on the X-axis to hide the Raman spectra of Si at ~520 cm^{-1}, which corresponds to the typical one-phonon band of

crystalline silicon (c-Si). As observed in figure 4.5(b), the SERS spectra from the regions (2) and (3) demonstrated a significantly enhanced signal of all the Raman bands of MB compared with SERS signal from the region (1). The SERS spectrum of MB within microgroove [region (1)] was observed to be less intense. This could be due to the large depths (few tens of micrometers) associated with the microgroove limiting the interaction of excitation laser with the dye molecules. It was observed that in the case of the region (3) on Si MSA and the surface of plain Si with Ag-Au NPs (case 4), a similar SERS enhancement was observed. This could be owing to the lower number of hot spots generated from the well-dispersed Ag-Au alloy NPs on the respective surfaces. The SERS signal at the edges of micro-square, i.e., in the region (2), was superior to that of SERS signals were obtained in all the cases. This observation could be explained as due to the formation of a large number of hotspots through accommodating many Ag-Au alloy NPs by the micro-protrusions or nano-cavities originated from a redistribution of ablated mass. These structures enhance the local evanescent fields and, in turn, the Raman signal of the analyte.

4.4.2 Detection of MB from different Si MSA substrates

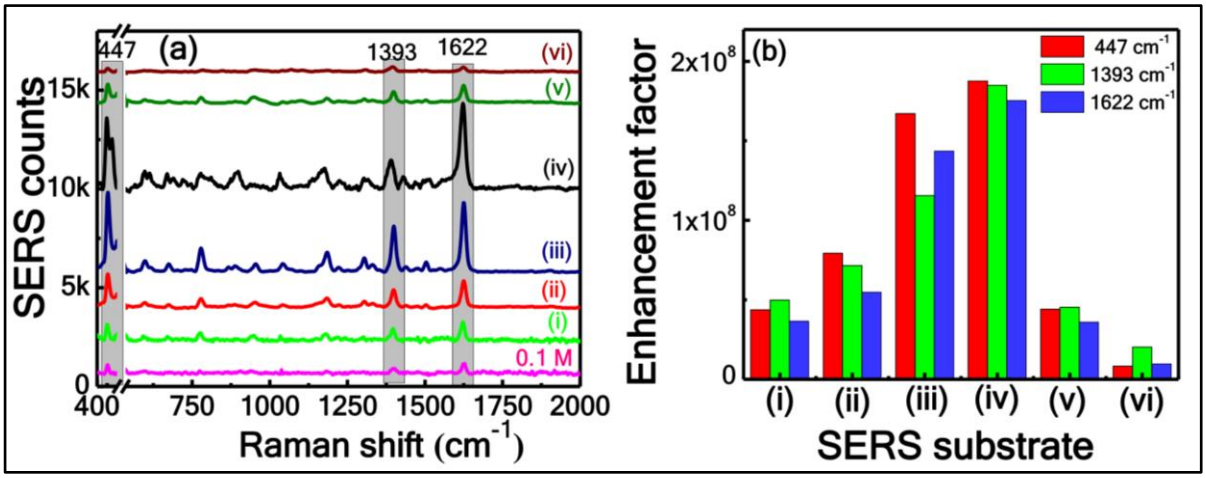

Figure 4.6 (a) SERS spectra of MB (5 nM) adsorbed on Ag–Au alloy NPs decorated on (i) bare Si and Si MSA fabricated at different laser energies (ii) 10 (iii) 20 (iv) 30 (v) 50 and (vi) 100 µJ and, (b) The histogram of EF from all the substrates. The Raman spectra MB (0.1 M) is shown in pink color.

The SERS spectra of MB (5 nM) were recorded using a portable Raman spectrometer with 785 nm excitation source from the Ag–Au alloy NPs deposited on plain Si [Figure 4.6(a) (i)] and Si MSA. The normal Raman spectra of MB (0.1 M) on the plain Si (without NPs) is shown in Fig. 4.6(a) [pink colour, bottom curve]. The measurements for optimization of the SERS substrate were performed on Si MSA fabricated at five different pulse energies to investigate and understand the effect of their morphology/roughness on the SERS performance. The

obtained SERS spectra from all the substrates with Ag–Au alloy NPs are shown in figures 4.6(a) (ii) - (iv). From the data of figure 4.6(b), it is evident that the Raman intensity increased as the laser pulse energy increased from 10 µJ to 30 µJ and then it decreased for a further increase in the fluence from 50 µJ to 100 µJ. The EFs of three modes of MB, i.e., 447 cm^{-1}, 1393 cm^{-1}, and 1622 cm^{-1} from all the substrates, were calculated and are illustrated in Fig. 4(b). The EFs obtained for 1622 cm^{-1} peak were 3.64×10^{7}, 5.46×10^{7}, 1.43×10^{8}, 1.75×10^{8}, 3.58×10^{7} and 9.53×10^{6} for plain Si with NPs and Si MSA with NPs at pulse energies of 10 µJ, 20 µJ, 30 µJ, 50 µJ, and 100 µJ, respectively. With the increased pulse energy from 10 to 20 µJ, EF increased by 2.7 times and 3.2 times for 10 µJ. Later it was observed that the EF decreased to 0.65 and 0.18 times for energies of 50 and 100 µJ when compared to that of the EF obtained at an energy of 10 µJ. A similar trend was also observed in the EFs of two other modes. Si MSA obtained at 30 µJ exhibited the optimum SERS signals in comparison with other Si MSA substrates. This could be ascribed to (i) the presence of semi-spherical and rod-shaped Si/SiO_X NPs with a larger quantity of nano-voids/gaps etc., which could possibly have accommodated a higher number of Ag–Au alloy/bimetallic NPs (ii) aggregation of NPs over the edge of MSA leading to the formation of again a higher number of hot spots and (iii) modifications of local fields under the influence of shape and size of the nanostructure which enhances the scattering efficiency. Subsequently, the Si MSA fabricated at 30 µJ was utilized to perform further SERS studies because of its superior SERS activity.

4.4.3 Sensitivity studies of the optimized substrate

For the real-time/practical applications, a stable and reproducible response is mandated from the SERS active substrates. It is expected that Ag–Au alloy NPs coated on a plain surface might be one of the conceivable substrates for SERS reproducibility studies. Here, SERS sensitivity and reproducibility were investigated for the Ag-Au alloy NPs dispersed on the Si MSA over a large area, fabricated at a fluence of 30 µJ, as it exhibited the highest EFs in the present study. Figure 4.7(a) shows the SERS spectra of MB at various concentrations (from 10^{-11} M to 10^{-6} M). It is evident from the data that 1622 cm^{-1} mode intensity decreased with a decrease in concentration and is feebly observed at 10^{-11} M concentration. Thus, a sensitivity of picomolar (pM) concentration was achieved for MB dye molecule, corroborating the superior sensitivity of this SERS active substrate. A linear dependence of SERS intensity with analyte concentration was verified by fitting log I versus log C plot by considering three major peaks of MB. Figure 4.7(b) shows the linear plots of 447 cm^{-1}, 1393 cm^{-1}, and 1622 cm^{-1} modes with

considerable R^2 values of ~0.99, ~0.98, and ~0.96, respectively, demonstrating a good linear variation of intensity versus concentration. To quantitatively characterize the SERS ability, the estimated the EFs of three major peaks of MB for 10^{-11} M, and the estimated EFs were 0.85×10^{10}, 1.2×10^{10}, and 1.2×10^{10} for 447 cm^{-1}, 1393 cm^{-1} and 1622 cm^{-1} modes, respectively.

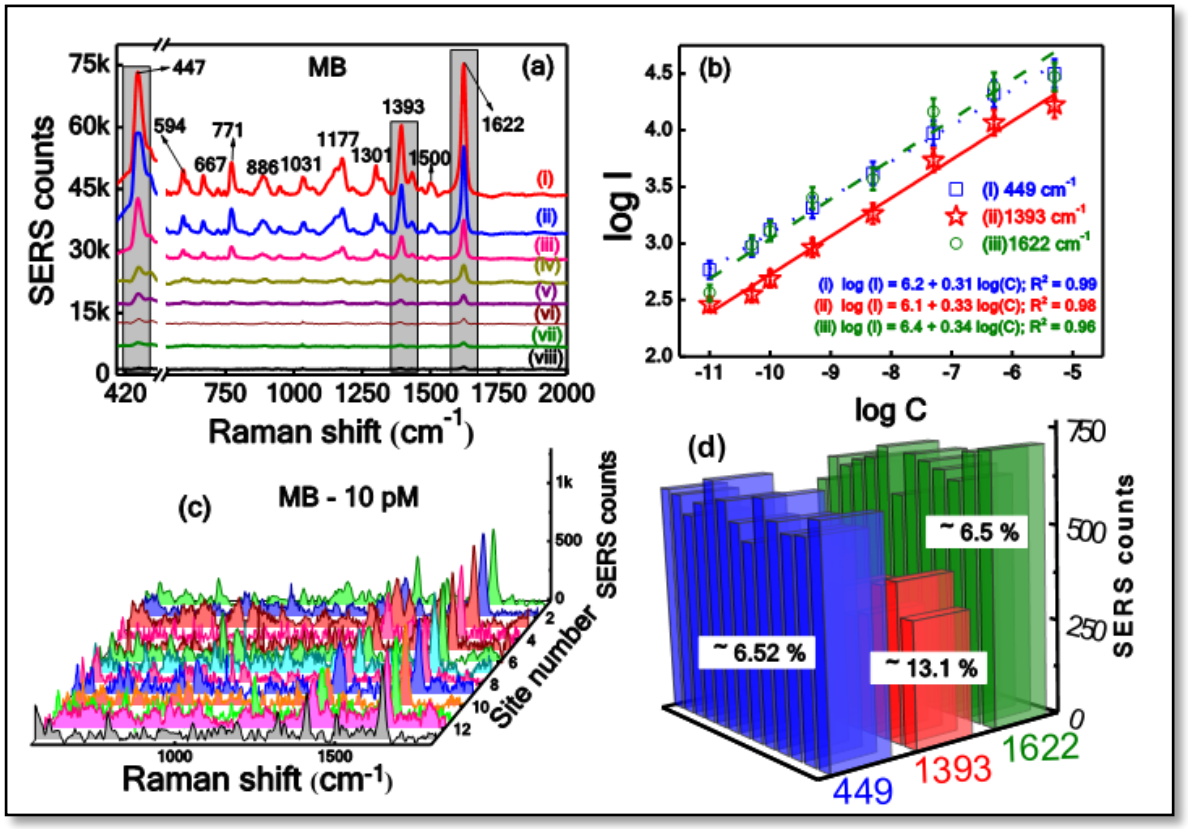

Figure 4.7 SERS spectra of (a) MB [(i) 5 µM (ii) 500 nM (iii) 50 nM (iv) 5 nM (v) 500 pM (vi) 100 pM (vii) 50 pM and (viii) 10 pM] (b) linear dependence log plots of Raman mode intensity versus concentration for the major modes of MB (c) Reproducibility of SERS spectra of MB (10 pM) and (d) histogram of SERS intensity versus site number at three modes of MB adsorbed on Ag-Au NPs coated Si MSA fabricated at 30 µJ.

4.4.4 Reproducibility studies of the optimized substrate

Apart from sensitivity, the reproducibility of the SERS targets is a significant concern owing to the requirement of robust usage. The reproducibility of the SERS substrate was demonstrated by recording the SERS signals of MB at 10 pM concentration. Figure 4.7(c) shows the SERS spectra of MB (10^{-11} M) recorded at 13 randomly selected places on the Ag–Au alloy NPs coated Si MSA. The intensity histograms for the three significant peaks observed at 447, 1393, and 1622 cm^{-1} with their respective RSD values of 6.52%, 13.1%, and 6.5%, shown in figure 4.7(d). Similarly, another dye molecule crystal violet (CV) with a concentration of 5 µM spectra collected from 17 different locations from the same substrate, shown in figure 4.8(a). All the

peaks observed coincided with previous reports and assignments are summarized in Appendix A. Two major peaks of CV were considered to estimate the intensity variation and the obtained RSD values were 12.2% and 14.1% for 1175 cm^{-1} and 1618 cm^{-1}, respectively, as depicted in figure 4.8(b). The obtained results clearly demonstrate the high sensitivity as well as good reproducibility (RSD <15%) of Si MSA. This data suggests that the Au–Ag Alloy NPs coated Si MSA substrate can be considered as a potential SERS substrate for practical applications.

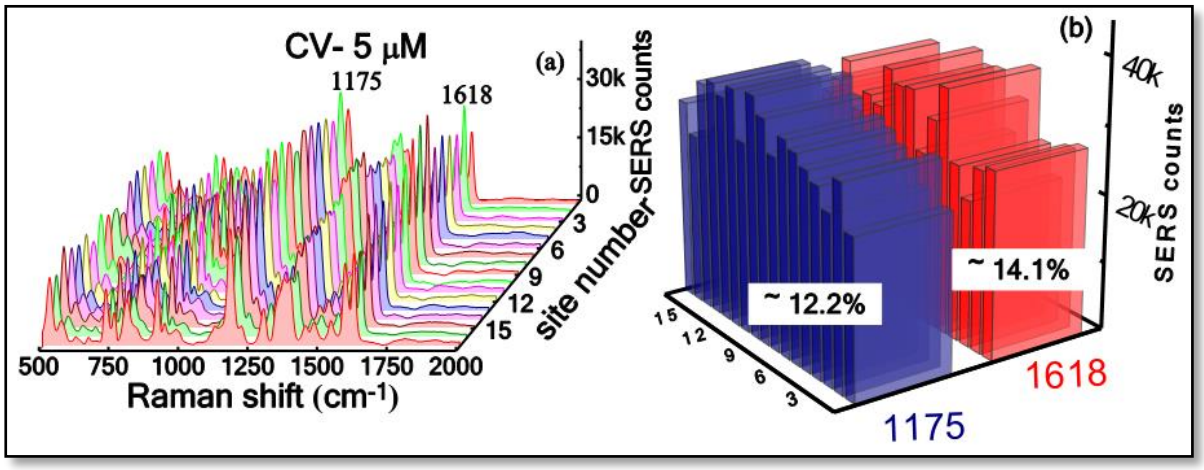

Figure 4.8 (a) Reproducibility of the CV (5 µM) SERS spectra and (b) histogram of SERS intensity versus site number at two modes of CV adsorbed on Ag-Au NPs coated Si MSA fabricated at 30 µJ.

4.4.4.1 Substrate to Substrate Reproducibility

SERS activity in terms of reproducibility was verified with a dye molecule, malachite green (MG-500 pM), on an optimized Si MSA substrate. To inspect the batch-to-batch reproducibility, these two Si MSA were prepared under the same optimized conditions, i.e., at 30 µJ and the same quantity of Ag-Au alloy NPs were drop costed on both the substrates. The signals were collected from 10 different locations from both the substrates, shown in figures 4.9(a) and 4.9(b). The peaks observed at 1169 cm^{-1}, 1393 cm^{-1}, and 1614 cm^{-1} coincided well with the previous reports.[33] The most prominent peak at 1614 cm^{-1} was considered to evaluate the intensity variation. The corresponding histogram with RSD values of 6.48% and 8.11% illustrated in figure 4.9(c) and 4.9(d), respectively. The RSD in the SERS intensity of the 1614 cm^{-1} peak was utilized to investigate the batch-to-batch reproducibility, and it was found to be <10%.[34] Therefore, the repeatability and reproducibility were confirmed with reasonable good RSD values.

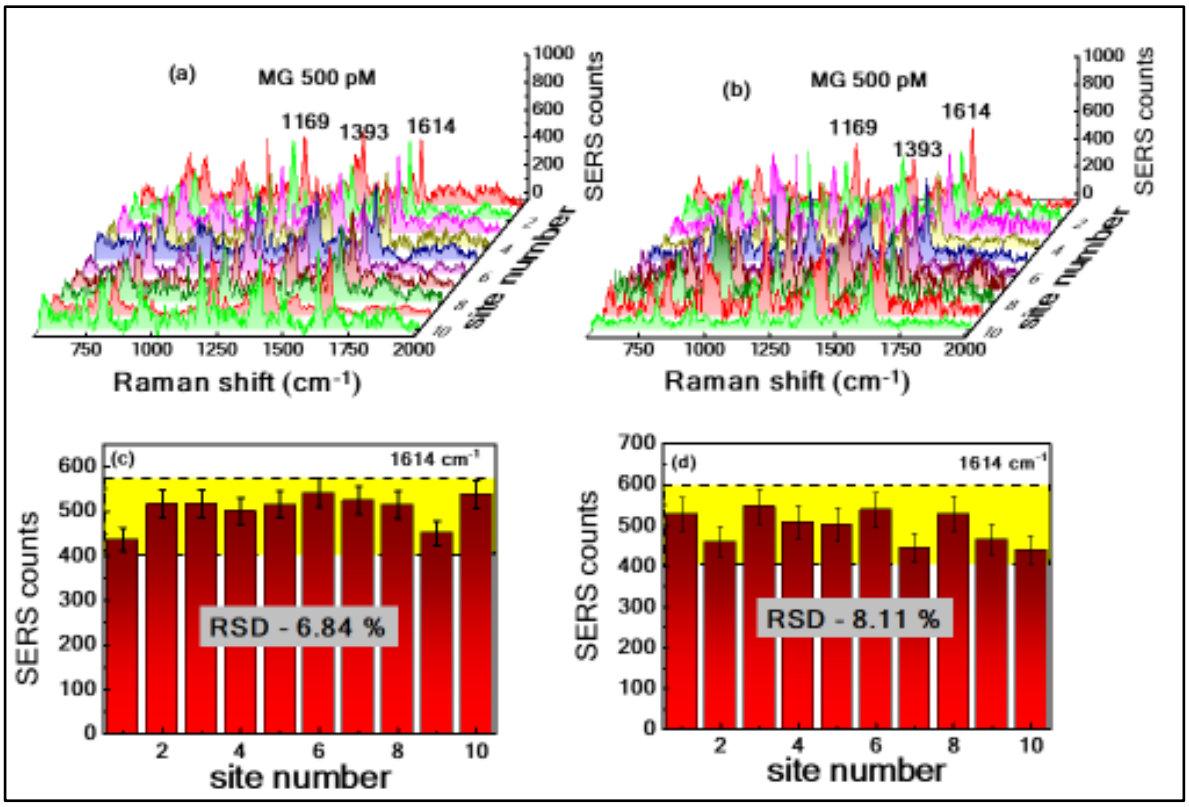

Figure 4.9 Substrate to substrate reproducibility (a) and (b) SERS spectra of MG-500 nM from 10 different locations on each substrate (c) and (d) the corresponding intensity (1614 cm^{-1}) histogram with RSD values.

4.4.5 Detection of explosive molecules

The versatility of the investigated SERS substrate was demonstrated by detecting and analyzing explosive molecules in their pure form and in complex mixtures. Si MSA substrate fabricated at 30 µJ with Ag–Au alloy NPs was used to detect two different explosive molecules, i.e., PA and RDX, in their pure form at minimum concentrations. Figure 4.10(a) depicts the SERS spectra of PA with different concentrations ranging from 500 µM to 50 nM i.e. (i) 500 µM (ii) 50 µ M (iii) 5 µM (iv) 500 nM (v) 50 nM. At a lower concentration of PA (50 nM), only two major peaks, positioned at 820 cm^{-1} and 1338 cm^{-1}, were identified. Figure 4.10(b) illustrates the linear variation in the SERS signal intensity of the 820 cm^{-1}, 1338 cm^{-1} modes versus analyte concentration (log plot) with correlation coefficients of 0.94 and 0.97, respectively. PA was detected even at 50 nM concentration with two major peaks at 820 cm^{-1} and 1338 cm^{-1} with their respective EFs being 2.2×10^6 and 0.8×10^6. A significant improvement (2-orders of magnitude) was achieved in the sensitivity of explosive molecules and is apparent from a comparison of the results obtained from this study (EF ~10^6) with the previous studies (Chapter 3) using Ag–Au alloy NPs on the plain Si as SERS active substrate (EFs of ~10^4).

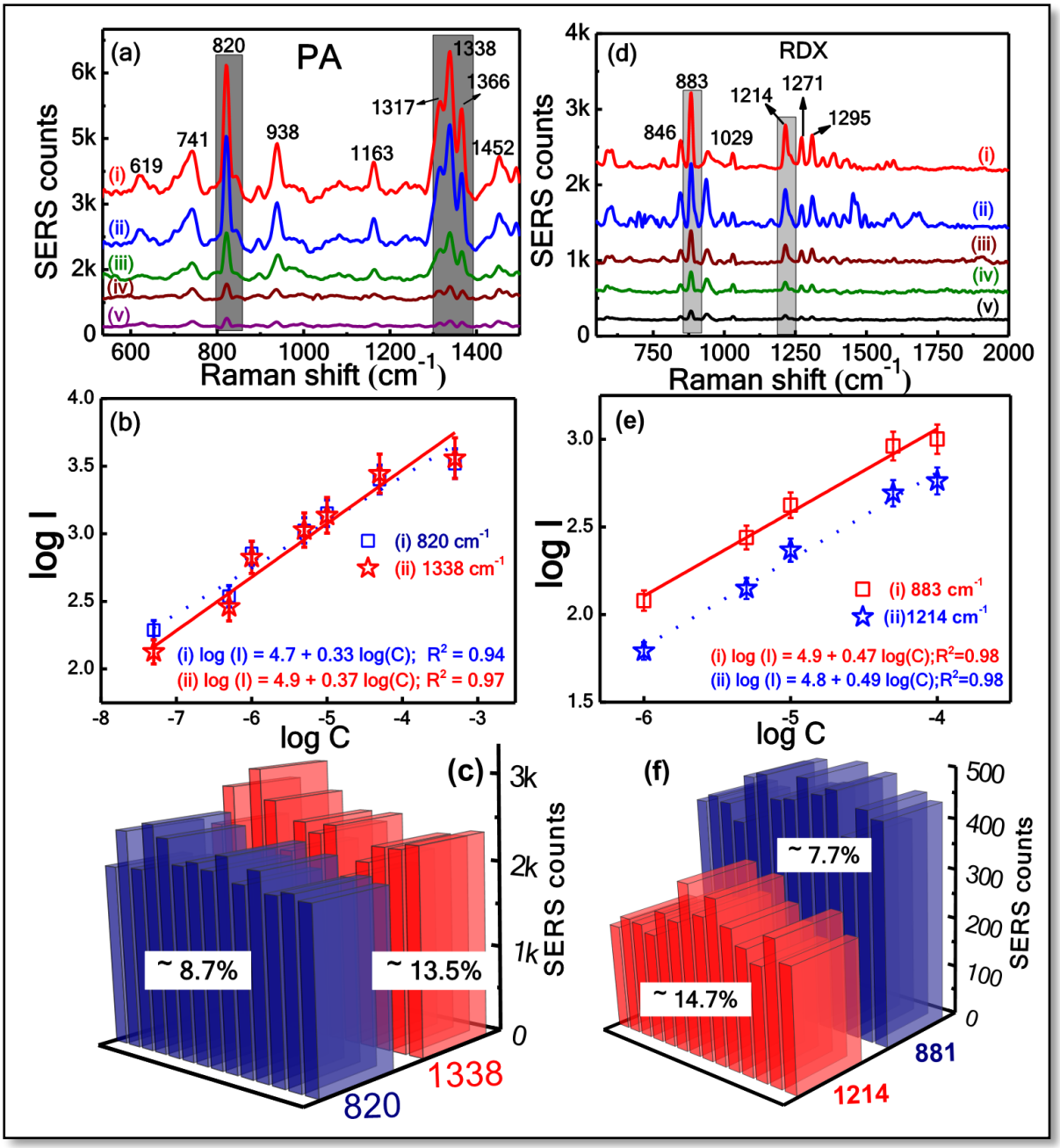

Figure 4. 10 SERS spectra of (a) PA [(i) 500 µM (ii) 50 µ M (iii) 5 µM (iv) 500 nM (v) 50 nM] (d) RDX [(i) 100 µM (ii) 50 µ M (iii) 10 µM (iv) 5 µM (v) 1 µM]. (b) and (e) linear dependence log plots of Raman mode intensity vs. concentration for the major modes of PA and RDX, respectively. (c) and (f) SERS intensity spectra of PA-50 µM and RDX-50 µM histograms from 14 different sites from the optimized SERS substrate.

The reproducibility test was carried out at 14 random sites for PA and the estimated RSD for the characteristic peak of PA at 820 cm^{-1} and 1338 cm^{-1} were 8.7% and 13.5%, as shown in figure 4.10(c). Besides high sensitivity, the SERS substrate also demonstrated good reproducibility. Further, the SERS performance of the optimized Si MSA substrate was verified by choosing RDX as the target analyte molecule[35]. There were no Raman spectra observed for

1 μM RDX molecule, which was adsorbed on Ag–Au alloy NPs with plain Si substrate (data not presented here). However, the Ag–Au alloy NPs coated Si MSA substrate has helped us to detect Raman signals even from 1 μM. For 883 cm^{-1} and 1214 cm^{-1} modes, the obtained EFs are ~$9.3\times10^{4,}$ and 7.5×10^{4}. The concentration-dependent SERS spectra of RDX from 100 to 1 μM [(i) 100 (ii) 50 (iii) 10 (iv) 5 (v) 1 μM] are shown in figure 4.10(d). The observed Raman modes and assignments of RDX are presented in Appendix A. Figure 4.10(e) illustrates the linear dependence of log plot intensity of the SERS signal intensity (883 cm^{-1} and 1214 cm^{-1}) versus analyte concentration with an R^2 value of 0.98. The reproducibility of SERS spectra of RDX [50 μM data is depicted in figure 4.10(f)] with histogram plots of 883 cm^{-1} and 1214 cm^{-1} peaks from 14 different spots with reasonable RSD values of 7.7% and 14.7%, respectively.

4.4.6 Limit of detection (LOD) calculations

To estimate the limit of detection (LOD) for all the three molecules investigated, the most prominent peaks of MB at 1622 cm^{-1}, PA at 822 cm^{-1}, and RDX at 883 cm^{-1} have opted for analysis. Here, the LOD value was calculated using the formula LOD = 3σ/b, where 'σ' is the standard deviation of the blank, and 'b' is the gradient of the linear equation. The slope "b" is obtained from the intensity versus concentration plots. Figures 4.11(a)-4.11(c) represent the Intensity versus C plots of MB, PA, and RDX, and figures 4.11(d)-4.11(f) depict the linear fit used to calculate "b" at a lower concentration. It is clear that their relationship is linear at the lower concentration region and the saturated signal at the higher concentration, shown in figures 4.11(a), 4.11(b) and 4.11(c), respectively. The data points outside the saturation region, i.e., obtained at low concentrations, were used to calculate LOD. The linear equation was $y = 948.28 + 3.86 \times 10^{12}$ C, with a correlation coefficient (R^2) of 0.89, where y is the intensity of SERS Raman peak at 1622 cm^{-1} and C is the MB concentration. Also the linear trend of relationship was observed for PA and RDX with $y = 139.16 + 5.51 \times 10^{08}$ C, R^2 of 0.98 and $y = 94.55 + 3.32 \times 10^{07}$ C, R^2 of 0.99, depicted in figure 4.11 (d)-(f). The estimated LOD values for the MB, PA, and RDX were ~5 pM, ~36 nM, and ~400 nM, respectively. The variations in EFs and LOD from sample to sample on the same substrate could possibly be attributed to the affinity and orientation of these molecules on the SERS substrate. The EFs achieved in Chapter 4 for the colloidal SERS substrates and the EFs achieved in the present chapter 5 for hybrid SERS substrate are summarized in Table 4.1. The EFs accomplished in this case (Ag–Au alloy NPs decorated on Si MSA substrates) indicates that these substrates could be used as an effective sensor for molecular detection at trace level.

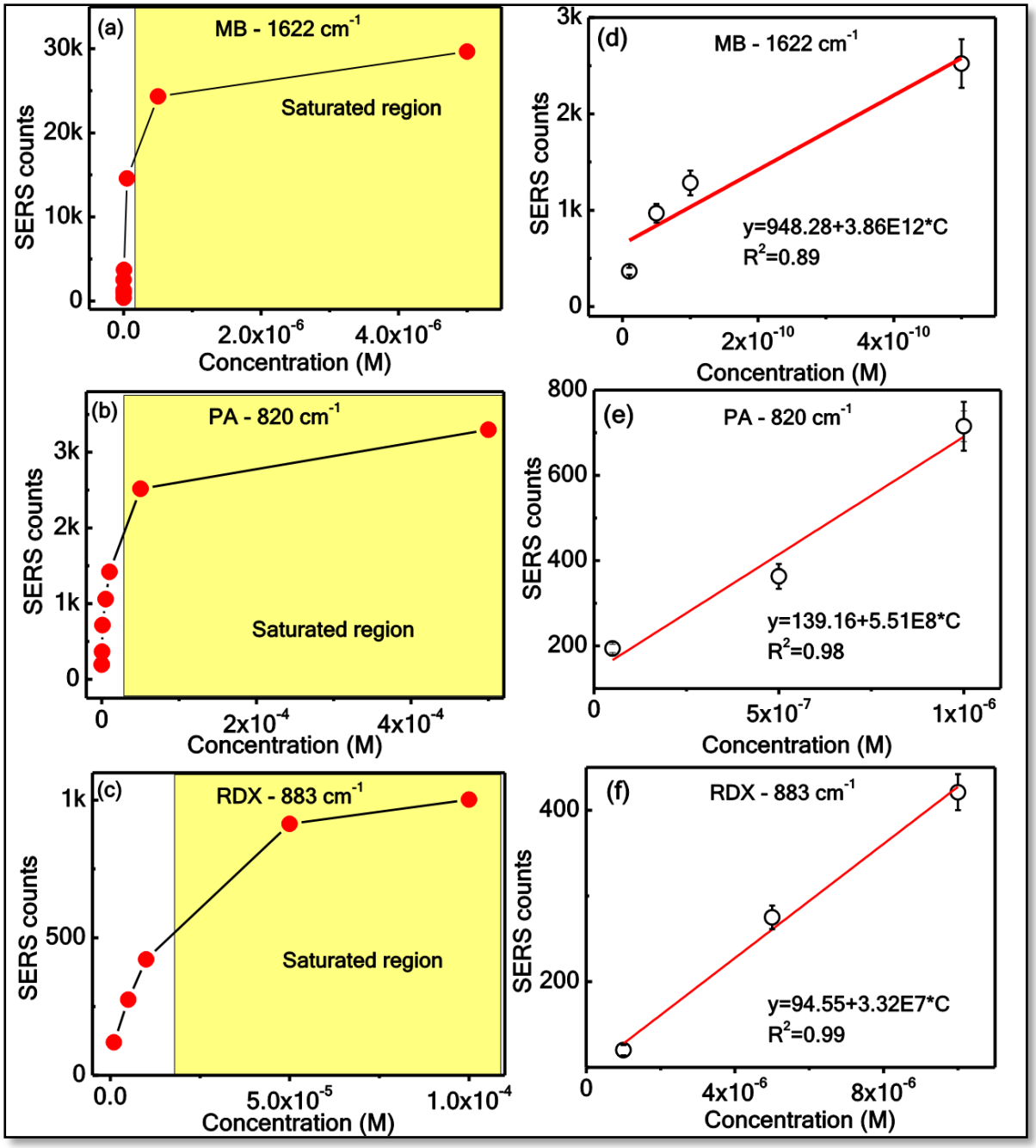

Figure 4.11 SERS intensity as a function of concentration for (a) MB -1622 cm^{-1} (b) PA-820 cm^{-1} (c) RDX- 883 cm^{-1} and (d-f) shows the linear dependence of corresponding molecules at lower concentration.

The hybrid SERS substrates have recently received strong attention because they demonstrated huge enhancements in the Raman signals of various analytes. Various hybrid SERS substrates (i.e., plasmonic coating or NPs deposition on different patterned dielectrics or semiconductors) are becoming interesting areas of research in SERS. Wali et al.[36] recently demonstrated penicillin G-10^{-9} M detection using aggregated Au NPs based porous Si substrate with EF of 5× 10^{7}. Jiang et al.[37] demonstrated superior enhancement of MoS_2@AgNPs@pyramidal Si

compared to MoS_2@AgNPs@flat-Si in the detection of R6G (10^{-11} M). Tan et al.[38] noticed ~2.9 times higher enhancement factor in the SERS signal using Ag-Au bimetallic NPs compared to monometallic Ag NPs. Li et al.[39] reported the fabrication of Au NPs and graphene on Si nanowires using galvanic deposition followed by chemical vapor deposition and used as SERS substrate for the detection of R6G with an EF of ~10^7. MacKenzie et al.[40] fabricated Ag NPs on fused Si by laser pulse (350 fs, 1047 nm, 500 kHz) photo-reduction of $AgNO_3$ solution and detected CV with an EF of 10^{11}. Recently, our group demonstrated laser textured morphologies on Si/Fe/Ni coated with plasmonic metals as SERS substrates. Femtosecond laser prepared Si periodic structures decorated with Ag and Au NPs were used as SERS substrate in the detection of MB (10^{-9} M), DNT (10^{-6} M) and ANTA (10^{-6} M).[41] Ag decorated ZnO nanostructures by thermal evaporation were used to detect FOX-7, ANTA, and CL-20 with EFs of ~10^7, ~10^7, and ~10^4, respectively.[42] A three dimensional Si nanowire substrate decorated with Ag by electroless etching utilized to detect R6G- 10 nM and ammonium perchlorate (AP)- 10^{-5} M and cytosine protein - 10^{-5} M with EFs of ~10^7, ~10^4, and ~10^5, respectively.[43] Au coated iron (Fe) ripple-like nanostructures fabricated by fs laser ablation followed by thermal evaporation used as SERS substrate to detect MB - 5× 10^{-10} M, MG - 5×10^{-9} M and PA - 5× 10^{-6} M.[33] Therefore, it is established that these Si-MSA with Ag-Au alloy NPs SERS substrates yielded considerably higher EF when compared to the above mentioned reports.

Table 4.1: The comparison table of the obtained EF with Ag-Au alloy NPs drop cost on plain Si (Chapter 3) and the optimized Si MSA (presented in chapter 4).

S. No	SERS Substrate	Probe Molecule Detected	Concentration	Enhancement Factor (EF)
1	Plain Si with Ag-Au alloy NPs	MB	5 nM	3.45×10^7
		PA	5 µM	8.22×10^4
		DNT	1 µM	7.50×10^5
2	Si MSA with Ag-Au alloy NPs	MB	10 pM	1.20×10^{10}
		PA	50 nM	2.20×10^6
		RDX	1 µM	9.30×10^4

4.4.7 SERS based Detection of Complex Mixtures

Apart from the sensitivity, selectivity (i.e., the ability of the technique to provide individual/specific response to various materials of interest) is also an important aspect in the explosive analysis. However, in real-time scenarios, the explosive samples inevitably coexist in mixed form with several multiple interferants. Thus, rendering the quantitative and qualitative detection of each molecule from the mixed form has been one of the most important and challenging applications of SERS. Few approaches have been reported for specific molecule detection in the form of mixtures.[44-49] Tian et al.[9] explored the quantitative detection of multiple analytes using graphene-based SERS (G-SERS) and showed that the concentrations, the adsorption constants, and the competing species Raman scattering cross-sections are the key factors in quantitating detection. Here, the same substrate utilized, i.e., Ag–Ag NPs dispersed on Si MSA fabricated at 30 µJ to detect the explosive mixtures.

Three binary mixtures/solutions were prepared with MB, PA, and DNT (PA-MB, DNT-MB, PA-DNT) at different concentrations by mixing the analyte solutions in equal volumes. Figure 4.12 (a) illustrates the SERS spectrum of PA (5 µM) + MB (5 nM) binary mixture in comparison with pure SERS spectra of PA (5 µM) and MB (5 nM). The SERS spectrum of PA + MB mixture consisted of vibrational modes of PA and MB. Similarly, the SERS spectra of a second binary mixture comprising of a dye and an explosive molecule, i.e., MB-DNT (0.5 nM + 0.5 µM) were also recorded and as shown in figure 4.12(b). In the SERS spectra of a mixture the peaks were observed with a small shift and with a decreased intensity. Further, the SERS spectra of PA-MB mixture were recorded by varying the MB concentration from 5 nM to 50 pM [(i) 5 nM (ii) 500 pM and (iii) 50 pM] at a fixed concentration of PA molecule (5 µM) and the data shown in figure 4.12 (c). With a decrease in the concentration of MB, the intensity of characteristic peaks of MB (447, 1620 cm^{-1}) decreased as well but the PA peak intensity (820 cm^{-1}) remains unchanged. Similarly, the concentration of PA was changed from 50 µM to 50 nM at a fixed concentration of MB (500 pM) and the data is illustrated in figure 4.12(d). The intensity of the MB peak at 1620 cm^{-1} was observed to be constant but the intensity of the PA peak at 820 cm^{-1} changed (decreased) with the concentration. It was evident that Raman modes of both compounds were identified in the mixture

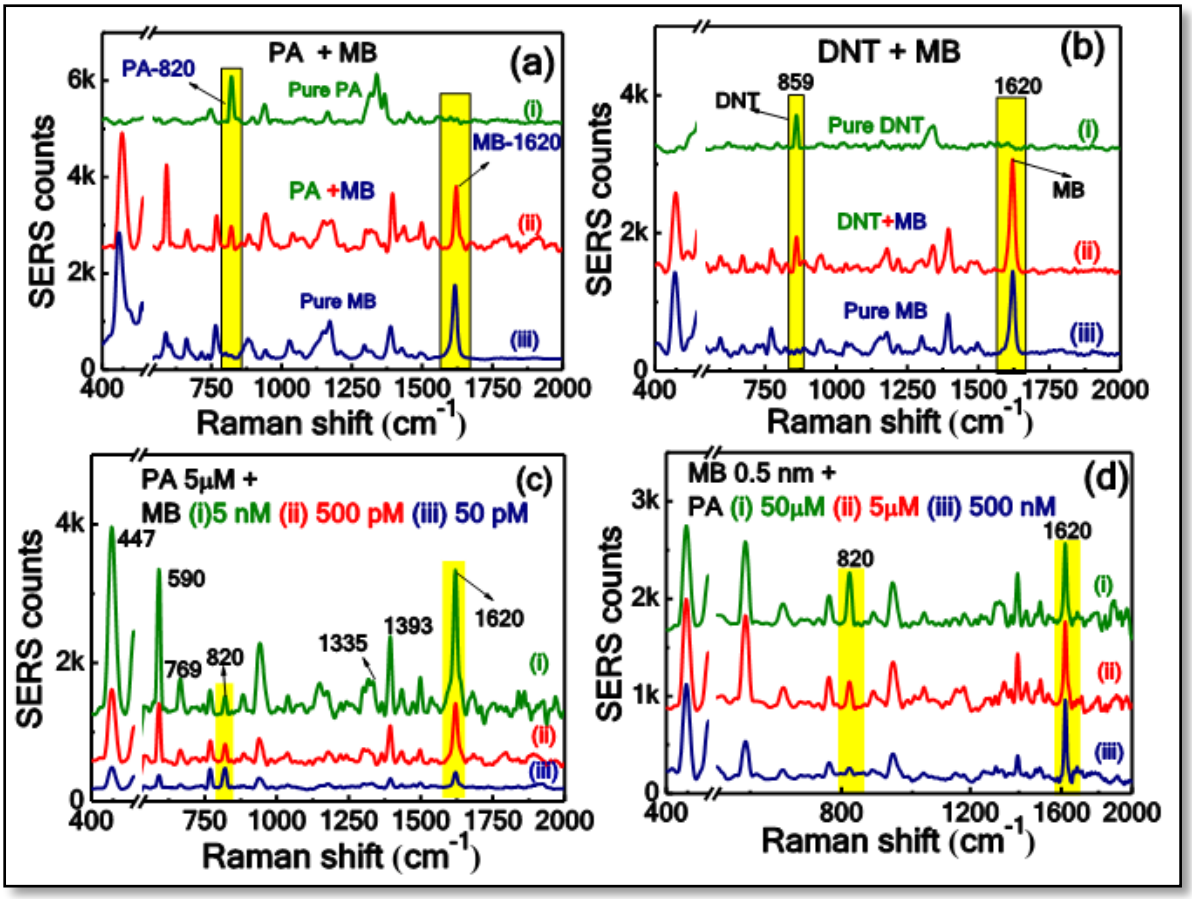

Figure 4.12 SERS spectra of (a) PA + MB mixture [(i) MB (5 nM) (ii) PA (5 μM)+MB (5 nM) and (iii) PA (5 μM)] (b) DNT + MB mixture [(i) MB (0.5 nM) (ii) DNT (0.5 μM) + MB (0.5 nM) and (iii) DNT (0.5 μM)] (c) SERS spectra of PA (5 μM) constant and different MB concentrations (i) 5 nM (ii) 500 pM (iii) 50 pM, (d) with MB (500 pM) constant and different PA concentration (i) 50 μM (ii) 5 μM (iii) 500 nM, adsorbed on the Ag–Au NPs coated Si MSA substrate, fabricated at 30 μJ.

Additionally, the homogeneity of the substrate was verified by collecting the SERS spectra of PA + MB mixture at 12 random sites and data is shown in figure 4.13(a). The corresponding histogram plots of 820 cm^{-1} (PA) and 1620 cm^{-1} (MB) peaks with reasonable RSD values of 9.6% and 7.3%, respectively, illustrated in figure 4.13(b). The SERS spectra of PA+DNT mixture were collected from more than 10 random sites and data is shown in figure 4.13(c). The corresponding histogram plots of 820 cm^{-1} (PA) and 851 cm^{-1} (DNT) peaks demonstrated reasonable RSD values of 11.35% and 9.8%, respectively. The obtained results establish that Au–Ag alloy NPs dispersed Si MSA was able to achieve effective SERS sensitivity and high reproducibility towards the detection of explosive molecules in the binary mixture form. The intensities of Raman modes corresponding to explosive molecules in mixtures were lower albeit their concentration (μm) was higher in comparison to dyes (nM). This could be attributed to the (i) high Raman cross-sections of dye molecules compared to that of explosive molecules

and (ii) the differences in binding affinity of molecules/analytes with the Alloy NPs with Si MSA and (iii) plasmonic response of the molecule to the excitation wavelength.

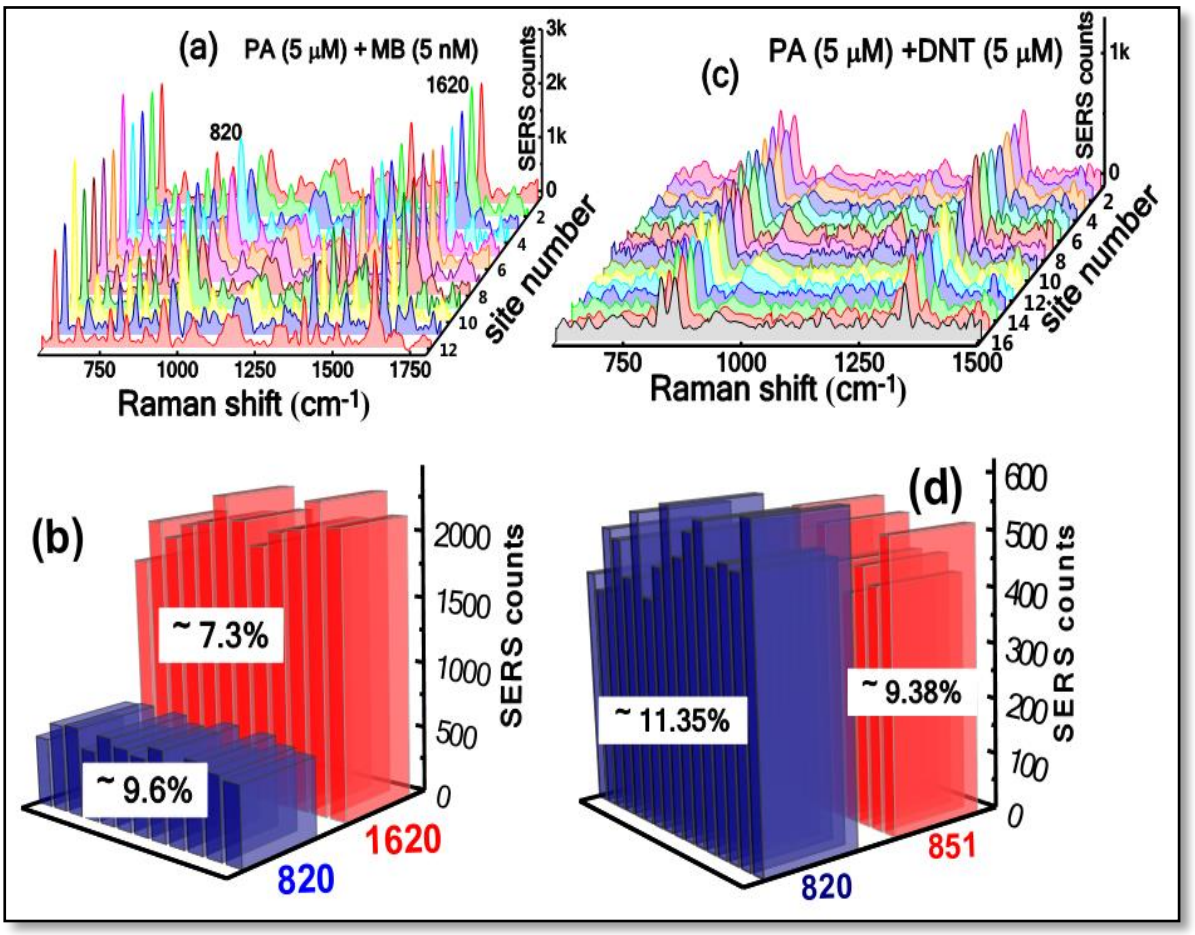

Figure 4.13 (a) Reproducibility spectra of PA (5 µM) + MB (5 nM) mixture (b) SERS intensity histogram of most prominent peaks of PA (820 cm^{-1}) and MB (1620 cm^{-1}) respectively at various random sites. (c) Reproducible spectra of PA and DNT mixture having a concentration 5 µM (d)SERS intensity histogram of most prominent peaks of PA (820 cm^{-1}) and DNT (851 cm^{-1}), respectively.

To evaluate the efficacy of the substrates the studies were extended to detect the binary mixtures containing two explosive molecules. The identification of explosive molecules mixed with other explosive molecules can be more challenging due to the interference and spectral overlap of different analytes. Therefore, in this study, a binary mixture of two explosive molecules, i.e., PA and DNT, were detected at various concentrations using the same SERS active substrate. The SERS spectra of pure PA, DNT, and PA-DNT mixture (4 combinations) are shown in figure 4.14. The prominent peak of PA at 820 cm^{-1} and DNT at 851 cm^{-1} are highlighted with yellow and green color rectangles. Even though both the analytes (PA, DNT) are of the same

concentration (5 µM), a small variation in SERS intensities and shifts were observed. This could be attributed to the combined effect of the orientation of the analytes and interaction between the analyte molecules as well as the adsorption of analyte molecules on the generated plasmonic hotspots. The observation of prominent Raman band intensities of both molecules even at diverse concentrations in the binary mixtures demonstrates the efficacy of Si MSA coated Ag–Au NPs substrates.

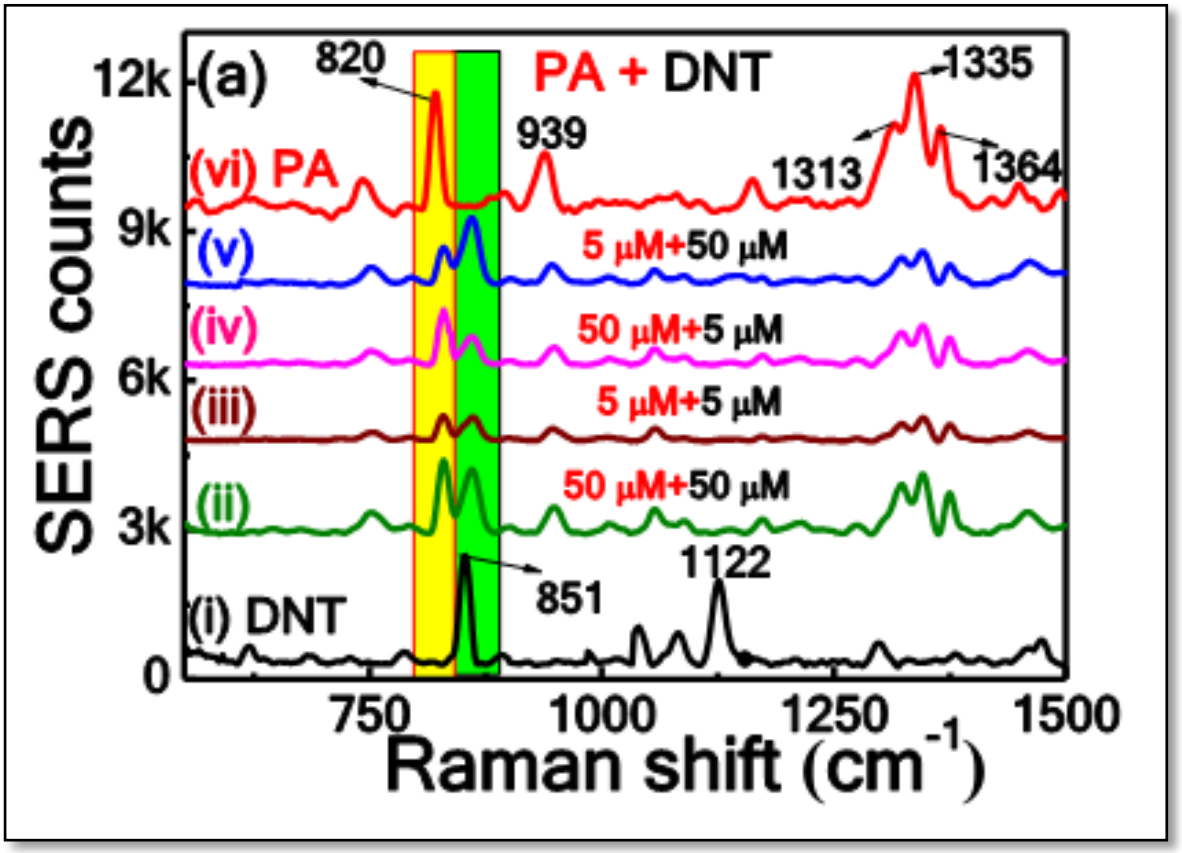

Figure 4.14 SERS spectra (a) explosive mixture PA + DNT (i) DNT (50 µM) (ii) PA (50 µM) +DNT (50 µM) (iii) PA (5 µM) +DNT (5 µM) (iv) PA (50 µM) +DNT (5 µM) (v) PA (5 µM) +DNT (50 µM) and (vi) PA (50 µM).

Subsequently, the Si MSA coated Ag–Au alloy NPs substrate again was employed for detecting the SERS spectra of a mixture of three molecules. A tertiary mixture composed of two explosives and a dye molecule was studied as a proof of concept for the simultaneous detection of multiple analytes using the SERS technique. Figure 4.15 represents a typical SERS spectrum of the tertiary mixture containing PA (5 µM), DNT (5 µM), and MB (5 nM) as analytes. The prominent characteristic peaks of these three molecules were distinguished clearly even when the mixture was in µM concentration for explosives and nM concentration for dye molecules.

The peaks are labeled with different box colors (pink for MB, yellow for PA, and green for DNT). These characteristic peaks can potentially be used for the rapid screening of analytes in complex matrices. Hence, Si MSA covered with Ag–Au NPs substrate possesses potentiality for quick and convenient identification of trace-level explosive (or) organic analytes in real-time applications.

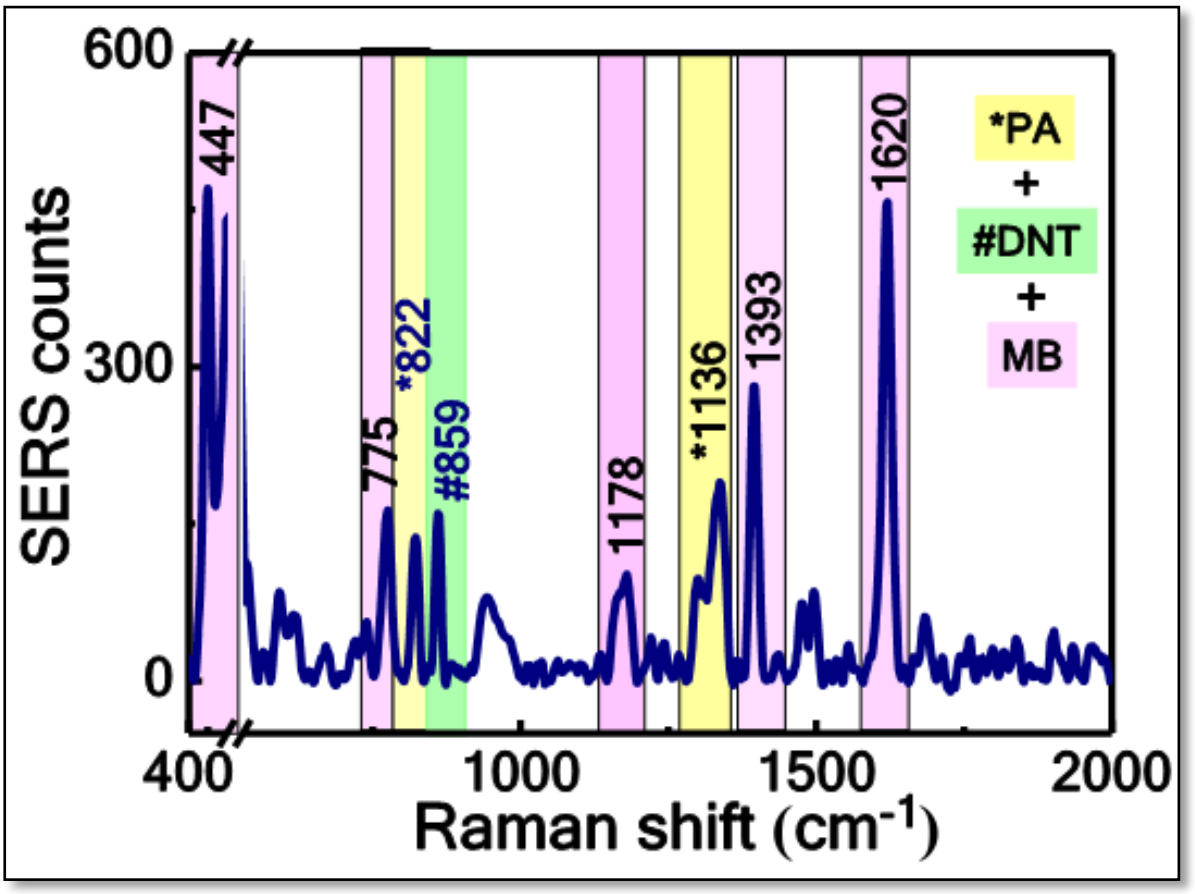

Figure 4.15 SERS spectra complex mixture PA (5 µM) +DNT (5 µM) +MB (5 nM), adsorbed on the Ag–Au NPs coated Si MSA substrate, fabricated at 30 µJ the major characteristic peaks of PA, DNT and MB are labeled with the yellow, green and pink, respectively

4.5 Comparison with a commercial rigid-SERS substrate

In an exercise to prove the usefulness and versatility fabricated rigid SERS substrate in this work was verified through the comparison studies with a readily available commercial Ag-based SERS substrate (SERSitive).[50] The photograph of the Ag NPs electrodeposited on the ITO substrate with a dimension of 5×4 mm^2 shown in figure 4.16(a). The morphology of the substrate examined with SEM illustrated in figure 4.16 (b).

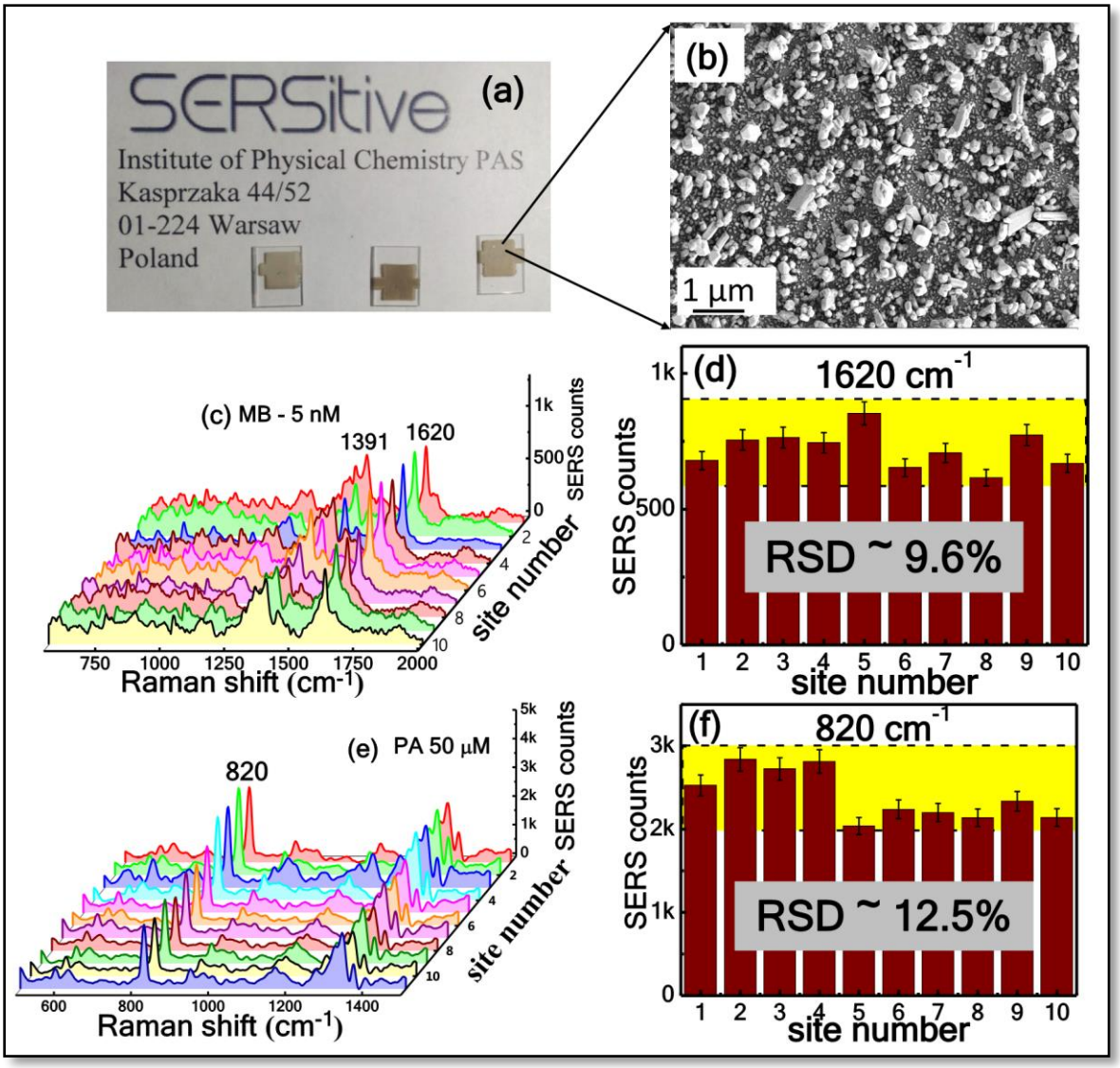

Figure 4.16 (a) Photograph of commercial Ag-based ITO substrates (b) SEM image of the substrate; SERS spectra and reproducibility with RSD histogram of (c) and (d) MB (5 nM) (e) and (f) PA (50 µM), respectively, using Ag-based commercial substrate from SERSitive[50].

Two probe molecules (i) MB (ii) PA was considered to verify the SERS performance of these substrates. Figure 4.16 (c) and (d) and (e) and (f) present the SERS spectra of MB (5 nM) and PA (50 µM). The obtained EFs were ~2.6×10^{7} and ~1.2×10^{4} for MB (1620 cm^{-1}) and PA (820 cm^{-1}), respectively. The observed Raman enhancement from Si MSA with the Ag-Au substrate was, at least, two orders of magnitude higher than that from a commercially available substrate. The intensity histogram representing the reproducibility of the substrate with RSD ~9.6% for MB and ~12.5% for PA, as shown in figures 4.16(e) and 4.16(f). Our substrate has demonstrated superior performance compared to the commercially available substrate by demonstrating EFs of two orders of magnitude higher than the latter towards explosive

detection. However, the commercially obtained SERS substrates were in transit for 3–4 weeks, and this possibly could have affected their performance. Thus, we firmly believe that the performance of hybrid SERS active substrates fabricated using femtosecond laser pulses is superior to the commercially available substrates.

4.6 Conclusions

- In summary, highly active SERS substrates that comprise of fs laser-generated Si MSA covered with Ag–Au alloy NPs fabricated with superior sensitivity, selectivity, and reproducibility for nitro-based explosives detection using a simple, portable spectrometer.
- The edges of the Si MSA facilitated the accommodation of a large number of Ag–Au NPs in the nanogaps and micro/nano-cavities, which could produce a large number of hot spots and resulting in considerable enhancements in the Raman signals.
- The fabrication of Si MSA was performed in air at different laser energies 10 -100 µJ. The Si MSA (fabricated at 30 µJ), which exhibited the highest enhancement for MB, was utilized to probe other explosives and their mixtures. A sensitivity of 10 pM for MB (~10^{10}; typically, acceptable value for the detection of single-molecule), 50 nM for PA (~10^{6}), and 1 µM for RDX (~10^{4}) was observed in their pure form. Moreover, the robustness of the substrate for multi-analyte detection was demonstrated through the detection of complex mixtures of explosives and dye molecules (PA + MB, DNT + MB, and PA + DNT).
- The RSD values of prominent mode intensities for all the molecules being less than 15% throughout the substrate establish the reproducibility of Si MSA.
- Furthermore, the detection of a tertiary complex mixture (MB + PA + DNT) confirmed the potential of these substrates for real-time sensing applications.

4.7 References

1. Doiron, B.; Mota, M.; Wells, M. P.; Bower, R.; Mihai, A.; Li, Y.; Cohen, L. F.; Alford, N. M.; Petrov, P. K.; Oulton, R. F., Quantifying Figures of Merit for Localized Surface Plasmon Resonance Applications: A Materials Survey. *ACS Photonics* **2019**, *6*, 240-259.
2. Jeon, T. Y.; Kim, D. J.; Park, S.-G.; Kim, S.-H.; Kim, D.-H., Nanostructured Plasmonic Substrates for Use as SERS Sensors. *Nano Convergence* **2016**, *3*, 18.
3. Liu, X.; Wu, D.; Chang, Q.; Zhou, J.; Zhang, Y.; Wang, Z., Grooved Nanoplate Assembly for Rapid Detection of Surface Enhanced Raman Scattering. *Nanoscale* **2017**, *9*, 15390-15396.
4. Jiang, T.; Song, J.; Zhang, W.; Wang, H.; Li, X.; Xia, R.; Zhu, L.; Xu, X., Au-Ag@Au Hollow Nanostructure with Enhanced Chemical Stability and Improved Photothermal Transduction Efficiency for Cancer Treatment. *ACS Appl. Mater. and Interf.* **2015**, *7*, 21985-21994.
5. Cao, J.; Sun, T.; Grattan, K. T. V., Gold Nanorod-Based Localized Surface Plasmon Resonance Biosensors: A Review. *Sens. Actuators, B* **2014**, *195*, 332-351.
6. Xu, J. Y.; Wang, J.; Kong, L. T.; Zheng, G. C.; Guo, Z.; Liu, J. H., SERS Detection of Explosive Agent by Macrocyclic Compound Functionalized Triangular Gold Nanoprisms. *J. Raman Spectros.* **2011**, *42*, 1728-1735.
7. Pellacani, P.; Torres-Costa, V.; Agulló-Rueda, F.; Vanna, R.; Morasso, C.; Manso Silván, M., Laser Writing of Nanostructured Silicon Arrays for the SERS Detection of Biomolecules with Inhibited Oxidation. *Colloids Surf., B* **2019**, *174*, 174-180.
8. Alamri, M.; Sakidja, R.; Goul, R.; Ghopry, S.; Wu, J. Z., Plasmonic Au Nanoparticles on 2d Mos2/Graphene Van Der Waals Heterostructures for High-Sensitivity Surface-Enhanced Raman Spectroscopy. *ACS Appl. Nano Mater.* **2019**, *2*, 1412-1420.
9. Tian, H.; Zhang, N.; Zhang, J.; Tong, L., Exploring Quantification in a Mixture Using Graphene-Based Surface-Enhanced Raman Spectroscopy. *Appl. Mater. Today* **2019**, *15*, 288-289.
10. Li, Y.; Dykes, J.; Chopra, N., Silicon Nanowire-Gold Nanoparticle Heterostructures for Surface-Enhanced Raman Spectroscopy. *Nano-Structures & Nano-Objects* **2016**, *7*, 12-22.
11. Huang, Z.; Geyer, N.; Werner, P.; De Boor, J.; Gösele, U., Metal-Assisted Chemical Etching of Silicon: A Review: In Memory of Prof. Ulrich Gösele. *Adv. Mater.* **2011**, *23*, 285-308.
12. Zhang, C.; Jiang, S. Z.; Yang, C.; Li, C. H.; Huo, Y. Y.; Liu, X. Y.; Liu, A. H.; Wei, Q.; Gao, S. S.; Gao, X. G., Gold@ Silver Bimetal Nanoparticles/Pyramidal Silicon 3d Substrate with High Reproducibility for High-Performance SERS. *Sci. Rep.* **2016**, *6*, 1-8
13. Wang, J.; Jia, Z.; Lv, C., Enhanced Raman Scattering in Porous Silicon Grating. *Opt. Express* **2018**, *26*, 6507-6518.
14. Redko, S.; Dolgiy, A.; Zhigulin, D.; Kholyavo, V.; Khinevich, N.; Zavatski, S.; Bandarenka, H. In *Fabrication and Simulation of Silver Nanostructures on Different Types of Porous Silicon for Surface Enhanced Raman Spectroscopy*, Physics and Simulation of Optoelectronic Devices XXVII, International Society for Optics and Photonics: **2019**, 109121O.
15. Novara, C.; Dalla Marta, S.; Virga, A.; Lamberti, A.; Angelini, A.; Chiadò, A.; Rivolo, P.; Geobaldo, F.; Sergo, V.; Bonifacio, A., SERS-Active Ag Nanoparticles on Porous Silicon and Pdms Substrates: A Comparative Study of Uniformity and Raman Efficiency. *J. Phys. Chem. C* **2016**, *120*, 16946-16953.

16. Lin, H.; Mock, J.; Smith, D.; Gao, T.; Sailor, M. J., Surface-Enhanced Raman Scattering from Silver-Plated Porous Silicon. *J. Phys. Chem. B* **2004**, *108*, 11654-11659.
17. Rao, G.; Jian, X.; Lv, W.; Zhu, G.; Xiong, J.; He, W., A Highly-Efficient Route to Three-Dimensional Nanoporous Copper Leaves with High Surface Enhanced Raman Scattering Properties. *Chem. Eng. J.* **2017**, *321*, 394-400.
18. Chang, S.; Ko, H.; Singamaneni, S.; Gunawidjaja, R.; Tsukruk, V. In *Nanoporous Substrate with Mixed Nanoclusters for Surface Enhanced Raman Scattering*, APS Meeting Abstracts, **2009**.
19. Restaino, S. M.; White, I. M., A Critical Review of Flexible and Porous SERS Sensors for Analytical Chemistry at the Point-of-Sample. *Anal. Chim. Acta* **2018**, *1060*, 17-29
20. Lin, C.-H.; Jiang, L.; Chai, Y.-H.; Xiao, H.; Chen, S.-J.; Tsai, H.-L., One-Step Fabrication of Nanostructures by Femtosecond Laser for Surface-Enhanced Raman Scattering. *Opt. Express* **2009**, *17*, 21581-21589.
21. Yang, J.; Li, J.; Du, Z.; Gong, Q.; Teng, J.; Hong, M., Laser Hybrid Micro/Nano-Structuring of Si Surfaces in Air and Its Applications for SERS Detection. *Sci. Rep.* **2014**, *4*, 6657.
22. Bharati, M. S. S.; Chandu, B.; Rao, S. V., Explosives Sensing Using Ag–Cu Alloy Nanoparticles Synthesized by Femtosecond Laser Ablation and Irradiation. *RSC Adv.* **2019**, *9*, 1517-1525.
23. Tang, L.; Li, S.; Han, F.; Liu, L.; Xu, L.; Ma, W.; Kuang, H.; Li, A.; Wang, L.; Xu, C., SERS-Active Au@ Ag Nanorod Dimers for Ultrasensitive Dopamine Detection. *Biosens. Bioelectron.* **2015**, *71*, 7-12.
24. Khaywah, M. Y.; Jradi, S.; Louarn, G.; Lacroute, Y.; Toufaily, J.; Hamieh, T.; Adam, P.-M., Ultrastable, Uniform, Reproducible, and Highly Sensitive Bimetallic Nanoparticles as Reliable Large Scale SERS Substrates. *J. Phys. Chem. C* **2015**, *119*, 26091-26100.
25. Podagatlapalli, G. K.; Hamad, S.; Rao, S. V., Trace-Level Detection of Secondary Explosives Using Hybrid Silver–Gold Nanoparticles and Nanostructures Achieved with Femtosecond Laser Ablation. *J. Phys. Chem. C* **2015**, *119*, 16972-16983.
26. Byram, C.; Soma, V. R., 2, 4-Dinitrotoluene Detected Using Portable Raman Spectrometer and Femtosecond Laser Fabricated Au–Ag Nanoparticles and Nanostructures. *Nano-Structures & Nano-Objects* **2017**, *12*, 121-129.
27. Ageev, E.; Potorochin, D.; Sachenko, D.; Odintsova, G., Generation of Web-Like Structures and Nanoparticles by Femtosecond Laser Ablation of Silicon Target in Ambient Air. *Optical and Quantum Electronics* **2017**, *49*, 40.
28. Bi, L.; Dong, J.; Xie, W.; Lu, W.; Tong, W.; Tao, L.; Qian, W., Bimetallic Gold–Silver Nanoplate Array as a Highly Active SERS Substrate for Detection of Streptavidin/Biotin Assemblies. *Anal. Chim. Acta* **2013**, *805*, 95-100.
29. Jeschke, H. O.; Garcia, M. E.; Lenzner, M.; Bonse, J.; Krüger, J.; Kautek, W., Laser Ablation Thresholds of Silicon for Different Pulse Durations: Theory and Experiment. *Appl. Surf. Sci.* **2002**, *197*, 839-844.
30. Stoian, R.; Rosenfeld, A.; Hertel, I.; Bulgakova, N.; Campbell, E., Comment on "Coulomb Explosion in Femtosecond Laser Ablation of Si (111)"[Appl. Phys. Lett. 82, 4190 (2003)]. *Appl. Phys. Lett.* **2004**, *85*, 694-695.
31. Zhang, N.; Zhu, X.; Yang, J.; Wang, X.; Wang, M., Time-Resolved Shadowgraphs of Material Ejection in Intense Femtosecond Laser Ablation of Aluminum. *Phys. Rev. Lett.* **2007**, *99*, 167602.
32. Wu, Z.; Zhang, N.; Wang, M.; Zhu, X., Femtosecond Laser Ablation of Silicon in Air and Vacuum. *Chin. Opt. Lett.* **2011**, *9*, 093201.

33. Byram, C.; Moram, S. S. B.; Soma, V. R., Surface-Enhanced Raman Scattering Studies of Gold-Coated Ripple-Like Nanostructures on Iron Substrate Achieved by Femtosecond Laser Irradiation in Water. *J. Raman Spectros.* **2019**, *50*, 1103-1113.
34. Lee, S.; Choi, J.; Chen, L.; Park, B.; Kyong, J. B.; Seong, G. H.; Choo, J.; Lee, Y.; Shin, K.-H.; Lee, E. K., Fast and Sensitive Trace Analysis of Malachite Green Using a Surface-Enhanced Raman Microfluidic Sensor. *Anal. Chim. Acta* **2007**, *590*, 139-144.
35. Ghosh, M.; Wang, L.; Asher, S. A., Deep-Ultraviolet Resonance Raman Excitation Profiles of Nh4no3, Petn, Tnt, Hmx, and Rdx. *Appl. Spectros.* **2012**, *66*, 1013-1021.
36. Wali, L. A.; Hasan, K. K.; Alwan, A. M., Rapid and Highly Efficient Detection of Ultra-Low Concentration of Penicillin G by Gold Nanoparticles/Porous Silicon SERS Active Substrate. *Spectrochimica Acta Part A: Molecular and Biomolecular Spectroscopy* **2019**, *206*, 31-36.
37. Jiang, S.; Guo, J.; Zhang, C.; Li, C.; Wang, M.; Li, Z.; Gao, S.; Chen, P.; Si, H.; Xu, S., A Sensitive, Uniform, Reproducible and Stable SERS Substrate Has Been Presented Based on Mos2@Ag Nanoparticles@Pyramidal Silicon. *RSC Adv.* **2017**, *7*, 5764-5773.
38. Tan, C. L.; Lee, S. K.; Lee, Y. T., Bi-SERS Sensing and Enhancement by Au-Ag Bimetallic Non-Alloyed Nanoparticles on Amorphous and Crystalline Silicon Substrate. *Opt. Express* **2015**, *23*, 6254-6263.
39. Li, Y.; Dykes, J.; Gilliam, T.; Chopra, N., A New Heterostructured SERS Substrate: Free-Standing Silicon Nanowires Decorated with Graphene-Encapsulated Gold Nanoparticles. *Nanoscale* **2017**, *9*, 5263-5272.
40. MacKenzie, M.; Chi, H.; Varma, M.; Pal, P.; Kar, A.; Paterson, L., Femtosecond Laser Fabrication of Silver Nanostructures on Glass for Surface Enhanced Raman Spectroscopy. *Sci. Rep.* **2019**, *9*, 17058.
41. Hamad, S.; Bharati Moram, S. S.; Yendeti, B.; Podagatlapalli, G. K.; Nageswara Rao, S.; Pathak, A. P.; Mohiddon, M. A.; Soma, V. R., Femtosecond Laser-Induced, Nanoparticle-Embedded Periodic Surface Structures on Crystalline Silicon for Reproducible and Multi-Utility SERS Platforms. *ACS Omega* **2018**, *3*, 18420-18432.
42. Shaik, U. P.; Hamad, S.; Ahamad Mohiddon, M.; Soma, V. R.; Ghanashyam Krishna, M., Morphologically Manipulated Ag/ZnO Nanostructures as Surface Enhanced Raman Scattering Probes for Explosives Detection. *J. Appl. Phys.* **2016**, *119*, 093103.
43. Vendamani, V.; Nageswara Rao, S.; Venugopal Rao, S.; Kanjilal, D.; Pathak, A., Three-Dimensional Hybrid Silicon Nanostructures for Surface Enhanced Raman Spectroscopy Based Molecular Detection. *J. Appl. Phys.* **2018**, *123*, 014301.
44. Laserna, J. J.; Campiglia, A. D.; Winefordner, J. D., Mixture Analysis and Quantitative Determination of Nitrogen-Containing Organic Molecules by Surface-Enhanced Raman Spectrometry. *Anal. Chem.* **1989**, *61*, 1697-1701.
45. Kudelski, A., Raman Studies of Rhodamine 6g and Crystal Violet Sub-Monolayers on Electrochemically Roughened Silver Substrates: Do Dye Molecules Adsorb Preferentially on Highly SERS-Active Sites? *Chem. Phys. Lett.* **2005**, *414*, 271-275.
46. González-Vidal, J.; Perez-Pueyo, R.; Soneira, M.; Ruiz-Moreno, S., Automatic Identification System of Raman Spectra in Binary Mixtures of Pigments. *J. Raman Spectros.* **2012**, *43*, 1707-1712.
47. Zhang, Y.; Yang, P.; Habeeb Muhammed, M. A.; Alsaiari, S. K.; Moosa, B.; Almalik, A.; Kumar, A.; Ringe, E.; Khashab, N. M., Tunable and Linker Free Nanogaps in Core–Shell Plasmonic Nanorods for Selective and Quantitative Detection of Circulating Tumor Cells by SERS. *ACS Appl. Mater. & Interf.* **2017**, *9*, 37597-37605.

48. Wei, W. Y.; White, I. M., Chromatographic Separation and Detection of Target Analytes from Complex Samples Using Inkjet Printed SERS Substrates. *Analyst* **2013**, *138*, 3679-3686.
49. Zrimsek, A. B.; Wong, N. L.; Van Duyne, R. P., Single Molecule Surface-Enhanced Raman Spectroscopy: A Critical Analysis of the Bianalyte Versus Isotopologue Proof. *J. Phys. Chem. C* **2016**, *120*, 5133-5142.
50. https://www.sersitive.eu/.

Intentional bank page

Chapter 5

Flexible SERS substrates

5A. Aggregated Ag/Au NPs loaded filter paper

5B. Anisotropic Au NPs loaded filter Paper

5C. Electrospinning-Nanofibers with Au NPs

5A. Aggregated Ag/Au NPs loaded filter paper

Abstract

The first section of this chapter discusses the synthesis of flexible filter paper (FP) SERS substrates achieved by loading salt-induced aggregated Ag/Au nanoparticles (NPs). The aggregation effect was investigated by adding different concentrations of NaCl (1 mM to 1 M) to the prior prepared Ag and Au NPs. These Ag/Au NPs were prepared using femtosecond (fs) laser [~50 fs, 800 nm, 1 kHz] ablation in liquids technique. Subsequently, the flexible SERS substrates were prepared by a simple soaking method. The fabricated colloidal Ag/Au NPs were characterized by UV−visible absorption and high-resolution transmission electron microscopic techniques. The morphologies of the FP substrates loaded with aggregated Ag/Au NPs were investigated using field-emission scanning electron microscopy. The optimization in the aggregation of NPs was studied by performing the SERS measurements for a dye molecule (MB) with the FP substrates loaded with aggregated Ag/Au NPs at different NaCl concentrations. Further, an optimized FP substrate was used to detect multiple explosive molecules such as PA (5 μM), DNT (1 μM), and NTO (10 μM) along with a dye molecule (MB, 5 nM). Moreover, flexible FP substrates reproducibility and stability studies were are also performed.

The work presented in this chapter has been published as

M. S. S. Bharati, C. Byram, S.N. Shibu, B.M. Chilukamarri, V.R. Soma, Ag/Au nanoparticle loaded paper-based versatile surface-enhanced Raman spectroscopy substrates for multiple explosives detection, ACS Omega. **3** (2018) 8190-8201.

5A.1 Introduction

Numerous methods have been employed to fabricate SERS platforms such as atomic layer deposition, focused ion-beam lithography, electron beam lithography, and ultrafast pulsed laser ablation for producing a variety of patterned nanostructures.[1-5] These experimental techniques are expensive and also complex procedures need to be followed in the preparation of such SERS substrates. In practical applications, the prepared traditional rigid (based on Silicon, glass, and metal) substrates have some difficulties while collecting the sample and, additionally, are relatively expensive. Ideally, SERS substrates should not only have a large number of hotspots, sensitivity, and reproducibility but also should be versatile in many other features such as cost, flexibility, and scalability. The main task for the SERS community has been to develop the substrates with low cost, and easy to handle, as well as flexible for sample collection.[6-8] A common filter paper (FP) loaded with metal NPs serves as a versatile SERS substrate and such studies have attracted attention in various applications such as cancer screening, solar cell, food safety, sensing devices, paper electronics (to design a distinct electronic component such as a diode, transistor, antenna, superconductors, etc.).[9-10] The great attributes of cellulose FP are sample storage capability, thinness of cellulose fibers, porosity, disposable nature, lightweight, handy, flexible (ex. they can be rolled or folded), and renewability. Diverse methods are available for the fabrication of low-cost and straightforward paper-based SERS substrates such as (a) inkjet and wax printing of NPs (b) soaking of FP in already prepared NPs (c) soaking of FP in metal salts (in-situ synthesis).[11-17] These techniques, however, require proper viscosity and surface tension of the NPs to avoid blockage in the nozzle. Mu et al.[18] recently demonstrated superior performance in the case of flexible paper SERS substrate compared to the rigid glass substrate with Au NPs in the detection of R6G while using a simple drop-costing method. Further, the comparison studies were performed on three different types of papers (printing papers, filter papers, and envelope papers) and they concluded that the best choice 3D SERS substrate base as filter papers. In this chapter, a filter paper-based SERS platform was developed and its efficacy was improved by following the two routes (1) salt-induced aggregation and (2) paper-induced aggregation.[19] The metal NPs tend to aggregate in the presence of ionic liquids under specific chemical conditions, termed as salt-induced aggregation. The transition of metal NPs in colloidal solution to the 3D network of cellulose fibers on FP enables the

aggregation of NPs, called paper-induced aggregation. During the Raman measurements, it yields high field strength at the junctions of metal NPs which are many orders of magnitude higher than the fields generated at the surface of individual NP.[20-21] This could be attributed to the coupling of their transition dipoles, i.e., each particle enhanced field at the surfaces interferes coherently at the junction between the firmly attached NPs. Numerous reports have shown a significant improvement in the SERS signals from deliberately aggregated Au and Ag NPs. Recently Xu et al.[22] noticed the enhancement field depends on the distance between the Ag NPs from 5.5 nm to 1 nm and demonstrated single-molecule detection of hemoglobin with EFs of $\sim 10^{10}$ at 1 nm separation. Kneipp et al.[23] found an increase in EF by 7−8 orders of magnitude with NaCl (10^{-2} M)-activated Ag colloidal aggregates possessing sizes in the range of 15-60 nm for the detection of CV. Theoretical simulations of electric field contours of spherical NPs aggregates separated by 2 nm also proved the enhancement of field in the inter-particle gaps of (hot-spots) closely spaced spherical NPs with 632 nm excitation.[24]

In the present case, Ag/Au NPs were fabricated through the LAL technique, which has the advantages of fast, easy, and green approach,[25] bereft of any long reaction times and multi-step chemical processes.[26] Subsequently, the salt-induced aggregated NPs were achieved by mixing the pure Ag/Au NPs in various concentrations of NaCl. Flexible SERS substrates were prepared by soaking the FP in Ag/Au NP aggregates, which are self-assembled in solution by the addition of the NaCl molecule. The aggregation effects of NPs significantly improved the number of hotspots (interstitial gaps to entrap the analyte molecule which enhance the SERS signal).[27] These Ag/Au embedded flexible SERS substrates were enabled to detect the MB-5nM and explosives such as PA-5 μM, DNT-1 μM, and NTO-10 μM with typical EF of $\sim 10^4$ using a portable Raman spectrometer.

5A.2 Experimental details

5A.2.1 Synthesis of Ag and Au NPs

Pure and cleaned Ag and Au targets were ablated with a regenerative fs (Ti: sapphire) amplifier (~50 fs, 800 nm, 1 kHz) with pulse energy ~500 μJ. The laser pulses were focused through a 100 mm plano-convex lens onto the target surface. The sample was placed in a glass beaker with 10 mL of distilled water. The beaker was placed on a

computer-controlled translational stage and scanned with 100 μm/s speed along with X and Y directions, to avoid repeated ablation at a single spot.[26, 28-32] Schematic NPs synthesis and FP substrate preparation are shown in figure 5A.1.

5A.2.2 Synthesis of Ag/Au aggregated NPs

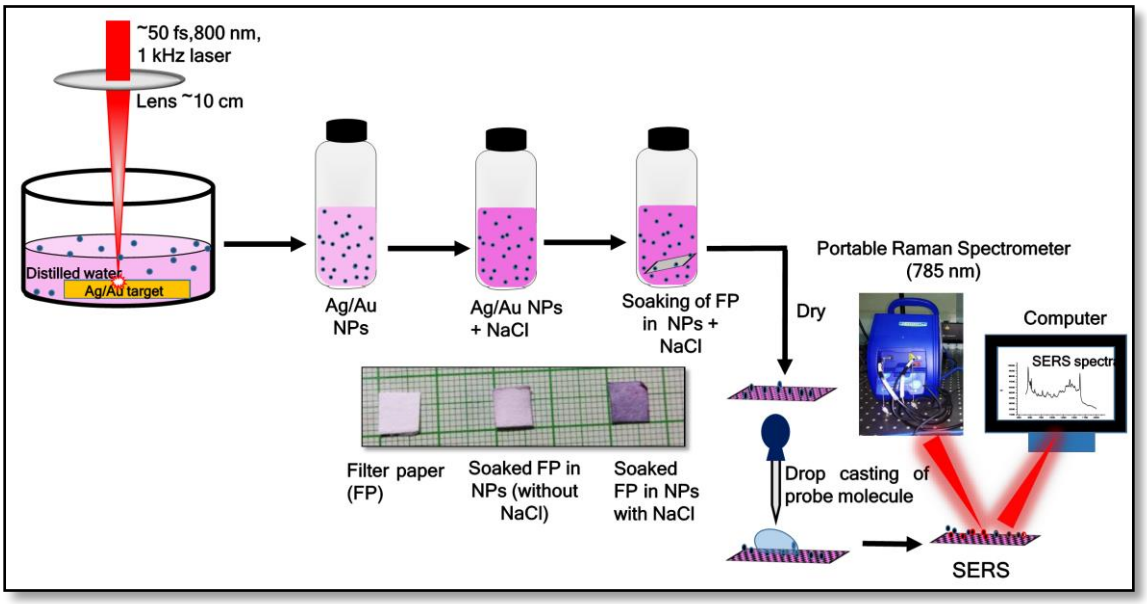

Figure 5A.1 Schematic representation of SERS studies using paper-based SERS substrates (Ag/Au aggregated NP-decorated filter paper). Inset shows a photograph of prepared Au NP-decorated filter papers.

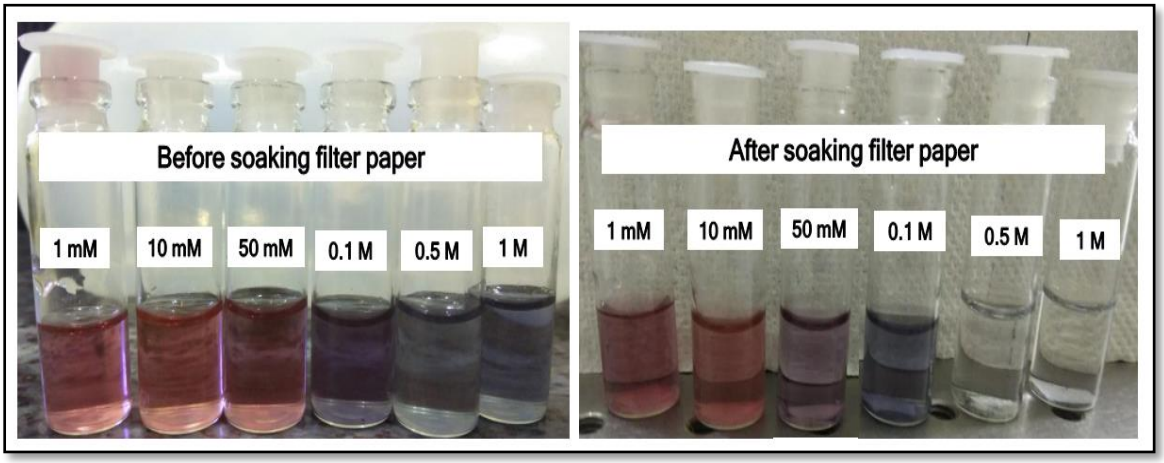

Figure 5A.2 Photograph of Au NPs in different concentrations of NaCl [before (left side) and after (right side) soaking of FP]

Alkali halides (NaF, NaCl, NaBr, NaI, KCl, KBr, etc.), $NaNO_3$, and K_2SO_4 have been suggested to boost the aggregation in colloidal NPs.[33 34-35] In this work simple NaCl was used as an aggregation agent. In the present case, various concentrations of NaCl ranging

from 1 mM to 1M (1 mM, 10 mM, 50 mM, 0.1 M, 0.5 M, and 1 M) was mixed with 1:1 ratio of pure Ag/Au NPs. After the addition of NaCl we noticed a change in the color of NPs [Figure 5A. 2 (left) shows colloidal Au NPs before FP soaking].

5A.2.3 SERS Substrates Preparation

Filter paper (FP) was cut into small pieces (1 cm^2) and then soaked for ~30 minutes in the prepared Ag/Au NPs colloidal solution. The integration of these NPs with the FP was obvious from the color of FP+NPs, which means they have got transferred to the FP. The color of the colloidal NPs [Figure 5A.2 (right) shows colloidal Au NPs after soaking FP] and the color of the soaked FP loaded with Ag/Au NPs at different concentrations of NaCl was also changed. The photographs obtained using a digital camera are shown in figure 5A.3. The loading of NPs on to the FP was different at different concentrations, i.e., at higher concentrations of NaCl; the loading of NPs was lower because of over aggregation. Schmucker et al.[36], from their detailed studies, suggested that the NPs immobilized on the paper remain stable under various complex environmental conditions. The soaked FP was cut into four strips of 2.5 mm^2 size. Subsequently, 10 µL of the volume of the probe molecule was pipetted on to the flexible FP SERS substrate. SERS measurements were performed on these substrates after the probe molecule was dried.

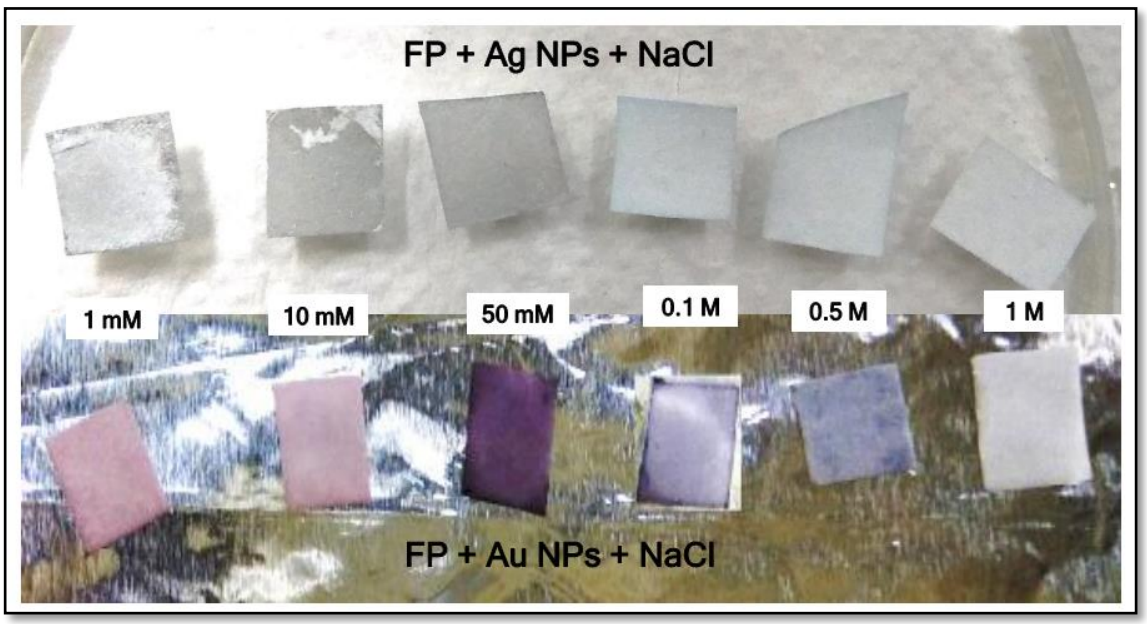

Figure 5A.3 The coloration of soaked FP in aggregated Ag/Au NPs in different concentrations of NaCl at 1, 10, 50, 100, 500 to 1000 mM (left to right).

5A.3 Characterization

5A.3.1 UV-Visible absorption studies

Figures 5A.4(a) and 5A.4(b) illustrate the absorption spectra of Ag and Au colloidal solution mixed with NaCl at different concentrations, respectively. The SPR position was located at ~404 nm and ~520 nm for pure Ag NPs and Au NPs, respectively. The decrease in absorption, broadening, and redshift in the plasmon band (~512 nm) was noticed with the addition of NaCl solution, possibly because of the aggregation effects. The redshift is clearly represented in the inset of figure 5A.4(a).

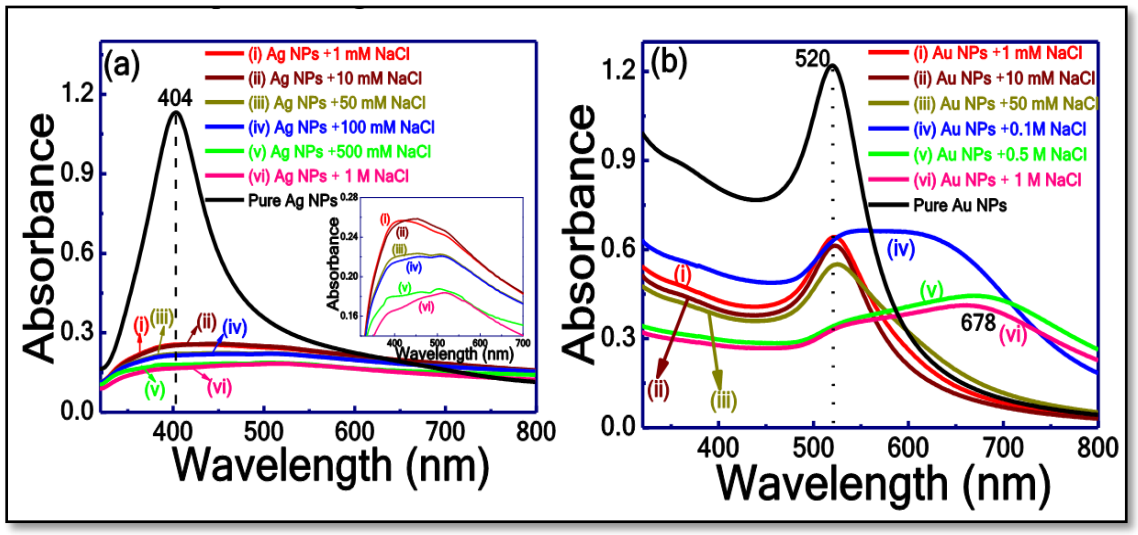

Figure 5A.4 UV−visible absorption spectra of non-aggregated and aggregated spherical (a) Ag NPs (b) Au NPs with different NaCl concentrations.

In the case of pure Au NPs with different concentrations of NaCl (up to 50 mM), a small redshift and a slight broadening in the SPR peaks were observed which could be attributed to the formation of the small aggregates in Au colloidal NPs. However, at higher NaCl concentrations (from 100 mM and above), a redshift (SPR peak near 678 nm) and more broadening were observed. The possible reason for this is the replacement of smaller aggregates into larger aggregates at higher concentrations. The shift in the plasmon peak position and broadening of the SPR peak was noticed because of the surrounding ionic medium (NaCl) and the aggregation effect. The obtained results from this study matched with the investigations of Mehrdel and co-workers.[37] They reported theoretical and experimental investigations on 10 nm size Au NPs in different volume fractions (5, 10, 20, 25, and 30%) of NaCl (0.01 M -0.1 M). And observed the broadening of SPR peak and

an increase in the FWHM of absorption spectra with increasing NaCl concentration from 0.01 M to 1M. This could be because of "chemical interface damping" and surface plasmon coupling.[38-40] The addition of salt into the colloidal solution allows the interaction between the NPs and decreases the energy barrier, subsequently causing aggregation. The change in the color of the colloidal solution is also evidence of the tuning of the SPR peak to redshift,[41] depicted in figure 5A.2.

5A.3.2 TEM Data Analysis

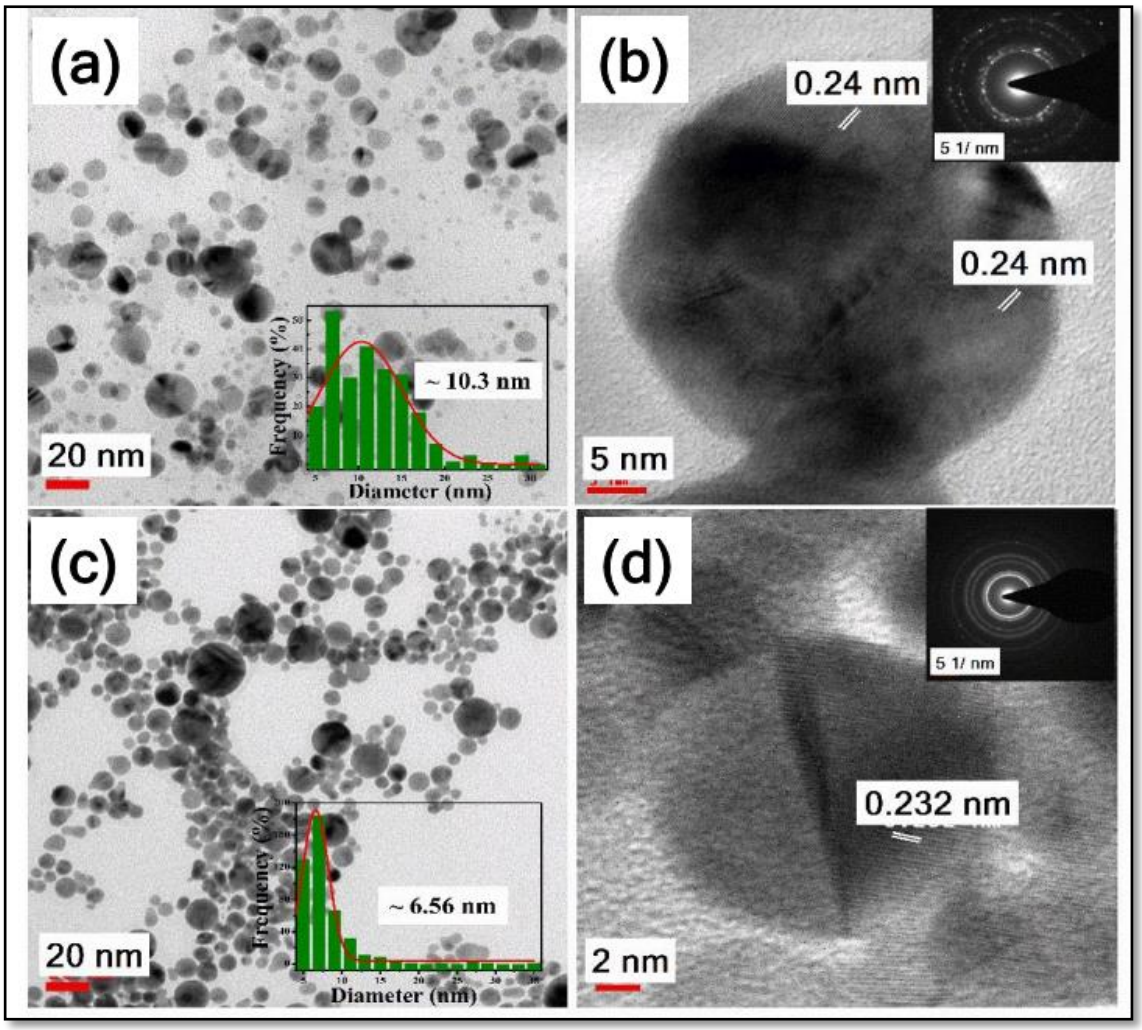

Figure 5A.5 TEM and HRTEM images of (a and b) Ag NPs and (c and d) Au NPs. Inset of (a, c) and (b, d) represents their size distribution and SAED patterns, respectively.

The morphology and sizes of the NPs were investigated using the TEM data analysis. The shapes of Ag and Au NPs were almost spherical, data of which is shown in figure 5A.5.

From the size distribution histogram data, the obtained mean sizes were ~10.3 nm and~ 6.5 nm for Ag and Au NPs, respectively, and the data is shown in insets of figures 5A.5(a) and 5A.5(c). The inter-planar spacing (d_{111}) obtained through the HRTEM images was 0.24 nm and 0.232 nm for Ag and Au NPs, respectively, which are illustrated in figures 5A.5(b) and 5A.5(d). The polycrystalline nature of synthesized Ag/Au NPs was revealed from the SAED patterns, shown as insets of figures 5A.5(b) and 5A.5(d). The aggregation of Ag and Au NPs after the addition of NaCl at 50 mM was also confirmed from the TEM images depicted in figures 5A.6(a) and 5A.6(b), respectively

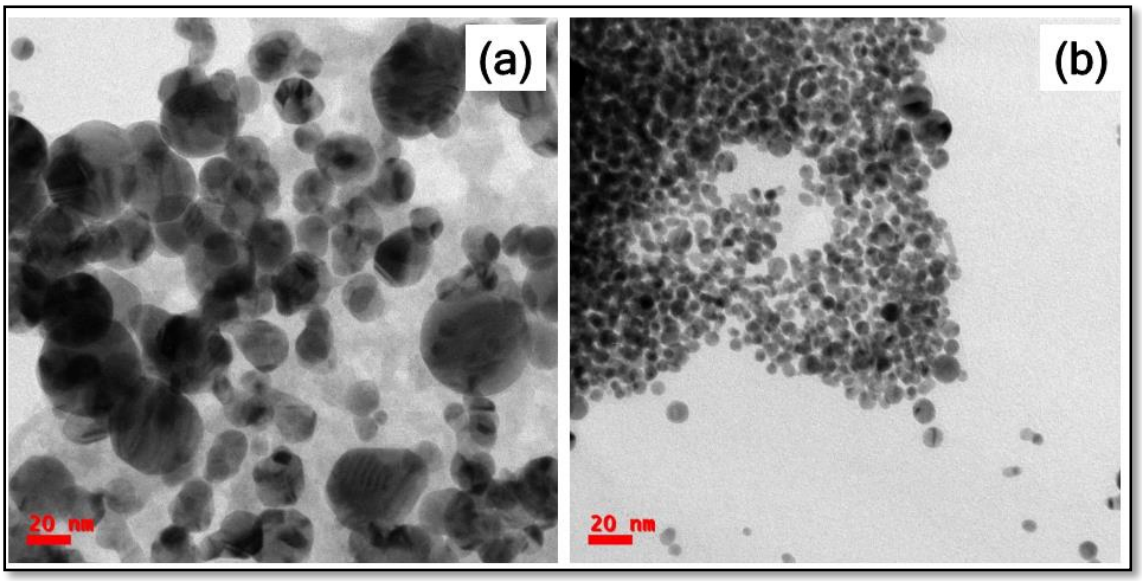

Figure 5A.6 TEM images of (a) Ag NPs and (b) Au NPs mixed with NaCl solution at a concentration of 50 mM.

5A.3.3 FESEM Data Analysis

To facilitate the lower magnification FESEM images, a thin conductive layer of gold was sputtered on the FP because of the non-conductive nature of FP. Additionally, to reveal the interweaved cellulose fibers of FP, the lower and higher magnification FESEM images of a bare FP without NPs were also recorded, and data is presented in figures 5A.7(a) and 5A.7(b), respectively. Further, the FP loaded with Ag and Au NPs without NaCl, FESEM images are provided in figures 5A.8(a) and 5A.8(b), respectively. A few NPs aggregates on the surface of cellouse fibers were observed because of paper induced aggregation.

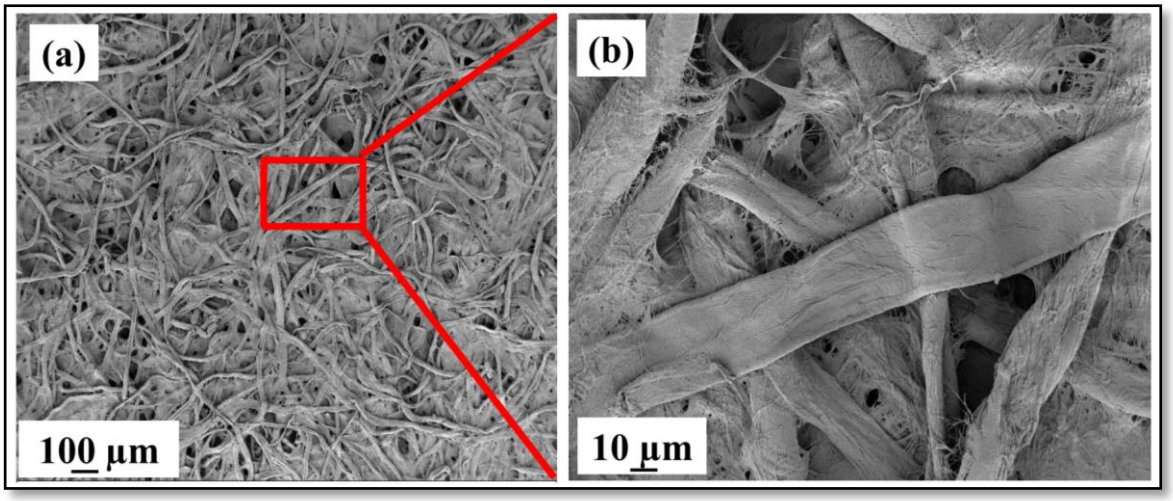

Figure 5A.7 FESEM image of bare FP at (a) lower and (b) higher magnification

.

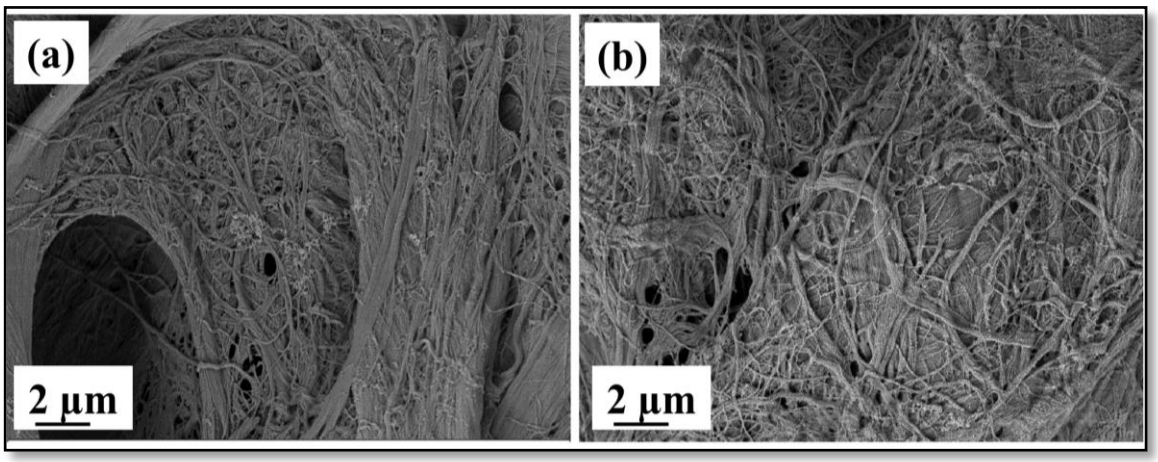

Figure 5A.8 FESEM image of FP soaked in (a) Ag and (b) Au NPs (without NaCl).

The FPs embedded with aggregated Ag NPs at different concentrations of NaCl (from 1 mM to 1 M) are illustrated in figures 5A.9 (a)− 5A.9(f) and 5A.10(a)− 5A.10(f) at lower and higher magnification images, respectively. Similarly, lower and higher magnification images of FPs loaded with aggregated Au NPs (concentrations ranging from 1 mM to 1000 mM) are shown in figures 5A.11 and 5A.12 from (a)−(f), respectively. In the case of FP loaded with Ag NPs at very lower concentrations of NaCl (1 and 10 mM), fairly few aggregates were noticed and were found to be distributed on the fibers of FP. At higher concentrations of NaCl (500 mM and 1 M), a large number of NP aggregates were observed because of an excessive amount of NaCl. The excess aggregation of NPs may limit the number of hotspots or help in forming the precipitate on the cellulose fibers, which may also inhibit the formation of hotspots. Therefore, a higher concentration of NaCl solution will induce a significant impact on an aggregation of Ag/Au NPs and form

clusters on the fibers of FP. The higher magnification images revealing the distribution of aggregated Ag/Au NPs on the paper substrates could be because of the salt-induced aggregation in addition to the paper-induced aggregation. From the higher magnification images it is evident that the distribution of NPs and over-precipitate of aggregated NPs on the FP fibers.

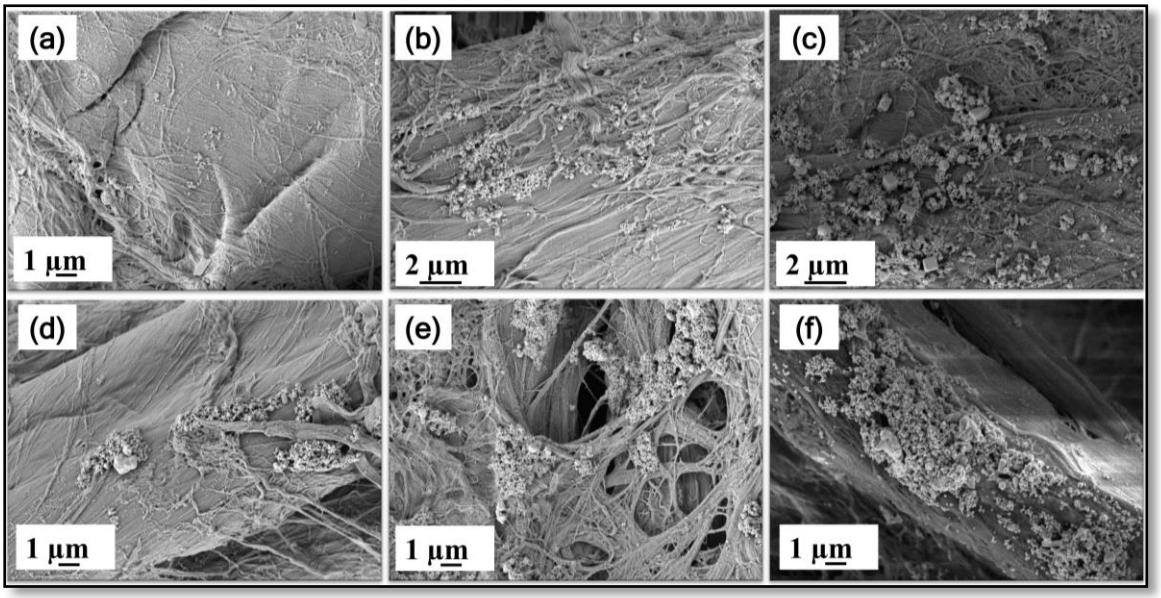

Figure 5A.9 Lower magnification FESEM images of FP loaded with aggregated Ag NPs at different concentrations of NaCl: (a) 1 mM, (b) 10 mM, (c) 50 mM, (d) 0.1 M, (e) 0.5 M, and (f) 1 M with the same magnification 10KX.

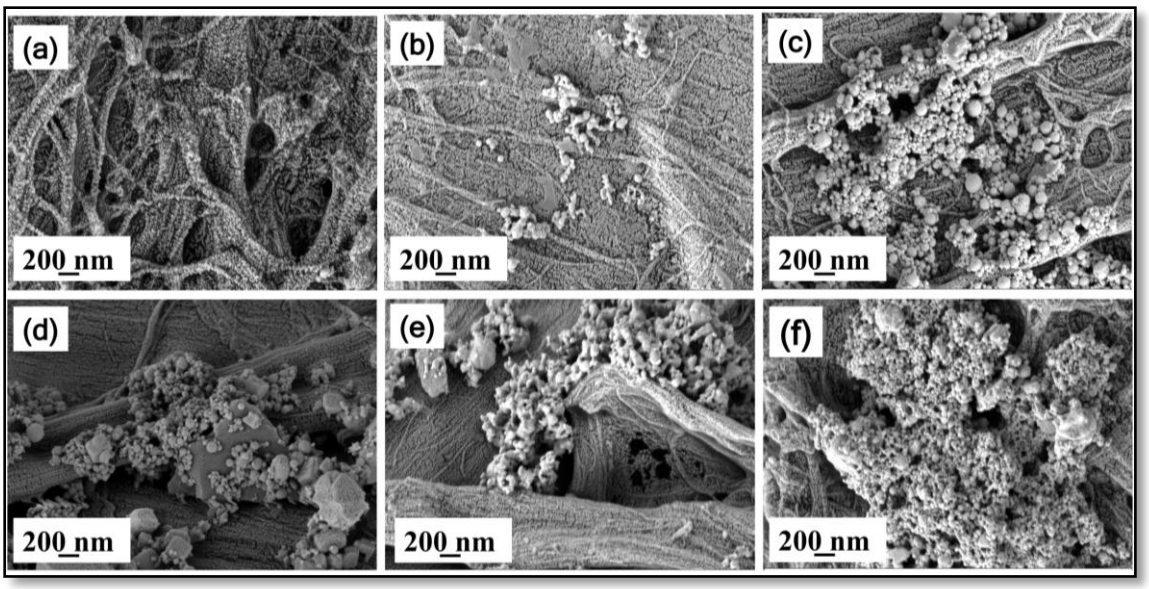

Figure 5A.10 Higher magnification FESEM images of FP loaded with aggregated Ag NPs at different concentration of NaCl (a) 1 mM (b) 10 mM (c) 50 mM (d) 0.1 M (e) 0.5 M (f) 1 M with same magnification of 50 KX.

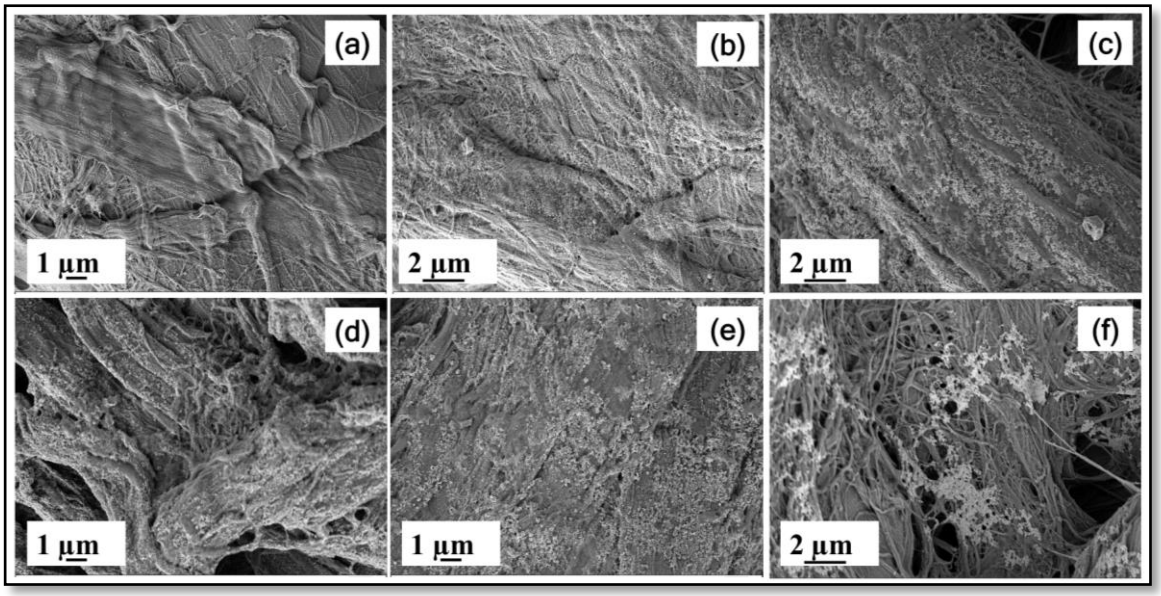

Figure 5A.11 Lower magnification FESEM images of FP loaded with aggregated Au NPs with different concentration of NaCl (a)1 mM (b)10 mM (c) 50 mM (d) 0.1 M (e) 0.5 M (f) 1 M with the same magnification 10KX.

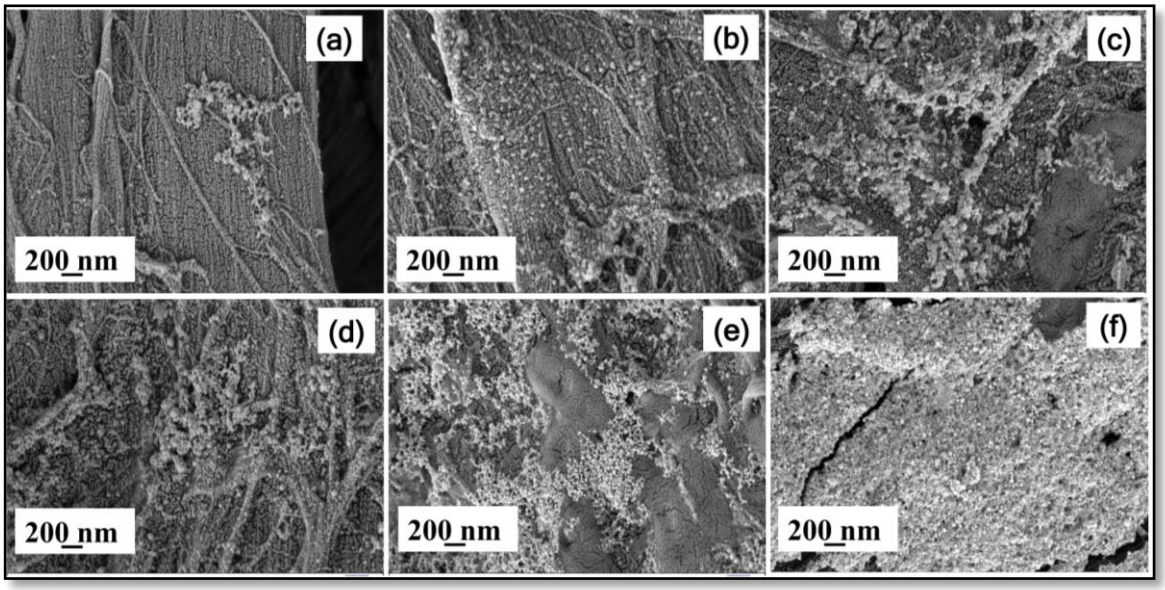

Figure 5A.12 Higher magnification FESEM images of FP loaded with aggregated Au NPs with different concentration of NaCl (a) 1 mM (b) 10 mM (c) 50 mM (d) 0.1 M (e) 0.5 M (f) 1 M with same magnification of 50 KX.

The weight present of Ag and other elements was further examined with the FESEM-EDS spectrum. Noticed a ~80% weight percentage of Ag and low % of Na and Cl on the FP surface (presented in figure 5.13). And also the key elements of filter papers such as carbon (C) and oxygen (O) are also observed.

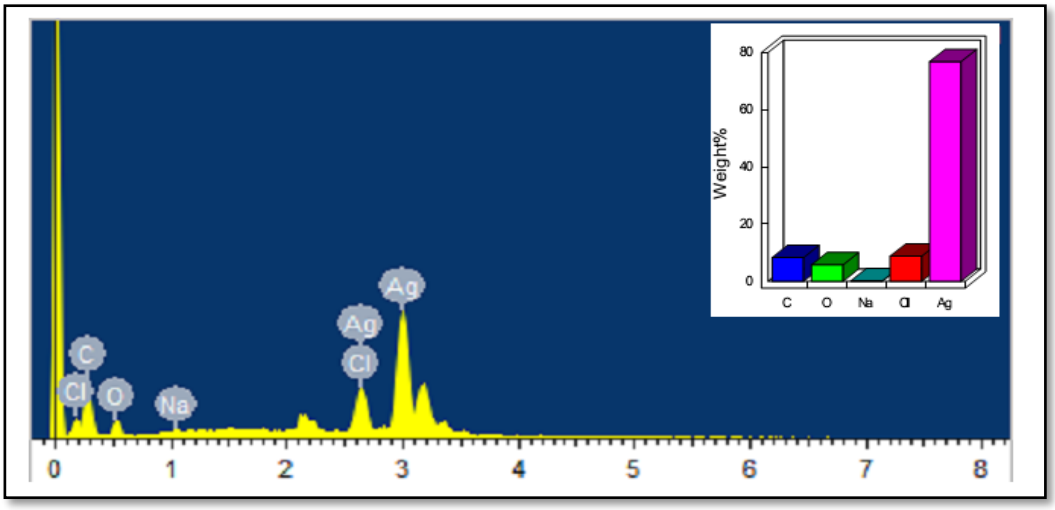

Figure 5A.13 EDS data represent the composition of the elements on the sensing region of FP loaded with Ag NPs at 50 mM NaCl; inset shows the weight % of elements.

5A.4 SERS studies

5A.4.1 Salt Aggregation Effect on SERS

Hot spots play a vital role in the enhancement of SERS signals; the aggregation of NPs leads to the generation of more hotspots.[19, 42-43] Jana et al.[35] have proposed that the SERS signals will be affected depending on the salt-induced particle aggregation. They suggested three reasons: (a) an increase in the EM field at the junction between the particles (b) chemical enhancement also possibly contributes to the enhancement and (c) absorption/reorientation of the analyte was likely because of the induced anion. Initially, the SERS spectra of MB were collected in the presence of NaCl. Diverse SERS substrates were studied to understand the aggregation effect: (i) FP soaked in aggregated Ag/Au NPs solution (with NaCl) and (ii) pure colloidal NPs (without NaCl). The photo of soaked FP with and without NaCl is mentioned in the schematic (inset of figure 5A.1). The color of aggregated NPs (mixed with NaCl) loaded on FP was much darker than that of the pure NPs (figure 5A.1) indicating that NaCl has dramatically improved the loading of NPs on the FP. The aggregation of metal NPs was influenced by environmental parameters (pH and ionic strength) along with external factors such as light and heat. The SERS spectra of MB with and without the addition of NaCl are illustrated in figure 5A.14. The NPs were immobilized on the scaffold porous and fibrous surface of FP leading to SERS signal without a salt solution. Moreover, the presence of NaCl induced the aggregation of NPs

rendering a narrow inter-particle gap of adjacent NPs, which possibly cooperated with plasmons leading to an improved SERS signal. Nobel metal NP aggregates on FP support a large number of plasmonic hotspots within the wide range of hotspots, which yielded the highly enhanced SERS signals. The increment in the Raman signal observed was nearly three and two times from the salt-induced aggregation of the plasmonic Ag and Au NPs, respectively (Ag: 2451, Au: 889) than that of the paper-induced aggregation of Ag and Au NPs (595) for the MB-1620 cm^{-1} mode. The strongest SERS signals were observed in the case of FP loaded with aggregated Ag NPs compared to Au NPs and this could be attributed to strong plasmonic effect offered by the Ag NPs.

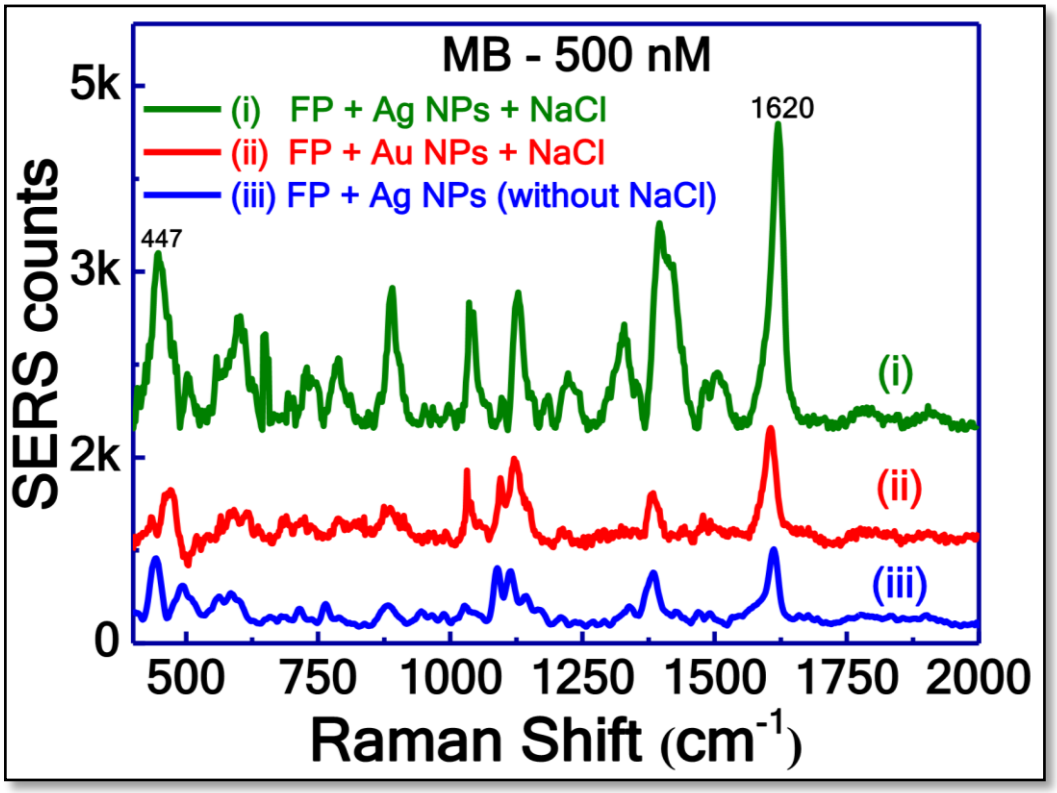

Figure 5A.14 SERS spectra of MB-500 nM collected from FP loaded with Ag and Au NPs with and without NaCl.

5A.4.2 Optimization of SERS substrate with NaCl concentration

To optimize the NaCl concentration, the achieved SERS substrates with Ag/Au NPs mixed with various concentrations of NaCl solution were thoroughly investigated with MB as a probe molecule. Initially, FP targets embedded with aggregated Ag NPs prepared using multiple concentrations of NaCl (1 mM, 10 mM, 50 mM, 100 mM, 500 mM, and 1 M) were evaluated by collecting the SERS signals of MB (5 μM) and the spectra are presented

in figure 5A.15(a). It is well-established fact that the intensity of the SERS signal is affected by the plasmonic coupling of the metal inter-particle distance and also depends on the concentration of NaCl. While increasing the NaCl concentration from 1 mM to 1 M range, the lowest EF (~1.9×10^4) was observed at 1 mM NaCl. This was expected because the NP aggregation is the least at this concentration. We expected more hotspots with increasing NaCl concentration, but interestingly, the maximum EF (~4.3×10^5) observed for 50 mM NaCl, an intermediate state of aggregation. The decrease in the EF to ~7×10^3 when the NaCl concentration increased from 50 mM to 1 M might be because of the excessive aggregation of NPs. The over-aggregated Ag NPs would have affected the homogeneity of the substrate and possibly could have played a crucial role in the resulting of inferior SERS signal. Furthermore, over-aggregation probably decreased the number of SERS-active hotspots. Figure 5A.15(b) presents the estimated EFs for the characteristic mode of MB (1620 cm^{-1}) with varying NaCl concentrations. However, the SEM images of FP loaded with Ag/Au NPs at NaCl concentration of 50 mM demonstrated a uniform distribution of a small cluster of NPs on the cellulose fibers. These clusters of NPs produce the more hotspots and gives maximum SERS signal.

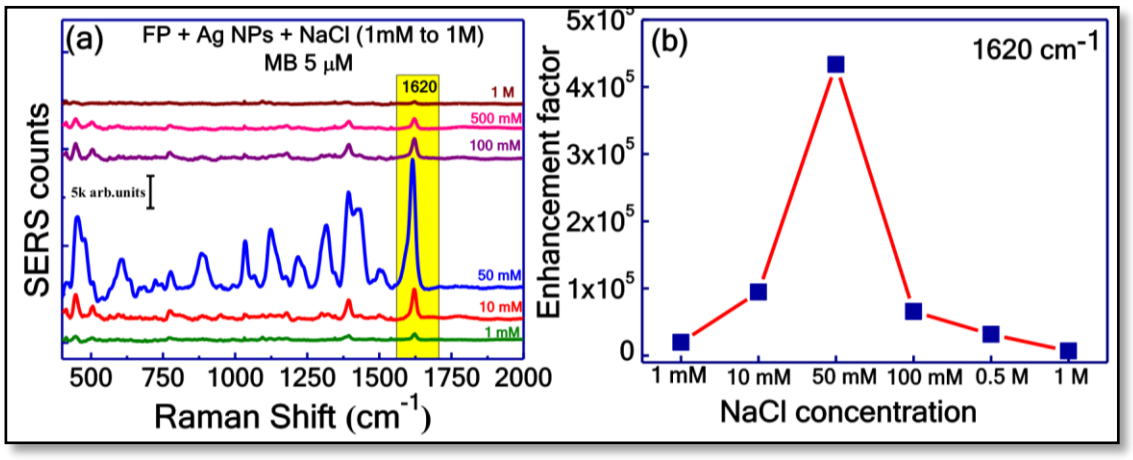

Figure 5A.15 (a) SERS spectra of MB -5µM acquired from FP embedded with aggregated Ag NPs at different concentrations of NaCl and (b) obtained EF at 1620 cm^{-1} as a function of NaCl concentration.

The homogeneity of the SERS signal is a significant parameter in evaluating the practical applicability of the SERS substrates. To test the reproducibility of this optimized SERS substrate (FP + AgNPs+ NaCl 50 mM), more than ten SERS spectra were acquired at randomly selected sites on the paper substrate for the dye molecules of MB (5 µM), shown in figure 5A.16 (a). The three single characteristic peaks intensities of 449 cm^{-1}, 1031

$cm^{-1,}$ and 1620 cm^{-1} and their relative standard deviation (RSD) histograms are shown in figures 5A.16(b) and 5A.16(e), 5A.16(c) and 5A.16(f), and 5A.16(d) and 5A.16(g), respectively. The calculated RSD values for three characteristic peaks of 449 cm^{-1}, 1031 $cm^{-1,}$ and 1620 cm^{-1} were found to be 7.97%, 13.08%, and 11.22 %, respectively. From the observed results we concluded that FP soaked in Ag NPs (50 mM NaCl) demonstrated a highly sensitive and reproducible SERS response.

Similarly, aggregated Au NPs FP SERS substrate response was evaluated with MB (5 µM). Figure 5A.17(a) presents the SERS spectra of MB (5 µM) detected using FP loaded with Au NPs with different concentrations of NaCl. The EF was calculated for the 1620 cm^{-1} peak and plotted as a function of NaCl concentration, data of which is shown in figure 5A.17(b). At lower concentrations of NaCl (1 and 10 mM), the attained EF was $\sim 1\times10^4$. While increasing the NaCl concentration to 500 mM and 1000 mM, a low SERS signal was noticed and the corresponding EF was estimated to be $\sim 10^3$. The maximum EF was achieved at 50 mM NaCl, i.e., $\sim 7.6\times10^4$, and a decrease in the SERS signal was observed when the concentration of NaCl exceeded 50 mM. The high salt-concentration factor could have led to the aggregation and precipitation of NPs on the FP. Thus, we understood that a moderate addition of NaCl concentration promotes the over aggregation of NPs. A sufficient amount of halide ions is required to achieve a higher number of hotspots, i.e., a smaller amount of chloride ions would not overcome the electrostatic repulsion between the NPs and larger amount induces excessive aggregation or precipitation of the NPs.

The reproducibility of better SERS substrate (FP + Au NPs +NaCl 50 mM) was examined by collecting the SERS spectra from more than 10 different spots, depicted in figure 5A.18(a). The calculated RSD values for the prominent peaks of 446 cm^{-1} and 1620 cm^{-1} were 5.78% and 7.37%, respectively, shown in figures 5A.18(b), 5A.18(d) and 5A.18(c), 5A.18(e), respectively. It can be concluded that FP soaked in Au NPs with 50 mM NaCl demonstrated strong SERS signal and relatively lower RSD values. Under these experimental conditions, the optimum condition for the best SERS performance was observed at 50 mM NaCl concentration for both Ag/Au NP paper-based substrates. The optimized Ag substrates presented in this work depicted higher EFs ($\sim 4.3\times10^5$) than the Au substrate EFs ($\sim 7.6\times10^4$).

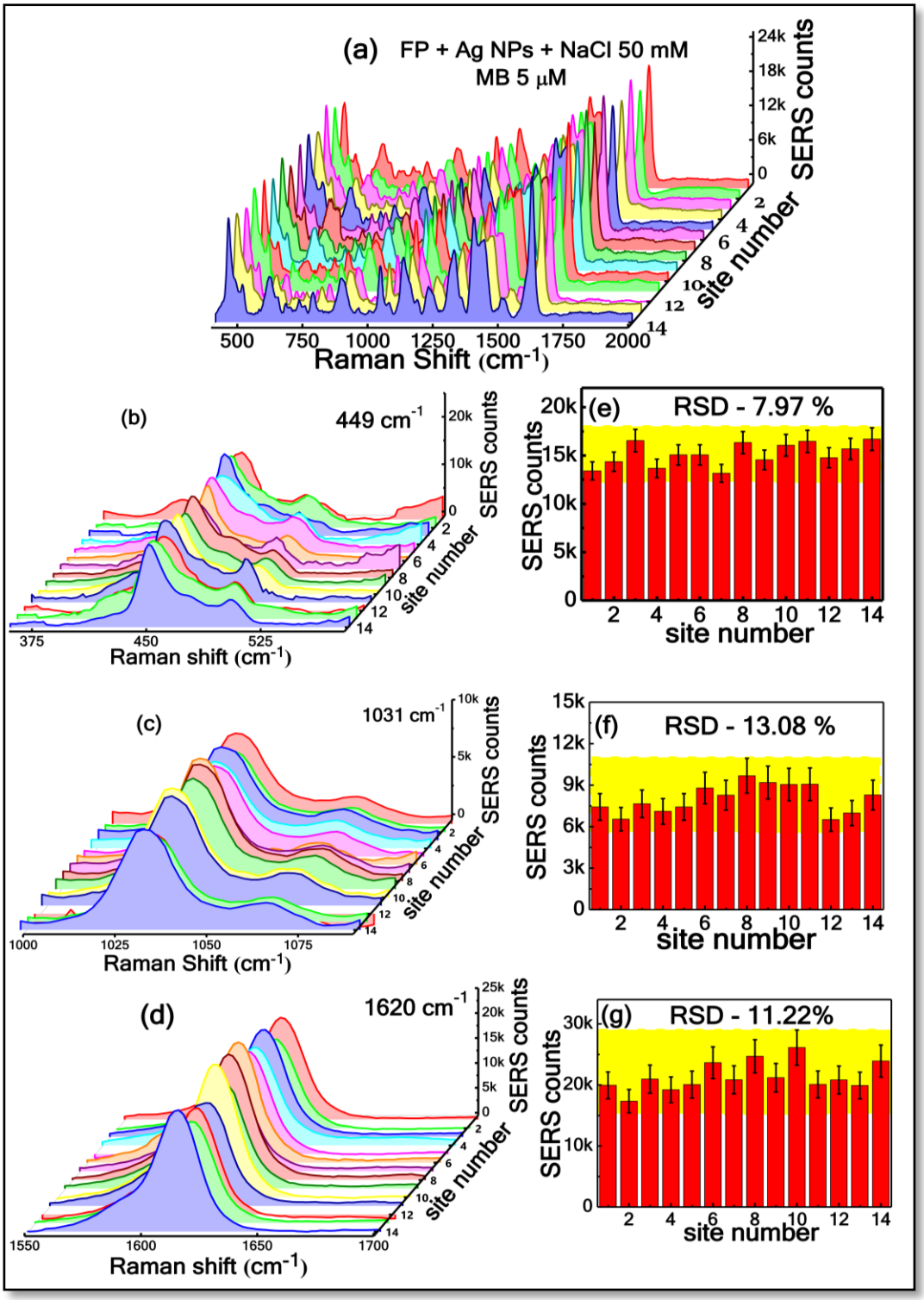

Figure 5A.16: Reproducibility SERS spectra of (a) MB (5 µM) from 14 different spots within the paper substrate with Ag NPs at NaCl 50 mM; (b, c & d) represents the single peak intensities and (e, f, & g) represents their corresponding histograms for the peaks at 449, 1031 and 1620 cm^{-1}.

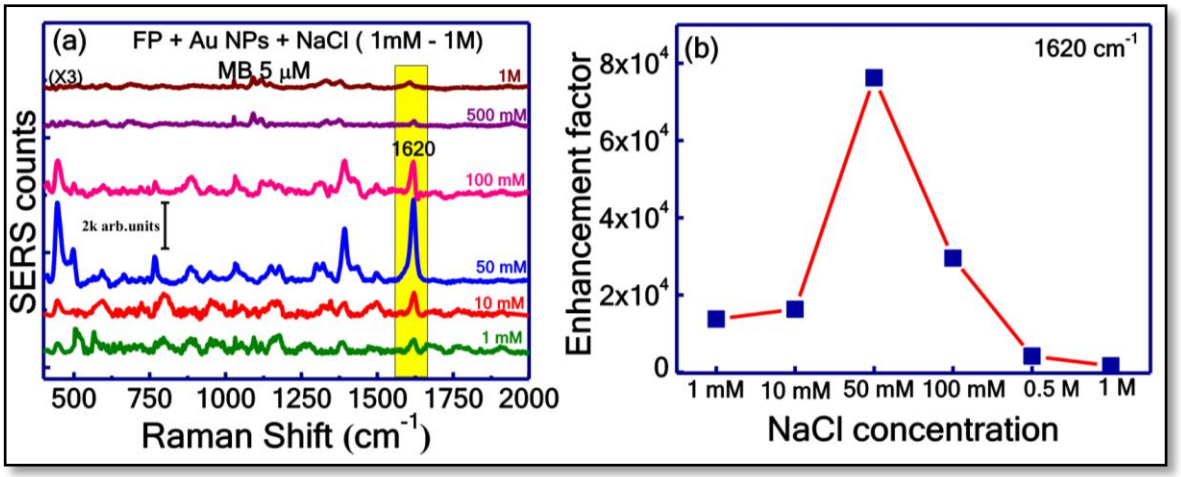

Figure 5A.17 (a) SERS spectra of MB from Au NP-based FP with different concentrations of NaCl and (b) corresponding EF at 1620 cm^{-1} as a function of concentration

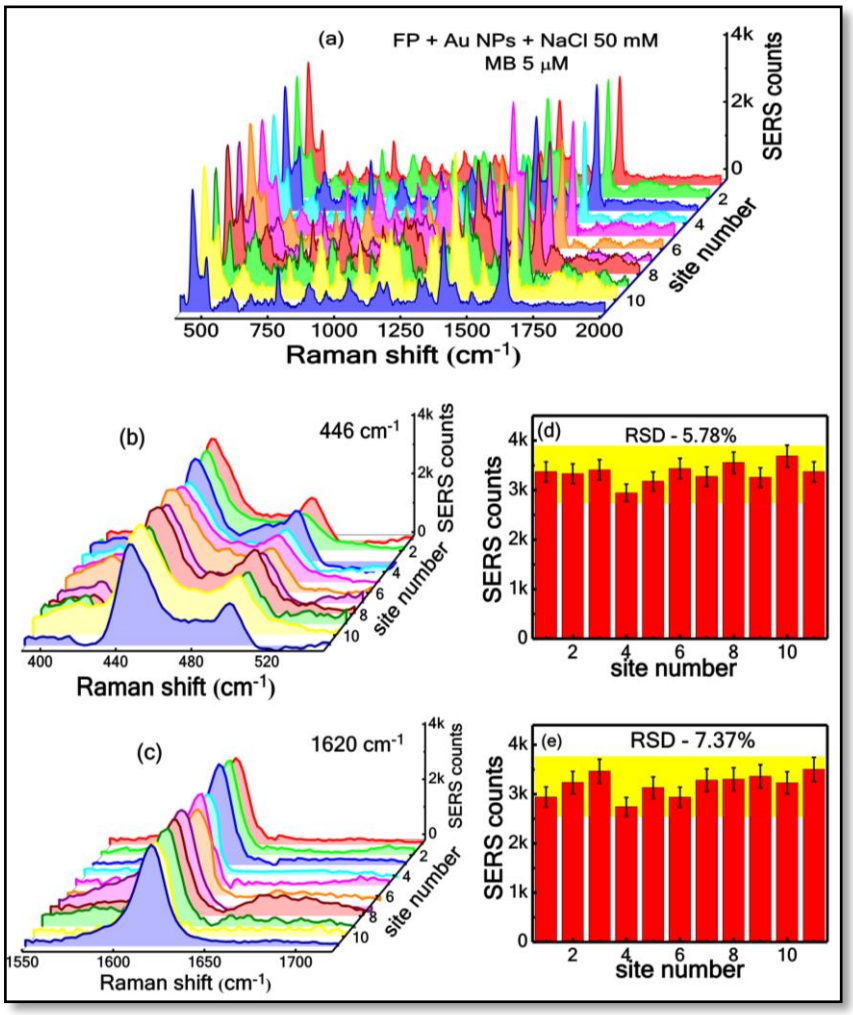

Figure 5A.18 Reproducibility SERS spectra of (a) MB -5 μM recorded within FP substrate loaded with Au NPs at NaCl 50 mM from 11 different locations (b, d) and (c, e) represents the single peak intensity and their corresponding histogram for 446 and 1620 cm^{-1}.

5A.4.3 Detection of Dye (MB) Molecules

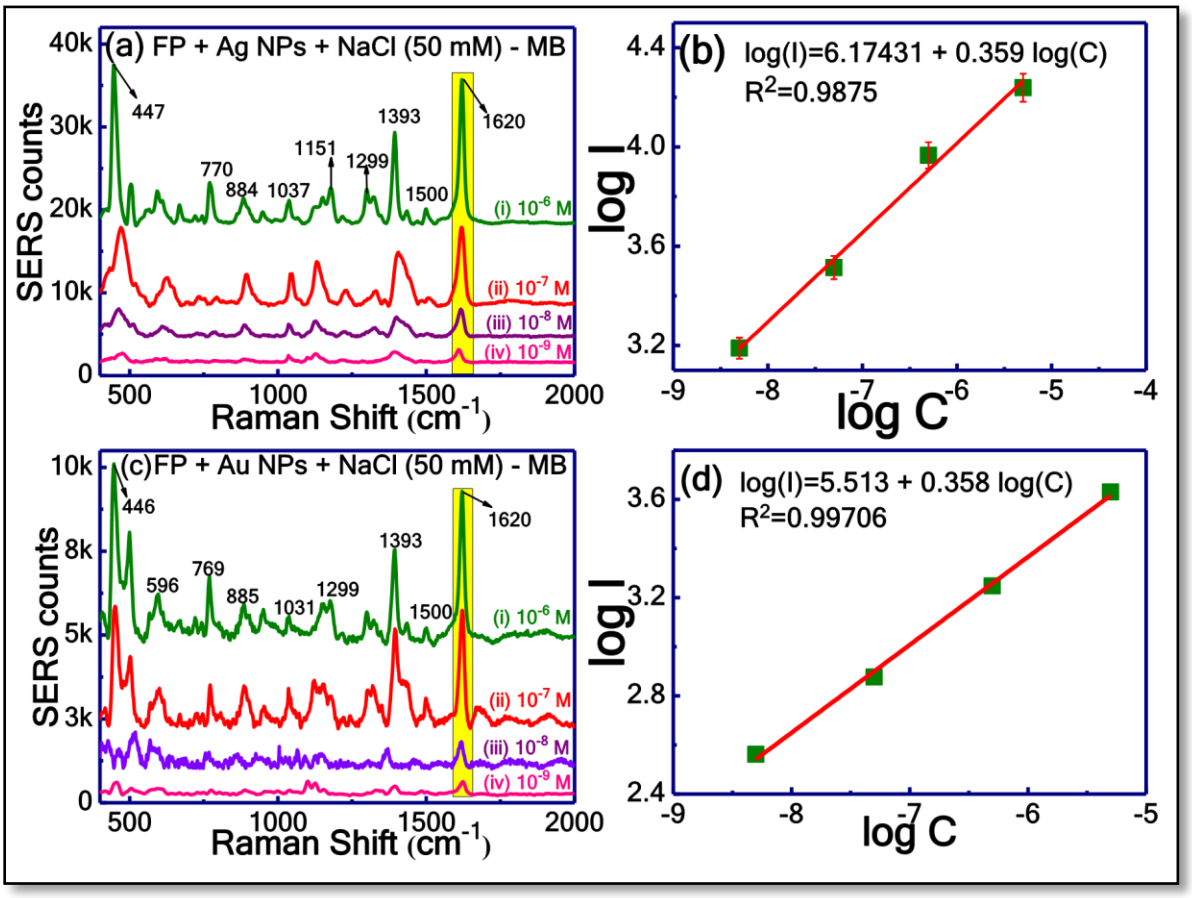

Figure 5A.19 SERS spectra of MB with various concentrations from 10 $^{-6}$ M to 10 $^{-9}$ M using FP loaded with NPs (50 mM NaCl) (a) Ag NPs and (c) Au NPs (b) and (d) corresponding linear calibration curves for the most prominent peak 1620 cm^{-1}

As a result of excellent sensitivity and reproducibility, the optimized FP substrates aggregated Ag/Au NPs at 50 mM NaCl were chosen for the studies of detection of explosive/dye molecules. A systematic study was performed with different concentrations of MB (5 μM, 500 nM, 50 nM, and 5 nM) using aggregated Ag and Au NPs (mixed with 50 mM NaCl) incubated on FP and the data are shown in figures 5A.19(a) and 5A.19(c), respectively. A good correlation was observed between the prominent peak (1620 cm^{-1}) intensity with the concentration of MB. Figures 5A.19(b) and 5A.19(d) illustrate the plot where Y-axis corresponds to the Raman peak intensity at 1620 cm^{-1} (in log scale) while the X-axis corresponds to the MB concentration (in log scale) and the achieved R^2 was ~0.98 and ~0.997 for aggregated Ag and Au NPs loaded FPs, respectively. A superior sensitivity was observed with the highest EF for MB 5 nM using FP with aggregated Ag

NPs (EF ~3.4×10^7) when compared to FP with aggregated Au NPs (EF ~7.9×10^6), and this can be attributed to the superior plasmonic properties.

5A.4.4 Detection of Explosives molecules

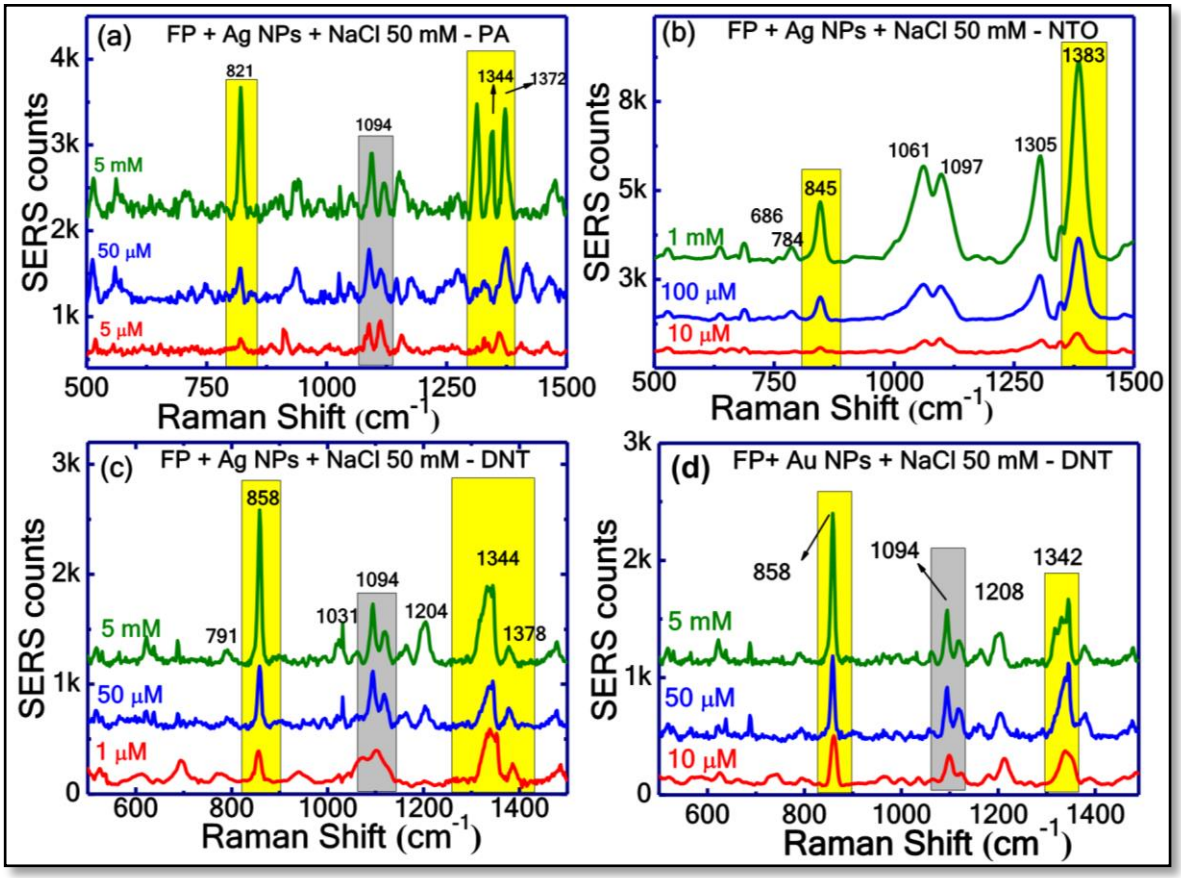

Figure 5A.20 (a) SERS spectra of explosives: (a) PA [5 mM, 50 µM, and 5 µM], (b) NTO [1 mM, 100 µM, and 10 µM], (c) DNT [5 mM, 50 µM, and 1 µM] by using FP loaded with Ag NPs aggregated by optimized concentration of NaCl (50 mM). (d) SERS spectra of DNT [5 mM, 50 µM and 10 µM] using FP loaded with Au NPs with 50 mM NaCl concentration.

The SERS performance of optimized FP SERS substrates at NaCl 50 mM was examined with the explosive molecules such as PA, DNT, and NTO (nitroaromatic explosives). The SERS spectra of PA and NTO at different concentrations were recorded with an optimized Ag-FP substrate, and the data are shown in figures 5A.20(a) and 5A.20(b). The EFs were estimated for PA, and NTO using Ag paper-based SERS substrate and were ~2.5×10^4 and ~2.1×10^4, respectively. Similarly, the as-prepared Ag and Au-FP substrates were verified with the other explosive molecule DNT, data of which is shown in figures 5A.20(c) and 5A.20(d), respectively. The characteristic peak of DNT 858 cm^{-1} was chosen to calculate the EFs and were estimated to be ~1.9×10^4 and ~1.5×10^4. The Ag NPs based FP substrates

depicted 4.2 and 1.2 times better performance than Au NPs based substrates in dye and explosive detection, respectively. The characteristic Raman peaks of PA, DNT and NTO matched with previous reports and their assignments are summarized in Appendix A. A superior EF was observed for Ag paper substrates compared to Au substrates and this could possibly be attributed to the UV broadening [(Ag: 400−700 nm); (Au: 500−600 nm)] as well as the larger mean size. Polavarapu et al.[44] demonstrated the effect of Raman excitation wavelength (532, 633, and 785 nm), size, and shape of different NPs (Au NP, Au NR, and Ag NP inks on paper) on SERS intensities and observed the superior EFs for the substrate loaded with Ag NPs.

5A.4.5 Reproducibility Studies

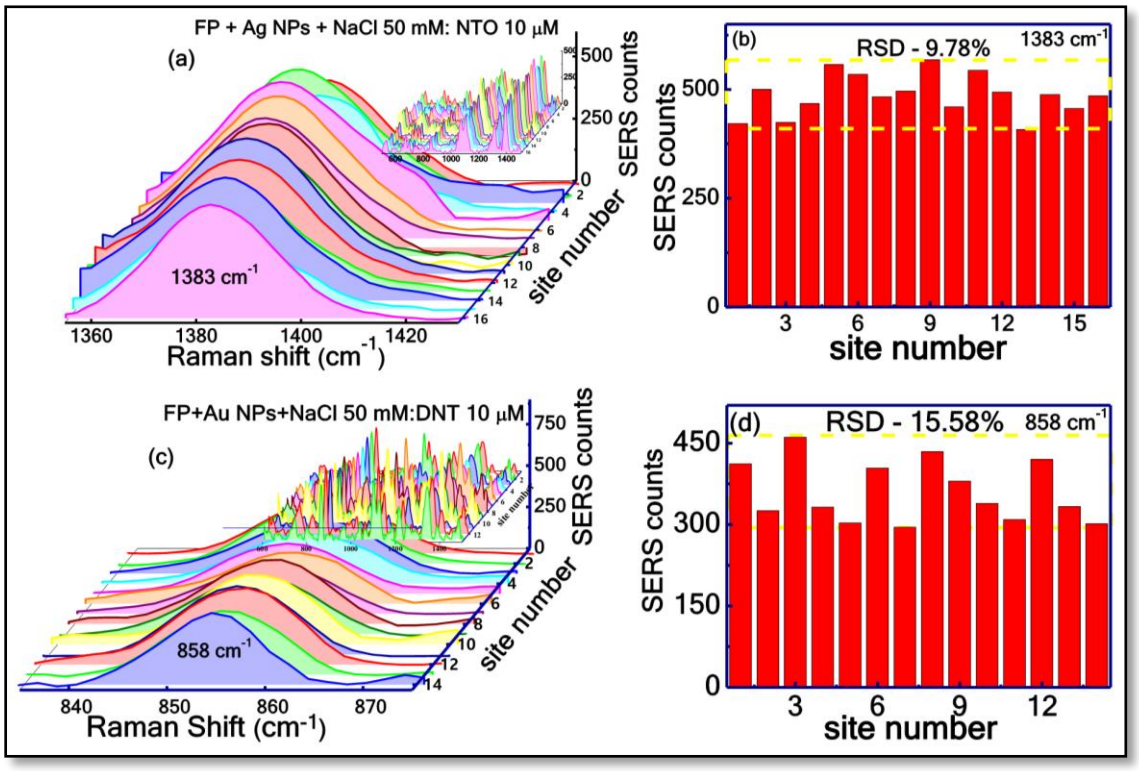

Figure 5A.21 Reproducibility SERS spectra from different spots within FP substrate with Ag NPs and Au NPs at 50 mM NaCl (a) NTO -10 µM and (c) DNT - 10 µM (b) and (d) the corresponding histogram of peak intensity at 1383 cm $^{-1}$ at 858 cm^{-1} of NTO and DNT, respectively.

The reproducibility measurements were also carried for NTO (10 µM) and DNT (10 µM) by recording the SERS spectra from different randomly selected points on the optimized FP with aggregated Ag and Au NPs substrates which are shown in figures 5A.21(a) and 5A.21(c). The SERS signal intensity at 1383 cm^{-1} mode of NTO and 858 cm^{-1} of DNT from different spots provided RSD values of 9.78% and 15.58%, respectively, revealing

a good spot-to-spot reproducibility [shown in figures 5.21(b) and 5.21(d)]. The multicomponent analyte detection was also verified using the optimized FP substrate (FP+Ag NPs+NaCl 50 mM). The dye and explosive mixtures were prepared with proper mixing of MB with 50 nM and PA with 5 µM concentrations in equal volumes. The SERS signature of the explosive molecule (PA) was dominated by the dye molecule (MB) signature (see figure 5A.22). However, we could clearly distinguish both (dye and explosive molecule) the Raman peaks.

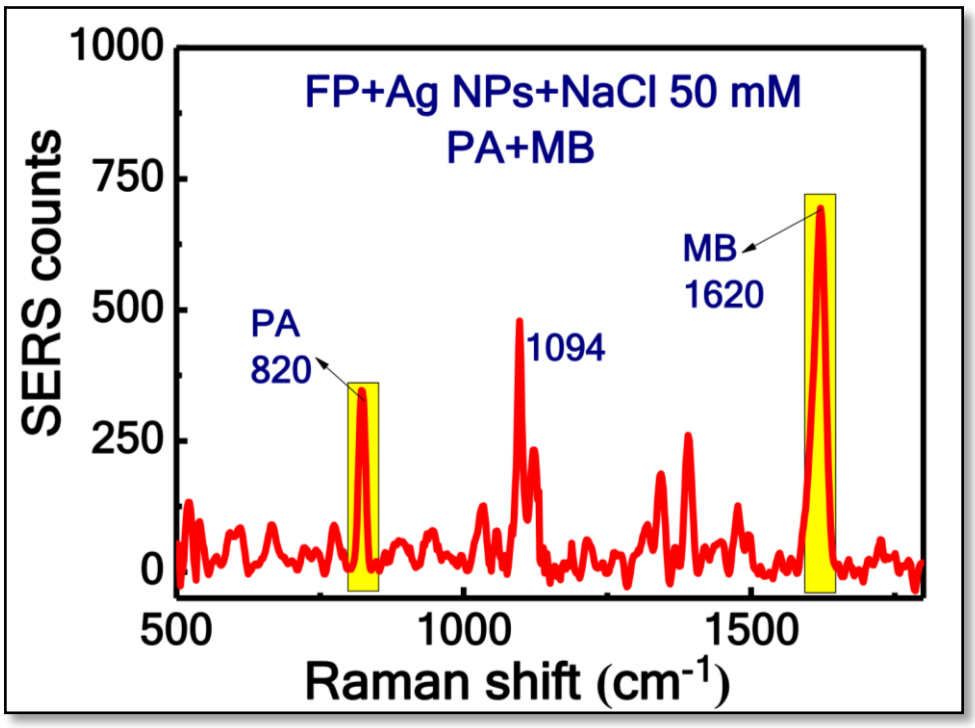

Figure 5A.22 SERS spectra complex dye+explosive molecule (PA 5 µM + MB 50 nM).

5A.4.6 Stability of SERS substrate

The stability (variation of SERS intensity with respect to time) of the Ag and Au NPs loaded filter paper substrates against exposure to atmospheric conditions was studied under 785 nm excitation with a portable Raman spectrometer. The substrates stability studied for a period of 45 days, and the SERS measurements were carried out at different intervals of time. Figures 5.23(a) and 5A.23(d) present the time-dependent SERS spectra of MB (5 µM), and thiram (10 µM) on the Ag loaded FP substrates. Figures 5A.23(b) and 5A.23(e) present the time-dependent SERS spectra of MB on the Au NPs loaded FP substrates. The stability over the large area could be verified by collecting the Raman

spectra from more than five different locations on the substrate. The stability was estimated by monitoring the most prominent peaks intensities of the 1620 cm^{-1} mode in MB and 1375 cm^{-1} mode in thiram. The temporal variations are shown in figures 5A.23(c) and 5A.23(f), respectively. The Au loaded FP substrates exhibited highly stable behavior in comparison with Ag loaded FP substrate over a span of 45 days. Within the time period, the Raman signal intensity of the analyte molecule on Ag NPs embedded FP was significantly decreased compared to Au NPs embedded FP. This could be due to the oxidation of Ag NPs. The oxidation increases with time, leading to the weakening of the plasmonic properties of Ag NPs and the SERS activity. Thus, within a short period of time, Ag NPs loaded FP depicted superior SERS performance, and for an extended period of time, Au NPs loaded FP demonstrated consistent SERS performance.

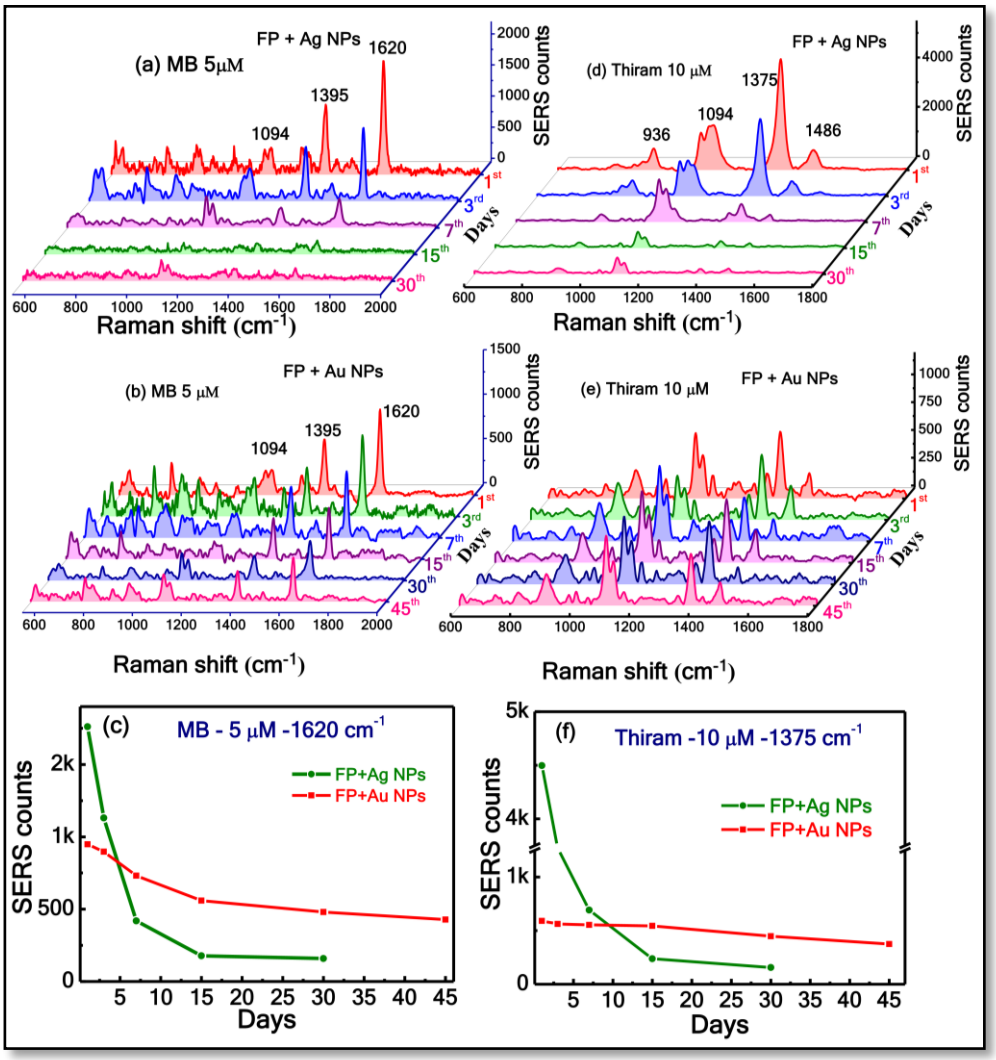

Figure 5A.23 Temporal stability SERS spectra of (a and b) MB (d and e) Thiram using FP loaded with Ag and Au NPs, respectively. (c and f) SERS intensity variation with respect to the number of days.

5A.5 Conclusions

Table 5.1 The flexible Ag/Au FP substrates SERS features

Parameters	Ag-based FP substrate	Au based FP substrate
Dye (MB) molecule detection and EF	5 nM ~3.4×10^{7}	5 nM ~7.9×10^{6}
Explosive (DNT) molecule detection and EF	1 µM ~1.9×10^{4}	10 µM ~1.5×10^{4}
RSD	~ 10%	~ 15%
Stability	15 days	45 days

Flexible, low-cost, eco-friendly SERS substrates were fabricated by using FP as a base and were loaded with Ag/Au NPs that were also produced by green and straightforward technique of LAL. To achieve the maximum number of hot spots, the aggregated colloids were prepared by adding NaCl into the already prepared NPs. Individually, spherical Ag and Au NPs were loaded for an optimally aggregated configuration yielded the maximum SERS signal enhancements. These detailed experiments indicated that the Ag/Au NPs with 50 mM NaCl concentration is helpful for optimal SERS performance under these conditions. FP-based Ag substrate performance was nearly 5 and 2 times better than the FP based Au substrate in the detection of dye and explosive molecules, respectively. The FP Ag-based SERS substrate was helpful for the detection of four adsorbed molecules (MB-5 nM, PA-5 µM, DNT-1 µM, and NTO-10 µM) with high specificity, sensitivity, and reproducibility. Overall, a simple, inexpensive technique offers a decrease in the cost of analysis using FP-based SERS targets and utilizing a portable Raman instrument, which is portable to the point of diagnostics of interest. The stability studies were conducted on FP with Ag and Au NPs in the detection of dye (MB – 5 µM) and pesticide (Thiram-10 µM) molecules. The SERS signal intensity drops ~89 % and ~40% for Ag and Au substrates in 15 days. Because of the high plasmonic nature, Ag demonstrated better SERS signal in the early days compared to Au based substrate. From the stability studies, observed a ~ 90% drop of SERS intensity in ~ 30 days for FP with Ag NPs and ~55 % drop in 45 days for FP with Au NPs. Therefore, we concluded that Au NPs loaded FP have exhibited consistent SERS performance

5A.6 References

1. Krishna Podagatlapalli, G.; Hamad, S.; Tewari, S. P.; Sreedhar, S.; Prasad, M. D.; Venugopal Rao, S., Silver Nano-Entities through Ultrafast Double Ablation in Aqueous Media for Surface-Enhanced Raman Scattering and Photonics Applications. *J. Appl. Phys.* **2013**, *113*, 073106.
2. Zhao, Y.; Zhao, S.; Zhang, L.; Liu, Y.; Li, X.; Lu, Y., A Three-Dimensional Au Nanoparticle-Monolayer Graphene-Ag Hexagon Nanoarray Structure for High-Performance Surface-Enhanced Raman Scattering. *RSC Adv.* **2017**, *7*, 11904-11912.
3. Hamad, S.; Podagatlapalli, G. K.; Tewari, S. P.; Rao, S. V., Influence of Picosecond Multiple/Single Line Ablation on Copper Nanoparticles Fabricated for Surface-Enhanced Raman Spectroscopy and Photonics Applications. *J. Phys. D: Appl. Phys.* **2013**, *46*, 485501.
4. Zhang, M.; Zheng, Z.; Liu, H.; Wang, D.; Chen, T.; Liu, J.; Wu, Y., Rationally Designed Graphene/Bilayer Silver/Cu Hybrid Structure with Improved Sensitivity and Stability for Highly Efficient SERS Sensing. *ACS Omega* **2018**, *3*, 5761-5770.
5. Vendamani, V.; Nageswara Rao, S.; Venugopal Rao, S.; Kanjilal, D.; Pathak, A., Three-Dimensional Hybrid Silicon Nanostructures for Surface Enhanced Raman Spectroscopy Based Molecular Detection. *J. Appl. Phys.* **2018**, *123*, 014301.
6. Joshi, P.; Santhanam, V., Paper-Based SERS Active Substrates on Demand. *RSC Adv.* **2016**, *6*, 68545-68552.
7. Chamuah, N.; Hazarika, A.; Hatiboruah, D.; Nath, P., SERS on Paper: An Extremely Low-Cost Technique to Measure Raman Signal. *J. Phys. D: Appl. Phys.* **2017**, *50*, 485601.
8. Betz, J. F.; Yu, W. W.; Cheng, Y.; White, I. M.; Rubloff, G. W., Simple SERS Substrates: Powerful, Portable, and Full of Potential. *Phys. Chem. Chem. Phys.* **2014**, *16*, 2224-2239.
9. Gall, E. T.; Siegel, J. A.; Corsi, R. L., Modeling Ozone Removal to Indoor Materials, Including the Effects of Porosity, Pore Diameter, and Thickness. *Environ. Sci. Technol.* **2015**, *49*, 4398-4406.
10. Lin, Y.; Gritsenko, D.; Liu, Q.; Lu, X.; Xu, J., Recent Advancements in Functionalized Paper-Based Electronics. *ACS Appl. Mater. & Interf.* **2016**, *8*, 20501-20515.
11. Nery, E. W.; Kubota, L. T., Sensing Approaches on Paper-Based Devices: A Review. *Anal. Bioanal. Chem* **2013**, *405*, 7573-7595.
12. Ge, S.; Zhang, L.; Zhang, Y.; Lan, F.; Yan, M.; Yu, J., Nanomaterials-Modified Cellulose Paper as a Platform for Biosensing Applications. *Nanoscale*, **2017**, *9*, 4366-4382.
13. Ngo, Y. H.; Li, D.; Simon, G. P.; Garnier, G., Gold Nanoparticle–Paper as a Three-Dimensional Surface-Enhanced Raman Scattering Substrate. *Langmuir*, **2012**, *28*, 8782-8790.
14. Zheng, G.; Polavarapu, L.; Liz-Marzan, L. M.; Pastoriza-Santos, I.; Perez-Juste, J., Gold Nanoparticle-Loaded Filter Paper: A Recyclable Dip-Catalyst for Real-Time Reaction Monitoring by Surface-Enhanced Raman Scattering. *Chem. Commun.* **2015**, *51*, 4572-4575.
15. Lee, M.; Oh, K.; Choi, H.-K.; Lee, S. G.; Youn, H. J.; Lee, H. L.; Jeong, D. H., Subnanomolar Sensitivity of Filter Paper-Based SERS Sensor for Pesticide

Detection by Hydrophobicity Change of Paper Surface. *ACS Sensors* **2018**, *3*, 151-159.
16. Lee, C. H.; Hankus, M. E.; Tian, L.; Pellegrino, P. M.; Singamaneni, S., Highly Sensitive Surface-Enhanced Raman Scattering Substrates Based on Filter Paper Loaded with Plasmonic Nanostructures. *Anal. Chem.* **2011**, *83*, 8953-8958.
17. Polavarapu, L.; Liz-Marzan, L. M., Towards Low-Cost Flexible Substrates for Nanoplasmonic Sensing. *Phys. Chem. Chem. Phys.* **2013**, *15*, 5288-5300.
18. Mu, Y.; Zhang, X., A Paper-Fiber-Supported 3d SERS Substrate. *Plasmonics*, **2019**, 1-8.
19. Bell, S. E. J.; McCourt, M. R., SERS Enhancement by Aggregated Au Colloids: Effect of Particle Size. *Phys. Chem. Chem. Phys.* **2009**, *11*, 7455-7462.
20. Blatchford, C.-G.; Campbell, J.; Creighton, J. A., Plasma Resonance—Enhanced Raman Scattering by Absorbates on Gold Colloids: The Effects of Aggregation. *Surf. Sci.* **1982**, *120*, 435-455.
21. Chen, M. C.; Tsai, S. D.; Chen, M. R.; Ou, S. Y.; Li, W. H.; Lee, K. C., Effect of Silver-Nanoparticle Aggregation on Surface-Enhanced Raman Scattering from Benzoic Acid. *Physical Review B*, **1995**, *51*, 4507-4515.
22. Xu, H.; Bjerneld, E. J.; Käll, M.; Börjesson, L., Spectroscopy of Single Hemoglobin Molecules by Surface-Enhanced Raman Scattering. *Phys. Rev. Lett.* **1999**, *83*, 4357.
23. Kneipp, K.; Kneipp, H., Surface-Enhanced Raman Scattering on Silver Nanoparticles in Different Aggregation Stages. *Israel Journal of Chemistry* **2006**, *46*, 299-305.
24. Mock, J.; Norton, S.; Chen, S.-Y.; Lazarides, A.; Smith, D., Electromagnetic Enhancement Effect Caused by Aggregation on SERS-Active Gold Nanoparticles. *Plasmonics*, **2011**, *6*, 113-124.
25. Zhang, D.; Gökce, B.; Barcikowski, S., Laser Synthesis and Processing of Colloids: Fundamentals and Applications. *Chem. Rev.* **2017**, *117*, 3990-4103.
26. Rao, S. V.; Podagatlapalli, G. K.; Hamad, S., Ultrafast Laser Ablation in Liquids for Nanomaterials and Applications. *J. Nanosci. Nanotechnol* **2014**, *14*, 1364-1388.
27. Sergiienko, S.; Moor, K.; Gudun, K.; Yelemessova, Z.; Bukasov, R., Nanoparticle-Nanoparticle Vs. Nanoparticle-Substrate Hot Spot Contributions to the SERS Signal: Studying Raman Labelled Monomers, Dimers, and Trimers. *Phys. Chem. Chem. Phys.* **2017**, *19*, 4478-4487.
28. Byram, C.; Soma, V. R., 2, 4-Dinitrotoluene Detected Using Portable Raman Spectrometer and Femtosecond Laser Fabricated Au–Ag Nanoparticles and Nanostructures. *Nano-Structures & Nano-Objects* **2017**, *12*, 121-129.
29. Byram, C.; Moram, S. S. B.; Shaik, A. K.; Soma, V. R., Versatile Gold Based SERS Substrates Fabricated by Ultrafast Laser Ablation for Sensing Picric Acid and Ammonium Nitrate. *Chem. Phys. Lett.* **2017**, *685*, 103-107.
30. Leitz, K.-H.; Redlingshöfer, B.; Reg, Y.; Otto, A.; Schmidt, M., Metal Ablation with Short and Ultrashort Laser Pulses. *Physics Procedia* **2011**, *12*, 230-238.
31. Amendola, V.; Meneghetti, M., What Controls the Composition and the Structure of Nanomaterials Generated by Laser Ablation in Liquid Solution? *Phys. Chem. Chem. Phys.* **2013**, *15*, 3027-3046.
32. Podagatlapalli, G. K.; Hamad, S.; Rao, S. V., Trace-Level Detection of Secondary Explosives Using Hybrid Silver–Gold Nanoparticles and Nanostructures Achieved with Femtosecond Laser Ablation. *J. Phys. Chem. C* **2015**, *119*, 16972-16983.

33. Zhang, Z.; Li, H.; Zhang, F.; Wu, Y.; Guo, Z.; Zhou, L.; Li, J., Investigation of Halide-Induced Aggregation of Au Nanoparticles into Spongelike Gold. *Langmuir*, **2014**, *30*, 2648-2659.
34. Yaffe, N. R.; Blanch, E. W., Effects and Anomalies That Can Occur in SERS Spectra of Biological Molecules When Using a Wide Range of Aggregating Agents for Hydroxylamine-Reduced and Citrate-Reduced Silver Colloids. *Vib. Spectrosc.* **2008**, *48*, 196-201.
35. Jana, N. R.; Pal, T., Anisotropic Metal Nanoparticles for Use as Surface-Enhanced Raman Substrates. *Adv. Mater.* **2007**, *19*, 1761-1765.
36. Schmucker, A. L.; Tadepalli, S.; Liu, K.-K.; Sullivan, C. J.; Singamaneni, S.; Naik, R. R., Plasmonic Paper: A Porous and Flexible Substrate Enabling Nanoparticle-Based Combinatorial Chemistry. *RSC Adv.* **2016**, *6*, 4136-4144.
37. Mehrdel, B.; Abdul Aziz, A.; Yoon, T. L.; Lee, S. C., Effect of Chemical Interface Damping and Aggregation Size of Bare Gold Nanoparticles in NaCl on the Plasmon Resonance Damping. *Opt. Mater. Express*, **2017**, *7*, 955-966.
38. Hendrich, C.; Bosbach, J.; Stietz, F.; Hubenthal, F.; Vartanyan, T.; Träger, F., Chemical Interface Damping of Surface Plasmon Excitation in Metal Nanoparticles: A Study by Persistent Spectral Hole Burning. *Appl. Phys. B* **2003**, *76*, 869-875.
39. Thompson, D. W.; Collins, I. R., Electrical Properties of the Gold—Aqueous Solution Interface. *J. Colloid Interface Sci.* **1992**, *152*, 197-204.
40. Hövel, H.; Fritz, S.; Hilger, A.; Kreibig, U.; Vollmer, M., Width of Cluster Plasmon Resonances: Bulk Dielectric Functions and Chemical Interface Damping. *Physical Review B*, **1993**, *48*, 18178.
41. Zhang, X.; Servos, M. R.; Liu, J., Ultrahigh Nanoparticle Stability against Salt, Ph, and Solvent with Retained Surface Accessibility Via Depletion Stabilization. *J. Am. Chem. Soc.*, **2012**, *134*, 9910-9913.
42. Bengter, H.; Tengroth, C.; Jacobsson, S. P., New Light on Ag-Colloid Preparation for Surface-Enhanced Ft-Raman Spectroscopy: The Role of Aggregation. *J. Raman Spectros.* **2005**, *36*, 1015-1022.
43. Ashley, M. J.; Bourgeois, M. R.; Murthy, R. R.; Laramy, C. R.; Ross, M. B.; Naik, R. R.; Schatz, G. C.; Mirkin, C. A., Shape and Size Control of Substrate-Grown Gold Nanoparticles for Surface-Enhanced Raman Spectroscopy Detection of Chemical Analytes. *J. Phys. Chem.C* **2018**, *122*, 2307-2314.
44. Polavarapu, L.; Porta, A. L.; Novikov, S. M.; Coronado-Puchau, M.; Liz-Marzán, L. M., Pen-on-Paper Approach toward the Design of Universal Surface-Enhanced Raman Scattering Substrates. *Small* **2014**, *10*, 3065-3071.

5B. Anisotropic Au NPs loaded filter Paper

Abstract

The second section of chapter-5 describes the SERS performance of filter paper (FP) loaded with anisotropic gold nanoparticles (Au NPs). Here, three different shapes (spherical, triangular and stars) of Au NPs were synthesized and their SERS performance was verified. Spherical Au NPs were synthesized using femtosecond (fs) laser ablation of Au target in distilled water while the other two anisotropic (triangular and star-shaped) Au NPs were prepared by chemical methods. The Au NPs were characterized using UV-Visible absorption studies and TEM. The FP loaded with Au NPs were characterized by absorption spectra and FESEM techniques. Subsequently, the SERS studies were performed on FP loaded with three different shaped Au NPs. From the obtained SERS results we noticed the star-shaped Au NPs loaded FP substrates were found to be superior compared to the triangular and spherical Au NPs loaded FP substrates. The presence of sharp tips/edges of NPs localizes the filed generating a higher number of hotspots and play a role in the enhancement of Raman signal. Our detailed studies suggest that star-shaped Au NPs loaded FP are capable of detecting 10 pM -NB with an estimated enhancement factor of ~3.7×10^{10}. COMSOL multiphysics simulations were performed to investigate near field distributions of these different shaped Au NPs, and as expected, the strongly enhanced near-field intensity at the sharp features was observed. Furthermore, a comparative study has been performed on the aggregated spherical (Au NPs with NaCl 50 mM [which demonstrated a better SERS signal in chapter 5A] and star-shaped Au NPs loaded on FP [present chapter 5B]. These FP substrates were subsequently used for the detection of a dye (Nile blue -NB) and an explosive molecule (Picric acid -PA). The same order of EF was observed in both the cases of aggregated spherical Au NPs and star-shaped Au NPs loaded FP.

The work presented in this chapter has been published as

M. S. S. Bharati, B. Chandu, S. Venugopal Rao, "Gold Nanoparticles and Nanostars loaded Paper-based SERS Substrates for Sensing Nanogram-level Picric Acid with a Portable Raman Spectrometer" Bull. Mater. Sci., (Indian Academy of Sciences), **43,** 53, 2020.

M. S. S. Bharati, B. Chandu, K Nehra, P. S. Kumar, and S. Venugopal Rao, Filter Paper Loaded with Gold Nanoparticles as Flexible SERS Substrates for Sensing Applications. *AIP Conf. Proc.*, 2020, In Press.

5B.1 Introduction

Anisotropic metal nanoparticles (MNPs) have attracted interest from the scientific community for their potential in numerous applications ranging from sensing to cell imaging to drug delivery[1-2] owing to their shape-dependent physical properties. The physical, chemical and photo-stability combined with the ability of tuning of optical properties with various sizes/shapes support the plasmonic properties of MNPs. Currently, the surface-enhanced Raman scattering (SERS) substrates based on different shaped MNPs are used to increase the efficiency of the Raman scattering. Primarily, the enhanced electromagnetic field locations i.e., "hotspots" depend on the existence of ultra-small gaps/sharp tips in the nanostructures (NSs) or narrow slits between the plasmonic NPs. Other than the aggregation effect, the creation of sharp edges/tips is another effective way to enhance the number of "hotspots," on the NPs due to the localized surface plasmon resonance (LSPR) effect.[3-4] Thus, the Raman signals of molecules at these sites are preferred to promote the SERS activity significantly. The plasmonic nature of gold (Au) NPs is lower compared to silver (Ag) NPs, but intense research on Au NPs has been progressing during the last few decades because of their long-term stability and excellent biocompatibility. During the last few decades, different morphologies of Au NPs have been tested as SERS substrates because of their tunable plasmonic capability in the visible to NIR range and stability. Tian et al.[5] have studied the effect of NPs shapes (nanosphere, nanotriangle, and nanostar) on the SERS intensities of the probe molecule of R6G -5 µM with 785 nm excitation. Compared to other shapes, star-shaped Au NPs had shown better Raman signals because of possessing a higher number of sharp edges and corners. Minati et al.[6] synthesized Au nanostars by a one-step reduction process and using which they observed higher Raman signal enhancements than spherical NPs of the same dimension. Sandu et al.[7] analyzed the changes of LSPRs by varying the shape and simulated a variety of extinction spectra and coupling weights to the EM field with small changes in the shaped metal NPs. More recently, large numbers of techniques have been introduced and investigated to design various SERS substrates with a large number of hotspots.[8-9] Krajczewski et al.[10] followed one-pot procedures for synthesizing star-shaped Au NPs and Au core Au@SiO_2, Au@Ag, and Au@Ag@SiO_2 NSs.

Of late, many researchers have directed their efforts towards the fabrication of low-cost and highly sensitive SERS substrates by incorporating anisotropic NPs in filter paper. Among the solid-supported SERS based substrates, paper-based SERS substrates are attractive sensors for the detection of explosives, pesticides and also in bio-diagnostic applications.[11-17] With outstanding features such as low cost, flexibility, robustness, biodegradable, renewable, ease of use, and available sample collection leads, these paper SERS substrates are more favorable for a variety of practical applications. Weng et al.[18] synthesized Ag triangle shaped nanoplates with various sizes and SERS studies were performed on these different sized Ag nanoplates by depositing glass and paper. They concluded that the big sized Ag nanoplates (84 nm) displayed stronger SERS intensity on glass and small sized Ag nanoplates (30 nm) demonstrated superior SERS intensity on paper. Zhou et al.[19] demonstrated FP with Au porous nanospheres as a SERS substrate to detect 10 nM R6G with long term stability (30 days). Yadan Ma et al.[20] developed Ag NPs and graphene oxide on cellulose paper using a screen printing technique, used as SERS substrate for the detection of thiram (0.26 ng cm^{-2}), thiabendazole (28 ng cm^{-2}) and methyl parathion (7.4 ng cm^{-2}). He et al.[21] developed citrate capped Au nanostar immobilized FP substrates and used for the detection of 1 nM CV with EF 1.2 $\times 10^7$.

In this chapter, we discussed the results from the fabrication of sensitive FP-SERS substrates loaded with three different Au NPs (i.e., spheres, triangles, and stars). Spherical Au NPs were fabricated by fs laser ablation technique; triangular and star-shaped Au NPs were prepared by wet chemical methods. Three NPs loaded FP substrates SERS performance was verified with Nile blue (NB) molecule at a concentration of 5 nM. Compared to the FP embedded with spherical and triangular Au NPs, the SERS activity of the FP loaded with star-shaped Au NPs proved to be remarkable, boosted by the sharp tips. Further, COMSOL multiphysics simulations (2D) were performed on these three shapes of Au NPs and dimensions considered were similar to the experimental results. The obtained results confirmed the maximum electric field strength located at sharp edges/tips of the triangular and star-shaped Au NP. Moreover, FP loaded with star-shaped Au NPs substrate's sensitivity and reproducibility studies were performed with NB molecule at a concentration as low as 10 pM and with an RSD >15%.

Further, a comparison of SERS studies were performed with the (i) aggregated spherical shape Au NPs with the optimized NaCl concentration (50 mM) (Chapter 5A). (ii) Au

nanostars (NSs) (Chapter 5B). Both the SERS substrates performance was verified with a dye (NB- 5 nM) and explosive molecule (PA - 5µM). Reproducibility studies also verified with contour plot of prominent peak intensity from more than 10 different locations on the SERS substrate.

5B.2 Experimental details:

5B.2.1 Synthesis of Au NPs

Spherical Au NPs: Spherical Au NPs in 5 ml distilled water were fabricated using fs LAL technique. All the details are mentioned in chapter 5A.

Anisotropic Au NPs: Triangular and star-shaped Au NPs were synthesized using colloidal chemical methods by following the simple approach proposed by Kamalesh et al.[22] In this polyvinyl pyrrolidone (PVP, MW ~ 40k) was utilized as the reducing/capping agent. Triangular NPs prepared by 15 ml poly N-vinyl-2-pyrrolidone (PVP- 5 mM) dissolved in distilled water and mixed with hydrochloroauric acid ($HAuCl_4.3H_2O$ -0.27mM). And star shaped Au NPs were synthesized by PVP- 5 mM dissolved in dimethylformamide (DMF) mixed with sodium hydroxide (NaOH-1.5 mM), $HAuCl_4.3H_2O$ -0.27mM). These NPs were centrifuged in ethanol to remove the excess PVP.

Spherical aggregated Au NPs: Spherical NPs were fabricated by adding optimized NaCl concentration (50 mM) and the complete details are described in Chapter 5 A.

5B.3 Characterization

5B.3.1 UV-Visible absorption spectra

The optical absorption measurements were performed for all three shaped Au NPs in colloidal solutions [(i) liquid form] and loaded onto the FP [(ii) substrate]. Bare FP absorption spectra are illustrated in figure 5B.1(a), no significant absorption maxima were noticed in the visible and NIR region. Laser-ablated spherical Au NPs showed absorption maxima at ~527 nm figures 5B.1[b-(i)], corresponding to the plasmon resonance of spherical Au NPs. More than one peak was observed for triangular Au NPs; one was at located 538 nm while another broad peak with a maximum absorption was found at 835 nm revealing the anisotropic nature of Au NPs (data is presented in 5B.1[c-(i)]). Star-shaped Au NPs demonstrated a broad absorption peak from ~ 600 to ~ 900 nm in the

spectral range, as shown in figure 5B.1[d-(i)]. The broad SPR peak in the NIR region is the characteristics of the anisotropic NPs with sharper branches. The absorption spectra of all the three shapes of Au NPs loaded FP exhibited similar absorption spectra with broadening in SPR peak, shown in figure 5B.1[b-(ii), c-(ii), and d-(ii)]. The observed broadening of the SPR peak could be ascribed to the variation of NPs surrounding dielectric medium from the liquid in quartz cuvette to cellulose fibers, and also from the paper induced aggregation of the NPs.[23]

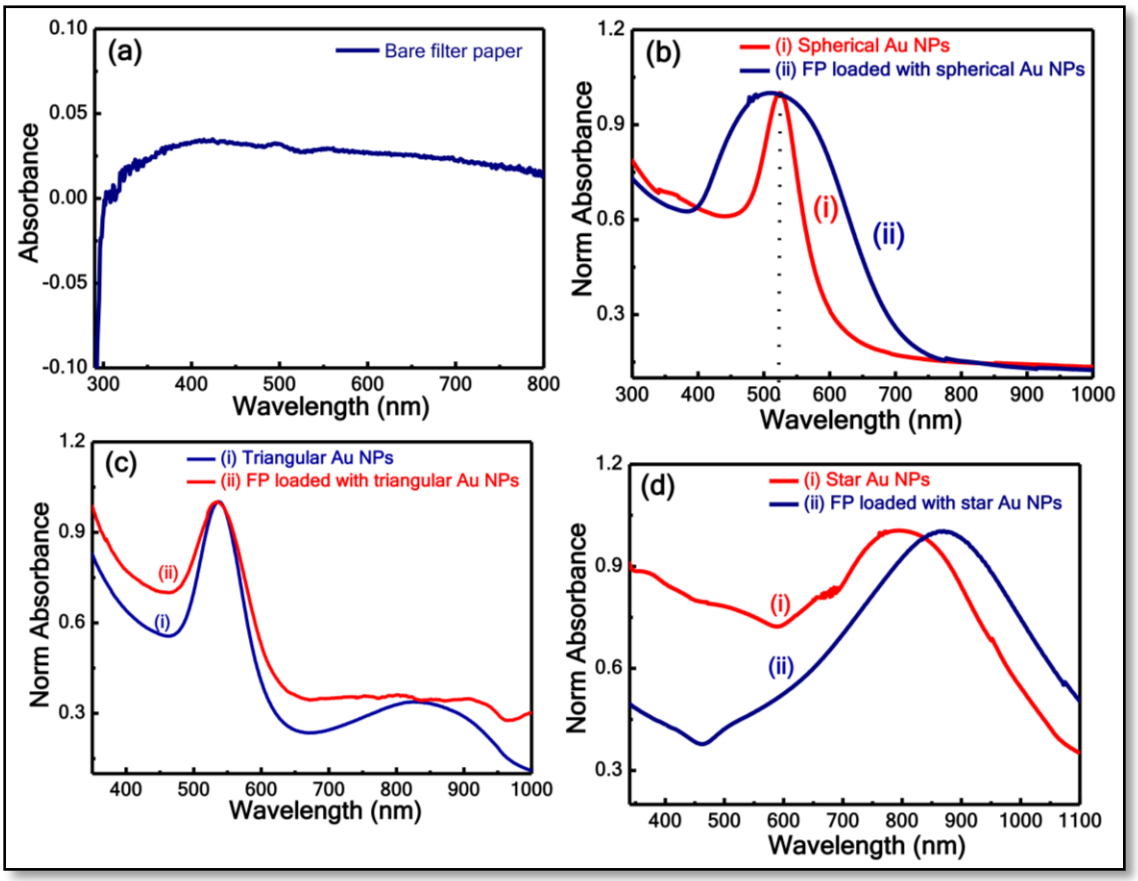

Figure 5B.1 (a) UV-visible absorption spectra of (a) bare FP (b) spherical Au NPs achieved by LAL (c) Triangular Au NPs (d) star-shaped Au NPs. The curves (i) represent colloidal Au NPs/NSs, while curves (ii) represent Au NPs/NSs loaded FP.

5B.3.2 TEM studies

The shape of obtained Au NPs was confirmed from the transmission electron microscope (TEM) measurements. Figures 5B.2(a)- 5B.2(b) depict the images of laser-ablated spherical Au NPs and the size distribution histogram with the average size of ~15.3 nm. The variation of size and few chain-like structures were observed, which could be ascribed to the laser-induced agglomeration among Au NPs in 5 ml liquid.[24] Figures 5B.2(c)-

5B.2(d) show the images of chemically synthesized Au NPs with different shapes (triangular, spherical).

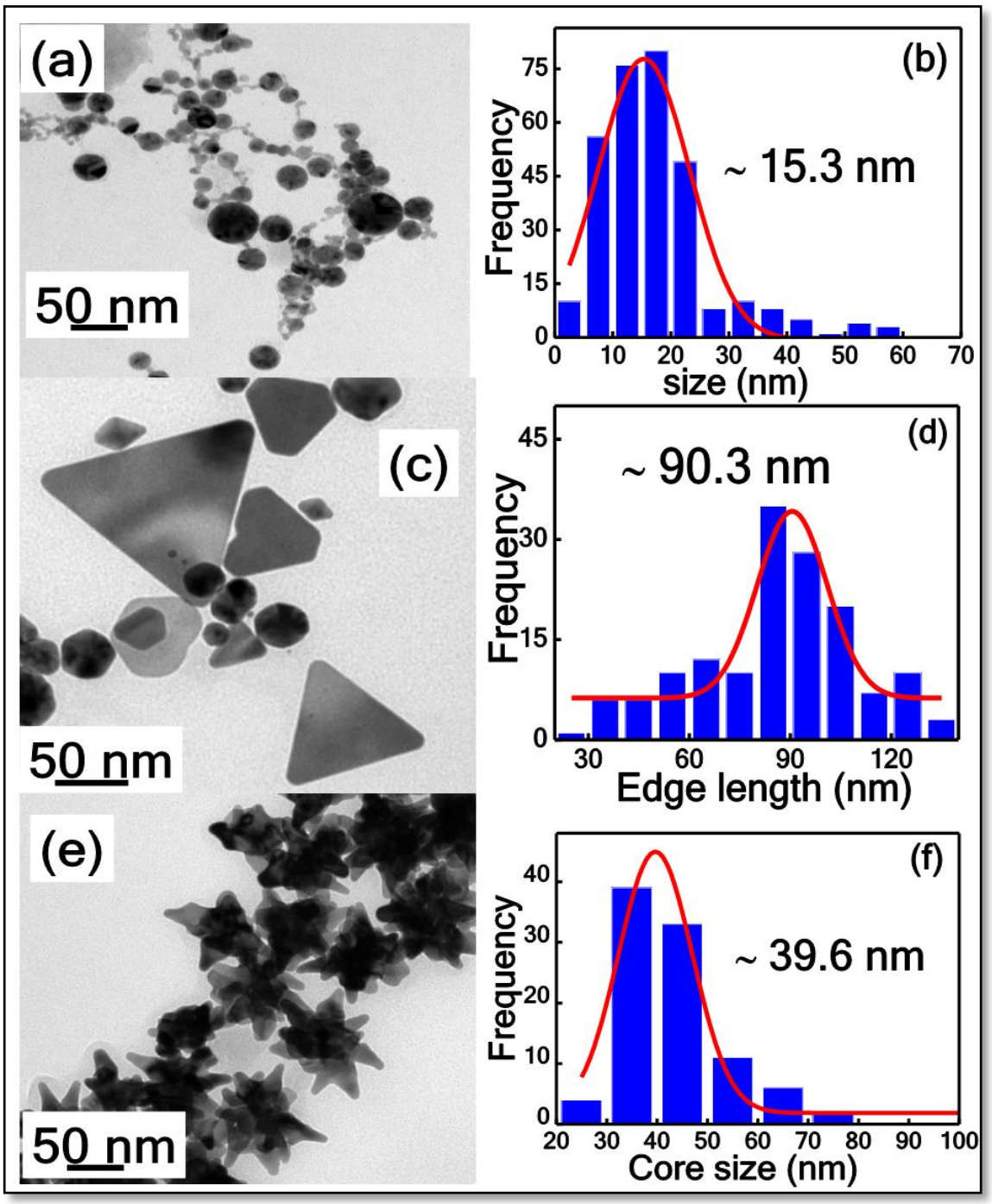

Figure 5B.2 TEM images of (a) spherical Au NPs achieved by LAL (c) Triangular (e) star Au NPs obtained by chemical methods (b), (d), and (f) represents the corresponding size distributions.

The edge length was found to be ~90.3 nm from the histogram data for Au triangles. However, the edge length of the triangular shaped NPs (~90 nm) was much higher than

the size of spherical Au NPs (~10 nm). Figures 5B.2(e)- 5B.2(f) depict the images of star-shaped Au NPs with more than ~6 tips and a histogram depicting the core size of ~39.6 nm. The difference in the size of the Au NSs and the tips could be attributed to the nucleation of anisotropic growth at multiple sites in the synthesis procedure.

5B.3.3 FESEM studies

Figure 5B.3 illustrates the FESEM images of bare FP and Au NPs loaded FP with the same scale bar of 200 nm. Figure 5B.3(a) displays the surface morphology of the bare FP with cellulose fibers and its porosity. The Au NPs deposition onto the FP and their distribution of spherical, triangular, and star-shaped Au NPs are illustrated in figures 5B.3[(b)-(d)], respectively. In all the cases Au NPs were uniformly distributed on the surface of the FP. A few NPs on the substrate seems to be agglomerated, preferably due to the porosity of the FP. This agglomeration plays a significant role in generating a more number of hotspots in the SERS measurements.

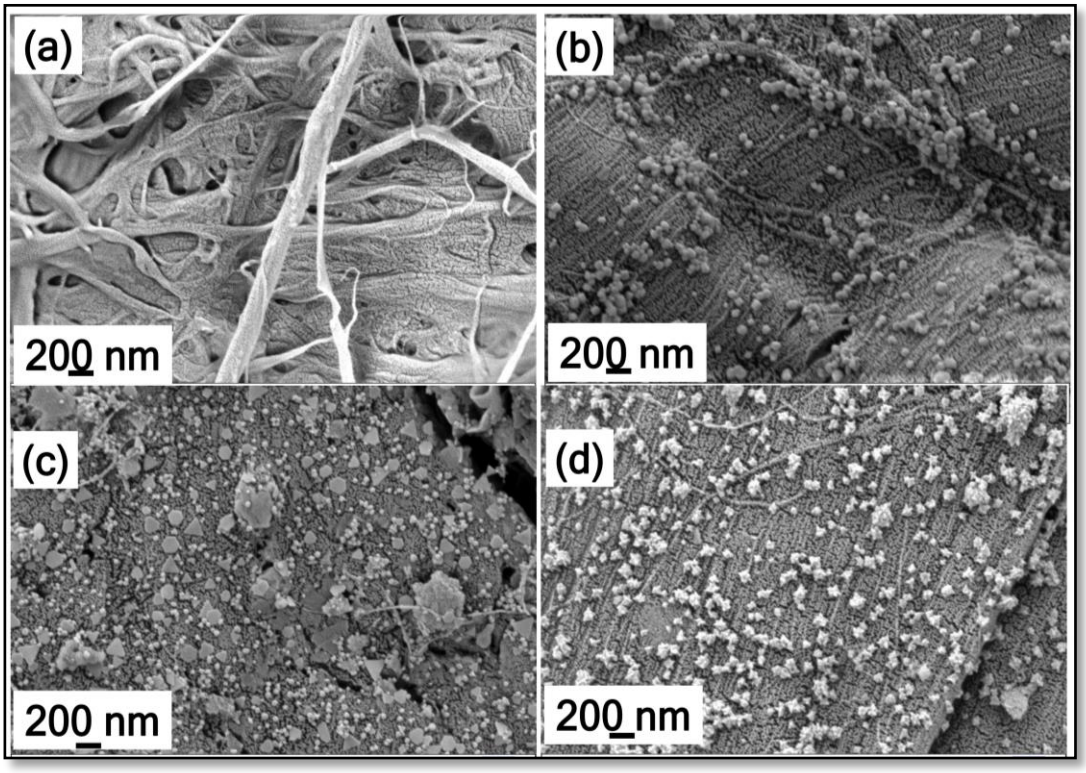

Figure 5B.3 FESEM images of (a) bare FP and FP loaded with (b) spherical (c) triangular (d) star Au NPs.

5B.4 SERS studies

5B.4.1 Effect of shape of NPs

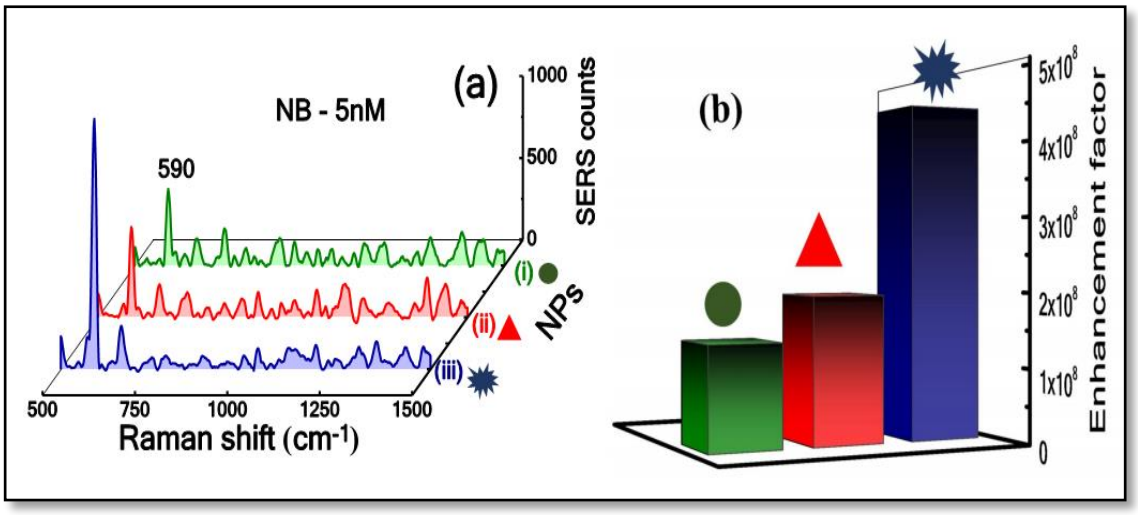

Figure 5B.4 (a) SERS spectra obtained from the spherical, triangular, and star-shaped Au NPs loaded the FP substrate after being dispersed with NB 5 nM. (b) Corresponding bar chart of estimated EFs for the most prominent peak of NB (590 cm $^{-1}$).

Nile blue (NB) is a highly toxic and low degradable dye molecule used widely in industry. The over usage of NB can significantly cause environmental issues for the world. The detection of these aromatic dyes was a great deal of concern to the environment as well as human health.[25] Figure 5B.4(a) shows the SERS spectra of NB (5 nM) drop-casted onto the NPs loaded FP substrate. The spectrum collected from Au spherical, triangular, and star-shaped NPs are represented with green, red, and blue colors. It was observed that NB molecule prominent mode was located at 590 cm^{-1} and is assigned to the C-C-C and C-N-C deformation, the peak assignment were mentioned in Appendix A.[26] The Raman intensity associated with the peak of 590 cm^{-1} in NB increased with increasing the hot-spots locations on the surface of the NPs i.e., spherical >triangular >star shaped NPs. The enhancement factors (EFs) were estimated by choosing the mode at 590 cm^{-1} observed from FP loaded with NPs in comparison with the typical Raman spectra (0.5 M) obtained from bare FP without NPs. The Raman spectra of 0.5 M NB on FP is provided in Appendix A. The sensitivity of the SERS substrate depends largely on the hotspots where local EM field is intense and, therefore, the Raman signals of the probe molecules at these locations are particularly strong and contribute to the main fraction of the signal. Here, compared to the spherical and triangular shapes, superior SERS signals were observed for star Au NPs

and this observation could be attributed to the more number of hotspots produced due to the presence of sharp features. The estimated EFs are ~1×10^8, ~1.9×10^8, and ~4.5×10^8 for spherical, triangular, and star-shaped Au NPs loaded FP, respectively. The histogram of the obtained EF's is shown in figure 5B. 4(b). Wang et al.[27] detected 10^{-5} M pATP with Ag nano triangles, nanosphere, and nanocubes based FP substrates and found that the SERS intensity varied as Ag nano triangles >Ag nanosphere >Ag nanocubes.

5B.4.2 Sensitivity and reproducibility SERS studies of FP with star-shaped Au NPs

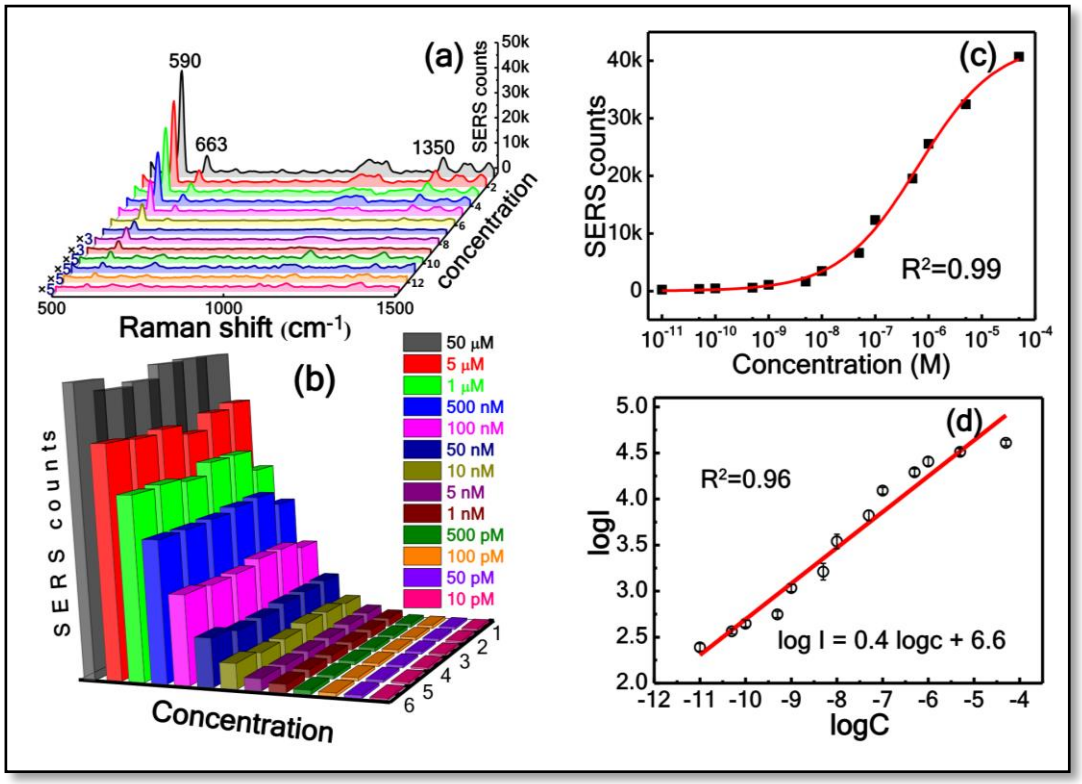

Figure 5B.5 (a) SERS spectra for the varying concentration of NB (50 µM to 10 pM). (b) NB peak intensity variation histogram for each concentration. (c) SERS counts vs. concentration of NB plot and (d) linear fit of the log I vs. log C plot of 590 cm^{-1}

The sensitivity of the FP loaded with star Au NPs was studied with the various concentrations of NB [ranging from 50 µM to 10 pM]. Even at a low concentration of 10 pM, the signals from NB were distinguishable and the data is presented in figure 5B.5(a). The estimated EF of NB at 10 pM was ~3.7×10^{10}. Recently, Xu et al.[25] achieved the LOD of NB as low as 0.5 nM using 3D porous Ni foam with gold cone array SERS substrate. SERS-based detection often suffers from the issue of poor signal repeatability, which

limits its practical applications. For each concentration, the SERS measurement was repeated six times, and further, the histogram of variation of the main peak (590 cm^{-1}) was considered for each concentration at six different positions on the same substrate, as shown in figure 5B.5(b). The small variation in the signal intensity justifies the uncontrolled distribution of hotspots in the FP substrate. Figure 5B.5(c) illustrates the SERS signal strength quantified using the height of the 590 cm^{-1} peaks. The data was fitted and the plot obtained is a Langmuir isotherm, with an R^2 of 0.99. Hoppmann et al.[28] studied the Langmuir isotherm fit of the 1207 cm^{-1} mode intensity versus concentration with an R^2 value of 0.99 for the trace level detection (1.8 ppb) of trans-1,2-bi-(4-pyridyl) ethylene (BPE) using Au NPs loaded inkjet printed FP substrate. Further, figure 5B.5(d) shows the log C versus log I, where the data is linear least square fitted with an R^2 value of 0.96. The error bars represent the standard deviation of the 590 cm^{-1} peak height. These studies indicate a high-quality fit and, therefore, FP loaded with star Au NPs has a strong potential as inexpensive SERS substrates in practical applications.

5B.5 COMSOL simulations

To understand the effects of near-field enhancement on these different shapes of Au NPs, simulations were conducted using commercially available COMSOL Multiphysics software. The shape and size of the NPs were almost intended as per TEM images viz spherical NPs with size as 15 nm, triangular shape with the edge as 90 nm and star shape with core as 40 nm with 8 tips of tip length ranging from 5 to 20 nm. The perfectly matched layer (PML) was created around the NPs to make a sense as an open boundary. This boundary was important to avoid any refection of the incident electromagnetic field and the physics controlled mesh was created with a resolution of 1 nm. The filed distribution was estimated in the electromagnetic wave frequency domain, the excitation wavelength of 785 nm, which was the same as the Raman excitation wavelength used to collect the SERS spectra. Observed electric fields near the NPs surface/edges/tips are significantly enhanced and the field falls off quickly as the distance from the NPs surface is increased. The obtained results are shown in figure 5B.6(a), 5B.6(b) and 5B.6(c). The maximum EF for spherical, triangular, and star-shaped NPs was 2.01 V/m, 4.64 V/m, and 7.79 V/m with an input electric field of 1 V/m (along X-axis). The Au NPs with sharp edges and tips exhibit significant field enhancement than the spherical shaped NPs. With the increase in the sharp features, an increase in field localization was observed.

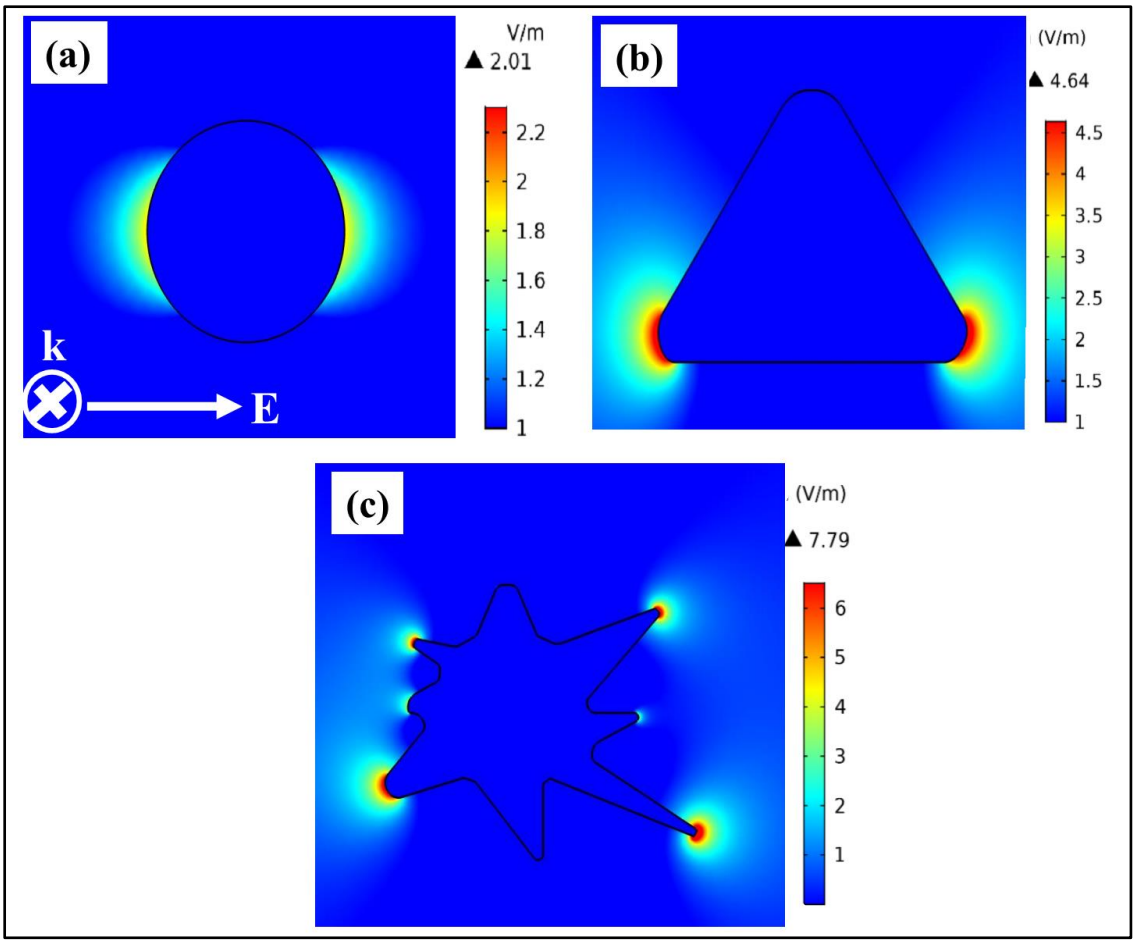

Figure 5B.6 (a) spherical, (b) triangle, and (c) star-shaped Au NPs simulated electromagnetic near-field distributions (indicated by the color bar) of a single NP. The field polarization direction is also mentioned in the figure.

Yukhymchuk et al.[29] simulated the starlike Au NPs and observed the maximum electric field distribution in the vicinity of the apex of the NP spikes. Rupali Das et al.[30] performed finite-difference time-domain simulations of electric field contour for Indium nano triangles and showed the maximum filed at the corners. Calderón et al.[31] reported the electric field distributions of Au bowtie nanoantennas (5 nm separation) with both lights polarized parallel and perpendicular to the axis of the nanoantennas using COMSOL Multiphysics simulations. They observed strong confinement of the field (100 times) within the gap with the light polarized electric field parallel to the major axis, and if the polarization is perpendicular, the enhancement was located around the other tips of the bowtie than the junction. Zhu et al.[32] examined the near filed distributions of Ag, Au, Cu, and Al pentagrams using the finite-difference time-domain (FDTD) and discrete dipole approximation (DDA) simulations. They noticed that Ag pentagrams exhibited the strongest resonance compared to Au and Cu pentagrams with the visible light, whereas Al

pentagram resonance is in the ultra-violet. Furthermore, the position of maximum electric field intensity along the flanks of the star for visible light, and at the tips of the star for near-infrared light excitations when the light was at 45° to the X and Y axes. Agrawal et al.[33] investigated the shape (sphere, round cube, cube, and octahedron) dependent filed enhancement of Indium-doped cadmium oxide nanocrystal using DDA numerical simulations. They noticed field enhancement was lower for spherical NPs with ~233 and ~260 times maximum enhanced field at the corners compared to edges and faces of a cube for cubes and octahedrons, respectively. William et al.[34] performed COMSOL multiphysics simulations on sprouted potato-shaped Au-Ag bimetallic NPs noticed maximum field at the tip of sprouts and also studied on dimers separated by 1 nm, 3 nm and 6 nm, perceived five times higher enhancement for sharp sprouts compared to blunt sprouts with 633 nm excitation. Liu et al.[35] simulated the energy dissipation of the spiky and urchin-like Ag-Au NPs and observed the enhancement of electrical field energy near the tips of the needle-like structures. Costa et al.[36] developed a method of moments (MoM) algorithm and presented a comparative study of circular and triangular Au nanodisks (same thickness and length) noticed four times enhancement in the near field for the triangular particle than a circular particle.

5B.6 Comparison SERS studies of star Au NPs with aggregated spherical NPs

The enormous electric field intensities were noticed at the junction between the two or more NPs and the sharp features of NPs called “hotspots” and these locations are the primary sources for higher SERS efficiency. In this study, the aggregation effect of spherical Au NPs (closely spaced NPs) was studied in chapter 5A and creating sharp features (star-shaped NPs) was studied previously in this chapter 5B. Here, the comparison SERS studies were performed on FP loaded with non-aggregated and aggregated spherical Au NPs, star-shaped Au NPs by choosing one dye molecule (NB) and one explosive molecule (PA) as the probe molecules.

5B.6.1 Dye molecule (NB) detection (aggregated spherical versus star-shaped Au NPs)

Non-aggregated spherical (fs laser ablated), aggregated spherical (fs laser ablated+NaCl 50 mM) and star shaped (chemical method) Au NPs loaded FP were considered as SERS substrates for the detection of dye NB (5 nM). The SERS data is shown in figure 5B.7(a). The Raman peaks of NB were observed at 590 cm^{-1} and 662 cm^{-1} (highlighted with yellow color) and the peak assignments were mentioned Appendix A. Compared to the pure NPs (without NaCl), superior SERS signals were observed for aggregated NPs, and the Au nanostars, which could be ascribed to the generated higher number of hotspots. For comparison, the Raman spectra of bare FP is shown with black color in figures 5B.7(a)-5B.7(i) and the prominent peak was observed at 1094 cm^{-1} (highlighted with grey color).

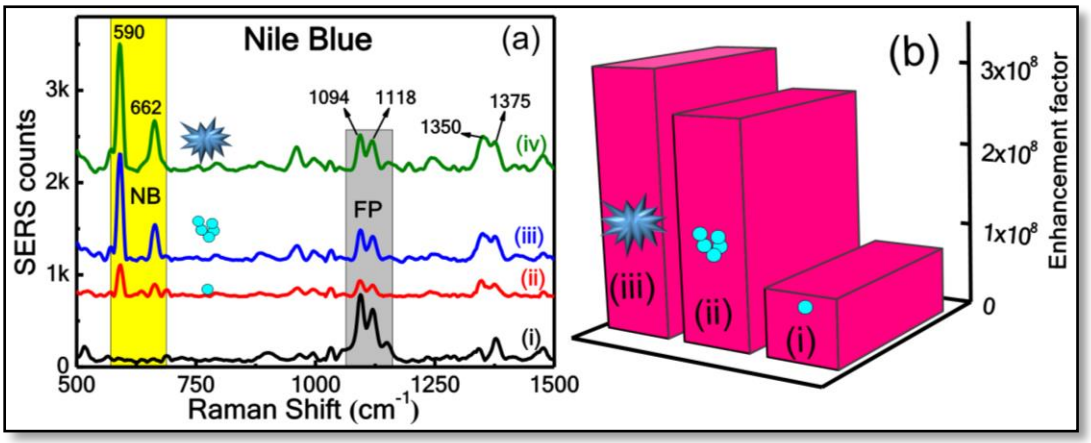

Figure 5B.7 Raman spectra (i) plain filter paper and the recorded SERS spectra of NB (5 nM) from NPs loaded FP (ii) laser-ablated Au NPs (spherical) (iii) salt-induced aggregated NPs (iv) Chemical synthesized Au nanostars. The highlighted grey colored region shows the Raman peaks from the FP while the yellow-colored area shows the Raman peaks exclusively from NB (b) The corresponding bar chart of estimated EFs for the most prominent peak of NB (590 cm^{-1}).

The main peak of 590 cm^{-1} was opted to calculate enhancement, and the EF comparison plot was shown in figure 5B.7(b). The achieved EFs were 8×10^7, 2.7×10^8, and 3.2×10^8 for non-aggregated spherical, aggregated spherical Au NPs and Au nanostars, respectively. The morphological features of particles could play a dominant role in SERS enhancements. We noticed the order of EF was the same in aggregated and star Au NPs loaded FP but ~4

times stronger SERS signals were observed for the Au nanostars compared to the non-aggregated Au NPs and ~1.2 times higher signals than the aggregated spherical Au NPs.

5B.6.2 Explosive molecule detection (aggregated spherical versus star shaped Au NPs)

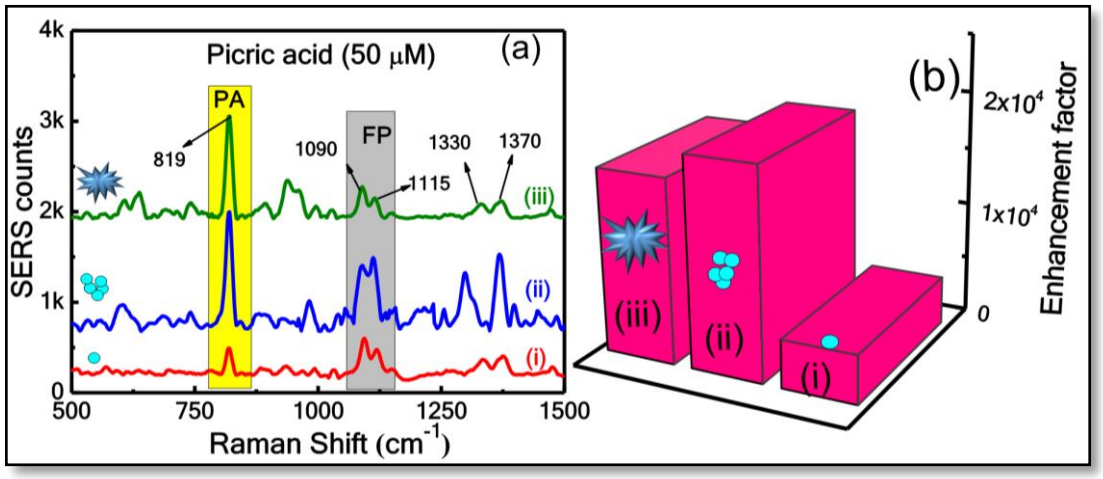

Figure 5B.8 (a) SERS spectra of PA (50 μM) on NPs loaded FP (i) laser-ablated spherical Au NPs (non-aggregated) (ii) salt-induced aggregated spherical Au NPs (iii) star-shaped Au NPs. The highlighted grey colored region shows the Raman peaks from the FP while the yellow-colored region shows the Raman peaks exclusively from PA (b) The corresponding bar chart of estimated EFs for the most prominent peak of PA (819 cm^{-1}).

Similarly, the SERS performance of all the FP based substrates was investigated using an explosive molecule (PA). SERS spectra of PA (50 μM) recorded from FP substrates were depicted in figure 5B.8(a). The most prominent peak of PA was found at 819 cm^{-1} (highlighted with yellow color); the peaks well coincide with previous work, and peak assignments were mentioned in the Appendix A. The EF's were calculated by choosing the 819 cm^{-1} peaks and the obtained EFs were ~ 4×10^3, ~1.8×10^4, and ~1.6×10^4 for non-aggregated spherical, aggregated spherical Au NPs, and Au nanostars, respectively, and the data is shown in figure 5B.8(b). The Raman spectra of PA- 0.1 M on the FP (without NPs) is provided in Appendix A. The aggregated Au NPs exhibited improved Raman signals than the non-aggregated Au NPs as well as the Au nanostars. These FP substrates were further tested for the detection of PA at lower concentrations (5 μM), and the data is depicted in figure 5B.9(a). At lower concentrations, the Raman signals from PA were not clearly identified with non-aggregated Au NPs. Aggregated NPs/NSs are expected to demonstrate higher SERS efficiency than individual NPs because of the more significant

SERS enhancement at their points of contact. The obtained EFs were 7.2×10^4 and 4×10^4 for the aggregated Au NPs and Au nanostars, respectively. A higher SERS signal (~1.8 times EF) was observed from the aggregated NPs compared to chemical synthesized Au nanostars.

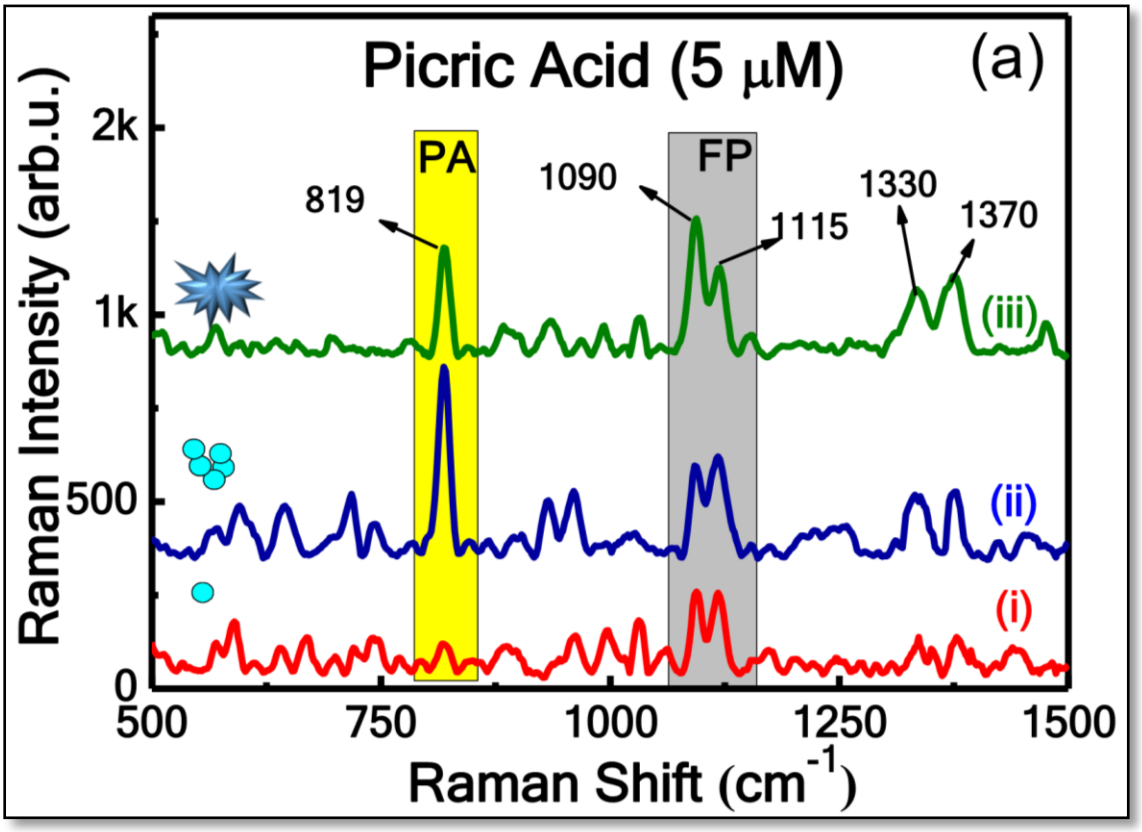

Figure 5B.9 SERS spectra of PA (5 μM) on NPs loaded FP (i) non -aggregated spherical Au NPs (ii) salt-induced aggregated spherical Au NPs (iii) star Au NPs. The highlighted grey colored region shows the Raman peaks from the FP while the yellow-colored region shows the Raman peaks exclusively from PA.

Therefore, FP loaded with both aggregated spherical Au NPs and star-shaped Au NPs demonstrated similar performance for dye/explosives detection. This could be attributed to the (i) the bare surface of laser-ablated NPs favoring the excitation of surface plasmons (ii) the presence of PVP in Au NSs (iii) absorption/orientation of the analyte molecule on the NPs surface. Besides the sensitivity and magnitude of EF, the reproducibility of a SERS substrate is also an essential parameter for practical applications, which is discussed in later sections.

5B.6.3 Reproducibility Studies

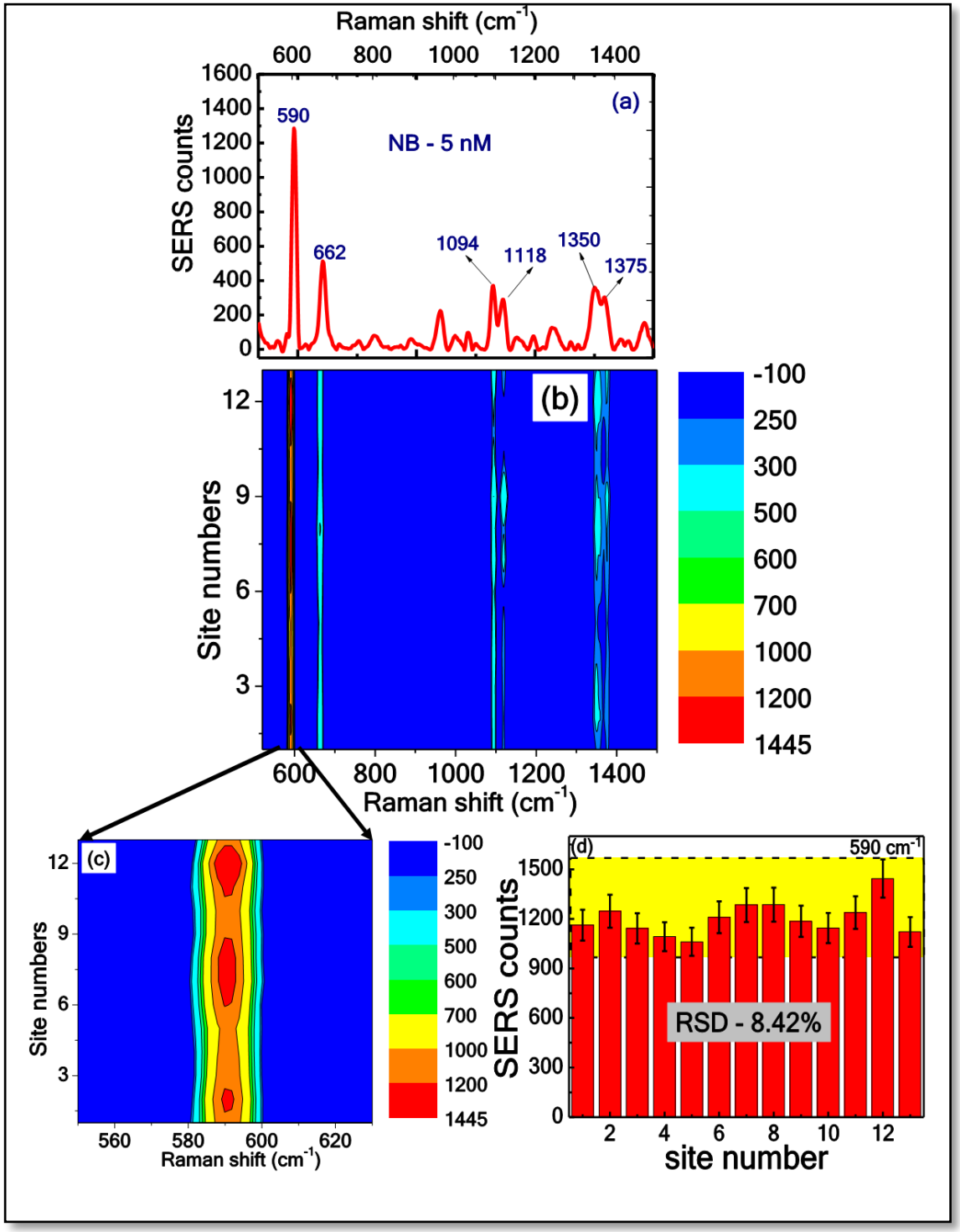

Figure 5B.10 Contour plot obtained from the 13 SERS spectra of NB (5 nM) recorded on FP loaded with aggregated Au NPs (a) SERS spectra of NB 5 nM (b) Contour plot represents the full spectra (c) magnified contour plot to represent single band 590 cm^{-1}. (d) Histogram plot of SERS intensities for the prominent NB Raman band (590 cm^{-1}) obtained from 13 spectra at different sites.

The reproducibility of FP with aggregated Au NPs and star-shaped Au NPs was verified using the dyes NB and PA. Figure 5B.10 presents NB-5 nm Raman contour plots[37] conveying both the reproducibility and intensity of the 13 spectral data sets corresponding to the FP with aggregated spherical Au NPs. Several bright lines were observed in figure 5B.10(b) and these represent the main Raman vibrations of NB (590 and 662 cm^{-1}) and FP (1094 and 1350 cm^{-1}). For comparison, one Raman spectra (out of 13) is provided in figure 5B.10(a). Origin software was utilized for carrying out this analysis. To further evaluate the uniformity of the measured SERS signals of the most prominent peak of NB 590 cm^{-1}, the single peak SERS contour was plotted and the data is depicted in figure 5B.10(c). The corresponding histogram is illustrated in figure 5B.10(d). The RSD of the intensity of 590 cm^{-1} was estimated to be 8.42%, which clearly demonstrates an excellent reproducibility of the FP substrates. Similarly, FP loaded with star-shaped Au NPs reproducibility data is presented as contour plot in figure 5B.11(a) while the corresponding histogram is shown in figure 5B.11(b) with an RSD of ~14.46 %.

Further, to manifest the uniformity of SERS signals using aggregated spherical and star shaped Au NPs loaded FP substrates was verified with the explosive molecule PA (5 µM). Figures 5B.11(c) and 5B.11(d) represents magnified contour plot and the corresponding histogram of the most significant Raman mode of PA 818 cm^{-1} from more than 10 different location using FP with aggregated spherical NPs. Figures 5B.11(e) and 5B.11(f) present the reproducibility data of PA (818 cm^{-1}) using FP with star Au NPs. The estimated RSDs values were found to be 5.8%, 18.8% for FP with aggregated and star Au NPs, respectively.

Therefore, the reproducibility results of both SERS substrates were evidenced that the of the major characteristic peak intensities variations having RSD values are >20%. These values indicate that numerous hotspots existed in the scanned area of the FP-SERS substrate, representing excellent uniformity. However, the narrow distribution of prominent peak intensities i.e., lower RSD values (> 9%), was noticed in the case of FP with aggregated spherical compared to FP with star-shaped Au NPs (>19%). Xian et al.[38] estimated the RSD for the SERS intensity of R6G- 1506 cm^{-1} peak as 4.29% from 15 different spots on Ag-based FP substrate. Lin and co-workers[39] reported spot to spot SERS signals variation of the CV (1617 cm^{-1}) with an RSD as 9.56% using FP with Au nanocubes. Lartey et al.[40] reported the RSD values of 4- nitrobenzenethiol-1332 cm^{-1} peak

as 21.2%, 14.0%, 13.8% and 13.2% using FP loaded with Ag NPs, Au NPs, Ag core-Au shell NPs and anisotropic Au NPs, respectively.

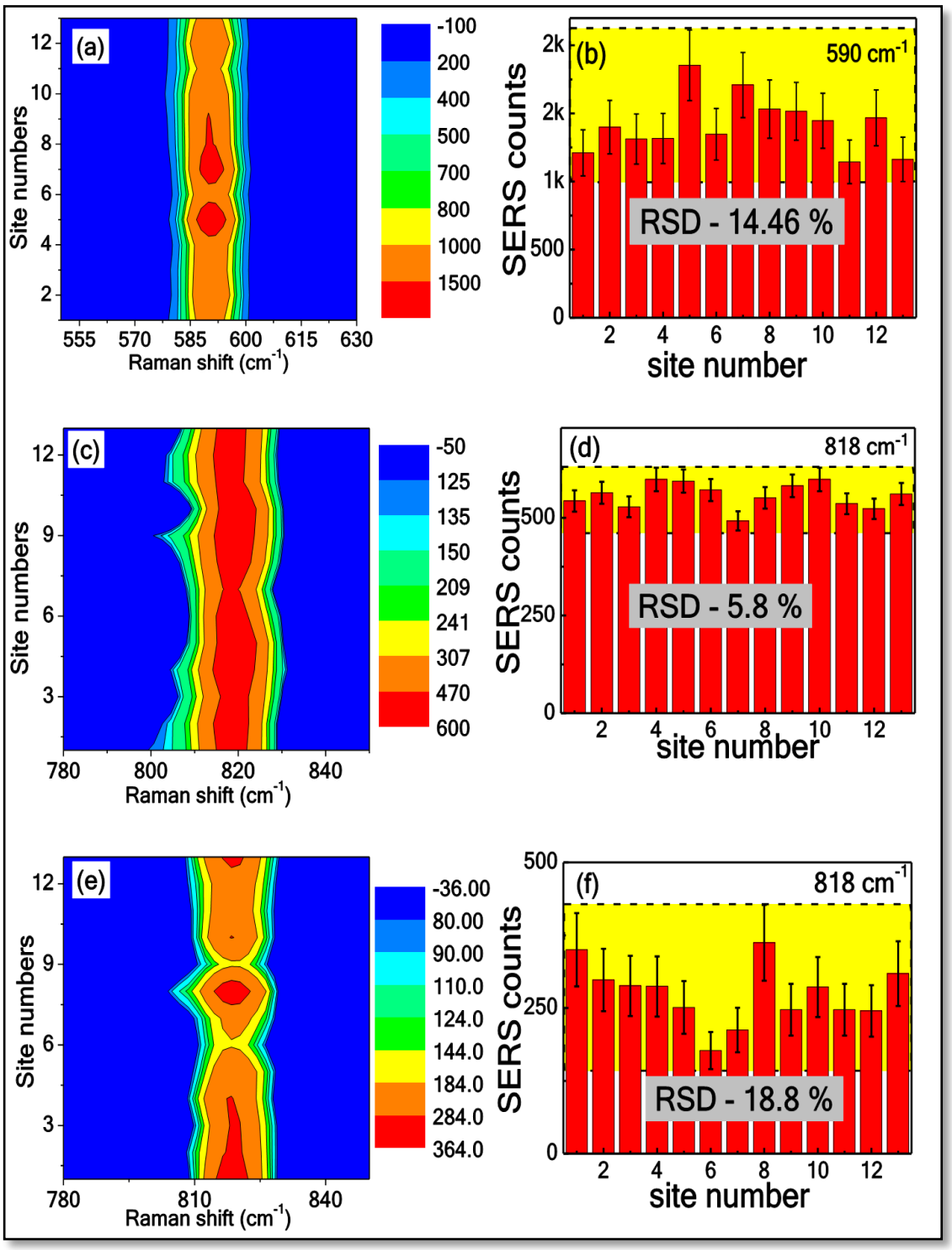

Figure 5B.11 SERS spectra contour plots and histogram plots of SERS intensities (a and b) NB 5 nM (590 cm^{-1}) using FP loaded with star Au NPs (c and d) PA 5 µM (818 cm^{-1}) using FP with aggregated spherical Au NPs (e and f) PA 5 µM (818 cm^{-1}) using FP with star Au NPs.

5B.7 Conclusions

Flexible FP substrate loaded different shaped Au NPs were prepared and their SERS performance was studied. Spherical NPs were synthesized by fs laser ablation technique and triangular; star-shaped Au NPs were synthesized by chemical routes. These Au NPs loaded onto FP and were further characterized by FESEM technique to confirm the distribution of NPs. The three-dimensional and porous structured FP- SERS substrates offer the benefits of superior surface area to localize the adsorption of NPs over the traditional rigid substrates. Through the COMSOL simulations (plasmonic properties of different shaped Au NPs), it was proved that the sharp edges and tips of the Au NPs boost the SERS activity. A similar trend i.e. EF of FP with spherical > triangular > star-shaped NPs was observed in experimental SERS studies during the detection of NB (5 nM). Further, the star Au NPs loaded onto the FP SERS substrate has exhibited the superior sensitivity even in the detection of 10 pM concentration, with an EF of 3.7×10^{10} and excellent reproducibility.

Taking a cue from the previous results, the optimized aggregated spherical (50 mM –NaCl) and star-shaped Au NPs were considered as superior flexible paper-based SERS substrates. The comparison studies were performed on both the FP substrate with NB-5 nM and PA-5 µM molecules. The aggregated and Au nanostars loaded FP acted as promising SERS substrates compared to non-aggregated NPs in the detection of the analytes and the achieved EF's for PA were 7.2×10^{4} and 4×10^{4} while for NB they were 2.7×10^{8} and 3.2×10^{8}, respectively. For dye and explosive molecules, the reproducibility studies proved that aggregated spherical NPs are >9% and >19% for aggregated spherical and star-shaped Au NPs FP.

5B.8 References

1. Song, G.; Zhou, H.; Gu, J.; Liu, Q.; Zhang, W.; Su, H.; Su, Y.; Yao, Q.; Zhang, D., Tumor Marker Detection Using Surface Enhanced Raman Spectroscopy on 3D Au Butterfly Wings. *J. Mater. Chem. B* **2017**, *5*, 1594-1600.
2. Feng, J.; Chen, L.; Xia, Y.; Xing, J.; Li, Z.; Qian, Q.; Wang, Y.; Wu, A.; Zeng, L.; Zhou, Y., Bioconjugation of Gold Nanobipyramids for SERS Detection and Targeted Photothermal Therapy in Breast Cancer. *ACS Biomater. Sci. & Eng.* **2017**, *3*, 608-618.
3. Ma, W.; Yang, H.; Hilton, J.; Lin, Q.; Liu, J.; Huang, L.; Yao, J., A Numerical Investigation of the Effect of Vertex Geometry on Localized Surface Plasmon Resonance of Nanostructures. *Opt. Express* **2010**, *18*, 843-853.
4. Shiohara, A.; Novikov, S. M.; Solís, D. M.; Taboada, J. M.; Obelleiro, F.; Liz-Marzán, L. M., Plasmon Modes and Hotspots in Gold Nanostar–Satellite Clusters. *J. Phys. Chem. C* **2015**, *119*, 10836-10843.
5. Tian, F.; Bonnier, F.; Casey, A.; Shanahan, A. E.; Byrne, H. J., Surface Enhanced Raman Scattering with Gold Nanoparticles: Effect of Particle Shape. *Anal. Methods* **2014**, *6*, 9116-9123.
6. Minati, L.; Benetti, F.; Chiappini, A.; Speranza, G., One-Step Synthesis of Star-Shaped Gold Nanoparticles. *Colloids Surf., A* **2014**, *441*, 623-628.
7. Sandu, T., Shape Effects on Localized Surface Plasmon Resonances in Metallic Nanoparticles. *J. Nanopart. Res.* **2012**, *14*, 905.
8. Shiohara, A.; Wang, Y.; Liz-Marzán, L. M., Recent Approaches toward Creation of Hotspots for SERS Detection. *J. Photochem. Photobiol. C; Photochem. Reviews* **2014**, *21*, 2-25.
9. Kleinman, S. L.; Frontiera, R. R.; Henry, A.-I.; Dieringer, J. A.; Van Duyne, R. P., Creating, Characterizing, and Controlling Chemistry with SERS Hotspots. *Phys. Chem. Chem. Phys.* **2013**, *15*, 21-36.
10. Krajczewski, J.; Michałowska, A.; Kudelski, A., Star-Shaped Plasmonic Nanostructures: New, Simply Synthetized Materials for Raman Analysis of Surfaces. *Spectrochimica Acta Part A: Molecular and Biomolecular Spectroscopy* **2020**, *225*, 117469.
11. Lee, H. K.; Lee, Y. H.; Koh, C. S. L.; Phan-Quang, G. C.; Han, X.; Lay, C. L.; Sim, H. Y. F.; Kao, Y.-C.; An, Q.; Ling, X. Y., Designing Surface-Enhanced Raman Scattering (SERS) Platforms Beyond Hotspot Engineering: Emerging Opportunities in Analyte Manipulations and Hybrid Materials. *Chem. Soc. Rev.* **2019**, *48*, 731-756.
12. Jeon, T. Y.; Kim, D. J.; Park, S.-G.; Kim, S.-H.; Kim, D.-H., Nanostructured Plasmonic Substrates for Use as SERS Sensors. *Nano Convergence* **2016**, *3*, 18.
13. Oliveira, M. J.; Quaresma, P.; Peixoto de Almeida, M.; Araújo, A.; Pereira, E.; Fortunato, E.; Martins, R.; Franco, R.; Águas, H., Office Paper Decorated with Silver Nanostars - an Alternative Cost Effective Platform for Trace Analyte Detection by SERS. *Sci. Rep.* **2017**, *7*, 2480.
14. Ge, S.; Zhang, L.; Zhang, Y.; Lan, F.; Yan, M.; Yu, J., Nanomaterials-Modified Cellulose Paper as a Platform for Biosensing Applications. *Nanoscale* **2017**, *9*, 4366-4382.
15. Mahadeva, S. K.; Walus, K.; Stoeber, B., Paper as a Platform for Sensing Applications and Other Devices: A Review. *ACS Appl. Mater. & Interf.* **2015**, *7*, 8345-8362.

16. Wang, S.; Chinnasamy, T.; Lifson, M. A.; Inci, F.; Demirci, U., Flexible Substrate-Based Devices for Point-of-Care Diagnostics. *Trends Biotechnol.* **2016**, *34*, 909-921.
17. Kwon, G.; Kim, J.; Kim, D.; Ko, Y.; Yamauchi, Y.; You, J., Nanoporous Cellulose Paper-Based SERS Platform for Multiplex Detection of Hazardous Pesticides. *Cellulose* **2019**, *26*, 4935-4944.
18. Weng, G.; Feng, Y.; Zhao, J.; Li, J.; Zhu, J.; Zhao, J., Size Dependent SERS Activity of Ag Triangular Nanoplates on Different Substrates: Glass Vs Paper. *Appl. Surf. Sci.* **2019**, *478*, 275-283.
19. Zhou, R.; Wu, Z.; Sun, Z.; Su, X., Sensitive Surface Enhanced Raman Scattering Substrates Based on Filter Paper Loaded with Au Porous Nanospheres. *Nanoscience and Nanotechnology Letters* **2015**, *7*, 801-805.
20. Ma, Y.; Wang, Y.; Luo, Y.; Duan, H.; Li, D.; Xu, H.; Fodjo, E. K., Rapid and Sensitive on-Site Detection of Pesticide Residues in Fruits and Vegetables Using Screen-Printed Paper-Based SERS Swabs. *Anal. Methods* **2018**, *10*, 4655-4664.
21. He, S.; Chua, J.; Tan, E. K. M.; Kah, J. C. Y., Optimizing the SERS Enhancement of a Facile Gold Nanostar Immobilized Paper-Based SERS Substrate. *RSC Adv.* **2017**, *7*, 16264-16272.
22. Nehra, K.; Pandian, S. K.; Bharati, M. S. S.; Soma, V. R., Enhanced Catalytic and SERS Performance of Shape/Size Controlled Anisotropic Gold Nanostructures. *New J. Chem.* **2019**, *43*, 3835-3847.
23. Lee, C. H.; Tian, L.; Singamaneni, S., Paper-Based SERS Swab for Rapid Trace Detection on Real-World Surfaces. *ACS Appl. Mater. & Interf.* **2010**, *2*, 3429-3435.
24. Byram, C.; Moram, S. S. B.; Shaik, A. K.; Soma, V. R., Versatile Gold Based SERS Substrates Fabricated by Ultrafast Laser Ablation for Sensing Picric Acid and Ammonium Nitrate. *Chem. Phys. Lett.* **2017**, *685*, 103-107.
25. Xu, F.; Lai, H.; Xu, H., Gold Nanocone Arrays Directly Grown on Nickel Foam for Improved SERS Detection of Aromatic Dyes. *Anal. Methods* **2018**, *10*, 3170-3177.
26. Rekha, C. R.; Sameera, S.; Nayar, V. U.; Gopchandran, K. G., Simultaneous Detection of Different Probe Molecules Using Silver Nanowires as SERS Substrates. *Spectrochimica Acta Part A: Molecular and Biomolecular Spectroscopy* **2019**, *213*, 150-158.
27. Wang, C.; Liu, B.; Dou, X., Silver Nanotriangles-Loaded Filter Paper for Ultrasensitive SERS Detection Application Benefited by Interspacing of Sharp Edges. *Sens. Actuators, B* **2016**, *231*, 357-364.
28. Hoppmann, E. P.; Wei, W. Y.; White, I. M., Highly Sensitive and Flexible Inkjet Printed SERS Sensors on Paper. *Methods* **2013**, *63*, 219-224.
29. Yukhymchuk, V. O.; Hreshchuk, O. M.; Dzhagan, V. M.; Sakhno, M. V.; Skoryk, M. A.; Lavoryk, S. R.; Rudko, G. Y.; Matveevskaya, N. A.; Beynik, T. G.; Valakh, M. Y., Experimental Studies and Modeling of "Starlike" Plasmonic Nanostructures for SERS Application. *physica status solidi (b)* **2018**, *2*, 1800280.
30. Das, R.; Soni, R., Synthesis and Surface-Enhanced Raman Scattering of Indium Nanotriangles and Nanowires. *RSC Adv.* **2017**, *7*, 32255-32263.
31. Calderón, J.; Álvarez, J.; Martinez-Pastor, J.; Hill, D. In *Bowtie Plasmonic Nanoantenna Arrays for Polarimetric Optical Biosensing*, Frontiers in Biological Detection: From Nanosensors to Systems VI, International Society for Optics and Photonics: **2014**; 89330I.

32. Zhu, S.; Cortie, M.; Blakey, I., Effect of Multimodal Plasmon Resonances on the Optical Properties of Five-Pointed Nanostars. *Nanomater. Nanotechnol.* **2015**, *5*, 5-22.
33. Agrawal, A.; Kriegel, I.; Milliron, D. J., Shape-Dependent Field Enhancement and Plasmon Resonance of Oxide Nanocrystals. *J. Phys. Chem. C* **2015**, *119*, 6227-6238.
34. William, R.; Das, G. M.; Dantham, V. R.; Laha, R., Enhancement of Single Molecule Raman Scattering Using Sprouted Potato Shaped Bimetallic Nanoparticles. *Sci. Rep.* **2019**, *9*, 1-12.
35. Liu, R.-S.; Cheng, L.-C.; Huang, J.-H.; Chen, H.; Lai, T.-C.; Hsiao, M.; Chen, C.-H.; Yang, K.-Y.; Tsai, D. P.; Her, L.-J., Highly Efficient Urchin-Like Bimetallic Nanoparticles for Photothermal Cancer Therapy. *SPIE Newsroom* **2013**, 2-4.
36. Costa, K. Q. d.; Dmitriev, V., Comparative Analysis of Circular and Triangular Gold Nanodisks for Field Enhancement Applications. *Journal of Microwaves, Optoelectronics and Electromagnetic Applications* **2010**, *9*, 123-130.
37. Quan, J.; Zhu, Y.; Zhang, J.; Li, J.; Wang, N., High-Performance Surface-Enhanced Raman Scattering Substrate Prepared by Self-Assembling of Silver Nanoparticles into the Nanogaps of Silver Nanoislands. *Appl. Opt.* **2017**, *56*, 5751-5760.
38. Xian, L.; You, R.; Lu, D.; Wu, C.; Feng, S.; Lu, Y., Surface-Modified Paper-Based SERS Substrates for Direct-Droplet Quantitative Determination of Trace Substances. *Cellulose* **2020**, *27*, 1483-1495.
39. Lin, S.; Lin, X.; Song, X.; Han, S.; Wang, L.; Hasi, W., Fabrication of Flexible Paper-Based Surface-Enhanced Raman Scattering Substrate from Au Nanocubes Monolayer for Trace Detection of Crystal Violet on Shell. *J. Raman Spectros.* **2019**, *50*, 1074-1084.
40. Lartey, J. A.; Harms, J. P.; Frimpong, R.; Mulligan, C. C.; Driskell, J. D.; Kim, J.-H., Sandwiching Analytes with Structurally Diverse Plasmonic Nanoparticles on Paper Substrates for Surface Enhanced Raman Spectroscopy. *RSC Adv.* **2019**, *9*, 32535-32543.

Intentional blank page

5C. Nanofibers with Au NPs for SERS obtained using electrospinning technique

Abstract

The third section of chapter 5 describes the preparation and characterization of electrospinning polymer nanofiber mats loaded with picosecond laser-ablated gold nanoparticles (Au NPs) as novel flexible SERS substrates. The electrospinning technique was initiated to synthesize flexible PVA-nanofibers by varying the concentration of the polymer poly-vinyl alcohol (PVA, 5%, 10%, and 30 wt%) with a fixed nozzle-collector distance and the applied electric potential. The optimized PVA concentration (10 wt%) was achieved by verifying the formation of smooth and long fibers (without beads) using FESEM data. Picosecond laser pulses (~30 ps, 1064 nm, 10 Hz) were used to fabricate Au NPs in distilled water and were added to PVA before the electrospinning process. The Au NPs were characterized by UV-Visible absorption and TEM techniques. The characterization of the polymer nanofiber with and without NPs was performed using FESEM, TEM, and XRD techniques. The prepared, flexible PVA-Au NPs substrates were used to detect the dye molecule methylene blue (MB- 5 µM) and methyl salicylate (MS - 10 mM) using the SERS technique. The obtained results indicate that plasmonic nanofiber mats represent novel, flexible SERS sensors and their sensitivity could be further improved by changing the polymer and different sized/shaped anisotropic metal NPs.

5C.1 Introduction

Electrospinning is recognized as one of the efficient methods to produce continuous nanofibers with low cost from a huge range of materials such as polymers, composites, ceramics, semiconductors, and metals.[1] In recent years nanofibers have attained great interest in various fields[2] including drug delivery,[3-4] filter media,[5] protective clothing,[6] tissue engineering,[7-8] antibacterial materials,[9] and as SERS substrates.[10] Although there are many versatile methods of producing SERS substrates, nanofiber substrates have grasped serious attention recently from SERS community because they offer several benefits such as flexibility, good mechanical strength, and continuously interconnected pores with their vast surface area to volume ratio helping to load a higher number of nanoparticles (NPs).[11-12] Technically, electrospinning is a process of converting polymer from solution to solid nanofibers in the presence of a strong electrical force. The morphology and thickness of produced fibers depend on the process parameters (applied voltage, flow rate, the distance between electrodes, collector type, etc.) and materials parameters (a type of polymer, molecular weight, surface tension, viscosity, etc.).[13-15] The conversion of polymer nanofibers into SERS active plasmonic fibers is possible in the presence of metal NPs. Various strategies are involved in the fabrication of plasmonic nanofibers, which include direct addition of already prepared NPs into the pre-electrospinning polymer solutions, vapor deposition/addition of NPs on post-spinning processes of nanofibers, in situ reduction method of metal salts into the polymer solution, photo-reduction and electrodeposition.[12, 16-25] Shi et al.[16] have fabricated polyacrylonitrile (PAN) nanofibers loaded with Ag NPs using silver mirror reaction, i.e. soaking small pieces of (2.5 cm^2) nano fibrous membrane soaked in (2 and 5 wt%) $AgNO_3$ solution in a dark container for one day and subsequently freeze-dried for one day. Recently, several reports have demonstrated the development of electrospun SERS active nanofiber by attaching MNPs.[26] For example, Zhang et al.[9] synthesized Ag-PVP nanofibers by adding Ag NPs to the PVA solution before electrospinning and used to detect 10^{-8} M 4-mercaptophenol (4-MPh) molecules. Chamuaha et al.[10] detected 10 nM MG using 30-nm thick gold-coated electrospun PVA nanofiber via thermal evaporation technique. Kong et al.[27] synthesized Ag NPs decorated polyimide (PI) nano fabric via ion exchange-in situ reduction and employed as a SERS platform for the detection of very low concentration of p-ATP (10^{-14} M). Zhang et al.[28] fabricated the SERS sensors with polyacrylonitrile

(PAN) loaded Ag NPs through electrospinning and seed-mediated electro-less plating and utilized to detect Rhodamine 6G at the concentration of 1000 ppb. Zhao et al.[29] fabricated TiO_2 Nanofibrous mat loaded with Ag NPs by electroless plating and verified the SERS efficiency with three molecule (4-MBA, R6G, and 4-ATP) and also investigated the UV-cleanable property. Zhang and co-workers[30] reported the detection of 10^{-4} M DTTCI (3,3′-diethylthi-atricarbocyanine iodide) using Au NRs/PVA nanofiber mat.

Here, poly-vinyl alcohol (PVA) nanofibers with Au NPs flexible SERS platform were prepared by the electrospinning technique on an aluminum foil. Initially, smooth continuous PVA nanofibers were fabricated by optimizing the PVA concentration. Pure Au NPs were fabricated using picosecond (30 ps, 1064 nm, 10 Hz) laser ablation of the Au target dipped in 5 ml of distilled water. The synthesized Au NPs were characterized by UV-visible absorption and TEM techniques. Later, these synthesized Au NPs were centrifuged and added to the PVA solution before electrospinning process. The plasmonic nanofibers were characterized by FESEM, TEM, and XRD techniques. Metal NPs doped nanofibers have a large number of exposed NPs on the surface, which offer a huge number of hotspots that enhance the Raman signals of any interested probe molecule. In the present chapter the SERS studies of PVA-Au NPs nanofiber substrates are presented, which were used to detect methylene blue (MB) and methyl salicylate (MS).

5C.2 Experimental details

5C.2.1 Fabrication of polymer nanofibers

Several polymers have been used to form nanofibers such as synthetic, semisynthetic, and biological polymers. However, all the polymers are not beneficial in forming solid nanofibers. PVA is a hydrophilic, biocompatible polymer and exhibits excellent physical properties, for example high strength, water-solubility, gas permeability, and good thermal stability.[14] Firstly, the electrospinning conditions were optimized by investigating the polymer solution concentrations, which is the crucial factor affecting the output. Three different concentrations of PVA 5 wt%, 10 wt%, and 30 wt % solutions were prepared in deionized water at 80 °C in the ultrasonic bath. For the deposition of PVA nanofibers, the electrospinning system (ESPIN-NANO, India) utilized at a voltage of 16 kV. The rotating disk collector used to collect the sample, which was covered by an aluminum foil. The collector was rotated at a speed of 1500 rpm. A 5 ml syringe was used to fill the PVA

solution without air bubbles and a flow rate of 0.5 ml per hour was maintained. The distance between the tip of the syringe needle and the collector was adjusted to 15 cm. All the three concentrations of PVA nanofibers were fabricated on an electrospinning apparatus operated at the same conditions. The best electrospinning condition was filtrated from the FESEM data of the obtained nanofibers. The photograph of the electrospinning and peeled nanofiber from the aluminum foil depicted in experimental details (chapter 2).

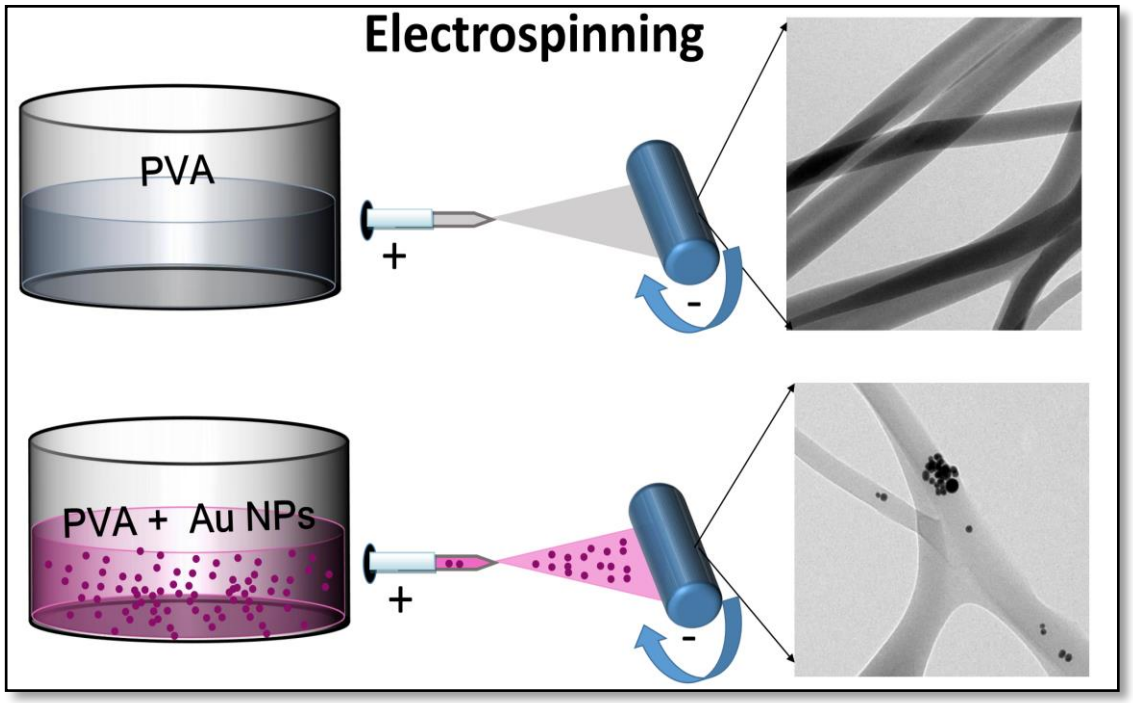

Figure 5C.1 Schematic of synthesis of PVA and Au NPs-PVA nanofibers using the electrospinning technique.

5C.2.2 Synthesis of Au NPs

Pure Au NPs were prepared laser ablation in liquid technique using picosecond (ps) laser ablation of the gold target in distilled water. The amplifier system delivers pulses of ~30 ps pulse duration at 335/532/1064 nm wavelengths operating at 10 Hz repetition rate. Here, ps laser delivered ~30 ps laser at 1064 nm while ~20 mJ input pulse energy was used to ablate the Au target. The Au sample was placed at the bottom of the glass beaker containing ~5 mL distilled water (DW), and it was mounted on a computer-controlled X-Y stage. The ps pulses focused onto the sample surface using a plano-convex lens with a focal length of 100 mm. While doing the laser ablation experiments, the sample was raster scanned to avoid the single point ablation on Au surface. The sample scanned with the help of motorized stages along X and Y directions at a speed of 0.1 mm per second.

5C.2.3 Fabrication Au NPs-PVA nanofibers

The optimized concentration of PVA solution with Au NPs was prepared by adding 9 ml of deionized water in 1 g PVA at 80 °C. The prepared Au NPs were centrifuged and dispersed in 1 ml of distilled water and added to the PVA solution [cooling off to room temperature] step by step to disperse uniformly through the solution using a magnetic stirrer. The color of the PVA solution transformed from transparent to dark pink. The Au NPs loaded PVA solution was placed in a 5 ml syringe for electrospinning; the same conditions have been applied. A schematic and images of bare PVA nanofiber and Au NPs loaded PVA nanofiber are illustrated in figure 5C.1

5C.3 Characterization

5C.3.1 UV-visible absorption spectra

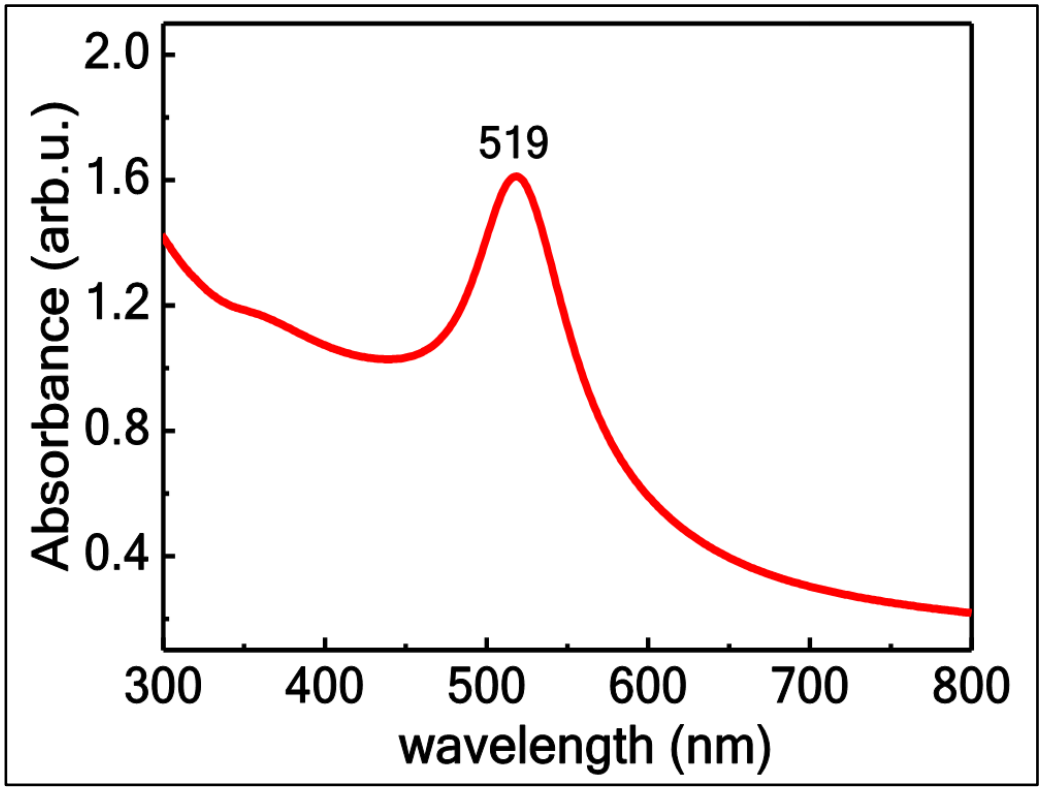

Figure 5C.2 UV-visible absorption spectra of the ps-laser ablated gold NPs.

5C.3.2 FESEM studies

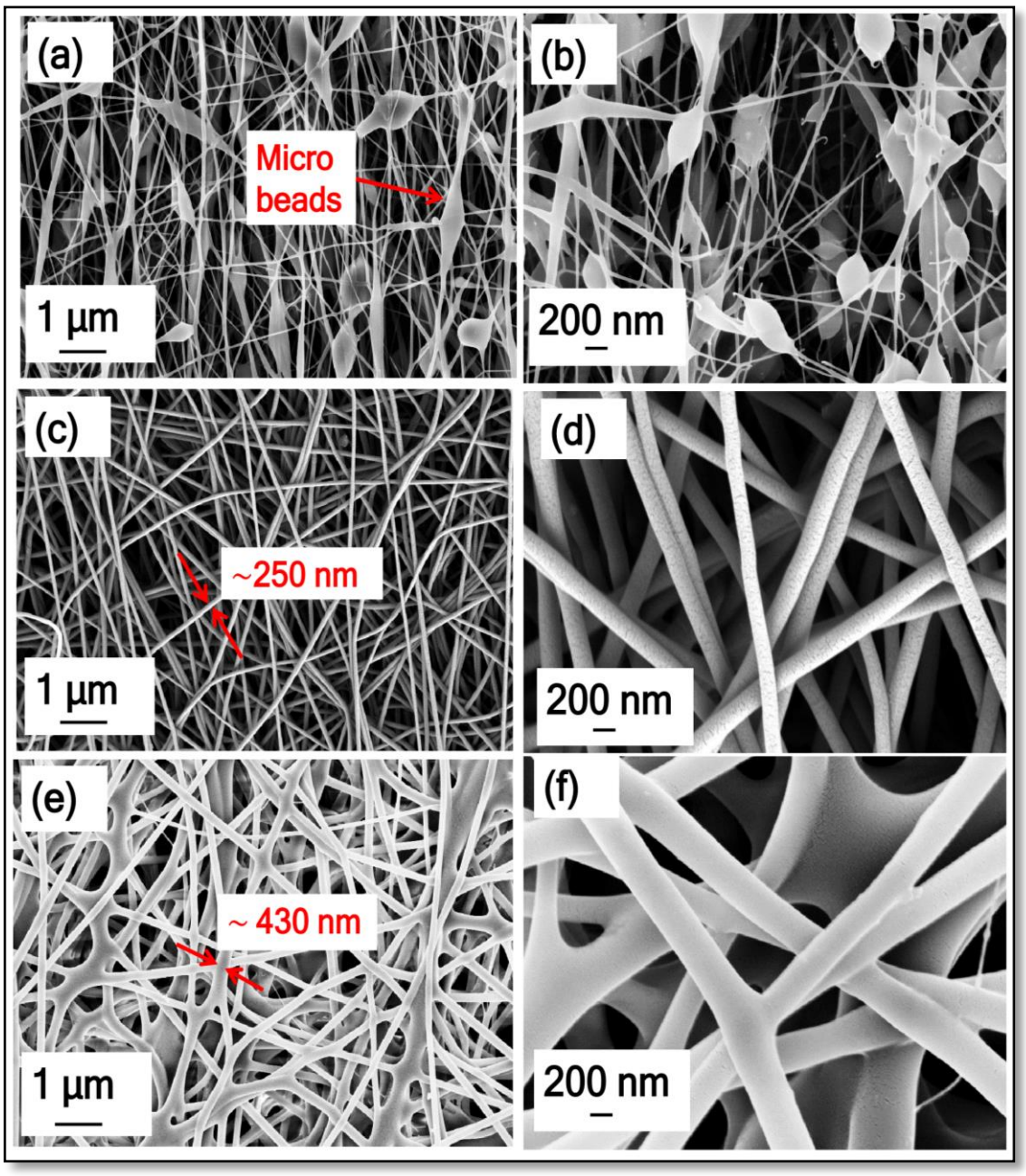

Figure 5C.3 FESEM images of PVA nanofibers obtained for (a) 5 wt%, lower magnification (b) 5 wt%, higher magnification (c) 10 wt%, lower magnification (d) 10 wt%, higher magnification (e) 30 wt%, lower magnification (f) 30 wt%, higher magnification

Figure 5C.2(a) represents the UV-Visible absorption spectra of the synthesized ps-LAL Au NPs in distilled water. The plasmon band of Au NPs was observed at ~519 nm. Previously, we have reported ps laser-ablated Au NPs (532 nm) at different pulse energies and utilized as SERS substrate for the detection of dye/explosive mixture.[31] The ablation rate depends on the wavelength and a higher ablation rate was noticed at 1064 nm laser

compared to 355 nm.[32] Therefore, with increasing wavelength of laser ablation the ablation rate was higher and, accordingly, the yield of the NPs was higher. Polymer fibers produced from electrospinning typically have diameters in the range of sub-microns to the nanometer. To verify the thickness of the prepared nanofibers, FESEM analysis was performed. A thin gold layer was sputtered on all the samples before the measurements. The SEM images of the nanofibers at three different concentrations 5 w%, 10 wt%, and 30 wt% were illustrated in figures 5C.3(a), 5C.3(b) and 5C.3(c), respectively. At 5 wt % of PVA, nanofibers with microbeads were observed. At higher concentrations, i.e., at 10 and 30 wt %, an electrospun mat containing only fiber without beads was noticed. The polymer solution has a sufficient molecular chain to prevent the formation of beads. The thickness of the fiber increased from ~250 nm to ~ 430 nm, with increasing concentration from 10 wt% to 30 wt%.[33] Husain et al.[34] studied fiber morphologies of the PLGA (poly lactic-co-glycolic acid) polymer between 2 and 25 wt% concentrations, noticed particles (<10 %), particles with beads on strings (<20 %) and bead-less fibers (>20 %) and smooth fibers observed with increasing concentration. Zhang et al.[9] observed a similar trend that when the PVA's concentration was at 6% → fibers were not continuous and large number of beads; at 7%-8% → uniform nanofibers and no beads and at 9%-10% → thick fibers tend to aggregate when arriving at the fiber collector. In the present case, at 10 wt % PVA smooth continuous nanofibers without beads were observed and used to prepare plasmonic nanofiber mat. The lower and higher magnification FESEM images of PVA nanofibers with and without Au NPs and their size distribution images are shown in figure 5C.4. It is evident that long microbeads free electrospun nanofibers were deposited under these experimental conditions. Furthermore, we observed a high percentage of the uniqueness of PVA nanofibrous structure. The average thickness of polymer nanofibers was estimated by considering more than 100 distinct nanofibers from the recorded SEM micrographs. The obtained data provided the average diameter as 274±32 nm, which is depicted in figure 5C.4(c). The images of PVA nanofibers loaded with Au NPs are illustrated in figures 5C.4(d)- 5C.4(f). The diameters of the fibers achieved were 95±19 nm. The fiber diameter was found to be decreased in embedded Au NPs-PVA in comparison with pure PVA nanofibers. The fine nanofibers with NPs formed because of the presence of metal, which could increase the conductivity of the PVA solution. It gives a more elongation force on the released polymer jets under the equal applied electric field, which resulted in improving the electrospinning conditions.[14]

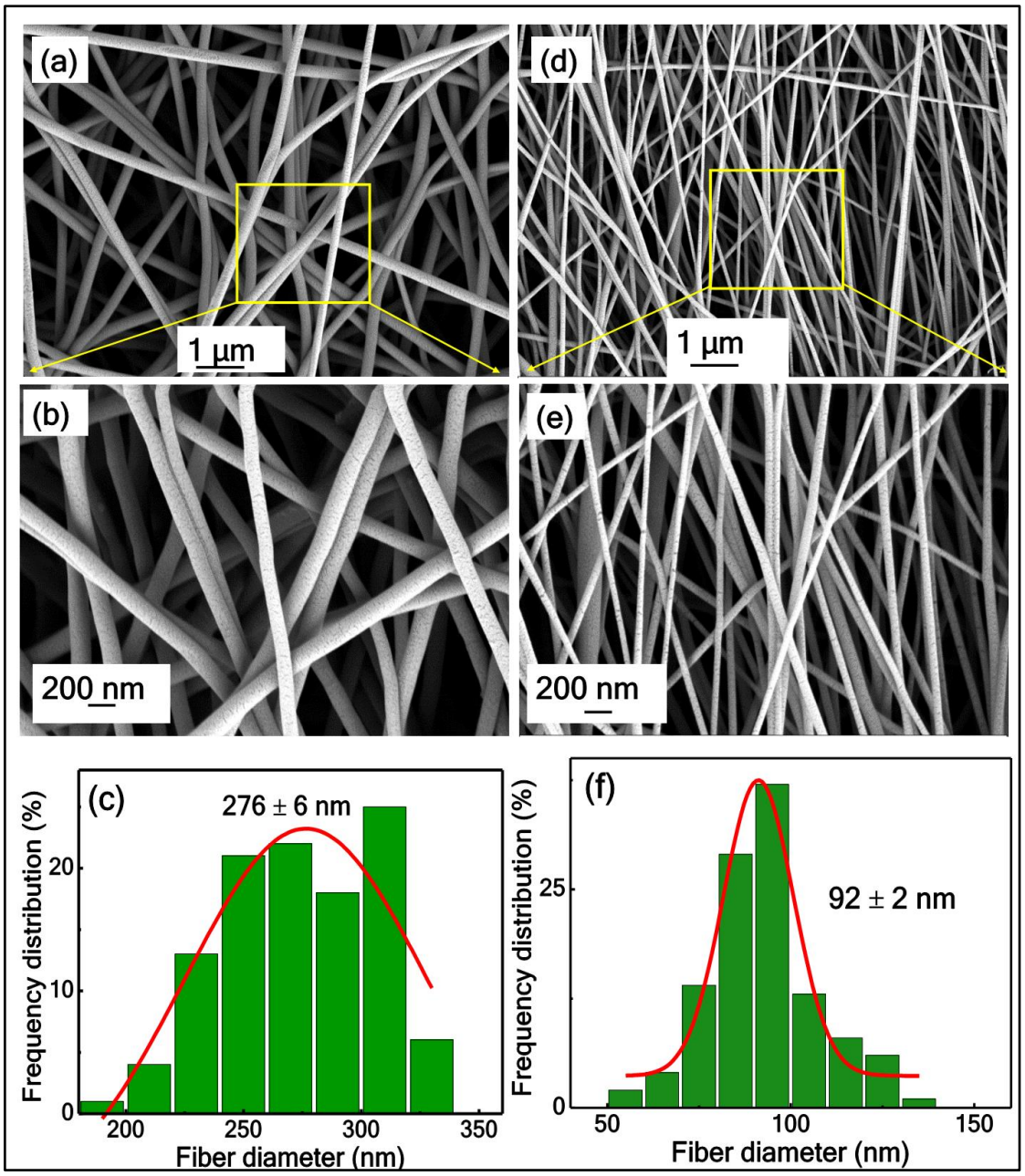

Figure 5C.4 SEM images electrospun PVA nanofibers (a, b) without (d and e) with Au NPs and (c and f) the corresponding fiber diameter distribution.

Motamedi et al.[8] in their studies noticed a decrease in the fiber diameter from 350 nm to 324 nm because of the presence of Au NPs in PVDF nanofibers. For application, nanofibers, in particular, have the edge over the other flexible substrates because they offer the extended one-dimensional nanostructures and these are aligned as a micro three-dimensional sheet with less porosity leading to the generation of high surface to volume ratio and provide excellent ease for the preparation of the SERS substrates by introducing the different metal NPs which can be easily fed in the polymer solution to be used for electrospinning.

5C.3.3 TEM analysis:

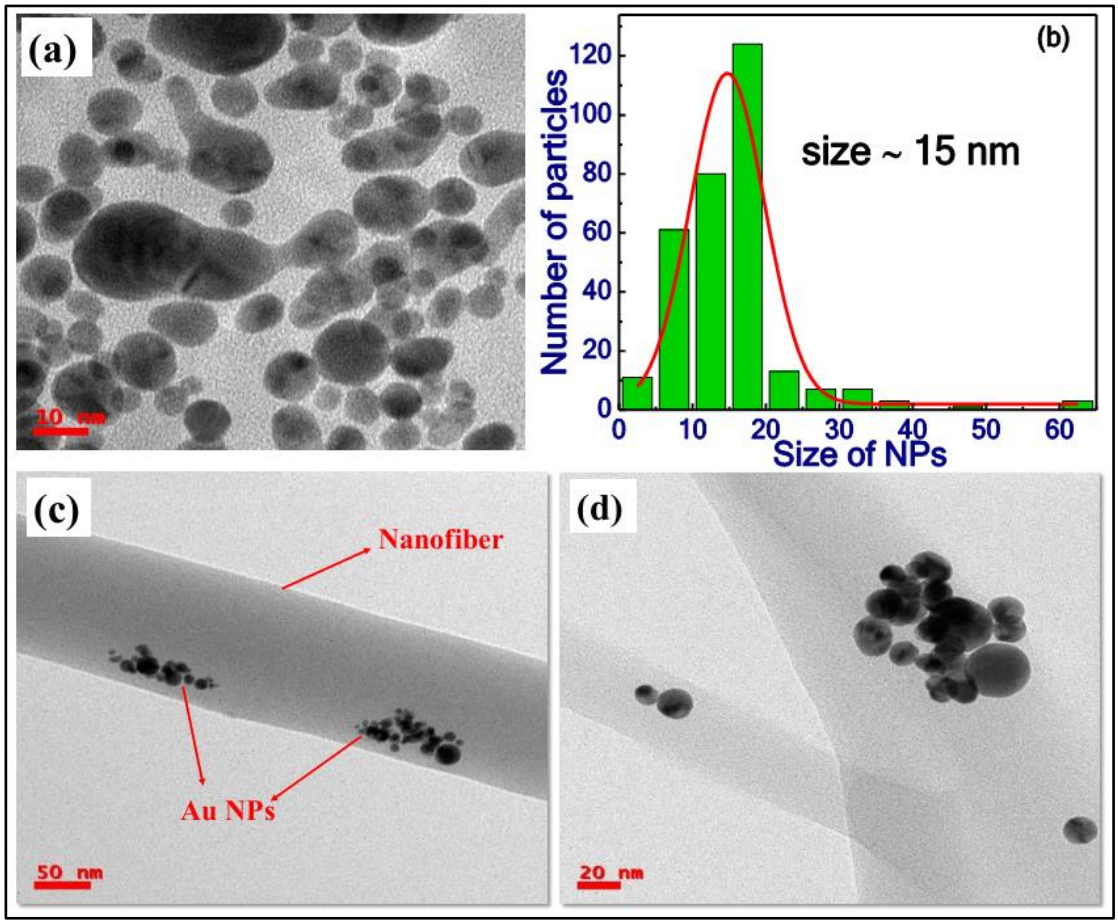

Figure 5C.5 TEM image (a) Au NPs (b) size distribution (c) and (d) Au NPs loaded PVA nanofiber having different magnifications.

TEM investigations were performed to determine the size of synthesized Au NPs by LAL at 1064 nm laser wavelength. The typical TEM micrograph is shown in figure 5C.5(a), in which diluted 2 µl Au NPs were drop-casted on a TEM grid. The estimated size distributions of synthesized Au NPs are illustrated in figure 5C.5(b). The diameter of NPs were calculated by collecting the diameter of 250–300 particles and estimated with the Gaussian fit. The average size of the Au NPs was ~15 nm. It is noteworthy that in the SEM images of Au NPs –PVA nanofiber, the embedded NPs on to fiber are not visible because of the low resolution. The presence and distribution of Au NPs in the PVA nanofiber mat were examined with TEM studies. A typical, different magnification TEM micrographs of the PVA nano fibrous membranes loaded with Au NPs are shown in Figures 5C. 5(c) and 5C.5(d) depicting the Au NPs were attached to a PVA nanofiber. Clearly, the loaded Au NPs and PVA nanofibers appear with amplitude contrast [dark regions-Au NPs and lighter region-PVA fiber] because of the higher density of metal than polymer.

5C.3.4 XRD studies

FESEM and TEM analysis describe the morphology of fibers and the distribution of NPs on the fibers. The presence of Au NPs on the nanofibers was also confirmed from XRD studies. Figure 5C.6 illustrates the XRD patterns of PVA nanofibers with and without the loading of Au NPs. The spectra were recorded in the range of 10^0 to 80^0. In the case of PVA nanofibers, no XRD peak was identified because of the amorphous nature of PVA. In the case of Au NPs loaded PVA nanofibers, the diffraction peaks corresponding to Au were observed and those were in good agreement with standard JCPDS data cards [Au: 04-0784]. The diffraction peaks observed at 2θ is equal to 38.6^0, 44.9^0, $65.2^{0,}$ and 78.3^0 correspond to the (111), (200), (220) and (311) Au lattice planes, respectively. The obtained result reveals that the loaded Au NPs are in the form of face-centered cubic (FCC) crystals in the PVA nanofiber mat.

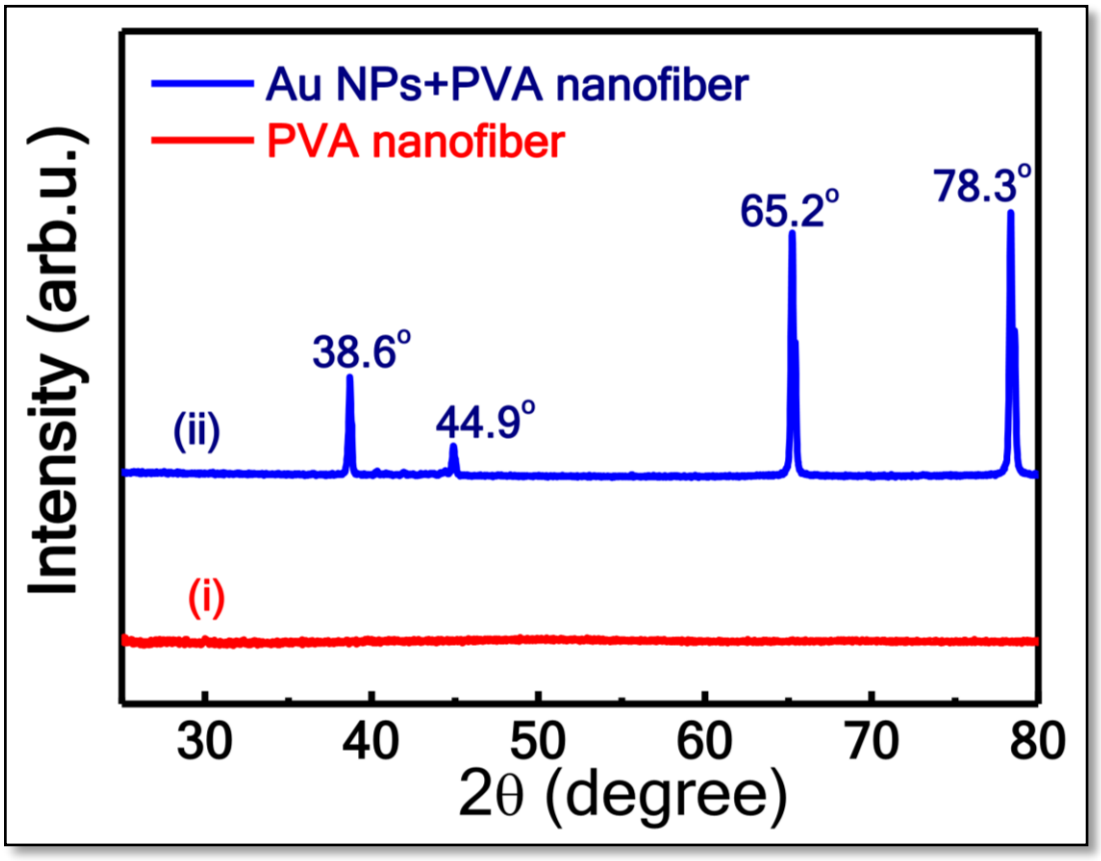

Figure 5C.6 XRD patterns of (a) PVA nanofibers (b) Au NPs-PVA nanofibers.

5C.4 SERS studies

5C.4.1 Detection of the dye molecule

Initially, SERS studies on the nanofibers of PVA- Au NPs were performed with a dye molecule. The obtained SERS spectra of methylene blue (MB) with a concentration of 5 µM are illustrated in figure 5C.7(iii). For comparison, the Raman signals of MB with the same concentration (5 µM) were also recorded using bare PVA nanofibers [figure 5C.7(ii)] and from bare Au NPs+PVA fiber without an analyte molecule [Raman spectra shown in figure 5C.7(i)]. The presented results demonstrate that the proposed Au NPs loaded PVA nanofiber SERS substrate strongly scatters resulting in huge Raman signals. No signature peaks of MB were observed from bare PVA nanofibers without Au NPs. Therefore, the interconnecting porous structure loaded with Au NPs generating the plasmonic nature led to enhancements in the Raman signal of the analyte molecule. All the Raman peaks assignment agree with the previous reports and are mentioned in Appendix A. The achieved EF was ~4×10^4 for 1620 cm^{-1} mode in this particular case.

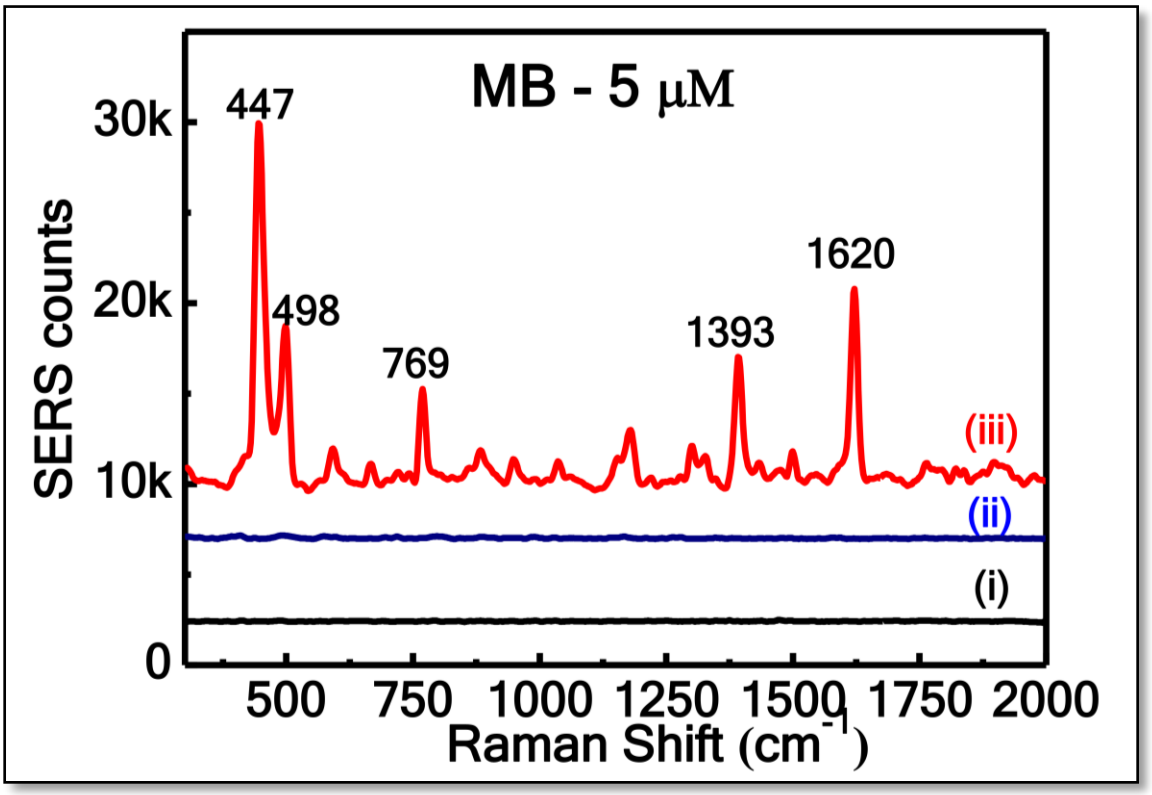

Figure 5C.7 Raman spectra (i) PVA + Au NPs (without analyte) (ii) PVA+MB (without Au NPs) (iii) PVA + Au NPs + MB 5 µM.

He et al.[35] detected R6G 10^{-6} M with Ag dimer/aggregated –PVA nanofiber mat and demonstrated long terms stability (1 year). Jia et al.[36] fabricated Ag nanoplates decorated on poly-m-phenylenediamine/polyacrylonitrile nanofibers used as SERS substrate in the detection of 4-MBA having concentration of 10^{-10} M. Amarjargal et al.[37] detected 10^{-4} M 4-MBA using Ag NPs embedded electrospun polyurethane nanofibers mat. Gao et al.[38] employed various metal NPs [Au NPs different sizes of ~13 nm, ~16 nm, ~40 nm; Ag NPs of ~43 nm; and Au nanorods of ~31/20 nm] doped PVP polymer fibers as SERS sensors and found Au nanorods loaded fiber able to detect 10^{-8} M of 4-MBA and 10^{-9} M of 4-MPY. Severyukhina et al.[39] demonstrated Au based chitosan nanofibers by soaking HAuCl4 at concentrations 0.5, 1, 5, 10, and 25 mM for 1 hour and used optimized 10 mM substrate and used in the detection of Rhodamine 6G and D-Glucose in µM concentration with EF ~10^5. Yang et al.[40] fabricated $AgNO_3$/PMAA/PVP nanofibers via electrospinning and in situ photo-reduction (UV lamp 365 and 254 nm) of silver ions into NPs for one day. These substrate utilized in the detection of MG-2 µM and CV -1 µM. Yang et al.[41] AgNPs/agar/PAN were fabricated by the electrospinning $AgNO_3$/agar/PAN solution followed by photo-reduction technique in the presence of 11 W UV light (365 and 254 nm). These substrates are used to detect p-ATP 10^{-4} M and MG-0.1 µM. Jalaja et al.[42] detected RDX (10^{-7} M) and DNT (10^{-7} M) using oval-shaped nanopores polystyrene nanofibers drop cast with Ag NPs.

5C.4.2 Detection of methyl salicylate

Methyl Salicylate (MS) is an organic compound that is naturally produced by some plants and also commercially available. It is widely used in cosmetics[43], chemical warfare agent simulant[44], volatile organic compound[45], ester agent[46]. A liquid form of MS ≥99% pure purchased from sigma Aldrich. The MS diluted in ethanol with different concentrations ranging from 7.7 M to 1 M; the Raman spectra were collected in liquid form. The obtained Raman spectra are shown in figure 5C.8; for comparison, pure ethanol Raman spectra were also recorded. All the observed Raman peaks in our case matched with the previous reports[47-48]. All the peak assignments are mentioned in Appendix A. The most prominent peaks of the MS (808 cm^{-1}) and ethanol (880 cm^{-1}) are highlighted with yellow and green colors, respectively. The detection of MS is important and only few reports are found in literature. Li et al.[43] detected 10^{-4} M MS using the SERS technique with

molecule/assistant/metal [MS/ 4, 4′-(hexafluoroisopropylidene) bis (benzoic acid)/Ag NPs] system.

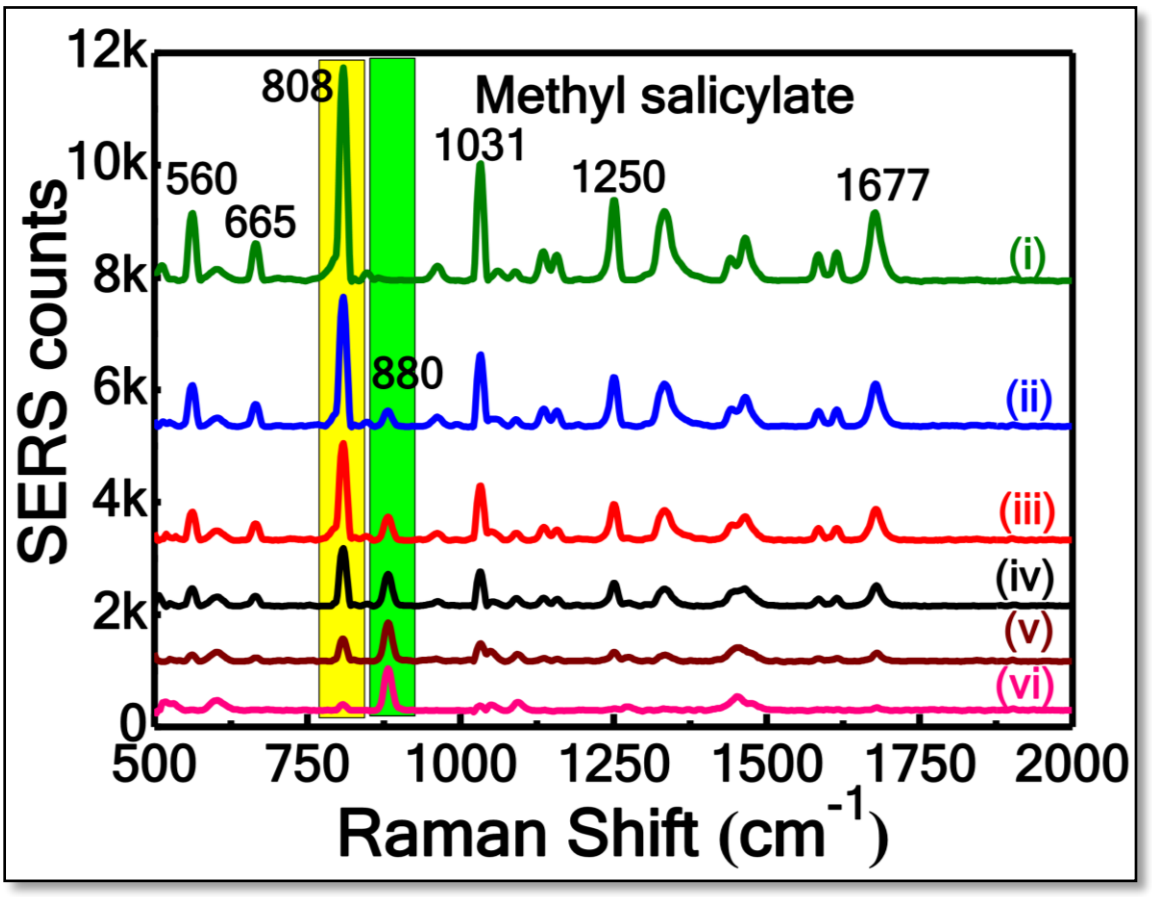

Figure 5C.8 Raman spectra of methyl salicylate diluted in ethanol (i) pure 7.7 M (ii) 6 M (iii) 5 M (iv) 3.8 M (v) 2.5 M (vi) 1 M (vii) pure ethanol [in liquid form].

Figure 5C.9(a) represents the Raman spectra of MS (1 M) using PVA nanofibers with and without Au NPs. The presence of the Au NPs leads to the enhancement of MS Raman signal, the intensity at the prominent peak (808 cm^{-1}), which was 39 times higher in the magnitude compared Raman signal obtained from the PVA nanofiber without Au NPs. The efficacy and sensitivity of the fabricated PVA nanofiber mat loaded with Au NPs substrate was evaluated as a function of varying concentration of the analyte molecules using a portable Raman spectrometer with 785 nm excitation wavelength. Figure 5C.9(b) presents the SERS spectra of MS with concentrations ranging from 1 M to 10 mM. The spectra display highly stable SERS spectra with distinct Raman features for the concentration of 10 mM. The relative Raman intensities were found to decrease with decreasing concentration of MS from 1 M to 10 mM. The performance of the substrate supported electrospinning nanofiber with Au NPs was extended to produce uniform and

repeatable Raman spectra with enhanced peak intensities. Figure 5C.9(c) depicts the color plot of the most prominent peak (808 cm^{-1}) intensity of SERS spectra obtained from 10 random locations on the as-prepared PVA nanofiber with Au NPs substrates for 10 mM-MS. The spectra display uniform, stable, and highly reproducible SERS signals with relatively small deviations in the relative signal intensities. Figure 5C.9(d) shows the histogram plots depicting the signal variations corresponding peak (880 cm^{-1}) with RSD value. The estimated RSD value of 10.1% reveals a high reproducibility of the Raman features. Therefore, this demonstrates that there was a near homogeneous distribution of Raman hotspots as well as analyte adsorption in a large number of nanoscale gaps on the porous surface of PVA nanofibers with Au NPs. Furthermore, the flexible SERS active substrates could be tailored into various shapes for more practical SERS applications.

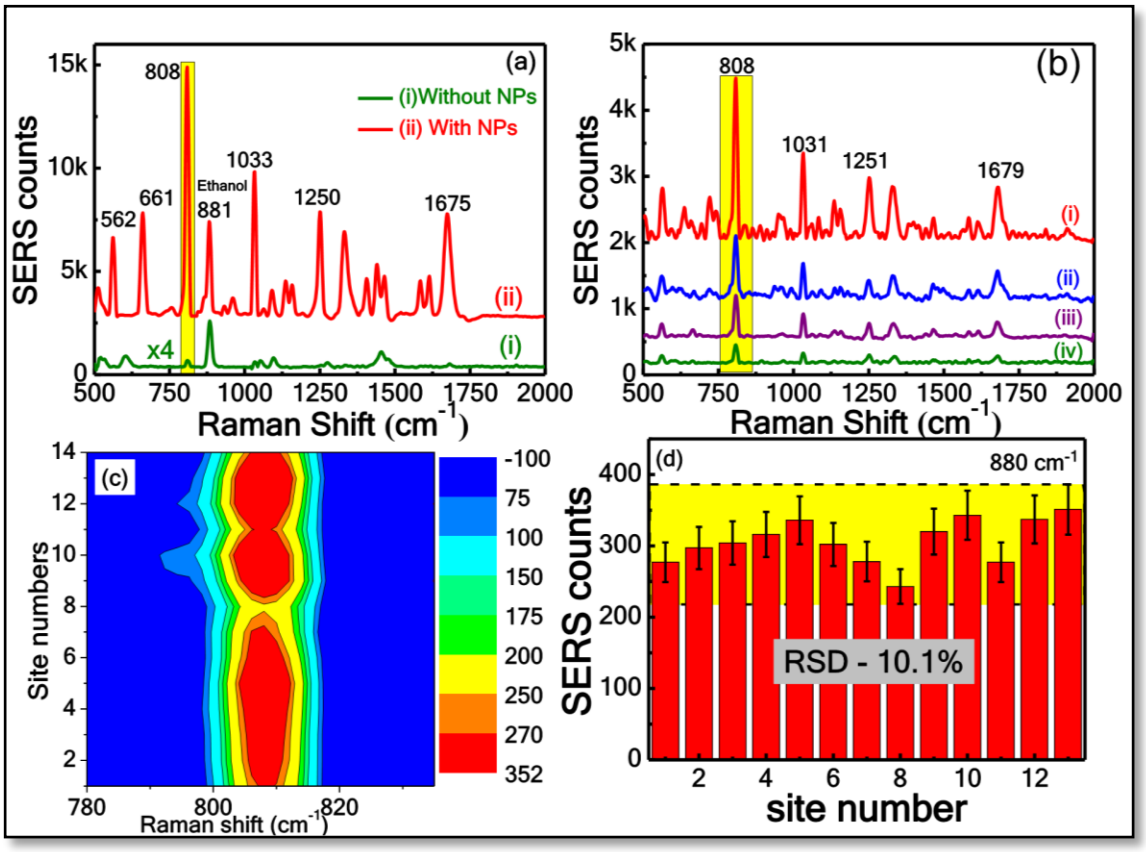

Figure 5C.9 (a) SERS spectra of Methyl salicylate (MS) having concentration 1 M with and without Au NPs. (b) concentration dependent spectra of MS (i) 1 M (ii) 100 mM (iii) 50 mM (iv) 10 mM (c) and (d) SERS spectra contour plots and histogram plots of SERS intensity of the most prominent peak of MS-880 cm^{-1}, respectively, using Au NPs loaded PVA nanofiber.

5C.5 Comparison with the commercial flexible-SERS substrate

Nowadays, different companies are developing SERS substrates using various methods and are commercially providing to the lab and for field usages. The details of commercially available SERS substrate and their properties are tabulated in Appendix-A. Recently. Liu et al.[49] provided a comprehensive evaluation of six commercial substrates [Enspectrc -1 (Si based), Q-SERS^{TM}-1 (Si based), Ocean optics-3 (paper based Ag, Au; glass based Ag/Au) and Hamamatsu substrate-1(Au NS on polypropylene)] including their sensitivity and reproducibility studies using MB, BPE, 4-MBA molecules. The SERS spectra recorded with XploRA-Plus Raman micro-spectrometer at 532 and 785 nm excitation wavelengths. From the results the authors observed optimized signals in the case of Enspectrc SERS substrate for all the three molecules at 532 nm; Q-SERS^{TM} substrate for 4-MBA and BPE at 785 nm; Hamamatsu substrate for MB with 785 nm excitation.

Here, we present results from the comparison of the flexible substrate performance with a readily available commercial Ag and Au loaded paper-based SERS substrate (Ω-Metrohm).[50] The photographs of the commercial filter paper substrates are shown in figure 5C.10(a) The color side (top) of the FP was the effective area of SERS substrate i.e. the area loaded with Ag/Au NPs. We cut each of these FP substrates into two pieces and utilized to detect two different dye molecules. Two probe dye molecules (i) MB (ii) CV were considered to verify the SERS performance of these substrates. Figures 5C.10(b) and 5C.10(c) illustrate the SERS spectra of CV (5 µM). The intensity histogram demonstrated the reproducibility of the substrate with RSD of ~7.02 % for CV 1175 cm^{-1} mode using Ag-based FP substrate. Figures 5C.10(d) and 5C.10(e) depict the SERS spectra of CV (5 µM) with the intensity histogram depicting the reproducibility with an RSD of ~11.4 % for CV 1175 cm^{-1} mode using Au-based FP substrate. Figures 5C.10(f) and 5C.10(g) show the SERS spectra of MB (5 µM) and the intensity histogram shows the reproducibility of the substrate with a RSD of ~12.37 % for MB 1620 cm^{-1} mode using the Ag-based FP substrate. Figures 5C.10(h) and 5C.10(i) illustrate the SERS spectra of MB (5 µM). In this case the intensity histogram shows the reproducibility with a RSD of ~6.94 % for MB 1620 cm^{-1} mode obtained using Au-based FP substrate. The obtained EF's were ~2.54×10^4 and ~1.46×10^4 for the main characteristic peak of MB 1620 cm^{-1} using Ag and Au based FP substrates, respectively. Similarly the obtained EFs were ~8.6×10^3 and ~2.2×10^3 for

the main characteristic peak of CV 1175 cm^{-1} using Ag and Au based FP substrates, respectively.

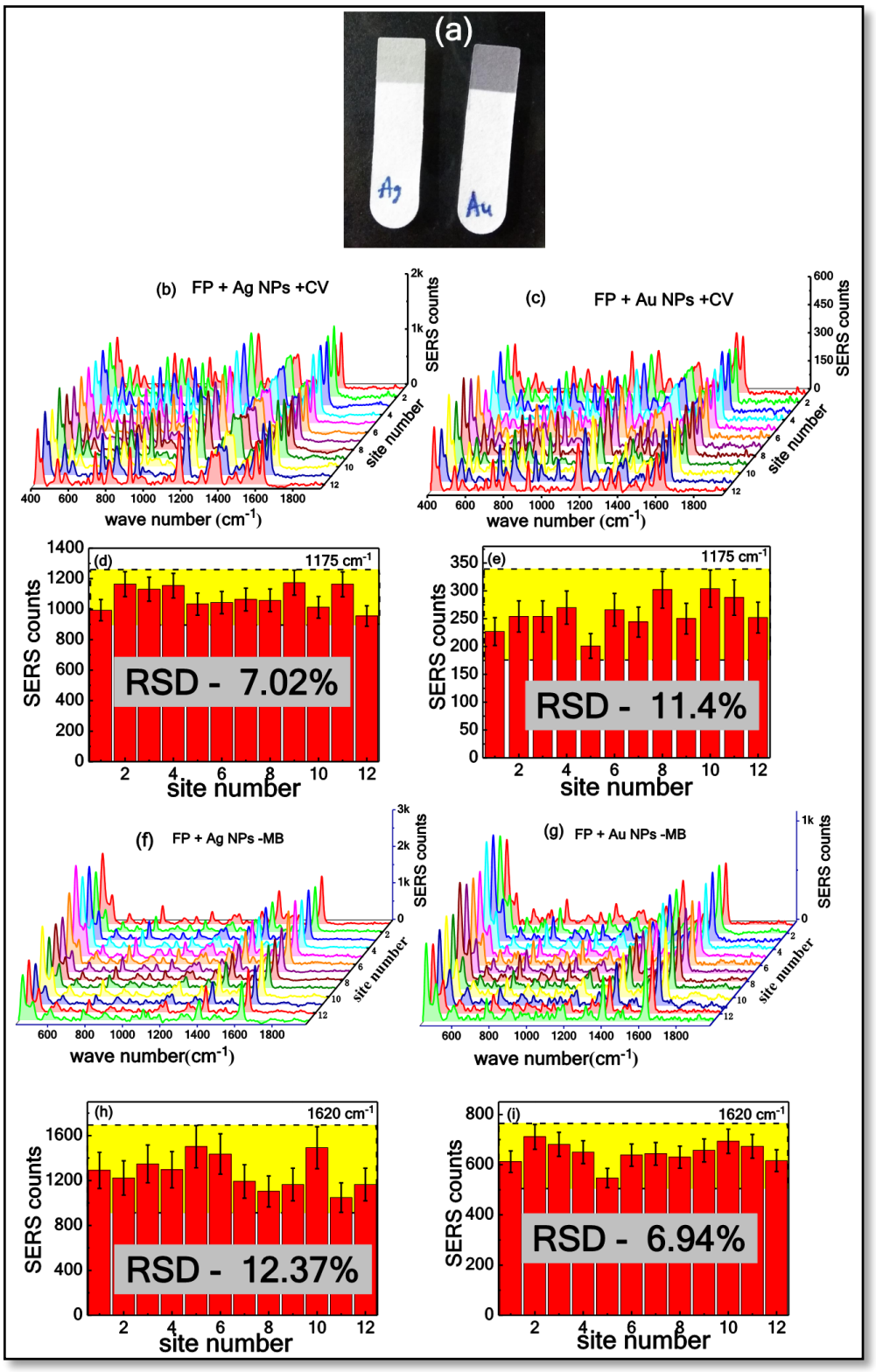

Figure 5C. 10 (a) photograph of Ag and Au based filter paper substrates (b,f) and (c,g) represents the CV-5 µM, MB-5 µM Raman spectra of Ag and Au based FP substrates (c,e) and (h, i) represent the corresponding histograms with RSD%.

5C.6 Conclusions

A fast and easy approach was demonstrated to prepare flexible plasmonic active SERS substrates by electrospinning technique. Au NPs were fabricated by ps laser ablation technique. The Au NPs loaded PVA nanofiber mat was fabricated by electron spinning of mixture Au NPs and PVA solution. These fibers were characterized by FESEM, TEM, and XRD. The recorded SERS spectra of MB using PVA-Au NPs fiber showed comparatively high intensity in Raman characteristic peaks of MB. Next, the plasmonic nanofiber sheet used to detect MS-10 mM with good reproducibility of ~10% using a portable Raman spectrometer. In the future, the efficiency of these plasmonic nanofiber substrates could be progressed by embedding anisotropic NPs and can be utilized to identify explosives in pure and mixture form. A commercial flexible filter paper-based SERS substrate was used for the detection of MB -5 µM and CV- 5 µM.

5C.7 References

1. Xue, J.; Xie, J.; Liu, W.; Xia, Y., Electrospun Nanofibers: New Concepts, Materials, and Applications. *Acc. Chem. Res* **2017**, *50*, 1976-1987.
2. Ding, Y.; Hou, H.; Zhao, Y.; Zhu, Z.; Fong, H., Electrospun Polyimide Nanofibers and Their Applications. *Progress in Polymer Science* **2016**, *61*, 67-103.
3. Cui, W.; Zhou, Y.; Chang, J., Electrospun Nanofibrous Materials for Tissue Engineering and Drug Delivery. *Sci. Technol. Adv. Mater.* **2010**, *11*, 014108.
4. Thakkar, S.; Misra, M., Electrospun Polymeric Nanofibers: New Horizons in Drug Delivery. *Eur. J. Pharm. Sci.* **2017**, *107*, 148-167.
5. Botes, M.; Eugene Cloete, T., The Potential of Nanofibers and Nanobiocides in Water Purification. *Crit. Rev. Microbiol.* **2010**, *36*, 68-81.
6. Schreuder-Gibson, H.; Gibson, P.; Senecal, K.; Sennett, M.; Walker, J., Protective Textile Materials Based on Electrospun Nanofibers. *J. Adv. Mater.* **2002**, *34*, 44-55.
7. Huang, L.; Nagapudi, K.; P. Apkarian, R.; Chaikof, E. L., Engineered Collagen–Peo Nanofibers and Fabrics. *J. Biomater. Sci., Polym. Ed.* **2001**, *12*, 979-993.
8. Motamedi, A. S.; Mirzadeh, H.; Hajiesmaeilbaigi, F.; Bagheri-Khoulenjani, S.; Shokrgozar, M. A., Piezoelectric Electrospun Nanocomposite Comprising Au Nps/Pvdf for Nerve Tissue Engineering. *J. Biomed. Mater. Res. Part A* **2017**, *105*, 1984-1993.
9. Zhang, Z.; Wu, Y.; Wang, Z.; Zou, X.; Zhao, Y.; Sun, L., Fabrication of Silver Nanoparticles Embedded into Polyvinyl Alcohol (Ag/PVA) Composite Nanofibrous Films through Electrospinning for Antibacterial and Surface-Enhanced Raman Scattering (SERS) Activities. *Mater. Sci. Eng.* **2016**, *69*, 462-469.
10. Chamuah, N.; Bhuyan, N.; Das, P. P.; Ojah, N.; Choudhary, A. J.; Medhi, T.; Nath, P., Gold-Coated Electrospun PVA Nanofibers as SERS Substrate for Detection of Pesticides. *Sens. Actuators, B* **2018**, *273*, 710-717.
11. Teo, W. E.; Ramakrishna, S., A Review on Electrospinning Design and Nanofibre Assemblies. *Nanotechnology* **2006**, *17*, 89-106.
12. Guo, B.; Zhao, S.; Han, G.; Zhang, L., Continuous Thin Gold Films Electroless Deposited on Fibrous Mats of Polyacrylonitrile and Their Electrocatalytic Activity Towards the Oxidation of Methanol. *Electrochim. Acta* **2008**, *53*, 5174-5179.
13. Subbiah, T.; Bhat, G.; Tock, R.; Parameswaran, S.; Ramkumar, S., Electrospinning of Nanofibers. *J. Appl. Polym. Sci.* **2005**, *96*, 557-569.
14. Li, Z.; Wang, C., *One-Dimensional Nanostructures: Electrospinning Technique and Unique Nanofibers*; Springer, **2013**, 15-29
15. Fridrikh, S. V.; Jian, H. Y.; Brenner, M. P.; Rutledge, G. C., Controlling the Fiber Diameter During Electrospinning. *Phys. Rev. Lett.* **2003**, *90*, 144502.
16. Shi, Y.; Li, Y.; Zhang, J.; Yu, Z.; Yang, D., Electrospun Polyacrylonitrile Nanofibers Loaded with Silver Nanoparticles by Silver Mirror Reaction. *Mater. Sci. Eng.* **2015**, *51*, 346-355.
17. Shi, Q.; Vitchuli, N.; Nowak, J.; Caldwell, J. M.; Breidt, F.; Bourham, M.; Zhang, X.; McCord, M., Durable Antibacterial Ag/Polyacrylonitrile (Ag/PAN) Hybrid Nanofibers Prepared by Atmospheric Plasma Treatment and Electrospinning. *Eur. Polym. J.* **2011**, *47*, 1402-1409.
18. Lee, C. H.; Tian, L.; Abbas, A.; Kattumenu, R.; Singamaneni, S., Directed Assembly of Gold Nanorods Using Aligned Electrospun Polymer Nanofibers for Highly Efficient SERS Substrates. *Nanotechnology* **2011**, *22*, 275311.

19. Cao, M.; Cheng, S.; Zhou, X.; Tao, Z.; Yao, J.; Fan, L.-J., Preparation and Surface-Enhanced Raman Performance of Electrospun Poly (Vinyl Alcohol)/High-Concentration-Gold Nanofibers. *J. Polym. Res.* **2012**, *19*, 9810.
20. Zhao, S.; Guo, B.; Han, G.; Tian, Y., Metallization of Electrospun Polyacrylonitrile Fibers by Gold. *Mater. Lett.* **2008**, *62*, 3751-3753.
21. Carlberg, B.; Ye, L. L.; Liu, J., Surface-Confined Synthesis of Silver Nanoparticle Composite Coating on Electrospun Polyimide Nanofibers. *Small* **2011**, *7*, 3057-3066.
22. Han, E.; Wu, D.; Qi, S.; Tian, G.; Niu, H.; Shang, G.; Yan, X.; Yang, X., Incorporation of Silver Nanoparticles into the Bulk of the Electrospun Ultrafine Polyimide Nanofibers Via a Direct Ion Exchange Self-Metallization Process. *ACS Appl. Mater. & Interf.* **2012**, *4*, 2583-2590.
23. Marega, C.; Maculan, J.; Rizzi, G. A.; Saini, R.; Cavaliere, E.; Gavioli, L.; Cattelan, M.; Giallongo, G.; Marigo, A.; Granozzi, G., Polyvinyl Alcohol Electrospun Nanofibers Containing Ag Nanoparticles Used as Sensors for the Detection of Biogenic Amines. *Nanotechnology* **2015**, *26*, 075501.
24. Szymborski, T.; Witkowska, E.; Adamkiewicz, W.; Waluk, J.; Kamińska, A., Electrospun Polymer Mat as a SERS Platform for the Immobilization and Detection of Bacteria from Fluids. *Analyst* **2014**, *139*, 5061-5064.
25. Qian, Y.; Meng, G.; Huang, Q.; Zhu, C.; Huang, Z.; Sun, K.; Chen, B., Flexible Membranes of Ag-Nanosheet-Grafted Polyamide-Nanofibers as Effective 3D SERS Substrates. *Nanoscale* **2014**, *6*, 4781-4788.
26. Shi, J.; You, T.; Gao, Y.; Liang, X.; Li, C.; Yin, P., Large-Scale Preparation of Flexible and Reusable Surface-Enhanced Raman Scattering Platform Based on Electrospinning Ag NPs/PCl Nanofiber Membrane. *RSC Adv.* **2017**, *7*, 47373-47379.
27. Kong, L.; Dong, N.; Tian, G.; Qi, S.; Wu, D., Highly Enhanced Raman Scattering with Good Reproducibility Observed on a Flexible Pi Nanofabric Substrate Decorated by Silver Nanoparticles with Controlled Size. *Appl. Surf. Sci.* **2020**, *511*, 145443.
28. Zhang, L.; Gong, X.; Bao, Y.; Zhao, Y.; Xi, M.; Jiang, C.; Fong, H., Electrospun Nanofibrous Membranes Surface-Decorated with Silver Nanoparticles as Flexible and Active/Sensitive Substrates for Surface-Enhanced Raman Scattering. *Langmuir* **2012**, *28*, 14433-14440.
29. Zhao, Y.; Sun, L.; Xi, M.; Feng, Q.; Jiang, C.; Fong, H., Electrospun TiO_2 Nanofelt Surface-Decorated with Ag Nanoparticles as Sensitive and UV-Cleanable Substrate for Surface Enhanced Raman Scattering. *ACS Appl. Mater. & Interf.* **2014**, *6*, 5759-5767.
30. Zhang, C. L.; Lv, K. P.; Cong, H. P.; Yu, S. H., Controlled Assemblies of Gold Nanorods in PVA Nanofiber Matrix as Flexible Free-Standing SERS Substrates by Electrospinning. *Small* **2012**, *8*, 648-653.
31. Byram, C.; Moram, S. S. B.; Soma, V. R., SERS Based Detection of Multiple Analytes from Dye/Explosive Mixtures Using Picosecond Laser Fabricated Gold Nanoparticles and Nanostructures. *Analyst* **2019**, *144*, 2327-2336.
32. Matsutani, R.; Inoue, K.; Wada, N.; Kojima, K., Wavelength Dependence of Polyyne Preparation by Liquid-Phase Laser Ablation Using Pellet Targets. *Chem. Commun.* **2011**, *47*, 5840-5842.
33. Thompson, C.; Chase, G. G.; Yarin, A.; Reneker, D., Effects of Parameters on Nanofiber Diameter Determined from Electrospinning Model. *Polymer* **2007**, *48*, 6913-6922.

34. Husain, O.; Lau, W.; Edirisinghe, M.; Parhizkar, M., Investigating the Particle to Fibre Transition Threshold During Electrohydrodynamic Atomization of a Polymer Solution. *Mater. Sci. Eng.* **2016**, *65*, 240-250.
35. He, D.; Hu, B.; Yao, Q.-F.; Wang, K.; Yu, S.-H., Large-Scale Synthesis of Flexible Free-Standing SERS Substrates with High Sensitivity: Electrospun PVA Nanofibers Embedded with Controlled Alignment of Silver Nanoparticles. *ACS nano* **2009**, *3*, 3993-4002.
36. Jia, P.; Chang, J.; Wang, J.; Zhang, P.; Cao, B.; Geng, Y.; Wang, X.; Pan, K., Fabrication and Formation Mechanism of Ag Nanoplate-Decorated Nanofiber Mats and Their Application in SERS. *Chemistry–An Asian Journal* **2016**, *11*, 86-92.
37. Amarjargal, A.; D TIJING, L.; Kim, C. S., Simple Fabrication of Ag Nanoparticle-Impregnated Electrospun Nanofibres as SERS Substrates. *Bull. Mater. Sci.* **2015**, *38*, 267-270.
38. Gao, W.; Chen, G.; Xu, W.; Yang, C.; Xu, S., Surface-Enhanced Raman Scattering (SERS) Chips Made from Metal Nanoparticle-Doped Polymer Fibers. *RSC Adv.* **2014**, *4*, 23838-23845.
39. Severyukhina, A. N.; Parakhonskiy, B. V.; Prikhozhdenko, E. S.; Gorin, D. A.; Sukhorukov, G. B.; Möhwald, H.; Yashchenok, A. M., Nanoplasmonic Chitosan Nanofibers as Effective SERS Substrate for Detection of Small Molecules. *ACS Appl. Mater. & Interf.* **2015**, *7*, 15466-15473.
40. Yang, H.; Huang, C. Z., Polymethacrylic Acid–Facilitated Nanofiber Matrix Loading Ag Nanoparticles for SERS Measurements. *RSC Adv.* **2014**, *4*, 38783-38790.
41. Yang, T.; Yang, H.; Zhen, S. J.; Huang, C. Z., Hydrogen-Bond-Mediated in Situ Fabrication of Agnps/Agar/Pan Electrospun Nanofibers as Reproducible SERS Substrates. *ACS Appl. Mater. & Interf.* **2015**, *7*, 1586-1594.
42. K, J.; S, B.; Ganiga, M.; R, D.; S, A.; Cyriac, J.; George, B. K., Effective SERS Detection Using a Flexible Wiping Substrate Based on Electrospun Polystyrene Nanofibers. *Anal. Methods* **2017**, *9*, 3998-4003.
43. Li, Y.; Li, Q.; Wang, Y.; Oh, J.; Jin, S.; Park, Y.; Zhou, T.; Zhao, B.; Ruan, W.; Jung, Y. M., A Reagent-Assisted Method in SERS Detection of Methyl Salicylate. *Spectrochim. Acta A: Molecular and Biomolecular Spectros.* **2018**, *195*, 172-175.
44. Patel, S. V.; Hobson, S. T.; Cemalovic, S.; Mlsna, T. E., Detection of Methyl Salicylate Using Polymer-Filled Chemicapacitors. *Talanta* **2008**, *76*, 872-877.
45. Park, J.; Thomasson, J. A.; Fernando, S.; Lee, K.-M.; Herrman, T. J., Complexes Formed by Hydrophobic Interaction between Ag-Nanospheres and Adsorbents for the Detection of Methyl Salicylate Voc. *Nanomaterials* **2019**, *9*, 1621.
46. Sulk, R.; Chan, C.; Guicheteau, J.; Gomez, C.; Heyns, J.; Corcoran, R.; Carron, K., Surface-Enhanced Raman Assays (SERA): Measurement of Bilirubin and Salicylate. *J. Raman Spectros.* **1999**, *30*, 853-859.
47. Schonbachler, N.; Luthy, W., Measurements of Raman Lines in Silica, Dimethyl-Methylphosphonate and Methyl Salicylate. *Bern: University of Bern* **2010**.
48. Varghese, H. T.; Yohannan Panicker, C.; Philip, D.; Mannekutla, J. R.; Inamdar, S. R., Ir, Raman and SERS Studies of Methyl Salicylate. *Spectrochimica Acta Part A: Molecular and Biomolecular Spectros.* **2007**, *66*, 959-963.
49. Liu, Y.; Zhang, Y.; Tardivel, M.; Lequeux, M.; Chen, X.; Liu, W.; Huang, J.; Tian, H.; Liu, Q.; Huang, G., Evaluation of the Reliability of Six Commercial SERS Substrates. *Plasmonics* **2019**, 1-10.
50. https://www.metrohm.com/en-in/products-overview/bwt-840000620.

Intentional blank page

Chapter 6

Conclusion and Future scope

6.1 Conclusions

The thesis work was focused towards the design and development of versatile SERS substrates with high enhancement factors and good reproducibility, and more importantly, using a portable Raman spectrometer towards the detection of various common explosive molecules. In order to explore the above themes, rigid and flexible SERS substrates were prepared and their superior performance was demonstrated successfully for the detection of various molecules of interest (e.g., dyes, explosives, pesticides) at low concentrations as well as in complex mixtures. Overall twelve probe molecules were identified and tested: (a) concentrations as low as µM for explosives with typical EF's ~10^5 (b) nM concentration for dye molecules with EF's of ~10^7. These studies were followed by other studies depicting reproducibility of <15%. The summary of all the SERS substrates investigated in this thesis shown in the table below.

S. No	SERS substrate	Substrate material	Active area	Sensitivity (EF)		Reproducibility	Preparation time (hours)	Stability (days)	Sample collection
				Dye	Explosive				
1	Rigid	Silicon (Si)	Ag-Cu	3×10^7	3×10^4	<12% ✓	3	-	Dipping/ drop-casting
			Ag-Au	3×10^7	8×10^4		2.3	-	
			Cu-Au	1×10^7	4×10^4		2.3	-	
2		Si MSA	Ag-Au	1×10^{10} ✓	2×10^6 ✓	<15%	3	-	
3	Flexible	Filter paper	Ag	3×10^7	2×10^4	<15%	1.2	15	Swabbing/ dipping/ drop-casting
			Au	8×10^6	1×10^4	<16%	1.2	45 ✓	
4			Star Au	3×10^{10} ✓	4×10^4	<18%	26	-	
5		Polymer nanofibers	Au	1×10^7	-	-	4		
6		DVD	Au	1×10^9	-	<11% ✓	1		Dipping/ drop-casting

Important conclusions from this thesis work:

* Initially, Ag-Cu alloy nanoparticles (NPs) were synthesized by femtosecond (~50 fs, 800 nm) laser irradiation of a mixture of prior synthesized Ag and Cu NPs in equal volumes. Pure Ag and Cu NPs were prepared by laser ablation in liquid technique. The alloy NPs formation was confirmed using UV-Visible absorption spectra, TEM, XRD, and FESEM-mapping. SERS studies of methylene blue (MB) proved that Ag-Cu alloy NPs were better with EF of ~7.2×10^3 compared to Ag and Cu NPs with EFs of ~5.5×10^3 and ~7.5×10^2, respectively. Subsequently, Ag-Cu alloy NPs were utilized for the detection of three molecules, MB, picric acid (PA), and ammonium nitrate (AN). The achieved EF were ~3×10^7 for MB 5 nM, ~2.8×10^4 for PA 5 µM and ~3.3×10^4 for AN 5 µM. The variation in the primary prominent peak intensity of the three molecules was verified by recording the SERS spectra from more than ten different locations, and the obtained RDS values were 7.08%, 8.04%, and 8.58 % and for MB (1621 cm^{-1}), PA (827 cm^{-1}) and AN (1047 cm^{-1}), respectively.

* Ag-Au and Cu-Au alloy NPs were also synthesized by a simple approach of using femtosecond laser ablation of Ag and Cu targets in 5 mM $HAuCl_4$ solution. After laser ablation, alloy NPs were centrifuged, washed in distilled water, and dispersed in 5 ml of ethanol. The single SPR peak in the UV-visible absorption spectra and the elemental composition mapping from FESEM-EDS indicated the formation of alloy NPs. XRD and HRTEM analyses revealed that the alloy NPs were composed of both the atoms. Both Ag-Au and Cu-Au NPs were utilized to detect MB-5 nM, PA-5 µM, DNT- 1 µM with EF's of ~10^7, ~10^4, and ~10^5, respectively. The reproducibility was verified and the achieved the RSD value was 7.5% and 12.5% for Ag-Au and Cu-Au alloy NPs. Among all the alloys NPs tested, Ag-Au alloy NPs were found to be superior SERS substrates.

* In our next effort, the improvement in SERS performance of Ag-Au alloy NPs was investigated by changing the base/support from plain silicon (Si) to laser textured Si. The base morphology effect on SERS was examined with MB using a micro-Raman spectrometer and noticed the enhanced in SERS signal compared to untextured Si. The femtosecond (~50 fs, 800 nm, 1 kHz) laser ablation technique used for patterning micro square arrays (MSA) on Si at different pulse energies 10, 20, 30,50, and 100 µJ. The variation in enhancement in the SERS signal with respect to the ablated pulse energy

was observed by choosing MB (5 nM) as a probe molecule and observed Si MSA fabricated at 30 µJ with Ag-Au alloy NPs as a better substrate. The optimized Si MSA at 30 µJ was utilized for the detection of MB-10 pM, PA-50 nM, and RDX 1 µM with EF 1.2×10^{10}, 2.2×10^{6} and 9.3×10^{4}. Interestingly, ~347 and ~26 times increment in the EF was noticed for MB and PA, respectively, compared to plain Si with Ag-Au alloy NPs. Furthermore, the robustness of the hybrid substrate Si- MSA with Ag-Au alloy NPs was demonstrated by using them for multi-analyte detection through the detection of complex mixtures of explosives and dye molecules PA + MB, DNT + MB, and explosive-explosive mixture PA + DNT. The reproducibility of the optimized hybrid substrate verified with the prominent mode intensities for all the molecules being less than 15%, shows better SERS substrate.

* Paper-based SERS substrates were fabricated by loading fs ablated Ag and Au NPs in distilled water. The performance of the Ag/Au NPs loaded FP was improved by adopting aggregation phenomena to generate a higher number of hot-spots. The aggregated Ag/Au NPs were achieved by addition of NaCl with various concentrations ranging from 1 mM to 1M (1 mM, 10 mM, 50 mM, 0.1 M, 0.5 M, and 1 M) in 1:1 ratio. Paper-based SERS substrate was prepared by simple soaking of already prepared aggregated Ag/Au NPs. The optimization of salt concentration was verified by recording the SERS spectra of MB-5µM using FP loaded with aggregated Ag/Au NPs at all NaCl concentrations. Initially, the SERS signal increased with increasing salt concentration through increasing the plasmonic effect because of decreasing the gap between the NPs. When the concentration was higher than the critical coagulation concentration (CCC), the SERS signal decreased because of the precipitation of colloidal NPs. It was further confirmed from the FESEM data of the FP substrates.

* FP substrates loaded with Ag and Au NPs with optimized NaCl concentration (50 mM) were utilized for the detection of MB -5 nM and the achieved EFs are 3.4×10^{7} and 7.9×10^{6}, respectively. Ag-based FP substrates demonstrated better SERS signals compared to Au based FP substrates. The Ag-based FP substrate at 50 mM NaCl was further examined for the detection of explosive molecules such as PA-5 µM, NTO- 10 µM and DNT-1 µM with EFs of ~10^{4}. The stability of FP substrates (the variation of signal intensity with respect to time) loaded with Ag and Au NPs was verified with MB (5 µM) and Thiram (10 µM) molecules. The SERS signal intensity drops ~ 89 % and ~

40% for Ag and Au substrates in 15 days. Because of the high plasmonic nature, Ag demonstrated better SERS signal in the early days compared to Au based substrate. From the stability studies, we observed a ~ 90% drop of the SERS intensity in ~30 days for FP with Ag NPs and a ~55 % drop in 45 days for FP with Au NPs. Therefore, we noticed that Au NPs loaded FP have exhibited consistent SERS performance.

* We further continued the FP based SERS studies with stable Au NPs. However, to improve the SERS performance other shapes of Au NPs were prepared and studied. FP based SERS studies were continued with the three different shaped Au NPs, i.e., spherical, triangular, and star shapes. Spherical Au NPs are fabricated by fs laser ablation techniques. The anisotropic Au NPs are prepared by chemical methods. The SERS performance was verified with the NB molecule; star Au NPs loaded FP have shown the superior signal than the other two shapes such as triangular and spherical. Furthermore, the FP loaded with star-shaped Au NPs was able to detect NB-10 pM with ~3.7×10^{10} EF. Electromagnetic near-field distributions of these shapes of Au NPs were simulated using COMSOL Multiphysics, and the results also proved that the sharp edges and tips of the star Au NPs boost the SERS activity. From the previous results, the optimized aggregated spherical (50 mM –NaCl) and star-shaped Au NPs were considered as superior flexible paper-based SERS substrates. The comparison studies were performed on both the FP substrate with NB-5 nM and PA-5 µM molecules. The achieved EF's for PA were 7.2×10^{4} and 4×10^{4}, for NB were 2.7×10^{8} and 3.2×10^{8} using FP with aggregated spherical and star-shaped Au NPs, respectively. The obtained RSD from the reproducibility studies were <9% and <19% for aggregated spherical and star-shaped Au NPs loaded FP substrates, respectively.

* Other flexible SERS substrates were prepared by the electrospinning technique. Initially, PVA-nanofibers were synthesized by varying the concentration of the PVA (5, 10, and 30 wt%) at a fixed applied electric potential and the nozzle-collector distance. The flexible plasmonic active SERS was prepared by electrospinning of the optimized PVA (10 wt%) concentration with picosecond laser (~30 ps, 1064 nm, 10 Hz) ablated Au NPs. The characterization of the polymer nanofiber with and without NPs was performed using FESEM, TEM, and XRD techniques. The PVA- Au NPs nanofiber mat was utilized for detecting MB with an EF of ~4×10^{4} for 1620 cm^{-1} mode.

SERS studies were continued further to detect ester agent methyl salicylate (MS-10 mM). A good reproducibility with ~10% RSD was noticed.

* Commercially available rigid and flexible SERS substrates performances were also verified, which were provided by SERSitive and Ω-Metrohm Company, respectively. The rigid SERSitive substrate was used to detect MB and PA and the obtained EFs and RSD were ~2.6×10^7 and ~9.6% for MB (1620 cm^{-1}) and ~1.2×10^4 and ~12.5% for PA (820 cm^{-1}). The Ag/Au paper-based flexible Ω-Metrohm substrate detected MB -5 µM and CV- 5 µM with EF's of 10^4 for MB and 10^3 for CV and a RSD >13%. The obtained SERS results of this thesis work were found to be superior/on par with the commercially available substrates in terms of sensitivity and reproducibility.

* The DVD was identified as a potential base of the SERS substrate instead of bare glass/Si. The presence of grating patterns and metallic film on DVDs play a role in the enhancement of the Raman signal. The tracks could be enabled to trap the drop-casted NPs. Here the presence of Au NPs on the DVD-W sample was verified with four dye molecules i.e, R6g (5 µM), MB (50 nM) NB (50 nM), and CV (50 nM) and noticed ~3 times intensity enhancement in the Raman signal in the presence of Au NPs on the DVD substrate compared to without Au NPs. The written DVD with Au NPs was able to detect NB having a concentration from 5 µM to 1 nM and achieved EF ~1.4×10^9. The reproducibility was verified from 14 different locations and the estimated RSD was ~10.46%.

6.2 Future scope

Our primary goal (at ACRHEM, UoH) is towards the identification of trace explosives in pure and mixed form and these can be used effectively extended for the detection of (a) explosive vapors (b) pesticides in foods (c) forensic analysis (d) narcotics identification (e) adulteration in oils and milk

There is scope for improvement in the enhancement factors and LOD achieved by

★ Bi/Tri metallic alloy NPs fabrication can be studied by varying the molar ratio of metal salts ($AgNO_3$, $HAuCl_4$), and varying laser ablation parameters more precisely yielding different compositions of NPs. The optimization of highly stable and sensitive alloy NPs has to be investigated for better SERS efficiency.

- Tuning the morphology of the Si MSA can be achieved by altering the laser parameters such as the angle of incidence, liquids, pulse duration, the scan speed of the sample during the fabrication of these structures. This in conjunction with the alloy NPs provides enormous scope for improving the SERS sensitivity. Si MSA with plasmonic coatings can be prepared in a single step by the laser texturing of Si in silver and gold salts at different molar ratios. The SERS enhancements can be improved further by loading the different densities of NPs on the nanostructures and also using hybrid structures that need to be taken up in the future.
- Electrospun nanofibers have to be further investigated by varying the experimental parameters to develop metallic hollow and core-shell nanofibers. Detailed investigations are also required to understand the fiber morphology with various NPs and the effect on the SERS enhancements, which could be explored under calcination effect at different temperatures.
- The presence of PVP on the star-shaped Au NPs is not resulting in a good efficiency in explosives detection. Therefore, it needs to be improved by preparing bare anisotropic Au NPs or Au-Ag alloy star NPs.
- Further, large scale production of SERS substrates is possible, thereby addressing the cost issues also. For that purpose, the creation of paper/fabrics/textiles based flexible SERS substrates will result in other low-cost SERS substrates, which can be taken to the point of interest.
- The shelf life of the SERS substrates can be improved by vacuum protection which can avoid contamination or deterioration due to oxidation effects.
- A hand-held Raman spectrometer can be employed to examine the sensitivity of fabricated substrates in on-field detection.
- COMSOL simulations have to be performed on the various NPs and NSs. Estimation of enhancement factors of different materials having various sizes/shapes in the UV to NIR excitation wavelengths is essential for understanding the hot spot effects.

Intentional blank page

Appendix-A

Table A.1 Molecular structures and other parameters of the molecules used in the thesis

S.No	Compound name	Chemical formula	Molar mass (g/mol)	Solubility	Molecular structure
1.	Picric acid / 2,4,6-trinitrophenol **(PA)**	$C_6H_3N_3O_7$	229.10	Methanol	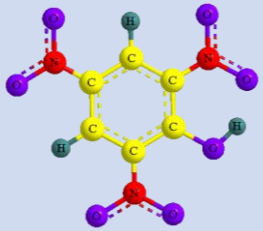
2.	2, 4 dinitro toluene/ 1-methyl-2,4-dinitrobenzene **(DNT)**	$C_7H_6N_2O_4$	182.13	Methanol	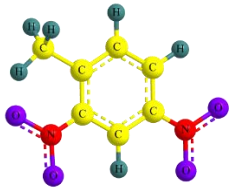
3.	1,3,5-Trinitro-1,3,5-triazinane **(RDX)**	$C_3H_6N_6O_6$	222.12	Acetonitrile	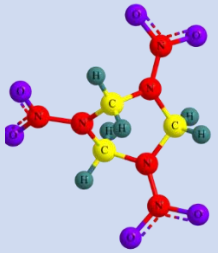

4.	Nitrotriazolone **(NTO)**	$C_2H_2N_4O_3$	130.06	Water	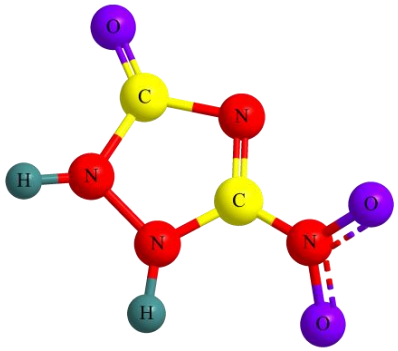
5.	Ammonium Nitrate (**AN)**	$(NH_4)(NO_3)$	80.04	Water	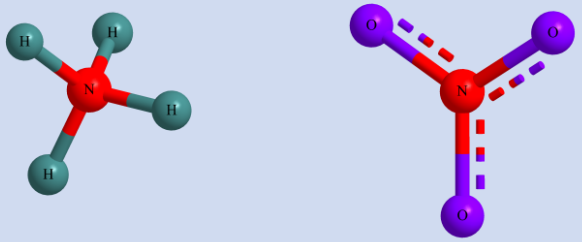
6.	Methylene blue **(MB)**	$C_{16}H_{18}ClN_3S$	319.85	Ethanol	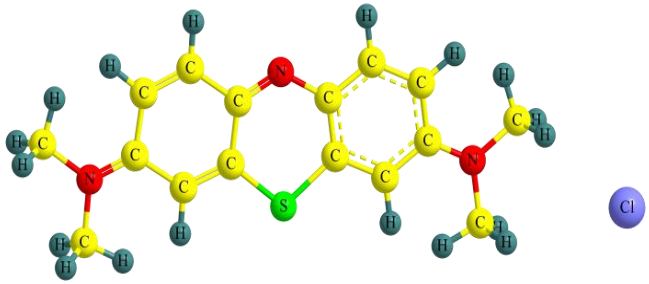

7.	Nile blue **(NB)**	$C_{20}H_{20}ClN_3O$	353.85	Ethanol	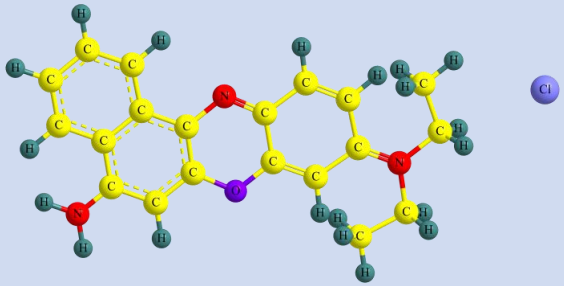
8.	Crystal violet **(CV)**	$C_{25}N_3H_{30}Cl$	407.9	Methanol	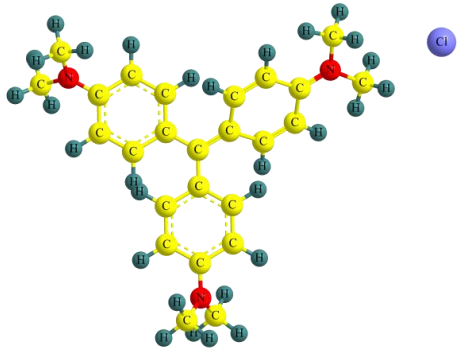
9.	Malachite green **(MG)**	$C_{23}H_{25}ClN_2$	364.9	Water	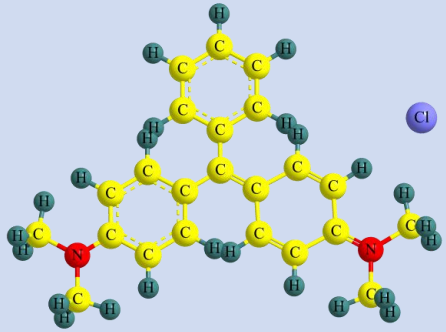

10	Rhodamine 6g **(R6g)**	$C_{28}H_{31}N_2O_3Cl$	479.02	Ethanol	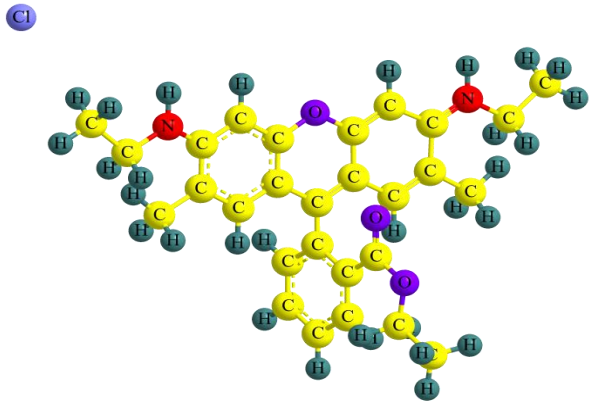
11	Thiram	$C_6H_{12}N_2S_4$	240.42	water	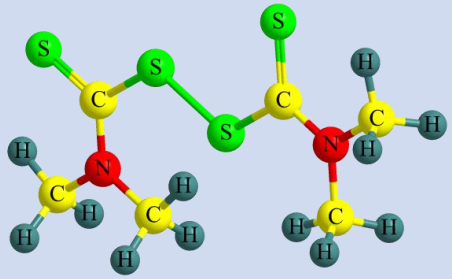
12	Methyl salicylate **(MS)**	$C_8H_8O_3$	152.14	Ethanol	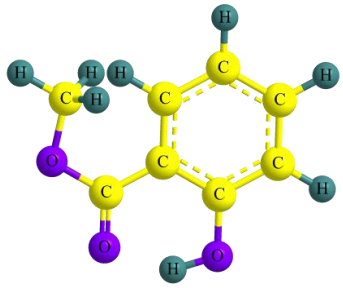

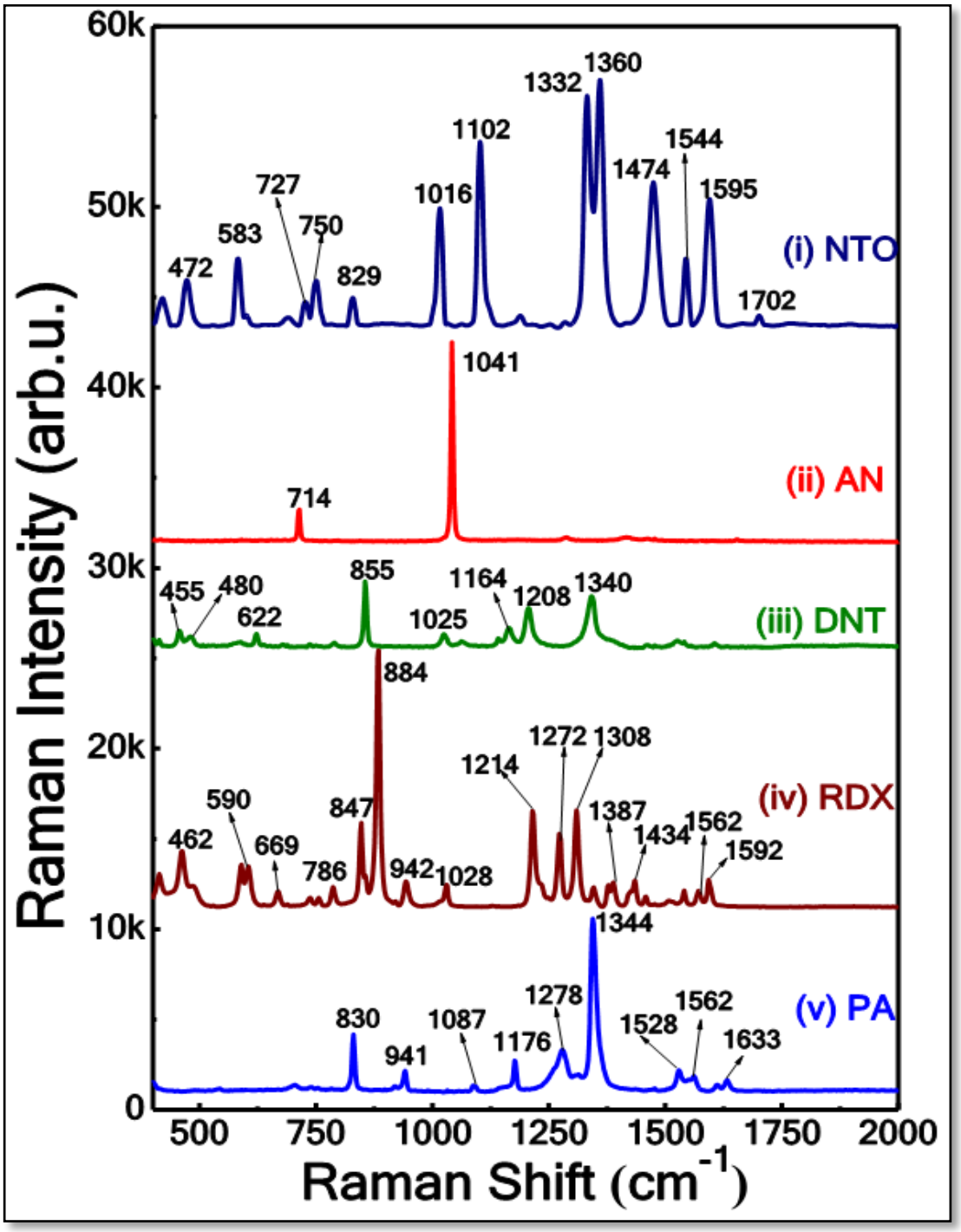

Figure A.1 Raman spectra of explosives (powder form) (i) NTO (ii) AN (iii) DNT (iv) RDX (v) PA studied in this work

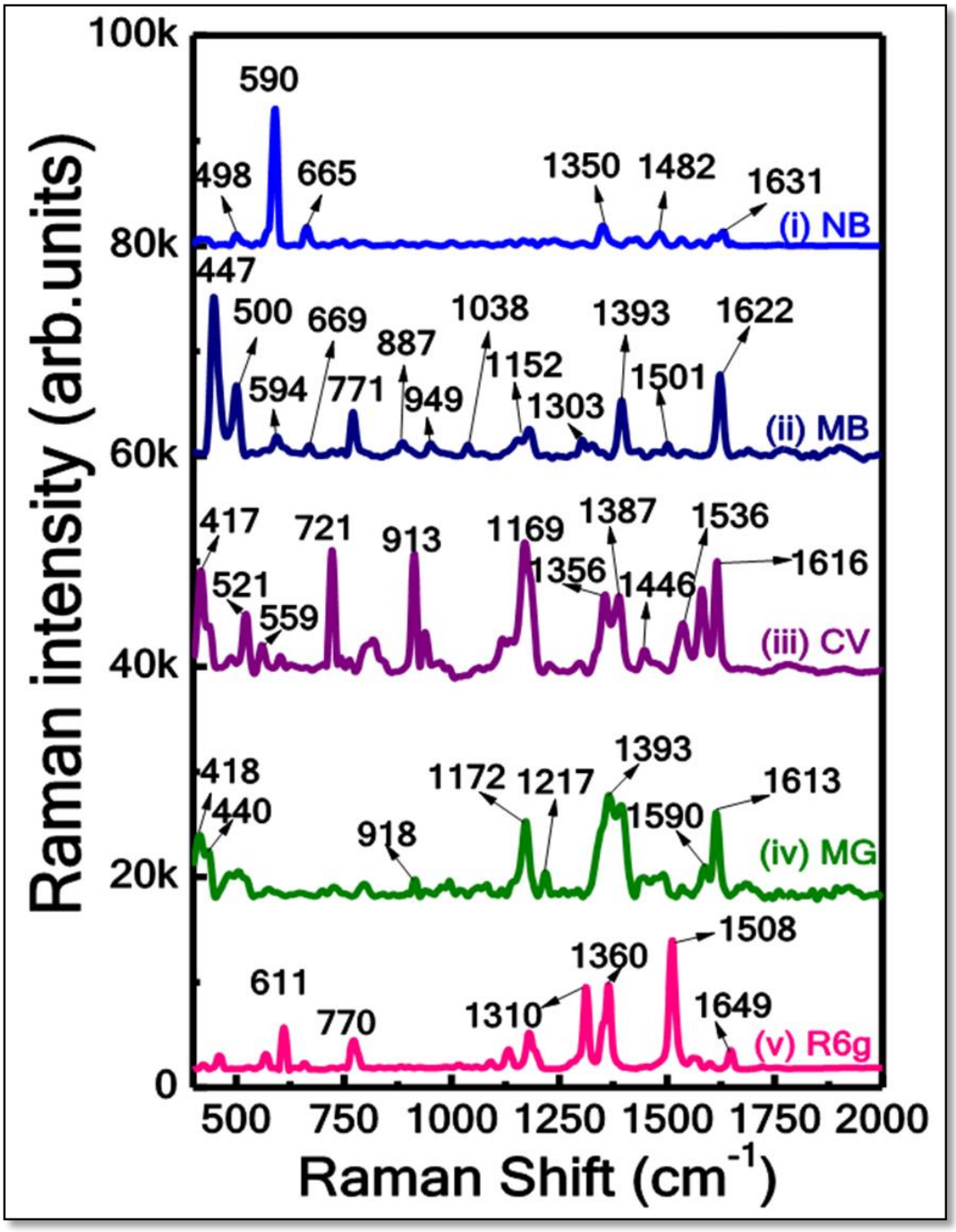

Figure A.2 Raman spectra of dyes (powder form) (i) NB (ii) MB (iii) CV (iv) MG (v) R6g studied in this work

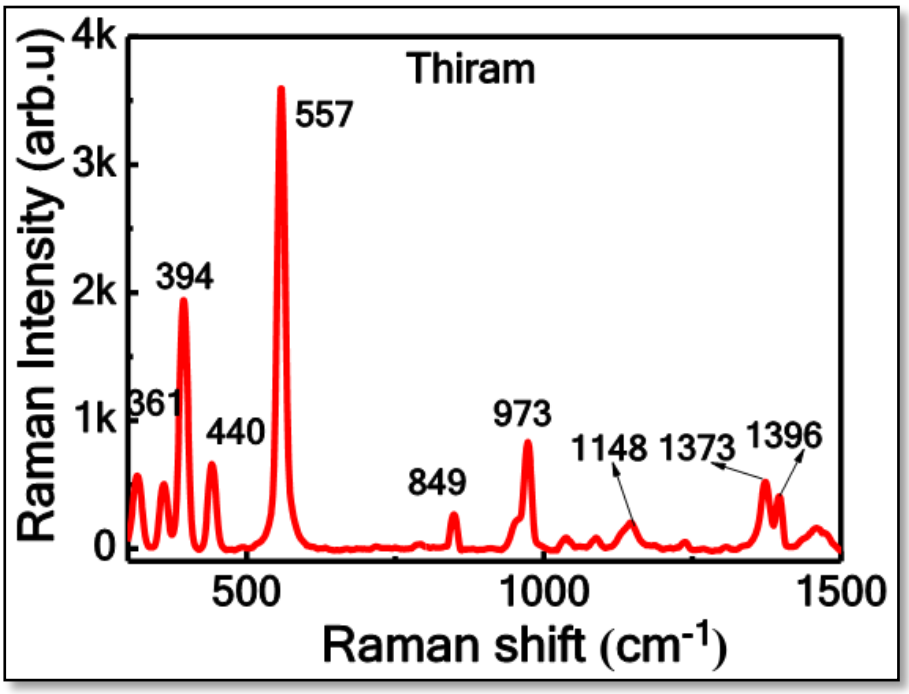

Figure A.3 Raman spectra of thiram (powder form)

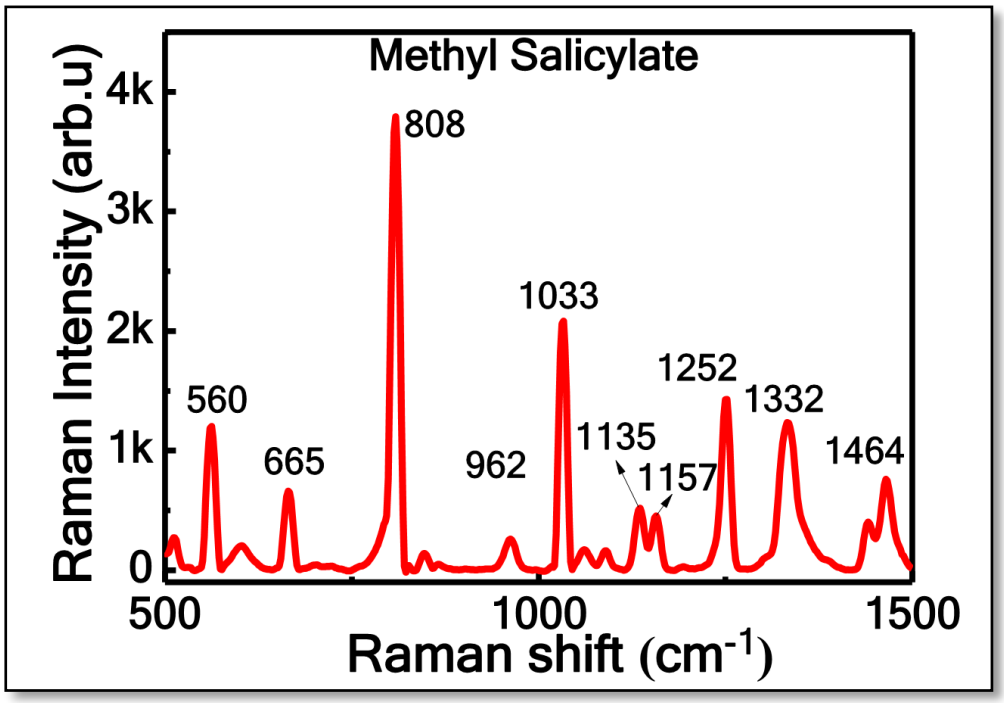

Figure A.4 Raman spectra of methyl salicylate (in liquid form, wintergreen oil-based)

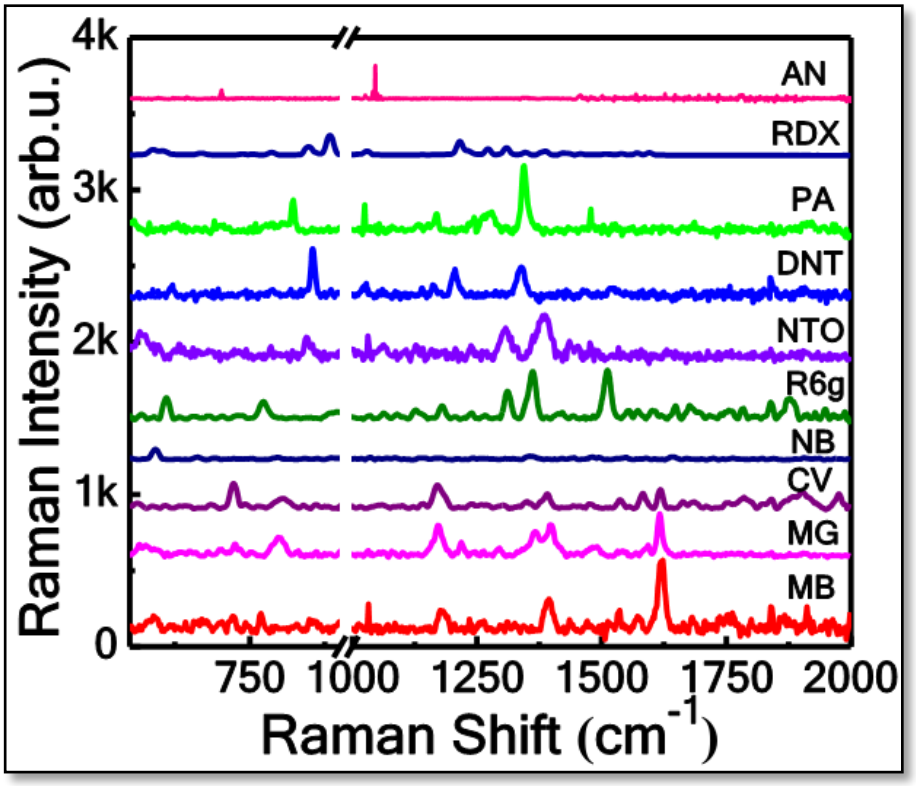

Figure A.5 Raman spectra of MB 0.1 M, MG 0.1 M, CV 5 mM, NB 0.5 M, R6g 2.8 mM, NTO 0.1 M, DNT 0.1 M, RDX 0.1 M, AN 0.1 M (without NPs)

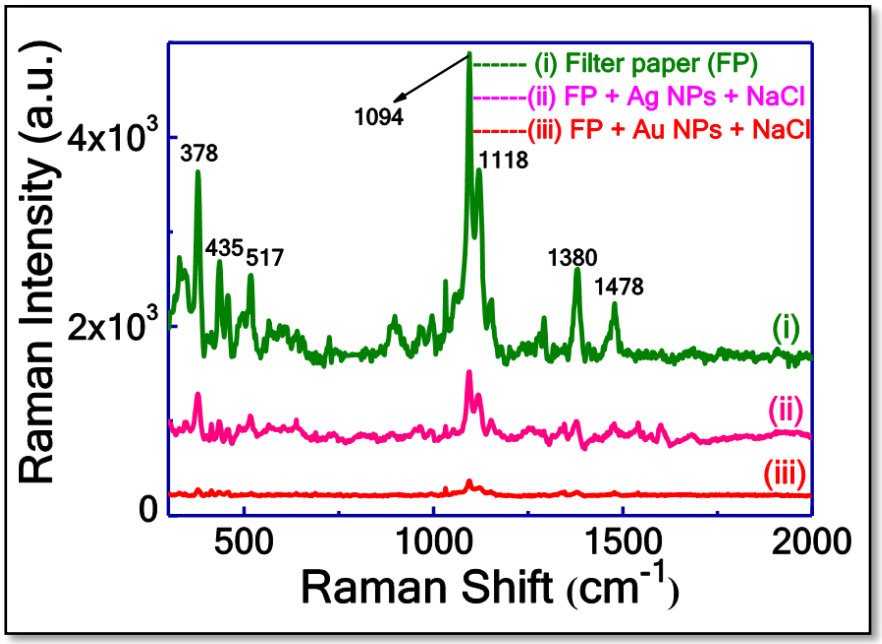

Figure A.6 Raman spectra of Whatman-1 filter paper (i) bare FP (ii and iii) SERS substrates loaded with Ag and Au NPs at NaCl 50 mM concentration.

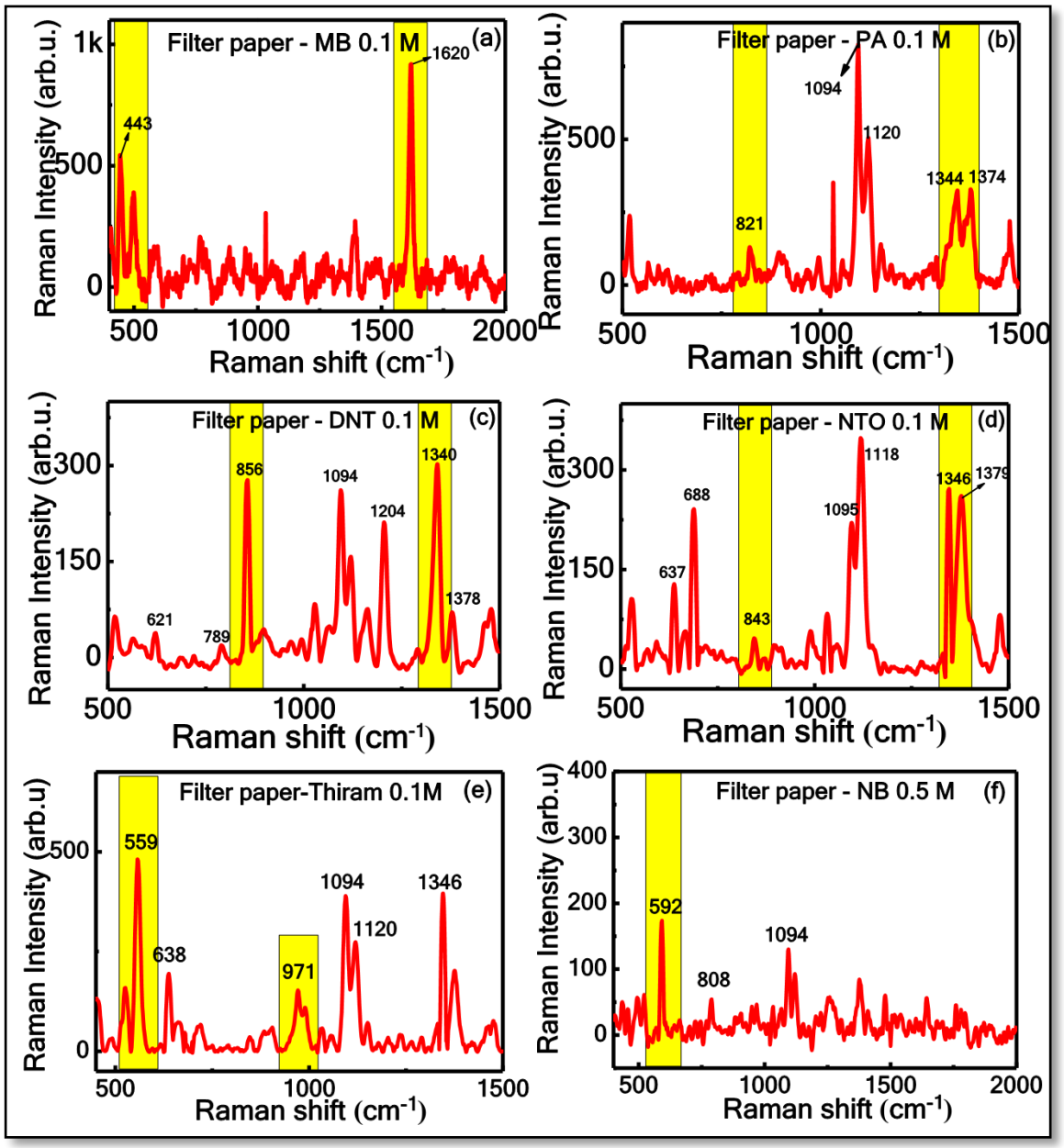

Figure A.7 Raman spectra (a) MB (b) PA (c) DNT (d) NTO at 0.1 M (e) Thiram 0.1 M (f) NB 0.5 M concentration on bare whatman-1 filter paper.

Raman peaks of analyte molecules and their assignments

Table A.2 Raman peaks and their assignments of PA[1]

S. No	Raman shifts (cm^{-1})			Peak Assignments
	Reported	Observed (Powder)	Observed (SERS,± 2)	
1	825	830	829	CN stretching; NO_2 scissoring in-plane deformation
2	935	941	941	CN stretching; ring CCC in-plane bending
3	1085	1087		In-plane CH bending
4	1165	1176	1175	CCC stretching; CN stretching
5	-	1278	1272	OH bending; CH bending
6	1320		1317	
7	1338	1344	1338	CN stretching; CO stretching; CH bending; CC stretching
8		1528, 1562	-	NO_2 symmetric stretching
9	1560	1560	-	NO_2 asymmetric stretching & ring CC stretching

Table A.3 Raman peaks and their assignments of DNT[2-4]

S. No	Raman shift (cm^{-1})			Peak Assignments
	Reported	Observed (Powder)	Observed (SERS)	
1	467	455	-	CH_3 rocking, ring twisting
2	-	480	-	
3	639	622	-	Ring twisting, C–H (ring) rocking, CH_3 rocking
4	859	855	855	NO_2 scissoring; ring in-plane deformation
5	1047	1025		CH_3 rocking
6	1134	1164		Methyl H-C-H asymmetric bend
7	1207	1208	1203	C–H in-plane rocking
8	1354	1340	1343	NO_2 symmetric stretching; C–N stretching

Table A.4 Raman peaks and their assignments of AN[5-6]

S. No	Raman shift (cm^{-1})			Peak Assignments
	Reported	Observed (powder)	Observed (SERS)	
1		714	712	-
2	1048	1041	1047	symmetric stretch mode of NO_3^-

Table A.5 Raman peaks and their assignments of NTO[7-8]

S. No	Raman shift (cm^{-1})			Peak Assignment
	Reported	Observed (powder)	Observed (SERS)	
1	473	472	-	N-H deformation; ring deformation out of a plane
2	585	583	-	N-H deformation; ring deformation out of a plane
3	729	727	686	Ring deformation out of a plane
4	750	750	784	Ring deformation; NO_2 deformation in plane
5	829	829	845	Ring deformation; NO_2 deformation in plane
6	1018	1016	1061	Ring deformation; N-H deformation; ring-NO_2 stretching in plane
7	1109	1102	1097	Ring deformation (N-N-C asymmetric stretching) in plane
8	1332	1332	1305	N-H deformation; ring deformation (N-N-C asymmetric stretching) in plane
9	1360	1360	1383	NO_2 deformation; NO_2 symmetric stretching; N-H deformation in plane
10	1475	1474	-	Ring deformation (N-C stretching);N-H deformation + NO_2 deformation in plane
11	1545	1544	-	Ring deformation (N-C-N); N-H deformation; NO_2 asymmetric stretching in plane
12	1599	1595	-	C=O stretching
13	1702	1702	-	N-H stretching

Table A.6 Raman peaks and their assignments of RDX[9]

S. No	Raman shift (cm^{-1})			Peak Assignments
	Reported	Observed (powder)	Observed (SERS)	
1	750			Ring bending with NO_2 scissoring
2	795	786		C–N stretching; NO_2 scissoring
3	850	847	846	N–N stretching; NO_2 axial scissoring
4	884	884	883	C–N stretching
5	1024	1028	1029	N–C stretching; CH_2 rocking
6	1216	1214	1214	N–C stretching

7	1270	1272	1271	N–N stretching; O–N–O stretching; CH_2 twisting
8	1314	1308	1295	N–N stretching; CH_2 twisting; NO_2 symmetric vibration
9	1352	1387	-	CH_2 wagging
10	1524	1562	-	CH_2 scissoring
11	1586	1592	-	O–N–O axial stretching, NO_2 antisymmetric vibration

Table A.7 Raman peaks and their assignments of MB[10]

S. No	Raman shift (cm^{-1})			Peak Assignments
	Reported	Observed (powder)	Observed (SERS)	
1	448	447	445	Skeletal deformation of C-N-C
2	501	500	478	Skeletal deformation of C-N-C
3	596	594	595	Skeletal deformation of C-S-C
4	671	669	-	Out of plane bending of C-H
5	770	771	805	In-plane bending of C-H
6	890	887	898	In-plane bending of C-H
7	951	949	-	In-plane bending of C-H
8	1040	1038	1036	In-plane bending of C-H
9	1154	1152	1150	In-plane bending of C-H
10	1302	1303	-	In-plane ring deformation of C-H
11	1394	1393	1388	Symmetric stretching of C-N
12	1502	1501	1504	Asymmetric stretching of C-C
13	1623	1622	1621	Ring stretching of C-C

Table A.8 Raman peaks and their assignments of NB[11]

S. No		Raman shift (cm^{-1})		Peak Assignments
	Reported	Observed (powder)	Observed (SERS)	
1	499	496	-	C-C-C deformation
2	595	590	590	C-C-C and C-N-C deformations

3	673	663	662	In-plane CCC or NCC deformations
4	1185	1185	1118	C-H bending
5	1351,1492, and 1643	1350, 1484 and 1629	1375	Ring stretching

Table A.9 Raman peaks and their assignments of CV [12] [13]

S. No	Raman shift (cm^{-1})			Peak Assignments
	Reported	Observed (powder)	Observed (SERS)	
1	425	417	418	Bending deformation of CNC
2	522	521	525	In-plane deformation of CNC
3	560	559	570	Out-of-plane deformation of CNC
4	715	721	728	Stretching CN
5	902	913	913	Bending of CCC
6	1165	1169	1175	Symmetric stretching CCC
7	1360	1356	1368	Asymmetric stretching CCC
8	1380	1387	1385	Bending CH
9	1462	1446	1445	Asymmetric Bending CH_3
10	1532	1536	1588	Stretching CN
11	1619	1616	1618	Symmetric stretching CC

Table A.10 Raman peaks and their assignments of MG[14-15]

S. No	Raman shift (cm^{-1})			Peak Assignments
	Reported	Observed (powder)	Observed (SERS)	
1	420	418	418	Out of plane benzene
2	435	440		Ring deformation
3	938	918		In-plane benzene
4	1177	1172	1169	In-plane C-H bending
5	1219	1217		N-C stretching
6	1368	1365		Phenyl-N stretching
7	1394	1393	1393	In-plane C−C and C−H stretching

8	1511	1590		In-plane phenyl ring stretching
9	1615	1613	1614	Phenyl-N and C−C stretching

Table A.11 Raman peaks and their assignments of R6g[16]

S. No	Raman shift (cm^{-1})			Peak Assignments
	Reported	Observed (powder)	Observed (SERS)	
1	613	609	611	C–C–C ring in-plane bending
2	775	770	771	C–H out-of-plane bending
3	1312	1310		In-plane ring breathing
4	1364	1360	1362	Ring stretching; in-plane CH bend
5	1512	1508	1511	Ring stretching; CN stretching; C-H and N-H bending
6	1651	1649	1650	Ring stretching; in-plane C-H bending

Table A.12 Raman peaks and their assignments of MS[17]

S. No	Raman shift (cm^{-1})			Peak Assignments
	Reported	Observed	Observed (SERS)	
1	566	560	562	Out-of-plane of the benzene ring
2	670	665	661	Out-of-plane and in-plane of a benzene ring
3	812	808	808	Stretching vibration of C-H
4	1033	1031	1033	In-plane of a benzene ring
5	1253	1250	1250	Stretching vibration of C-O

Table A.13 Raman peaks and their assignments of thiram [18]

S. No	Raman shift (cm^{-1})			Peak Assignments
	Reported	Observed (powder)	Observed (SERS)	
1	444	440		CH_3NC deformation and C-S stretching
2	559	557		S-S stretching
3	870	849		CH_3N stretching
4	932	973	936	C-Sand CH_3N stretching

5	1143	1148		C-N stretching mode
7	1376	1373	1375	CN stretching and symmetric deformation CH_3
8		1396	1486	

Table A.14 Raman peaks and their assignments of Whatman-1 filter paper[19-21]

S. No	Raman shift (cm^{-1})		Peak Assignments
	Reported	Observed (powder)	
1	520	517	some heavy atom bending and stretching
2	1095	1094	C−O−C bending mode
3	1120	1118	Bending of H-C-C and H-C-O at C6 heavy atom (C-C and C-O) stretching
4	1340	-	OH deformation vibration
5	1380	1380	CH deformation vibration
7	-	1478	-

Table A.15 Summary of the results obtained from paper-based SERS substrates reported in the literature

S. No.	NPs & Size	SERS Substrate	Fabrication Method	Analyte	EF	Spectrometer (Wavelength)	Ref
1	Ag	Whatman chromatography paper (Grade 1 CHR)	Silver mirror reaction	Rh6g - 10^{-11} M p-ATP – 10^{-9}M	10^5	Horiba Jobin Yvon (532 nm & 632 nm)	22
2	Ag (60 nm)	GSM grade paper	Pipetting NPs	Rh6g - 0.1 nM, MG - 1 nM.	10^7	Table Top Raman Spectrometer (785 nm)	23
3	Ag	Fisher brand chromatography paper	Inkjet Printer	Rh6G - 10 nM	10^5	Horiba Jobin Yvon HR-VIS Raman microscope (632.8 nm)	24
4	Ag	chromatography paper	Inkjet Printer	Rh6G - 95 fg, Organophosphate malathion - 413 pg, Heroin – 9 ng, Cocaine – 15 ng	-	Portable Spectrometer (785 nm)	25
5	Ag	Filter Paper	Silver mirror reaction	CV - 10^{-9} M Thiram - 10^{-7} M	-	Microscope Raman system -DeltaNu	26
6	Ag	Whatman No 3 grade Filter Paper	Soaking with NaCl Prior to NPs	Seminal Plasma Rh6G	10^7	Micro Raman System (785 nm)	27
7	Ag	Fisher brand chromatography paper	Inkjet Printer	Melamine- 5 ppm, Heroin – ng, Mixtures of Rh6G – 1 mM, MB - 1 mM,	-	Portable Spectrometer Ocean Optics (785 nm)	28

				MG - 1 mM			
8	Ag	Brushing	Microfluidic paper	Rh6G-1 nM MG-10 nM	10^7	DXR Raman Microscope (632.8 nm)	29
9	Au Nano Rods (60 nm long 18 nm diameter)	Whatman filter paper grade 1	Drop cast	Trans-1,2-bis (4-pyridyl) ethane (BPE)- 0.5 nM	5×10^6	Raman System (785 nm)	30
10	Ag NPs & Ag NSs (stars)	Whatman filter paper grade 1	Drop cast	Rhodamine (Rh6G)	10^7	Horiba Jobin Yvon (633 nm)	31
11	Ag Nano triangles	Filter paper	Immersion	PA- 10^{-6} M PATP -10^{-8} M	-	Titan Electro Optics Raman spectrometer (532 nm)	32
12	AgNPs (50 nm)	Filter paper	Cellulose self-sacrificing reduction	MB 6-TG	-	Raman Spectrometer Ocean Optics (785 nm)	33
13	Ag Nanowires	Millipore-Mixed cellulose membrane	Filtrating of Ag NS through hydrophilic filter	CV -1.0×10^{-8} mol·L^{-1} BPE-5.0×10^{-9}mol·L^{-1}	7.7×10^6 1.4×10^6	Renishaw InVia Raman Microscope (532, 633 & 785 nm)	34
14	Au Nanorods (5 – 100 nm)	Whatman filter paper grade 1, swab	Immersion	BDT -0.1 nM	5×10^5	Horiba Confocal Raman Spectrometer (785 nm)	35

15	Au NPs (5-100 nm)	Whatman filter paper grade 4	Drop cast	Trans-1,2-bis (4-pyridyl)-ethylene	3×10^4	Horiba Confocal Raman Spectrometer – (785 nm)	36
16	Au NPs	Whatman chromatography filter paper grade 1	Ink Jet Printing	CarboxyMethyle cellulose (CMC) & AuNPs (7:1),RH6G	1.8×10^4	SENTERRA Confocal Raman Spectrometer – (785 nm)	37
17	Anisotropic Au NPs (20 nm)	filter paper	Soaking	Benzenedithiol (BDT) - 1 µM Steronoin - 100 nM	-	Witec Alpha300 Raman Spectrometer (785 nm)	38
18	Au NPs	filter paper	Dropped	Mucin-1 nM	-	Confocal Raman Spectrometer (Renishaw) – (633 nm)	39
19	Au Nano Rods	filter paper	Dipping	Cancer Screening	-	Raman Microscope (Renishaw) – (785nm)	40
20	Au NPs	Whatman filter paper grade 1	Thermal Inkjet technology	2,4,6-trinitrotoluene -94 pg 2,4-dinitrotoluene -7.8 pg 1,3,5-trinitrobenzene -0.89 pg	-	Portable Spectrometer (R-3000QE, Agiltron) – 785 nm	41
21	Au@Ag 3o nm Au core &	Whatman 1 qualitative Filter Paper	Printing	Thiram - 10^{-9} mol L^{-1}	-	Micro Raman System (785 nm)	42

	7 nm Ag shell						
22	GO@Ag NPs@paper	Whatman 1 chromatography paper	Immersion and dip coating method	Rh6G – 10^{-19} M CV -10^{-20} M	-	Horiba HR evolution 800 Ar excitation laser (532 nm)	43
23	Au NPs (15–120 nm); Au NRs (50 nm long, 14 nm thick); Ag NPs (50-80 nm)	A4 paper Filter paper	Pen-on-paper	LOD < 10 atto moles-Dye < 10 ppb- Pesticide	-	Micro-Renishaw InVia Reflex system (532, 633 and 785 nm)	44
24	Au porous nanospheres (55 nm)	common laboratory filter paper	Soaking	Rh6G – 10 nM	2.3×10^{6}	Renishaw Invia Raman Microscope (633 nm)	45
25	Au NPs (different concentrations)	Whatman #1	Dipping	4-ATP	2×10^{8}	Renishaw Invia Raman Microscope (633 nm)	46
26	Au NRs	Whatman no. 1	Immersion and polyelectrolyte coating	R6G (100 aM)	-	Renishaw inVia confocal Raman Spectrometer (785 nm)	47
27	Au NPs	Chromatography paper	Inkjet print	BPE-1.8 ppb		QE65000 (Ocean Optics) portable	48

						spectrometer (785 nm)	
28	Au nanostars	Filter paper	Drop cast	MG - 1 ppm		Horiba Jobin-Yvon micro-Raman spectrometer (633 nm) with DuoScan mapping mode (785 nm)	49
29	Ag NPs	Filter papers	silver mirror reaction	R6G - 10^{-12} M RhB - 10^{-9} M	1.42×10^{10} 0.659×10^{6}	A WITec Alpha-300 micro-Raman spectrometer 532 nm	50
30	Ag NPs	cellulose nanofibril (CNF)-coated filter paper	drop and dry method	R6G 1 4-ATP 0.1 nM		custom-made Raman read-out system (643-nm)	51
31	Ag NPs	cellulose nanocrystals-paper	in situ reduction	Phenylethanolamine A - 5 nM Metronidazole -200 nM		Renishaw confocal Raman (785 nm)	52
32	Ag NPs	Whatman no. 1	In-situ	RhB-10^{-12} M	1.1×10^{9}	Senterra confocal Raman system (785 nm)	53
33	Ag NPs	Kimwipe™eL tissue paper.	inkjet	MY from toor dal - nM MG from green peas and green Chillies-nM	-	Metrohm portable Raman 532 nm	54
34	MoO_{3-x} nanosheets	Chromatography and filter paper	Inkjet	Rh6G – 10^{-7} M	3.3×10^{5}	Jobin Yvon Lab RAM HR800 (532 nm)	55

35	Ag NPs	Whatman no. 1	Wax priniting+spray	R6G 10^{-9} M	2×10^7	Thermo Fisher-confocal DXR Raman (632.8nm)	56
36	Ag NPs/GO	paper	screen printing	Thiram 0.26 ng cm^{-2} Thiabendazole-28 ng cm^{-2} and methylparathion.7.4 ng cm^{-2}	-	portable Raman B&W Tek Inc.(780 nm)	57
37	Au nanorods	Cellulose nanofiber	dispersion	Thiram-1 nM Tricyclazole-100 nM Carbaryl -1 µM	1.4×10^7	portable Raman QEPRO, Ocean Optics-785 nm	58
38	Au-Ag alloy	Whatman chromatography paper		folic acid		632.8 nm	59
39	Au NPs	pseudo-paper	In-situ	4-MBA-10^{-11} M Thiram-1.1 ng/cm^2	~10^6	portable Raman i-Raman Plus, B&W Tek Inc., (785 nm)	60
40	Ag NPs	nylon filter membrane	vacuum suction filtration	R6G- 1 pmol CV- 10 pmol MG 10 pmol		smartphone-based Raman analyzer	61
41	Ag+Au+SWNT	Filter paper	Drop cast	SWCNT	-	Bruker NIR-FT spectrophotometer (1064 nm)	62
42	Au film	Whatman® no. 42	Sputtering+KrF laser shots	R6G (10^{-15} M) 4-ATP (10^{-18} M)		He-Ne laser 633 nm	63
43	Au/Ag film	printer paper	laser techniques	Fungicide mancozeb (Dithane DG) and insecticide		RMS-310 µ-Raman spectrometer 532 nm	64

				thiamethoxam (Aktara 25 BG)			
44	Au NPs	Whatman No. 40	Dip coating	Bacteria		PerkinElmer Raman (785 nm)	65
45	Ag triangular nanoplates	Filter paper	drop casing	4-MBA- 10^{-6} M		HORIBA JOBIN YVON Raman (633 nm)	66
46	Ag NPs	Filter paper	Immerson in NaCl solution for 5 min +dip-coating	Melamine-1ppm Thiram -1 ppm MG -0.36 ppb		Jobin Yvon HR-800 (632.8 nm)	67
47	Ag NPs	Glass fiber paper	In-site reduction	MG –1 × 10^{-8} mol/L	1.3 × 10^{8}	confocal Raman system (XploRA, Horiba Jobin) 532 nm	68
48	Au nanostar	Filter paper A4 printing paper	dripping	CV-100pM	1.2 ×10^{7}	μ Raman Ci,TechnoSpex-785	69
49	Au NPs aggregates	Whatman No.1	Soaking in Au NPs with cationic polyacrylamide pre-treated	4-ATP -1nM	-	Renishaw Invia Raman (633 nm)	70
50	Au NPs	Filter paper	inkjet printing and seed mediated growth	R6g-10^{-10}M	-	HORIBA LabRAM Aramis -633 nm	71
51	Ag NPs	Filter paper	Drop casting	R6g- 10^{-5} M. CV- 10^{-4} M	-	Smartphone-based Raman-785nm	72
52	Au nanorods	Whatman No.1	Immersion	p-ATP - 10^{-12} M	-	Portable Raman (R3000CN)	73

						785 nm	
53	Au, Ag, Cu, and Ni film	standard printer, glossy and silicone paper	pulsed laser deposition	MB- 200 mg/L	-	portable Raman (DeltaNu) 785 nm	74
54	PVP capped Ag NPs	printing paper- different grade GSM	Drop casting	MG-0.1 nM R6G-0.1 nM BPE- 1µM	~10^7	Table-top Raman (EZ Raman Enwave Optronics) 785 nm	75
55	Ag NPs	Glass microfiber filter paper	Silver mirror reaction	Dye mixture 4×10^{-4} M [R6G,CR,CV,MO] extracted carotenoids (lycopene,β-carotene)		Thermo Scientific DXR Raman (Thermo Fisher Scientific)780 nm	76
56	Au NPs	Chromatography paper	self-assemble	Rhodamine -5×10^{-17} M MG-10 fM		Horiba XploRA confocal Raman (785 nm)	77
57	Au Nanostructures with addition of halides (KBr, KI)	A4 paper	In situ reduction	R6g- 10^{-5} M melamine -10 ppm		Raman (Kaiser Optical Systems) 785 nm	78
58	Ag NPs	photographic fixer	thiosulfate treatment	R6g			79
59	Ag NPs	Filter paper	Prior drop-casting of NPs calendaring and alkyl ketene dimer treatment	4-ATP- 0.6 nM Thiram - 0.46 nM Ferbam- 0.49 nM		custom-made Raman 643 nm	80

60	Au nanorods functionalized with mono-6-thio-cyclodextrin	Filter paper	Immersion	Sudan III -0.1 µM Sudan IV -0.5 µM	-	Lab RAM HR800 confocal Raman (Horiba) 632.8 nm	81
61	Au NPs	Filter paper	Dip-coating	1-NAT -0.1 nM		µ-Renishaw InVia Reflex system-633, 785 and 830 nm	82
62	Ag NPs	Filter paper	Dip-coating with the assistance of chloride ions	4-MBA- 10^{-8} M	6.4×10^{5}	Portable Raman (BWS415, B&W Tek) 785 nm	83
63	Sea urchin-like nano ZnO	Whatman chromatography paper -1	In-situ	Sulphite in wine-2 µg mL^{-1}.	-	Portable Raman (i-Raman, B&W Tek) 785 nm	84
64	Ag Nnaoflower	nylon-coated paper	immersion	CV ketoprofen	1.97×10^{4}	Confocal Raman (WITec GmbH, Ulm) 532 nm	85

Table A.16 Commercially available SERS substrates

S.No	Company	SERS substrate	Sensitivity	stability	Cost	Ref
1	stellarnet	Cellulose with gold NPs	~ 10^6	3 months	$199 (pack of 30)	86
2	Horiba France SAS	glass coated with Au nanorods prepared by dynamic oblique vacuum evaporation	-	-	-	87
3	sersitive	Electrodeposition of silver and gold nanoparticles on an ITO glass surface	~ 10^5 -10^6	4 months	5pc Ag- €115 5pc Ag-Au- €138	88
4	EnSpectr Inc	Si/Glass passivated with a thin transparent dielectric layer.	~ 10^6	stable when unpacked	-	89
5	silmeco	Nanostructured Si deposited with Gold (Au), Silver (Ag)	-	-	-	90
6	Hamamatsu	Au NS on polypropylene	-	3 months when unpacked	-	91
7	Integrated Optics	Ag/Au coating on silicate glass.		2 months	Ag-€ 15 Au-€ 18	92
8	Mesophotonics. Ltd Klarite	lithographic patterned Si coated with gold	-	-	-	93
9	Ω-Metrohm	Ag, Au based Filter paper				94
10	Q-SERS	Si wafer (5 mm^2) nanostructures	ppb-ppm	-	$50 / 2 pcs	95

References

1. Hakonen, A.; Wu, K.; Stenbæk Schmidt, M.; Andersson, P. O.; Boisen, A.; Rindzevicius, T., Detecting Forensic Substances Using Commercially Available Sers Substrates and Handheld Raman Spectrometers. *Talanta* **2018**, *189*, 649-652.
2. Ramos, C. M.; Alzate, L. F.; Hernández, N. M.; Hernández, S. P.; Mina, N., Density Functional Theory Treatment of the Structures and Vibrational Frequencies of 2, 4-and 2, 6-Dinitrotoluenes. *Journal of Molecular Structure: Theo.chem.* **2006**, *769*, 69-76.
3. Sylvia, J. M.; Janni, J. A.; Klein, J.; Spencer, K. M., Surface-Enhanced Raman Detection of 2, 4-Dinitrotoluene Impurity Vapor as a Marker to Locate Landmines. *Anal. Chem.* **2000**, *72*, 5834-5840.
4. Ben-Jaber, S.; Peveler, W. J.; Quesada-Cabrera, R.; Sol, C. W. O.; Papakonstantinou, I.; Parkin, I. P., Sensitive and Specific Detection of Explosives in Solution and Vapour by Surface-Enhanced Raman Spectroscopy on Silver Nanocubes. *Nanoscale* **2017**, *9*, 16459-16466.
5. Farrell, M. E.; Holthoff, E. L.; Pellegrino, P. M., Surface-Enhanced Raman Scattering Detection of Ammonium Nitrate Samples Fabricated Using Drop-on-Demand Inkjet Technology. *Appl. Spectros.* **2014**, *68*, 287-296.
6. Acosta-Maeda, T. E.; Misra, A. K.; Muzangwa, L. G.; Berlanga, G.; Muchow, D.; Porter, J.; Sharma, S. K., Remote Raman Measurements of Minerals, Organics, and Inorganics *Appl. Opt.* **2016**, *55*, 10283-10289.
7. Hiyoshi, R. I.; Kohno, Y.; Nakamura, J., Vibrational Assignment of Energetic Material 5-Nitro-2, 4-Dihydro-1, 2, 4-Triazole-3-One (NTO) with Labeled Isomers. *J. Phys. Chem. A* **2004**, *108*, 5915-5920.
8. Xu, Z.; Meng, X., Detection of 3-Nitro-1, 2, 4-Triazol-3-One (NTO) by Surface-Enhanced Raman Spectroscopy. *Vib. Spectrosc.* **2012**, *63*, 390-395.
9. Ghosh, M.; Wang, L.; Asher, S. A., Deep-Ultraviolet Resonance Raman Excitation Profiles of NH_4NO_3, PETN, TNT, HMX, and RDX. *Appl. Spectros.* **2012**, *66*, 1013-1021.
10. Li, C.; Huang, Y.; Lai, K.; Rasco, B. A.; Fan, Y., Analysis of Trace Methylene Blue in Fish Muscles Using Ultra-Sensitive Surface-Enhanced Raman Spectroscopy. *Food Control* **2016**, *65*, 99-105.
11. Bodelón, G.; Montes-García, V.; Fernández-López, C.; Pastoriza-Santos, I.; Pérez-Juste, J.; Liz-Marzán, L. M., Au@ pNIPAM SERRS Tags for Multiplex Immunophenotyping Cellular Receptors and Imaging Tumor Cells. *Small* **2015**, *11*, 4149-4157.
12. Canamares, M. V.; Chenal, C.; Birke, R. L.; Lombardi, J. R., DFT, SERS, and Single-Molecule SERS of Crystal Violet. *J. Phys. Chem. C* **2008**, *112*, 20295-20300.
13. Rekha, C. R.; Sameera, S.; Nayar, V. U.; Gopchandran, K. G., Simultaneous Detection of Different Probe Molecules Using Silver Nanowires as SERS Substrates. *Spectrochimica Acta Part A: Molecular and Biomolecular Spectroscopy* **2019**, *213*, 150-158.
14. Zhao, Y.; Tian, Y.; Ma, P.; Yu, A.; Zhang, H.; Chen, Y., Determination of Melamine and Malachite Green by Surface-Enhanced Raman Scattering Spectroscopy Using Starch-Coated Silver Nanoparticles as Substrates. *Anal. Methods* **2015**, *7*, 8116-8122.
15. Zhang, Y.; Huang, Y.; Zhai, F.; Du, R.; Liu, Y.; Lai, K., Analyses of Enrofloxacin, Furazolidone and Malachite Green in Fish Products with Surface-Enhanced Raman Spectroscopy. *Food Chem.* **2012**, *135*, 845-850.

16. Jensen, L.; Schatz, G. C., Resonance Raman Scattering of Rhodamine 6g as Calculated Using Time-Dependent Density Functional Theory. *J. Phys. Chem. A* **2006**, *110*, 5973-5977.
17. Schonbachler, N.; Luthy, W., Measurements of Raman Lines in Silica, Dimethyl-Methylphosphonate and Methyl Salicylate. *Bern: University of Bern* **2010**.
18. Zhu, J.; Liu, M.J.; Li, J.J.; Li, X.; Zhao, J.W., Multi-Branched Gold Nanostars with Fractal Structure for SERS Detection of the Pesticide Thiram. *Spectrochimica Acta Part A: Molecular and Biomolecular Spectroscopy* **2018**, *189*, 586-593.
19. Socrates, G., *Infrared and Raman Characteristic Group Frequencies: Tables and Charts*; John Wiley & Sons, **2004**.
20. Lee, C. H.; Tian, L.; Singamaneni, S., Paper-Based SERS Swab for Rapid Trace Detection on Real-World Surfaces. *ACS Appl. Mater. & Interf.* **2010**, *2*, 3429-3435.
21. Wanasekara, N. D.; Michud, A.; Zhu, C.; Rahatekar, S.; Sixta, H.; Eichhorn, S. J., Deformation Mechanisms in Ionic Liquid Spun Cellulose Fibers. *Polymer* **2016**, *99*, 222-230.
22. Li, Y.; Zhang, K.; Zhao, J.; Ji, J.; Ji, C.; Liu, B., A Three-Dimensional Silver Nanoparticles Decorated Plasmonic Paper Strip for SERS Detection of Low-Abundance Molecules. *Talanta* **2016**, *147*, 493-500.
23. Hazarika, A.; Hatiboruah, D.; Nath, P., SERS on Paper: An Extremely Low Cost Technique to Measure Raman Signal. *Journal of Physics D: Applied Physics* **2017**, *48*, 485601.
24. Yu, W. W.; White, I. M., Inkjet Printed Surface Enhanced Raman Spectroscopy Array on Cellulose Paper. *Anal. Chem.* **2010**, *82*, 9626-9630.
25. Wei, W. Y.; White, I. M., Inkjet-Printed Paper-Based SERS Dipsticks and Swabs for Trace Chemical Detection. *Analyst* **2013**, *138*, 1020-1025.
26. Zhu, Y.; Li, M.; Yu, D.; Yang, L., A Novel Paper Rag as 'D-SERS'substrate for Detection of Pesticide Residues at Various Peels. *Talanta* **2014**, *128*, 117-124.
27. Huang, Z.; Cao, G.; Sun, Y.; Du, S.; Li, Y.; Feng, S.; Lin, J.; Lei, J., Evaluation and Optimization of Paper-Based SERS Substrate for Potential Label-Free Raman Analysis of Seminal Plasma. *Journal of Nanomaterials* **2017**, 1-8.
28. Wei, W. Y.; White, I. M., Chromatographic Separation and Detection of Target Analytes from Complex Samples Using Inkjet Printed SERS Substrates. *Analyst* **2013**, *138*, 3679-3686.
29. Zhang, W.; Li, B.; Chen, L.; Wang, Y.; Gao, D.; Ma, X.; Wu, A., Brushing, a Simple Way to Fabricate SERS Active Paper Substrates. *Anal. Methods* **2014**, *6*, 2066-2071.
30. Lee, C. H.; Hankus, M. E.; Tian, L.; Pellegrino, P. M.; Singamaneni, S., Highly Sensitive Surface Enhanced Raman Scattering Substrates Based on Filter Paper Loaded with Plasmonic Nanostructures. *Anal. Chem.* **2011**, *83*, 8953-8958.
31. Oliveira, M. J.; Quaresma, P.; Peixoto de Almeida, M.; Araújo, A.; Pereira, E.; Fortunato, E.; Martins, R.; Franco, R.; Águas, H., Office Paper Decorated with Silver Nanostars - an Alternative Cost Effective Platform for Trace Analyte Detection by SERS. *Sci. Rep.* **2017**, *7*, 2480.
32. Wang, C.; Liu, B.; Dou, X., Silver Nanotriangles-Loaded Filter Paper for Ultrasensitive SERS Detection Application Benefited by Interspacing of Sharp Edges. *Sens. Actuators, B* **2016**, *231*, 357-364.
33. Meng, Y.; Lai, Y.; Jiang, X.; Zhao, Q.; Zhan, J., Silver Nanoparticles Decorated Filter Paper Via Self-Sacrificing Reduction for Membrane Extraction Surface-Enhanced Raman Spectroscopy Detection. *Analyst* **2013**, *138*, 2090-2095.

34. Wang, Q.; Zhao, X.; Yu, Z.; Tan, R.; Lan, J., Large Scale Preparation of Surface Enhanced Raman Spectroscopy Substrates Based on Silver Nanowires for Trace Chemical Detection. *Anal. Methods* **2015**, *7*, 10359-10363.
35. Lee, C. H.; Tian, L.; Singamaneni, S., Based SERS Swab for Rapid Trace Detection on Real-World Surfaces. *ACS Appl. Mater. & Interf.* **2010**, *2*, 3429-3435.
36. Ross, M. B.; Ashley, M. J.; Schmucker, A. L.; Singamaneni, S.; Naik, R. R.; Schatz, G. C.; Mirkin, C. A., Structure–Function Relationships for Surface-Enhanced Raman Spectroscopy-Active Plasmonic Paper. *J. Phys. Chem. C* **2016**, *120*, 20789-20797.
37. Kim, W.-S.; Shin, J.-H.; Park, H.-K.; Choi, S., A Low-Cost, Monometallic, Surface-Enhanced Raman Scattering-Functionalized Paper Platform for Spot-on Bioassays. *Sens. Actuators, B* **2016**, *222*, 1112-1118.
38. Ashley, M. J.; Bourgeois, M. R.; Murthy, R. R.; Laramy, C. R.; Ross, M. B.; Naik, R. R.; Schatz, G. C.; Mirkin, C. A., Shape and Size Control of Substrate-Grown Gold Nanoparticles for Surface-Enhanced Raman Spectroscopy Detection of Chemical Analytes. *The Journal of Physical Chemistry C* **2017**, *4*, 2307-2314.
39. Hu, S.-W.; Qiao, S.; Pan, J.-B.; Kang, B.; Xu, J.-J.; Chen, H.-Y., A Paper-Based SERS Test Strip for Quantitative Detection of Mucin-1 in Whole Blood. *Talanta* **2018**, *179*, 9-14.
40. Liu, Q.; Wang, J.; Wang, B.; Li, Z.; Huang, H.; Li, C.; Yu, X.; Chu, P. K., Paper-Based Plasmonic Platform for Sensitive, Noninvasive, and Rapid Cancer Screening. *Biosens. Bioelectron.* **2014**, *54*, 128-134.
41. Fierro-Mercado, P. M.; Hernández-Rivera, S. P., Highly Sensitive Filter Paper Substrate for SERS Trace Explosives Detection. *International Journal of Spectroscopy* **2012**, 1-7.
42. Zhu, J.; Chen, Q.; Kutsanedzie, F. Y.; Yang, M.; Ouyang, Q.; Jiang, H., Highly Sensitive and Label-Free Determination of Thiram Residue Using Surface-Enhanced Raman Spectroscopy (SERS) Coupled with Paper-Based Microfluidics. *Anal. Methods* **2017**, *9*, 6186-6193.
43. Yang, C.; Xu, Y.; Wang, M.; Li, T.; Huo, Y.; Yang, C.; Man, B., Multifunctional Paper Strip Based on GO-Veiled Ag Nanoparticles with Highly SERS Sensitive and Deliverable Properties for High-Performance Molecular Detection. *Opt. Express* **2018**, *26*, 10023-10037.
44. Polavarapu, L.; Porta, A. L.; Novikov, S. M.; Coronado-Puchau, M.; Liz-Marzán, L. M., Pen-on-Paper Approach toward the Design of Universal Surface Enhanced Raman Scattering Substrates. *Small* **2014**, *10*, 3065-3071.
45. Zhou, R.; Wu, Z.; Sun, Z.; Su, X., Sensitive Surface Enhanced Raman Scattering Substrates Based on Filter Paper Loaded with Au Porous Nanospheres. *Nanoscience and Nanotechnology Letters* **2015**, *7*, 801-805.
46. Ngo, Y. H.; Li, D.; Simon, G. P.; Garnier, G., Gold Nanoparticle–Paper as a Three-Dimensional Surface Enhanced Raman Scattering Substrate. *Langmuir* **2012**, *28*, 8782-8790.
47. Abbas, A.; Brimer, A.; Slocik, J. M.; Tian, L.; Naik, R. R.; Singamaneni, S., Multifunctional Analytical Platform on a Paper Strip: Separation, Preconcentration, and Subattomolar Detection. *Anal. Chem.* **2013**, *85*, 3977-3983.
48. Hoppmann, E. P.; Wei, W. Y.; White, I. M., Highly Sensitive and Flexible Inkjet Printed SERS Sensors on Paper. *Methods* **2013**, *63*, 219-224.
49. Mehn, D.; Morasso, C.; Vanna, R.; Bedoni, M.; Prosperi, D.; Gramatica, F., Immobilised Gold Nanostars in a Paper-Based Test System for Surface-Enhanced Raman Spectroscopy. *Vib. Spectrosc.* **2013**, *68*, 45-50.

50. Das, D.; Senapati, S.; Nanda, K. K., "Rinse, Repeat": An Efficient and Reusable SERS and Catalytic Platform Fabricated by Controlled Deposition of Silver Nanoparticles on Cellulose Paper. *ACS Sustain Chem Eng* **2019**, *16*, 14089-14101.
51. Oh, K.; Lee, M.; Lee, S. G.; Jung, D. H.; Lee, H. L., Cellulose Nanofibrils Coated Paper Substrate to Detect Trace Molecules Using Surface-Enhanced Raman Scattering. *Cellulose* **2018**, *25*, 3339-3350.
52. Xian, L.; You, R.; Lu, D.; Wu, C.; Feng, S.; Lu, Y., Surface-Modified Paper-Based SERS Substrates for Direct-Droplet Quantitative Determination of Trace Substances. *Cellulose* **2020**, *27*, 1483-1495.
53. Kim, W.; Kim, Y.-H.; Park, H.-K.; Choi, S., Facile Fabrication of a Silver Nanoparticle Immersed, Surface-Enhanced Raman Scattering Imposed Paper Platform through Successive Ionic Layer Absorption and Reaction for on-Site Bioassays. *ACS Appl. Mater. & Interf.* **2015**, *7*, 27910-27917.
54. Kumar, A.; Santhanam, V., Paper Swab Based SERS Detection of Non-Permitted Colourants from Dals and Vegetables Using a Portable Spectrometer. *Anal. Chim. Acta* **2019**, *1090*, 106-113.
55. Lan, L.; Hou, X.; Gao, Y.; Fan, X.; Qiu, T., Inkjet-Printed Paper-Based Semiconducting Substrates for Surface-Enhanced Raman Spectroscopy. *Nanotechnology* **2020**, *31*, 055502.
56. Li, B.; Zhang, W.; Chen, L.; Lin, B., A Fast and Low-Cost Spray Method for Prototyping and Depositing Surface-Enhanced Raman Scattering Arrays on Microfluidic Paper Based Device. *Electrophoresis* **2013**, *34*, 2162-2168.
57. Ma, Y.; Wang, Y.; Luo, Y.; Duan, H.; Li, D.; Xu, H.; Fodjo, E. K., Rapid and Sensitive on-Site Detection of Pesticide Residues in Fruits and Vegetables Using Screen-Printed Paper-Based SERS Swabs. *Anal. Methods* **2018**, *10*, 4655-4664.
58. Kwon, G.; Kim, J.; Kim, D.; Ko, Y.; Yamauchi, Y.; You, J., Nanoporous Cellulose Paper-Based SERS Platform for Multiplex Detection of Hazardous Pesticides. *Cellulose* **2019**, *26*, 4935-4944.
59. Park, M.; Hwang, C. S. H.; Jeong, K.-H., Nanoplasmonic Alloy of Au/Ag Nanocomposites on Paper Substrate for Biosensing Applications. *ACS Appl. Mater. & Interf.* **2017**, *10*, 290-295.
60. Luo, W.; Chen, M.; Hao, N.; Huang, X.; Zhao, X.; Zhu, Y.; Yang, H.; Chen, X., In Situ Synthesis of Gold Nanoparticles on Pseudo-Paper Films as Flexible SERS Substrate for Sensitive Detection of Surface Organic Residues. *Talanta* **2019**, *197*, 225-233.
61. Zeng, F.; Duan, W.; Zhu, B.; Mu, T.; Zhu, L.; Guo, J.; Ma, X., Paper-Based Versatile Surface-Enhanced Raman Spectroscopy Chip with Smartphone-Based Raman Analyzer for Point-of-Care Application. *Anal. Chem.* **2019**, *91*, 1064-1070.
62. Niu, Z.; Fang, Y., Surface-Enhanced Raman Scattering of Single-Walled Carbon Nanotubes on Silver-Coated and Gold-Coated Filter Paper. *J. Colloid Interface Sci.* **2006**, *303*, 224-228.
63. Yu, C.-C.; Chou, S.-Y.; Tseng, Y.-C.; Tseng, S.-C.; Yen, Y.-T.; Chen, H.-L., Single-Shot Laser Treatment Provides Quasi-Three-Dimensional Paper-Based Substrates for SERS with Attomolar Sensitivity. *Nanoscale* **2015**, *7*, 1667-1677.
64. Atanasov, P. A.; Nedyalkov, N. N.; Fukata, N.; Jevasuwan, W.; Subramani, T.; Terakawa, M.; Nakajima, Y., Surface-Enhanced Raman Spectroscopy (SERS) of Mancozeb and Thiamethoxam Assisted by Gold and Silver Nanostructures Produced by Laser Techniques on Paper. *Appl. Spectros.* **2019**, *73*, 313-319.

65. Villa, J. E.; Quiñones, N. R.; Fantinatti-Garboggini, F.; Poppi, R. J., Fast Discrimination of Bacteria Using a Filter Paper–Based SERS Platform and PLS-DA with Uncertainty Estimation. *Anal. Bioanal. Chem* **2019**, *411*, 705-713.
66. Weng, G.; Feng, Y.; Zhao, J.; Li, J.; Zhu, J.; Zhao, J., Size Dependent SERS Activity of Ag Triangular Nanoplates on Different Substrates: Glass Vs Paper. *Appl. Surf. Sci.* **2019**, *478*, 275-283.
67. Zhang, C.; You, T.; Yang, N.; Gao, Y.; Jiang, L.; Yin, P., Hydrophobic Paper-Based SERS Platform for Direct-Droplet Quantitative Determination of Melamine. *Food Chem.* **2019**, *287*, 363-368.
68. Deng, D.; Lin, Q.; Li, H.; Huang, Z.; Kuang, Y.; Chen, H.; Kong, J., Rapid Detection of Malachite Green Residues in Fish Using a Surface-Enhanced Raman Scattering-Active Glass Fiber Paper Prepared by in Situ Reduction Method. *Talanta* **2019**, *200*, 272-278.
69. He, S.; Chua, J.; Tan, E. K. M.; Kah, J. C. Y., Optimizing the SERS Enhancement of a Facile Gold Nanostar Immobilized Paper-Based SERS Substrate. *RSC Adv.* **2017**, *7*, 16264-16272.
70. Ngo, Y. H.; Li, D.; Simon, G. P.; Garnier, G., Effect of Cationic Polyacrylamides on the Aggregation and SERS Performance of Gold Nanoparticles-Treated Paper. *J. Colloid Interface Sci.* **2013**, *392*, 237-246.
71. Weng, G.; Yang, Y.; Zhao, J.; Zhu, J.; Li, J.; Zhao, J., Preparation and SERS Performance of Au NP/Paper Strips Based on Inkjet Printing and Seed Mediated Growth: The Effect of Silver Ions. *Solid State Communications* **2018**, *272*, 67-73.
72. Zeng, F.; Mou, T.; Zhang, C.; Huang, X.; Wang, B.; Ma, X.; Guo, J., Paper-Based SERS Analysis with Smartphones as Raman Spectral Analyzers. *Analyst* **2019**, *1*, 137-142.
73. Susu, L.; Campu, A.; Craciun, A.; Vulpoi, A.; Astilean, S.; Focsan, M., Designing Efficient Low-Cost Paper-Based Sensing Plasmonic Nanoplatforms. *Sensors* **2018**, *18*, 3035.
74. Nedyalkov, N.; Dikovska, A.; Nikov, R.; Atanasov, P.; Sliwinski, G.; Hirsch, D.; Rauschenbach, B., Laser-Induced Nanoparticle Fabrication on Paper. *Appl. Phys. A* **2017**, *123*, 570.
75. Chamuah, N.; Hazarika, A.; Hatiboruah, D.; Nath, P., SERS on Paper: An Extremely Low Cost Technique to Measure Raman Signal. *J. Phys. D: Appl. Phys.* **2017**, *50*, 485601.
76. Weatherston, J. D.; Seguban, R. K. O.; Hunt, D.; Wu, H.-J., Low-Cost and Simple Fabrication of Nanoplasmonic Paper for Coupled Chromatography Separation and Surface Enhanced Raman Detection. *ACS Sensors* **2018**, *3*, 852-857.
77. Zhang, K.; Zhao, J.; Xu, H.; Li, Y.; Ji, J.; Liu, B., Multifunctional Paper Strip Based on Self-Assembled Interfacial Plasmonic Nanoparticle Arrays for Sensitive SERS Detection. *ACS Appl. Mater. & Interf.* **2015**, *7*, 16767-16774.
78. Desmonda, C.; Kar, S.; Tai, Y., Formation of Gold Nanostructures on Copier Paper Surface for Cost Effective SERS Active Substrate – Effect of Halide Additives. *Appl. Surf. Sci.* **2016**, *367*, 362-369.
79. Joshi, P.; Santhanam, V., Paper-Based SERS Active Substrates on Demand. *RSC Adv.* **2016**, *6*, 68545-68552.
80. Lee, M.; Oh, K.; Choi, H.-K.; Lee, S. G.; Youn, H. J.; Lee, H. L.; Jeong, D. H., Subnanomolar Sensitivity of Filter Paper-Based SERS Sensor for Pesticide Detection by Hydrophobicity Change of Paper Surface. *ACS Sensors* **2018**, *3*, 151-159.
81. Wu, M.; Li, P.; Zhu, Q.; Wu, M.; Li, H.; Lu, F., Functional Paper-Based SERS Substrate for Rapid and Sensitive Detection of Sudan Dyes in Herbal Medicine. *Spectrochimica Acta Part A: Molecular and Biomolecular Spectroscopy* **2018**, *196*, 110-116.

82. Zheng, G.; Polavarapu, L.; Liz-Marzan, L. M.; Pastoriza-Santos, I.; Perez-Juste, J., Gold Nanoparticle-Loaded Filter Paper: A Recyclable Dip-Catalyst for Real-Time Reaction Monitoring by Surface Enhanced Raman Scattering. *Chem. Commun.* **2015**, *51*, 4572-4575.
83. Hasi, W.-L.-J.; Lin, X.; Lou, X.-T.; Lin, S.; Yang, F.; Lin, D.-Y.; Lu, Z.-W., Chloride Ion-Assisted Self-Assembly of Silver Nanoparticles on Filter Paper as SERS Substrate. *Appl. Phys. A* **2015**, *118*, 799-807.
84. Chen, M.; Yang, H.; Rong, L.; Chen, X., A Gas-Diffusion Microfluidic Paper-Based Analytical Device ([Small Mu]Pad) Coupled with Portable Surface-Enhanced Raman Scattering (SERS): Facile Determination of Sulphite in Wines. *Analyst* **2016**, *141*, 5511-5519.
85. Díaz-Liñán, M.; García-Valverde, M.; López-Lorente, A.; Cárdenas, S.; Lucena, R., Silver Nanoflower-Coated Paper as Dual Substrate for Surface-Enhanced Raman Spectroscopy and Ambient Pressure Mass Spectrometry Analysis. *Anal. Bioanal. Chem* **2020**, 1-11.
86. https://www.stellarnet.us/spectrometers-accessories/sers-substrates/.
87. https://www.horiba.com/en_en/products/detail/action/show/product/sers-substrates-1635/.
88. https://www.sersitive.eu/.
89. http://enspectr.com/portfolio/sers-substrates/.
90. https://www.silmeco.com/products/sers-substrate-serstrate/.
91. https://www.hamamatsu.com/jp/en/product/optical-components/sers-substrate/index.html.
92. https://integratedoptics.com/products/sers-substrates
93. https://www.trademed.com/products/6451/sers-substrates.html.
94. https://www.metrohm.com/en-in/products-overview/bwt-840000620.
95. http://www.q-sers.com/q.html.

Intentional blank page

Appendix-B

Commercial DVDs loaded with Au NPs for SERS based sensing

Motivation

The SERS research community is seriously working on versatile, cost-effective, robust substrates to make it readily available for all practical purposes (detection of hazardous materials, pesticides, contaminants, etc.). Nowadays, a massive number of CDs and DVDs have entered into a commercial world and, subsequently, they are transformed into nothing more than simple electronic waste. This electronic waste creates serious environmental pollution and has become a significant global issue. In this work, we explore the possibility of utilizing used (written) digital versatile disks (DVDs) as SERS platforms.

Experimental details

Both blank DVD [DVD-R (Rewritable) from FronTech (4.7 GB, Dual Layer)] and the data written DVD SERS performances were verified. The substrates were prepared by carefully peeling-off the protecting layer on DVD with a tweezer and was cut into small squares (sizes of ~1 cm^2). The polycarbonate layer on DVD was removed with ultra-sonication in ethanol and propanol solvents. Six different samples were prepared and labeled as (i) Blank DVD (DVD-B) (ii) Blank DVD cleaned in ethanol (DVD-B-Ethanol) (iii) Blank DVD cleaned in ethanol and propanol (DVD-B-Ethanol-Propanol) (iv) Written DVD (DVD-W) (v) Written DVD cleaned in ethanol (DVD-W-Ethanol) and (vi) Written DVD cleaned in ethanol and propanol (DVD-W-Ethanol-Propanol).

Fabrication of Au NPs

The femtosecond laser pulse (~50 fs, 1 kHz, 800 nm) ablation of Au target in distilled water was utilized to fabricate the pure Au NPs. [This was performed following the procedure mentioned in chapter 5A]. Typically 20 µl of Au NPs solution were drop-casted on the prepared DVD pieces and allowed for drying and examined SERS performance.

Results and discussions

FESEM characterization

The surface morphological studies of DVD-B and DVD-W-Ethanol with Au NPs were performed using the FESEM. DVD-B SEM micrographs are illustrated in figure B.1(a) and (b) depicting the large-scale periodic patterns. All the commercially available BRDVDs have a structural periodicity of 320 nm with a channel width of 100 nm. Such a structure is ideal for trapping of MNPs in the width of the channels.[1] The Ag film on DVD grating topography may generate the propagating SPPs. [1-2] Figures B.1(c) and B.1(d) depict the Au NPs distribution on DVD-W-Ethanol substrate at different magnifications. The micrographs presented revealed the distribution of Au NPs along the lines of DVD and aggregation within the patterned edge of the valleys.[3]

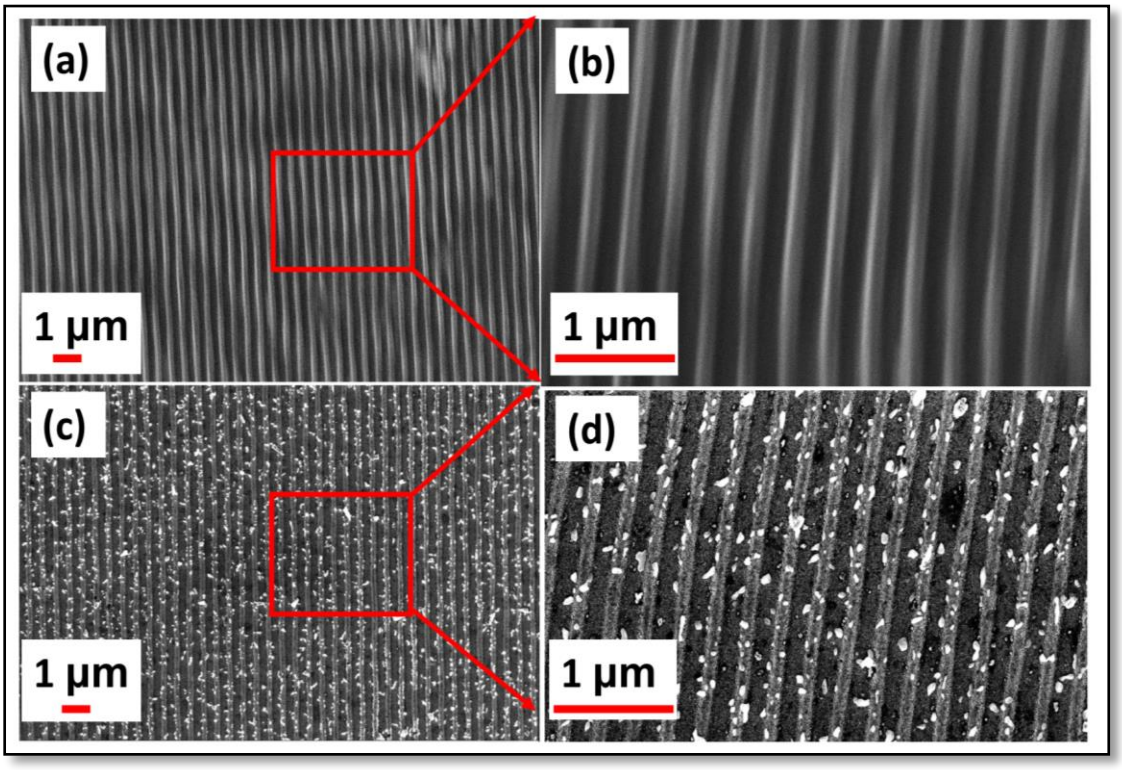

Figure B. 1 FESEM images of DVD-B at (a) lower and (b) higher magnification. FESEM images of DVD-W-Ethanol with Au NPs (c) lower and (d) higher magnifications.

SERS studies

Primarily, the SERS performance of DVDs substrates was examined with commonly used rigid platforms, i.e., glass slide and silicon wafer. Nile blue (NB-500 nM) was selected as an analyte molecule to evaluate the DVD as a base SERS substrate efficiency. Figure B.2(a) shows the appearance of the Raman peak (at 590 cm^{-1}) and this was observed only from the DVD while no significant Raman signatures were noticed from glass slide and Si wafer, which could be because of the presence of metallic coating (Ag film) and grooved pattern on the DVD. Figure B.2(b) demonstrates the collected Raman spectra of all six DVD samples. After cleaning in propanol (which means the removal of the metallic film along with the polycarbonate layer), we observed a rise in the Raman peaks from the base, as shown in figure B.2(b) and highlighted in grey color. The Raman spectra of NB-5×10^{-7} M on all six DVD substrates are presented in figure B.2(c). Figure B.2(d) shows the histogram plot of the observed intensities of the NB prominent peak (590 cm^{-1}) from six samples. DVD-B and DVD-W cleaned in ethanol demonstrated superior performance because the polycarbonate layer was dissolved in ethanol, and the metallic film (Ag) acted as a SERS sensor and provided a better enhancement of the Raman signal.

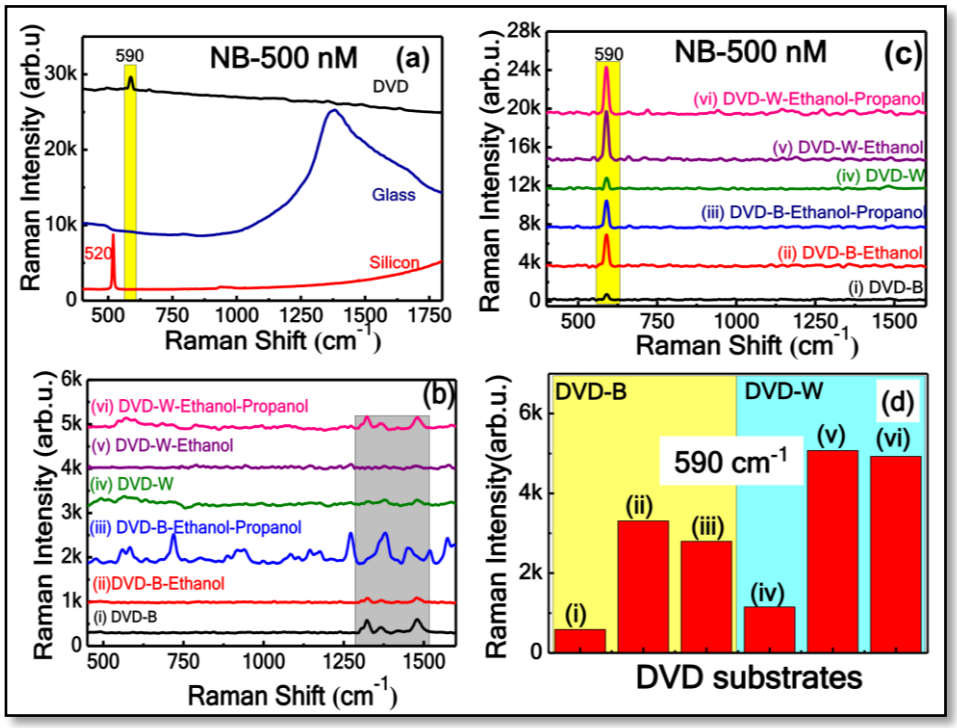

Figure B. 2 (a) Raman spectra of NB 500 nM on three solid substrates (b) Raman spectra of DVD (Blank and written) under different conditions (c) Raman spectra of NB on six different DVD substrates (d) NB 590 cm^{-1} peak intensity histogram on those six DVD substrates.

SERS performance of DVD-W substrates with Au NPs

The superior substrate DVD-W-Ethanol was further examined with fs-laser fabricated Au NPs deposition. Four dye molecules [R6G (5 ×10^{-6} M), MB (50×10^{-9} M) NB (50×10^{-9} M), and CV (50×10^{-9} M)] were considered and the corresponding spectra with and without Au NPs on DVD-W-ethanol are shown in figures B.3 (a)-(d), respectively. After drop-casting of the Au NPs, the intensity the Raman peaks increased and we observed that the EF's for R6G, NB, MB, and CV were increased by ~3 times in the existence of Au NPs on the DVD substrate.

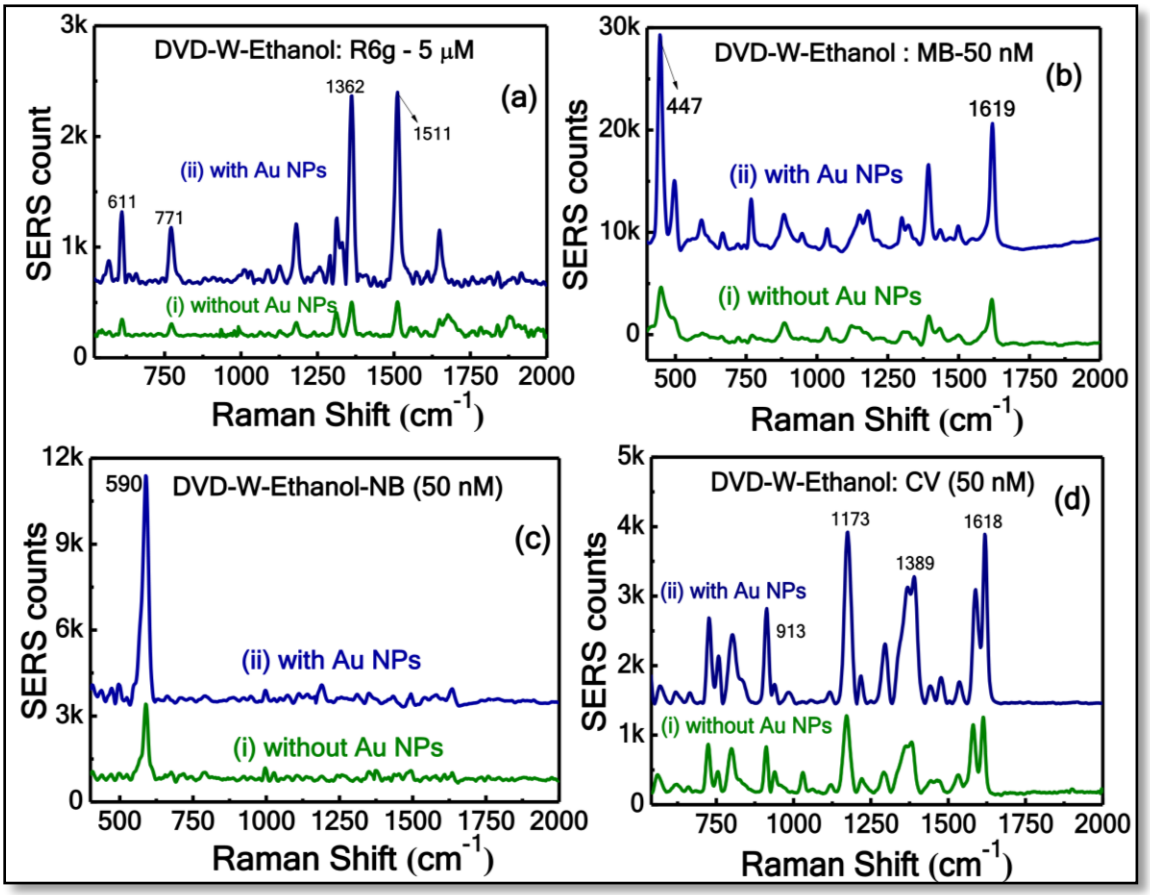

Figure B. 3 SERS of DVD-W-ethanol substrate (i) without and (ii) with Au NPs (a) R6g (5 µM) (b) MB (50 nM) (c) NB (50 nM) and (d) CV (50 nM)

Further, the DVD-W-ethanol substrate was prepared by drop-casting the Au NPs and its SERS sensitivity was explored by recording the Raman spectra of NB molecule with different concentrations ranging from 5 µM to 1 nM. Figures B.4(a)-B.4(d) depicts the SERS sensitivity and reproducibility studies using DVD-W-ethanol and Au NPs. Figure B.4(b) illustrates the linear calibration curve for the 590 cm^{-1} mode intensity versus the concentration of NB molecule. The obtained linear fitted with equation logI=6.9+0.4logC

with an adjusted correlation coefficient (R^2) of ~0.93. Clearly, the most prominent peak of NB was identified even at 1 nM concentration, revealing the superior sensitivity of the substrates. In addition to sensitivity, reproducibility is also an important factor in appraising the SERS efficiency. SERS spectra were collected from more than 10 random locations on DVD substrate, the corresponding intensity histogram of 590 cm^{-1} peak illustrated in figure B.4(c) and (d). The obtained RSD was ~10.46 % along with the achieved enhancement factor of 1.4×10^9 for the NB (1 nM concentration).

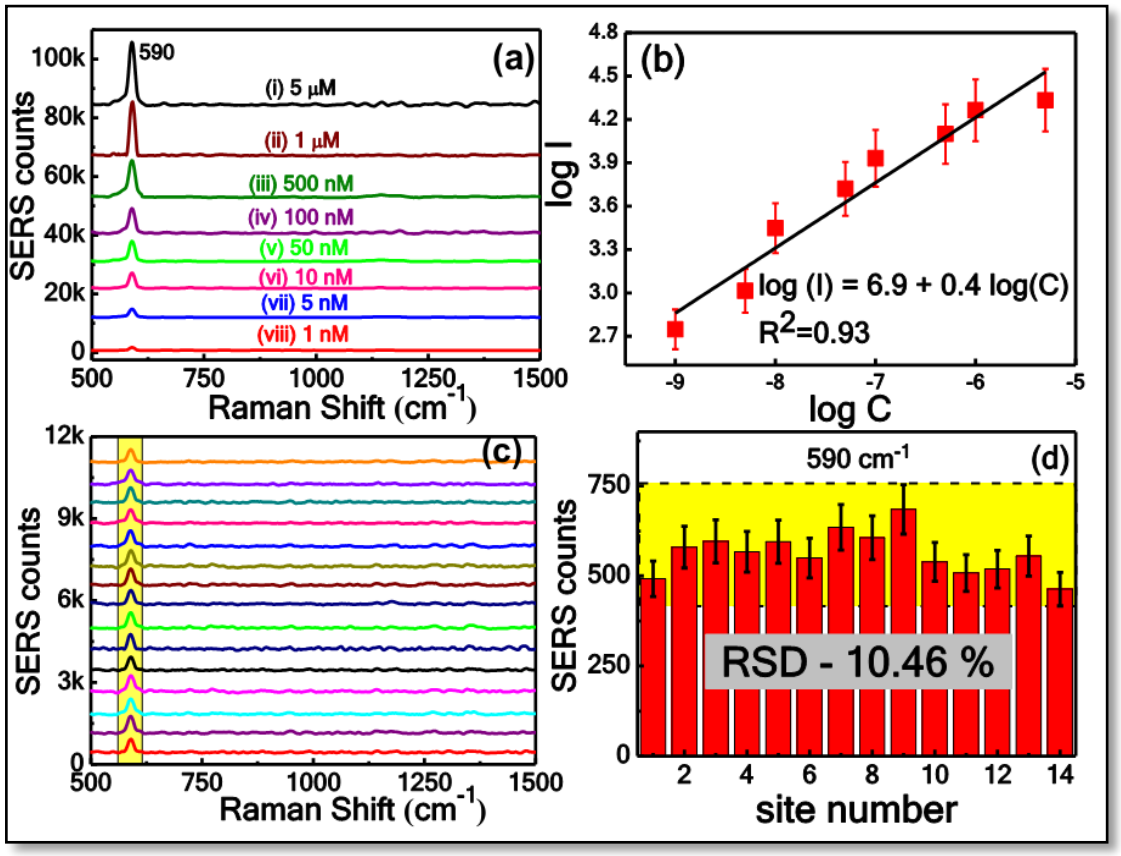

Figure B. 4 (a) SERS spectra for the varying concentration of NB (5 µM to 1 nM). (b) log I versus log C plot of NB peak 590 cm^{-1} (c) Reproducibility spectra of NB (1 nM) from 14 random locations (d) The corresponding intensity variation histogram with an RSD of 10.46%.

Conclusions

In this work, the new SERS active substrates were studied with cost-effective and easily available DVDs along with Au NPs. The polycarbonate film on DVD was peeled off and we performed ultrasonication in ethanol. Both written and blank DVD cleaned in ethanol and propanol were used as SERS substrates towards the detection of NB-500 nM. The

SEM micrographs revealed the grating patterns of DVDs could be utilized to trap Au NPs. The presence of Au NPs on the DVD-W sample was verified with the detection of four dye molecules R6G (5 $\times 10^{-6}$ M), MB (50×10^{-9} M) NB (50×10^{-9} M), and CV (50×10^{-9} M). The Raman signal intensity increased by ~3 times in the presence of Au NPs on the DVD substrate. The metallic film on the patterned surface and the Au NPs present on the DVD possibly favored the phenomenon of propagating and localized surface plasmons, which eventually led to enhancements of electric fields. The drop-casted Au NPs were trapped in these channel patterns and induce aggregation. The written DVD with Au NPs was able to detect NB having a concentration of 1 nM along with an intensity variation of ~10.46% (RSD) was observed. The written DVDs can be considered as low-cost, easy and efficient SERS substrates. This technique can be further exploited in order to detect the explosives, which is the course of our future work.

References

1. Chamuah, N.; Saikia, A.; Joseph, A. M.; Nath, P., Blu-Ray DVD as SERS Substrate for Reliable Detection of Albumin, Creatinine, and Urea in Urine. *Sensors and Actuators B Chemical* **2019**, *285*, 108-115.
2. Giallongo, G.; Pilot, R.; Durante, C.; Rizzi, G. A.; Signorini, R.; Bozio, R.; Gennaro, A.; Granozzi, G., Silver Nanoparticle Arrays on a DVD-Derived Template: An Easy&Cheap Sers Substrate. *Plasmonics* **2011**, *6*, 725.
3. Binczyk, M.; Nowak, M.; Skrobanska, M.; Tylkowski, B.; Runka, T.; Jastrzab, R., Silver Cd-R Based Substrate as a SERS Active Material. *Journal of the Iranian Chemical Society* **2016**, *13*, 841-845.

List of Publications

1. **M.S.S. Bharati**, S. Abdul Kalam, B. Chandu, S. Hamad, S. Venugopal Rao, "Instantaneous Trace Detection of Nitro-explosives and Mixtures with Nanotextured Silicon Decorated with Ag-Au Alloy Nanoparticles using the SERS Technique," *Analytica Chimica Acta* **1101,** 157-168, 2020.
2. **M.S.S. Bharati**, B. Chandu, S. Venugopal Rao, "Gold Nanoparticles and Nanostars Loaded Paper-based SERS Substrates for Sensing Nanogram-level Picric Acid with a Portable Raman Spectrometer," *Bulletin of Materials Science,* **43,** 53, 2020
3. **M.S.S. Bharati,** B. Chandu, S. Venugopal Rao, "Explosives Detection Using Ag-Cu alloy Nanoparticles Synthesized by Femtosecond Laser Ablation and Irradiation," *RSC Advances,* **9(3),** 1517-1525, 2019.
4. **M.S.S. Bharati,** B. Chandu, N.S. Sini, Ch. Bindumadhuri, S. Venugopal Rao, "Ag/Au Nanoparticle Loaded Paper-based Versatile SERS Substrates for Explosives Detection," *ACS Omega,* **3,** 8190-8201, 2018.
5. **M.S.S. Bharati,** B. Chandu, S. Venugopal Rao, "Femtosecond Laser Fabricated Ag@Au and Cu@Au Alloy Nanoparticles for SERS based Explosives Detection," *Frontiers in Physics (Optics and Photonics),* **6,** Art # 28, 2018.
6. **M.S.S. Bharati,** S. Bhattacharya, L. Giribabu, S. Venugopal Rao, "Femtosecond, Broadband NLO studies of a Zinc porphyrin and a Zinc phthalocyanine," Optics and Laser Technology, 108, 418-425, 2018.

Book chapter

7. S. Venugopal Rao, S. Abdul Kalam**, M.S.S. Bharati**, "Photonics for explosives detection," **Wiley Encyclopedia of Applied Physics, 1-31, 2019**. **(Book Chapter)** http://dx.doi.org/10.1002/3527600434.eap826

Conference Proceedings

8. **M.S.S. Bharati,** B. Chandu, P. Lakshmi, S. Venugopal Rao, "Commercial DVDs loaded with Femtosecond Laser Prepared Gold Nanoparticles as SERS Substrates," *IEEE WRAP-2019 Proc.,* 1-3, 2019.
9. **M. S. S. Bharati,** B. Chandu, K Nehra, P. S. Kumar, and S Venugopal Rao, Filter Paper Loaded with Gold Nanoparticles as Flexible SERS Substrates for Sensing Applications, *AIP Conf. Proc.*, 2020, In Press.
10. **M.S.S. Bharati**, Somdatta Bhattacharya, Giribabu Lingamallu, and Venugopal Rao Soma, "Broadband, Ultrafast Nonlinear Optical Properties of Porphyrin and Phthalocyanine," 13th International Conference on Fiber Optics and Photonics, December 04-08, (2016)

Co-authored Publications/proceedings

11. B. Chandu, **M.S.S. Bharati**, Pawel Albrycht, S. Venugopal Rao," Fabrication of nanocages on nickel using femtosecond laser ablation and trace level detection of malachite green and Nile blue dyes using surface enhanced Raman spectroscopic technique," Optics and Laser Technology, 2020.
12. A.Mangababua, G.Sarang Dev, B.Chandu, **M.S.S.Bharati**, S.Venugopal Rao, S.V.S.Nageswara Rao, "Fabrication and characterization of GaAs nanoparticles achieved using femtosecond laser ablation," Materials Today: Proceedings, 2020.

13. A.Mangababua, G.Sarang Dev, B.Chandu, **M.S.S.Bharati**, S.Venugopal Rao, S.V.S.Nageswara Rao, "Structural investigations of picosecond laser ablated GaAs nanoparticles in different liquids," Nano-Structures & Nano-Objects, 23, 100509, 2020
14. Athira K, Ranjana M, **M.S.S. Bharati**, Reddy B Narasimha, Babu TG Satheesh, Rao S Venugopal, Kumar Darbha V Ravi," Aggregation Induced, Formaldehyde Tailored Nanowire Like Networks of Cu and Their SERS Activity," Chemical Physics Letters, 748, 137390, 2020.
15. Tania K. Naqvi, **M.S.S.Bharati**, Alok K. Srivastava, Manish M. Kulkarni, Azher M. Siddiqui, S. Venugopal Rao, Prabhat K. Dwivedi, "Femtosecond Laser Textured Silver/Graphene Oxide Hybrid SERS Substrate for Detection of an Explosive Precursor 2,4-DNT," ACS Omega, 4, 17691-17701, 2019.
16. Kamalesh Nehra, P. Senthil Kumar, B. Chandu, **M.S.S. Bharati**, S. Venugopal Rao, "Comparison of Star and Hollow Shaped Au-Ag Alloy Nanoparticles Performance in Catalysis and SERS Applications," J. Phys. Chem. C., 123, 16210-16222, 2019.
17. K.N. Krishnakanth, **M.S.S. Bharati**, Chandu Byram, S.S.K. Raavi, S. Venugopal Rao, "Femtosecond Nonlinear Optical Properties and Ultrafast Excited-State Dynamics of Laser Processed Au and Ag50Au50 Nanoparticles," Optical Materials, 95, 109239, 2019.
18. Kamalesh Nehra, **M.S.S. Bharati**, P. Senthil Kumar, S. Venugopal Rao, "Shape and Size-Controlled Synthesis of Anisotropic Gold Nanostructures: Enhanced Applications in Catalysis and SERS," New J. Chem. 43, 3835-3847, 2019.
19. B. Chandu, **M.S.S. Bharati**, S. Venugopal Rao, "SERS Studies of Gold Coated Periodic Nanostructures on Iron Substrate Achieved by Femtosecond Laser Irradiation in Liquid," J. Raman Spectroscopy, 50, 1103-1113, 2019.
20. B. Chandu, **M.S.S. Bharati**, S. Venugopal Rao, "SERS Based Multiple Analyte Detection from Explosive Mixtures Using Picosecond Laser Fabricated Gold Nanoparticles, Nanostructures," Analyst, 144, 2327-2336 2019.
21. S. Hamad, **M.S.S. Bharati**, G.K. Podagatlapalli, Y. Balaji, M.A. Mohiddon, S.V.S. Nageswara Rao, A.P. Pathak, S. Venugopal Rao, "Femtosecond Laser-induced Nanoparticle Embedded Periodic Surface Structures on Crystalline Silicon for Reproducible and Multiple Utility Surface-Enhanced Raman Scattering Application," ACS Omega, 3(12), 18420-18432, 2019.
22. B. Chandu, **M.S.S. Bharati,** S. Abdul Kalam, S. Venugopal Rao, "Versatile gold-based SERS substrates fabricated by ultrafast laser ablation for sensing picric acid and ammonium nitrate," Chemical Physics Letters, 685, 103-107, 2017.
23. Anil Tumuluri, **M.S.S. Bharati**, S. Venugopal Rao, K.C. James Raju, "Structural, optical and femtosecond third-order nonlinear optical properties of LiNbO3 thin films," Materials Research Bulletin, 94, 342-351, 2017.
24. B. Chandu, **M.S.S. Bharati**, S. Venugopal Rao, "Femtosecond Laser-patterned and Au-coated Iron Surfaces as SERS Platforms for Multiple Analytes Detection," IEEE WRAP-2019 Proc., 1-3, 2019.
25. B. Chandu, **M.S.S. Bharati**, S. Venugopal Rao, "Ag Nanoparticles Coupled with Ag Nanostructures as Efficient SERS Platform for Detection of 2, 4-Dinitrotoluene," IEEE WRAP-2017 Proc., 1-3, 2018.
26. B. Chandu, **M.S.S. Bharati**, S. Venugopal Rao, "Picosecond Laser Fabricated Ag, Au and Ag-Au Nanoparticles for Detecting Ammonium Perchlorate Using a Portable Raman Spectrometer," AIP Conference Proceedings 1942, 050028 (2018)

27. K.N. Krishnakanth, **M.S.S. Bharati**, S. Hamad, S. Venugopal Rao, "Femtosecond Nonlinear Optical Properties of Laser Ablated Gold Nanoparticles in Water," AIP Conference Proceedings 1942, 050122 (2018)
28. Chandu Byram, **M.S.S. Bharati,** and Venugopal Rao Soma, "Gold-Silver Nanostructures Prepared by Femtosecond Ablation for Picric Acid Detection," 13th International Conference on Fiber Optics and Photonics, December 04-08, (2016).

Poster presentation

1. **M.S.S. Bharathi**, B. Chandu, Kamalesh Nehra, Senthil Kumar, and S. Venugopal Rao,"filter paper loaded with Au NPs as flexible SERS substrates for sensing applications", DAESSPS 2019, IIT Jodhpur, 18-22 December 2019.
2. **M.S.S. Bharathi**, B. Chandu, M. Sri Bhavya and S. Venugopal Rao, Third-order Nonlinear Optical Studies of Ti and hybrid Ti-Au Nanoparticles Generated by Laser Ablation in Liquids, XLIII symposium of optical society of India ICOL-2019,IRDE, Dehradun, October 19-22, 2019
3. **M.S.S. Bharathi**, B. Chandu, and S. Venugopal Rao,"Detection of Ammonium Nitrate and Picric Acid using Ag-Cu alloy Nanoparticles Synthesized by Femtosecond Laser Ablation and Irradiation", DAEBRNS (UFS2018). RRCAT, Indore, October 22-24, 2018.
4. B. Chandu, **M.S.S. Bharati,** S. Abdul Kalam, S. Venugopal Rao," Laser synthesized Graphene sheets decorated with Copper Nanoparticles for Detection of 2, 4-Dinitrotolune," National Laser Symposium, (NLS-26, BARC Mumbai, Dec 20-23, 2017),
5. B. Chandu, **M.S.S. Bharati**, S. Venugopal Rao," Ag-Au Bi-metallic Nanoparticles and Nanostructures Fabricated by Femtosecond Laser Ablation for Detection of 2- 4 Dinitrotolune," 11th International High Energy Materials Conference & Exhibits (HEMCE-2017, 23-25 Nov, 2017, HEMRL, Pune. (POSTER)
6. **M.S.S. Bharati**, B. Chandu, N. S. Sini and S. Venugopal Rao, "Versatile SERS Substrates Prepared using Ultrafast Laser Ablation Technique for Explosives Detection" in Ultrafast Science 2017 (UFS-2017), 02-04 November, 2017, University of Hyderabad.
7. S. Venugopal Rao, B. Chandu. **M.S.S. Bharati**, "Nanomaterials prepared using ultrafast laser for explosive detection: A perspective" in National conference on Physics at small scales and Advanced Materials (PSAM-2017), 8-9 Sept 2017, University of Hyderabad.
8. **M.S.S.Bharati**, B.Chandu, S. Venugopal Rao, "Femtosecond nonlinear Optical properties of Ag-Au alloy Nanoparticles", 25th DAE-BRNS National Laser Symposium, KIIT University, Bhubaneswar, 20-23rd December, 2016.

School/Conference/Workshop Attended

i. Science and Engineering Research Board (SERB) School on "Modern optics and its applications" Department of science and technology, IIT patna, Nov 30th-Dec18th (2015).
ii. Symposium on Frontiers in Nanoscience and technology, Center for Nanotechnology, University of Hyderabad, 6-7th April (2018).
iii. Workshop on "development of Binders and Plasticizers for Energetic Applications", ACRHEM, University of Hyderabad, 15th December (2017)

iv. IEEE Workshop on “Recent Advances on photonics-WRAP 2017”, Mahendra Ecole centrale, Hyderabad, 18-19th December (2017).

v. 10th International conference on High Energy Materials Conference & Exhibit, Hyderabad, 11th-13th February (2016).

vi. National conference on ”technologies for sustainable ecosystem”, MJCET, Hyderabad, 26th-27th March (2015)

vii. A National workshop on “Mathematical technology”, MJCET, Hyderabad, 27th-28th June (2014)

viii. National conference on “Absorption and Magnetic resonance spectroscopy and their integration to sustainable human development”, MJCET, Hyderabad, 30th-31st August (2014)

ix. Frontiers of “fundamental physics symposium 2013”, B M Birla Science centre complex, Hyderabad, 14th-16th (2013)

x. A National seminar on” Applied physics and materials science”, Vasavi college of Engineering, Hyderabad, 19th-20th July (2013)

xi. A National seminar on “Nanomaterial and technology” UGC-SKBR college, Amalapuram, 9th -10th Jan (2010)

xii. Pedagogy-A one work shop on microteaching and methodologies, Indo-Us collaboration for Engineering education, March 22 (2009)